Understanding the mechanism of X-ray and optical emission in Be/X-ray binary systems

A thesis submitted in partial fulfilment of

the requirements for the degree of

Doctor of Philosophy

by

Birendra Chhotaray

(Roll No. 19330007)

Under the guidance of

Prof. Sachindranatha Naik

Astronomy and Astrophysics Division

Physical Research Laboratory, Ahmedabad, India.

DEPARTMENT OF PHYSICS

INDIAN INSTITUTE OF TECHNOLOGY GANDHINAGAR

July, 2024

Declaration

I, Birendra Chhotaray, declare that this written submission represents my ideas in my own words. Where others' ideas or words have been included, I have adequately cited and referenced the original sources. I also declare that I have adhered to all principles of academic honesty and integrity and have not misrepresented, fabricated, or falsified any idea/data/fact/source in my submission. I understand that any violation of the above can cause disciplinary action by the Institute and can also evoke penal action from the sources which have thus not been properly cited or from whom proper permission has not been taken when needed.

(Signature)

(Name: Birendra Chhotaray)

(Roll No: 19330007)

Date:

Certificate

It is certified that the work contained in the thesis entitled **"Understanding the mechanism of X-ray and optical emission in Be/X-ray binary systems"** by **Mr. Birendra Chhotaray** (Roll number: 19330007) has been carried out under my supervision and that this work has not been submitted elsewhere for any degree or diploma.

I have read this dissertation and in my opinion, it is fully adequate in scope and quality as a dissertation for the degree of Doctor of Philosophy.

Prof. Sachindranatha Naik
(Thesis Supervisor)

Professor
Astronomy & Astrophysics Division
Physical Research Laboratory
Unit of Department of Space, Govt of India
Ahmedabad-380009, Gujarat, India.

Dedicated

to

My Family

Acknowledgements

As my PhD career draws to a close, I have endeavored to compile all my work, learnings, and knowledge in this thesis. I hope this mini collection will guide someone in the future. PhD is not the same thing that I had expected before joining the degree. It is much longer and deeper than my expectations. I cannot call it a degree; instead, I define it as a way of life. I want to take this opportunity to mention all those people who have selflessly supported and guided me throughout my PhD journey.

I will start with my PhD supervisor, Prof. Sachindranatha Naik, who introduced me to my PhD career. During my MSc, I became fascinated by exotic cosmic sources like neutron stars and black holes after listening to prominent researchers such as Stephen Hawking and Richard Feynman. This motivated me to research these extraordinary objects. Prof. Naik provided me the opportunity to delve deeper into this field, and I began my career as an observational astronomer under his guidance. Midway through my PhD, I realized that the remarkable results published by these prominent researchers are just the visible outcome of extensive background work. Achieving these fascinating results requires immense effort and dedication. I am deeply grateful to Prof. Naik for his continuous support and critical comments, which have been instrumental in my progress. Without his guidance, I would not be in the position I am today.

I express my sincere gratitude to my Doctoral Studies Committee (DSC) members, Dr. Veeresh Singh, Dr. Vishal Joshi, and Dr. Kinsuk Acharyya, for closely monitoring my progress throughout my PhD career. Each DSC meeting has been a humbling experience, reminding me of the vast amount of knowledge still to be learned. Dr. Singh has been consistently critical of my observations and interpretations. Dr. Joshi provided invaluable feedback on understanding the fundamentals of my work and the technical tools I use. Dr. Acharyya encouraged me to develop the skill of explaining complex concepts in a clear and simple manner. I am deeply thankful for their constructive guidance and unwavering support.

I would also like to thank my collaborators for their contributions to the successful completion of the projects I have worked on. I will start with Dr. Gaurava K. Jaisawal, one of my important collaborators, from whom I learned a great deal about professionalism in academic work. His guidance was especially valuable during the rejection of my second paper. We have collaborated on many projects and hope to continue to do so. Special mention goes to Dr. Shivangi Gupta for introducing me to X-ray data analysis during the starting period of my PhD career. Dr. Neeraj Kumari provided crucial guidance on optical observations and discussions on various X-ray phenomena related to AGNs. Dr. Prantik Nandi offered valuable insights into the theoretical aspects of the observational phenomena I studied. Dr. Arghajit Jana supported me in gathering AstroSat data. I also want to thank Mr. Narendranath Layek for our discussion on many topics, including data reduction procedures from new observatories, basic concepts of physical processes, and statistics in astronomy. Dr. Vipin Kumar assisted me with MFOSC-P/MIRO data reduction and solved many critical issues during optical observations from Abu. Finally, I am grateful to Mr. Goldy Ahuja for his help with HFOSC/IAO and LISA data reduction and resolving queries related to IRAF.

I extend my heartfelt gratitude to Prof. Anil Bhardwaj, Director of the Physical Research Laboratory (PRL), for providing the essential facilities for my research. I am sincerely *thankful to the PRL Dean, Academic Committee, Registrar, and Head of Academic Services for their unwavering support during my research tenure at PRL. Additionally, I appreciate Prof. Abhijit Chakraborty, the current Area Chairman of the Astronomy and Astrophysics Division at PRL, for his valuable support within the division. I am deeply indebted to all the faculty members of the Astronomy & Astrophysics division for engaging in academic discussions that enriched my research journey. My sincere thanks also go to my coursework instructors for their guidance and knowledge. Furthermore, I am grateful to the observatory staff at PRL and IAO for their invaluable assistance during observations. I would also like to express my appreciation to the Dean and Head of the Physics Department at the Indian Institute of Technology, Gandhinagar (IITGn), for their extended cooperation throughout my academic pursuits.*

I feel incredibly fortunate to have had the guidance and support of my seniors in the division, who have offered invaluable advice in both my academic and personal life. I would like to express my heartfelt gratitude to Sandeep, Aravind, Abhay, Sushant, and Abhijit for their guidance and encouragement. Special thanks to Naval and Vikas for being available to play every sport.

I am also deeply grateful to my wonderful friends, who have stood by me through the many challenges and joys of my PhD journey. Sharing both pain and happiness with them has been an essential aspect of this experience. My sincere thanks go to Vineet, Kimi, Saumya, Swagatika, Santanu, Neha, Vardaan, Tanya, Sandipan, and Anupam. I would like to give special mention to Vineet and Kimi, with whom I share a unique bond. Our daily tea breaks in the canteen were moments of shared frustration and joy that I will always cherish. Their dedication and hard work in research have been a constant source of inspiration for me. I also must mention my junior, Narendra, with whom I have shared meaningful moments both in and outside the office, discussing professional and personal milestones.

I am also thankful to the members of the PRL family group, the lunch group, the volleyball group, and the football group for their constant companionship, celebrations, and support, transforming even the difficult times into moments of celebration. Special thanks to Akansha, Trinesh, Aditya, Sanjay, Malika, Arup, Kiran, Varsha, Arijit, Saumik, Dibyendu, Anupam, Naval, Vikash, Namita, Sandeep, and Deepak.

My parents and siblings have been a crucial support system throughout my PhD, offering advice and guidance in ways that words cannot fully capture. I am also indebted to my MSc teachers, Prof. Swapna Mahapatra and Prof. Shesansu Sekhar Pal, for their inspiration and encouragement in pursuing a PhD. Finally, I would like to acknowledge my old friends Sonali, Sushree, Tabasum, Smruty, Harekrushna, and Sagar for their unwavering support and valuable time. Last but not least, I thank God for the unseen guidance that has directed me along this path.

- Birendra Chhotaray

Abstract

This thesis centers on the X-ray and optical investigations of Be/X-ray binaries (BeXRBs), the largest subgroup within the high-mass X-ray binaries (HMXBs). Typically, a BeXRB system consists of a neutron star as the compact object and a massive non-supergiant star (with a mass range of 10-20 $M_{\odot}$) acting as the binary companion. In these systems, the neutron stars derive their energy by accreting matter from the circumstellar discs of Be stars, emitting predominantly in the X-ray band of the electromagnetic spectrum. Notably, the companion Be stars in BeXRBs are also bright in optical and infrared wavelengths. These binaries display two distinct types of X-ray outbursts: normal (Type I) and giant (Type II) X-ray outbursts. The Be stars exhibit infrared excess and prominent emission lines such as HI, HeI, and FeII at various stages of their evolution. These emission lines show variability in shape and strength, influenced by the physical properties, orientation, and interactions within the circumstellar disc. Hence, studying these line parameters during transient and quiescent phases can enhance our understanding of the conditions within the circumstellar disc that lead to normal and giant X-ray outbursts from the neutron star.

Accretion-powered pulsars in BeXRBs emit X-ray photons by accreting matter from the circumstellar discs of Be stars. Neutron stars are among the most compact objects in the universe, containing more than a solar mass within a radius of approximately 10 km. This leads to an average density of around 10^{14} g/cm^3, comparable to nuclear matter. Furthermore, these neutron stars possess a surface magnetic field of the order of 10^{12} G, making them the most exotic objects in the universe. Studying the accretion mechanisms in these systems provides a unique opportunity to explore the properties of matter under extreme conditions, which cannot be replicated in laboratory experiments. During accretion, matter from the optical companion interacts with the strong magnetic field of the neutron star and follows the field lines to magnetic poles. This process results in forming an accretion column on top of the magnetic pole of the neutron star, where numerous complex processes give rise to X-ray emissions. The complex physical processes occurring in the accretion column vary significantly with changes in the mass accretion rate. Hence, studying emissions from accreting pulsars offers deeper insights into the dynamics of the accretion column.

In this thesis, we present results from the optical and X-ray studies of the Be/X-ray binary 1A 0535+262/HD 245770 during the October 2020 giant X-ray outburst, using the 1.2 m telescope at the Mount Abu Infrared Observatory and AstroSat, respectively. The peak flux of the source during the outburst is recorded at approximately 11 Crab in the 15-50 keV range, the highest ever observed from the pulsar. We conducted optical observations in the 6000-7200 Å band before, during, and after the X-ray outburst to examine the evolution of the circumstellar disc of the Be star between February 2020 and February 2022. Our optical spectra display prominent emission lines at 6563 Å(HI), 6678 Å(HeI), and 7065 Å(HeI). We observe significant variability in the Hα line, with the single-peaked profile appearing asymmetric with broad red and blue wings before and during the outburst. Post-outburst observations, however, reveal a double-peaked profile with asymmetry in the blue wing. Our pre-outburst observations confirm a larger Be disc that decreased in size as the outburst progressed. Furthermore, the observed variabilities in the Hα line profile and parameters suggest the presence of a highly misaligned, precessing, and warped Be disc.

AstroSat observations of the pulsar detected pulsations at approximately 103.55 s in the light curve up to 110 keV. We find strong energy-dependent pulse profiles with increasing contributions of the pulsing component in hard X-rays. The broadband spectral fitting in the 0.7-90.0 keV range confirmed the presence of the known cyclotron resonance scattering feature at approximately 46.3 keV.

Additionally, we investigate another Be/X-ray binary IGR J06074+2205 during its October and December 2023 X-ray outbursts using NuSTAR and NICER observations. Timing analysis reveals coherent pulsations from the neutron star at approximately 374.60 s. The pulse profiles are found to be strongly dependent on luminosity and energy, highlighting the complex nature of the emitting region. The 3-79 keV NuSTAR spectrum is well-described by a negative and positive power-law with an exponential cutoff model. An iron line at approximately 6.3 keV is detected in the NuSTAR spectra during the brighter phase at a luminosity of 5.56×10^{36} erg s^{-1}. A cyclotron absorption line at 50.7 keV, corresponding to a magnetic field of 5.69×10^{12} G, is detected during the brighter observation. An absorbed power-law model describes each NICER spectrum in the 1-7 keV band. Using the MAXI/GSC light curve, we estimate the possible orbital period of IGR J06074+2205 to be 80 or 80/n (n=2,3,4) days. We also investigate the evolution of the circumstellar disc of the Be star using optical spectroscopic observations between 2022 and 2024 from the Mount Abu Infrared Observatory and the Indian Astronomical Observatory. The optical spectra of the Be star reveal variable Hα and FeII emission lines with an increase in equivalent width with time, indicating the presence of a dynamic circumstellar disc. Our results from optical spectroscopy suggest that the circumstellar disc continuously evolves without any noticeable mass loss, even during the 2023 X-ray outbursts.

A remarkable transient X-ray outburst between 2017 and 2018 led to the discovery of Swift J0243.6+6124. Historically, the Swift/BAT (15-50 keV) telescope detected this source at a flux level of approximately 80 mCrab on 3 October 2017, marking the onset of its 2017-2018 giant X-ray outburst. Swift J0243.6+6124 is considered the first Galactic ultraluminous X-ray (ULX) source due to its intense X-ray luminosity reaching up to an order of 10^{39} erg s^{-1}. This thesis presents the results from detailed X-ray timing and spectral studies of Swift J0243.6+6124 during its giant and normal X-ray outbursts between 2017 and 2023, observed with NICER. Our study focuses on the timing analysis of the source during normal outbursts. A distinct break is detected in the power density spectra of the source, with the corresponding break frequency and slope of power-laws around the break varying with luminosity, indicating changes in accretion dynamics with the mass accretion rate. Interestingly, we detect quasi-periodic oscillations within a specific luminosity range, providing further insights into the underlying physical processes. We also study the spin period evolution of the neutron star and the luminosity variation in pulse profiles during the 2023 outburst. Our spectral analysis covers the giant and all other normal X-ray outbursts. We identify a double transition at luminosities of approximately 7.5×10^{37} and 2.1×10^{38} erg s^{-1} in the evolution of continuum parameters such as photon index and cutoff energy with luminosity. This indicates three distinct accretion modes experienced by the source, particularly during the giant X-ray outburst. A soft blackbody component with a temperature of 0.08-0.7 keV is also detected in the spectra. The observed temperature undergoes a discontinuous transition when the pulsar evolves from a sub- to a super-Eddington state. In addition to an evolving 6-7 keV iron line complex, a 1 keV emission line is observed during the super-Eddington state, implying X-ray reflection from the accretion disc or outflow material.

Through these comprehensive studies, this thesis aims to enhance our understanding on the dynamic and complex processes occurring in Be/X-ray binaries, the cause of the giant X-ray outbursts in these systems, and contributing valuable insights into the behavior of matter under extreme astrophysical conditions.

List of Publications

I. In Refereed Journals included in the Thesis

1. **Chhotaray, Birendra**, Naik, Sachindra, Jaisawal, Gaurava K., Ahuja, Goldy, 2024, **"Optical and X-ray studies of Be/X-ray binary IGR J06074+2205"**, MNRAS, 534, 2830-2847, 10.1093/mnras/stae2282

2. **Chhotaray, Birendra**, Jaisawal, Gaurava K., Nandi, Prantik, Naik, Sachindra, Kumari, Neeraj, Ng, Mason, and C. Gendreau, Keith, 2024, **"Long-term study of the first Galactic ultraluminous X-ray source Swift J0243.6+6124 using NICER"**, ApJ, 963,132, 10.3847/1538-4357/ad235d.

3. **Chhotaray, Birendra**, Jaisawal, Gaurava K., Kumari, Neeraj, Naik, Sachindra, Kumar, Vipin, and Jana, Arghajit, 2023, **"Optical and X-ray studies of Be/X-ray binary 1A 0535+262 during its 2020 giant outburst"**, MNRAS, 518, 5089-510, 10.1093/mnras/stac3354.

II. Additional Publications in Refereed Journals

1. Narendranath Layek, Prantik Nandi, Sachindra Naik, Neeraj Kumari, Arghajit Jana, and **Birendra Chhotaray**, 2024, **"Long-term X-ray temporal and spectral study of a Seyfert galaxy Mrk 6"**, MNRAS, 528, 5269-5285, 10.1093/mnras/stae299.

2. Jaisawal, G. K., Vasilopoulos, G., Naik, S., Maitra, C., Malacaria, C., **Chhotaray, B.**, Gendreau, K. C., Guillot, S., Ng, M., Sanna, A, 2023, **"On the cyclotron absorption line and evidence of the spectral transition in SMC X-2 during 2022 giant outburst"**, MNRAS, 521, 3951-3961, 10.1093/mnras/stad781.

3. Jana, Arghajit, Naik, Sachindra, Jaisawal, Gaurava K., **Chhotaray, Birendra**, Kumari, Neeraj, Gupta, Shivangi, 2022, **"AstroSat observation of X-ray dips and state transition in the black hole candidate MAXI J1803-298"**, MNRAS, 511, 3922-3936, 10.1093/mnras/stac315.

4. Jaisawal, Gaurava K., Naik, Sachindra, Epili, Prahlad R., **Chhotaray, Birendra**, Jana, Arghajit, Agrawal, P. C., 2021, **"AstroSat observations of eclipsing high mass X-ray binary pulsar OAO 1657-415"**, JAA, 42, 72, 10.1007/s12036-021-09701-x.

5. Jaisawal, Gaurava K., Naik, Sachindra, Gupta, Shivangi, Agrawal, P. C., Jana, Arghajit, **Chhotaray, Birendra**, Epili, Prahlad R, 2021, **"Detection of X-ray pulsations at the lowest observed luminosity of Be/X-ray binary pulsar EXO 2030+375 with AstroSat"**, JAA, 42, 33, 10.1007/s12036-021-09699-2.

6. Jana, Arghajit, Jaisawal, Gaurava K., Naik, Sachindra, Kumari, Neeraj, **Chhotaray, Birendra**, Altamirano, D., Remillard, R. A., Gendreau, Keith C, 2021, **"NICER**

observations of the black hole candidate MAXI J0637-430 during the 2019-2020 outburst", MNRAS, 504, 4793-4805, 10.1093/mnras/stab1231.

Conference proceedings and Astronomer's Telegrams

1. **Chhotaray, Birendra**, Naik, Sachindra, Jaisawal, Gaurava K., and Jana, Arghajit, 2024 **"NuSTAR observation of the SMC pulsar RX J0032.9-7348"**, ATel, 16930,1.

2. Sachindra Naik, **Birendra Chhotaray**, and Neeraj Kumari, 2024, **"Optical spectroscopy of 1A 0535+262 before, during, and after the 2020 giant X-ray outburst"**, Bulletin de la Societe Royale des Sciences de Liege, 93, 657-669, 10.25518/0037-9565.11829.

3. Chatterjee, Arka, Patra, Dusmanta, Jana, Arghajit, Patra, Narendranath, **Chhotaray, Birendra**, Naik, Sachindra, Safi-Harb, Samar,2023, **"uGMRT Monitoring of Swift J1727.8-1613 during the X-ray plateau of its decay phase"**, ATel, 16378,1.

4. Patra, Dusmanta, Jana, Arghajit, Patra, Narendranath, **Chhotaray, Birendra**, Naik, Sachindra, 2023, **"uGMRT observations of the recently discovered black hole X-ray binary candidate Swift J1727.8-3613"**, ATel, 16295,1.

5. Jana, Arghajit, Jaisawal, Gaurava K., **Chhotaray, Birendra**, Naik, Sachindra, Kumari, Neeraj, Gupta, Shivangi, 2021, **"AstroSat Observation of X-ray Binary MAXI J1803-298"**, ATel, 14629,1.

Contents

List of Tables

List of Figures

Physical Constants

Speed of light	$c = 2.997 \times 10^{10}$ cm s^{-1}
Planck constant	$h = 6.626 \times 10^{-27}$ erg s^{-1}
Gravitational constant	$G = 6.672 \times 10^{-8}$ cm^3 g^{-1} s^{-2}
Boltzmann's constant	$k_B = 1.380 \times 10^{-16}$ erg K^{-1}
Mass of electron	$m_e = 9.109 \times 10^{-28}$ g
Mass of proton	$m_p = 1.673 \times 10^{-24}$ g
Parsec	$\mathrm{pc} = 3.086 \times 10^{18}$ cm
Solar Mass	$M_\odot = 1.989 \times 10^{33}$ g
Solar Luminosity	$L_\odot = 3.826 \times 10^{33}$ egs s^{-1}
Solar Radius	$R_\odot = 6.959 \times 10^{10}$ cm

List of Abbreviations

XRB	X-ray binary
HMXB	High mass X-ray binary system
LMXB	Low mass X-ray binary system
ULX	Ultraluminous X-ray source
BH	Black hole
NS	Neutron star
WD	White dwarf
CV	Cataclysmic variable
SGXB	Supergiant X-ray binary
BeXRB	Be/X-ray binary
SMC	Small Magellanic Cloud
LMC	Large Magellanic Cloud
QPO	Quasi-periodic oscillation
RLOF	Roche Lobe overflow
CRSF	Cyclotron resonant scattering feature
XRT	X-ray Telescope
GRB	Gamma-Ray Burst
BAT	Burst Alert Telescope
NuSTAR	Nuclear Spectroscopic Telescope Array
FPM	Focal Plane Module
FWHM	Full width at half maximum
SAA	South Atlantic Anomaly
PDS	Power density spectrum
HXMT	Hard X-ray Modulation Telescope
NICER	Neutron star Interior Composition Explorer mission
XTI	X-ray Timing Instrument
GBM	Gamma-ray Burst Monitor

Chapter 1

Introduction

1.1 X-ray binaries: historical introduction

The history of X-ray binaries (XRBs) dates back to the 1960s. On June 18, 1962, an X-ray instrument comprising three large-area Geiger counters was launched aboard an `Aerobee` rocket. These are sounding rockets designed to carry scientific instruments to altitudes higher than the weather balloons but lower than the satellites. These rockets were used for a variety of scientific and technological experiments. The total flight time of Aerobee rockets is relatively short, often just a few minutes, with the rocket spending only a tiny fraction of that time at its highest altitude. The mission was designed to investigate the production of fluorescence X-rays from the surface of the moon caused by solar X-rays and to explore potential X-ray sources in the night sky. Launching the instrument through the rocket was essential because the atmosphere of the Earth is opaque to X-ray radiation. The total duration of the experiment was 350 seconds, conducted at an altitude exceeding 80 km, unexpectedly discovered the first extra-solar X-ray source, Scorpius X-1 (Sco X-1; Giacconi et al. 1962). Initially, the location of the source remained elusive. However, subsequent observations pinpointed it within the Scorpius constellation, with precision up to 1 arc-minute (Gursky et al., 1966). The name "Scorpius X-1" signifies its location and status as the first extra-solar X-ray source, laying the groundwork for the development of X-ray astronomy. Motivated by this discovery in the following years, various agencies and countries endeavored to identify other cosmic X-ray sources, employing rockets and balloons between 1963 and 1970. These efforts led to the discovery of 40 X-ray sources, including supernova remnants, Crab pulsar, and M87 galaxy. However, the limitations of rocket and balloon experiments, such as short duration and limited field of view, hindered a detailed understanding of these sources.

The first satellite dedicated to X-ray astronomy was `Uhuru`, launched on December 12, 1970, by the National Aeronautics and Space Administration (`NASA`). This was the first satellite of the Small Astronomy Satellite (SAS) series, which lasted for two years. The goal of Uhuru was to scan the entire sky for X-ray sources comprehensively. The satellite was effective in the 2-20 keV energy range, and by the end of the mission, it had cataloged a total of 339 X-ray sources (Forman et al., 1978). The major classes of X-ray sources observed were X-ray binaries, Seyfert galaxies, cluster of galaxies, and possibly supercluster of galaxies.

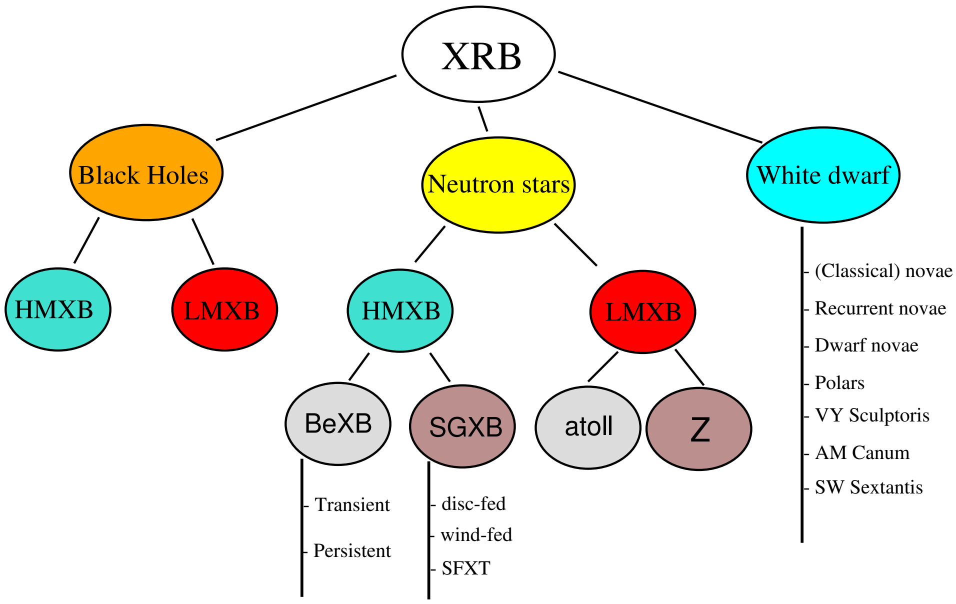

Figure 1.1: Classification of X-ray binaries (XRBs) depicted in a tree diagram, primarily based on the nature of the compact object and the companion star (Reig 2011).

An analysis of one year's worth of data from the X-ray source Centaurus X-3 (Cen X-3) in the Uhuru catalog by Schreier et al. (1972) revealed pulsed emissions with a period of 4.08 seconds, showing a sinusoidal variation over approximately 2.08 days. Additionally, a periodic fluctuation in the flux level was observed, with a periodicity of about 2.08 days. These observations suggested that the compact object is a neutron star and is present in an occulting binary system. This was the first evidence for an X-ray binary system. The following sections discuss the classification and formation of X-ray binaries in more detail.

1.2 X-ray binaries (XRBs): an overview and classification

X-ray binaries (XRBs) are systems consisting of two stars: a compact object (which can be a white dwarf, neutron star, or black hole) and an evolving optical star, both orbiting around a common center of mass (Lewin et al., 1997). The compact object is a strong emitter of X-rays, while the optical star shines brightly in the optical and infrared wavebands. X-ray emission from the compact object occurs through the accretion of mass from the companion star through various processes, as discussed in upcoming sections. In XRB terminology, the compact object is often called the "primary star" or "accretor" (due to its role in mass accretion). In contrast, the optical star is termed the "secondary star" or "donor" (as it donates mass to the compact object). The classification of XRBs is based on the nature of the compact object and its companion star. A comprehensive classification of XRBs is depicted in a tree diagram by Reig (2011) (see Figure 1.1).

As illustrated in Figure 1.1, the X-ray binaries (XRBs) are classified into three primary classes based on the nature of the compact objects: Black Hole X-ray Binaries (BH-XRBs), Neutron Star X-ray Binaries (NS-XRBs), and White Dwarf X-ray Binaries (WD-XRBs), also referred to as Cataclysmic Variables (CVs). When the primary star, or the compact object, is a neutron star or black hole, these XRBs can be further categorized based on the mass of the secondary or donor star ($M_{\rm sec}$). Specifically, the high-mass X-ray binaries (HMXBs) feature donor stars with mass $M_{\rm sec} \geq 10\ M_\odot$, while the low-mass X-ray binaries (LMXBs) have donor stars with mass $M_{\rm sec} \leq 1\ M_\odot$. In cases where the compact object is a white dwarf, these XRBs or CVs can be further divided into various sub-classes that depend on their outburst characteristics. Furthermore, there is an additional category of XRBs known as intermediate-mass X-ray binaries (IMXBs), where the mass of the secondary star ($M_{\rm sec}$) falls between 1 and 10 $M_\odot$ (Pfahl et al. 2003).

1.2.1 High mass X-ray binaries (HMXBs)

HMXBs consist of a black hole or neutron star as compact objects or primary stars and high mass companion stars with a mass greater than or equal to 10 $M_\odot$ as secondary stars. The companions are early-type (O & B spectral type) stars. HMXBs are relatively young XRBs with a characteristic age of $\leq 10^7$ years. They are mostly found in spiral galaxies and irregular galaxies where there is a higher star formation rate (Frank et al., 2002). Depending on the nature of O & B-type stars, HMXBs are further divided into two types: Supergiant X-ray binaries (SGXRBs), where the secondary is a supergiant OB star (luminosity class I-II) and Be X-ray binaries (BeXRBs), where the secondary star is a Be star (luminosity class III-V). According to the recent HMXB catalog by Fortin et al. (2023), there are a total of 152 HMXBs and candidates in the Milky Way galaxy. Additionally, Fortin et al. (2023) reports that the galaxy currently contains 52 SGXRBs and 74 BeXRBs.

The formation of an HMXB necessitates the presence of two progenitor stars with an initial mass exceeding 10 $M_\odot$. However, the secondary star may initially have mass below this threshold, provided it acquires sufficient mass from the primary star during its evolution to surpass the threshold. Figure 1.2 illustrates the formation and evolution processes of HMXBs. According to the scenario depicted in Figure 1.2, during the initial stage known as the Zero-age main sequence (ZAMS), the binary comprises two main sequence stars with masses of 14.4 $M_\odot$ and 8.0 $M_\odot$, respectively, with an orbital period of 100 days. The more massive star evolves first into a giant star and transfers its mass through Roche lobe overflow. A large amount of mass is transferred during overflow. As a consequence, the mass of the 8.0 $M_\odot$ star increases to 16 $M_\odot$ and the 14.4 $M_\odot$ becomes a helium star of mass 3.5 $M_\odot$. The helium star then undergoes a core-collapse supernova, and a neutron star will be formed. Due to the supernova, the orbit becomes wide and eccentric. The 16 $M_\odot$ star evolves to a giant phase that fills its Roche lobe, and the mass transfer happens onto the compact object. The compact object accretes mass and gives rise to X-ray emission. Then, the binary system will be detected as an HMXB. Further, the giant star becomes a helium star, then undergoes a core-collapse supernova and becomes a neutron star. At the final stage, the binary will consist of two young pulsars.

1.2.2 Low mass X-ray binaries (LMXBs)

An LMXB consists of a black hole or neutron star as the compact object or primary star, paired with a low-mass companion star with a mass less than or equal to 1 $M_\odot$ as a secondary star. The companion stars in LMXBs typically belong to spectral types of A or later. The

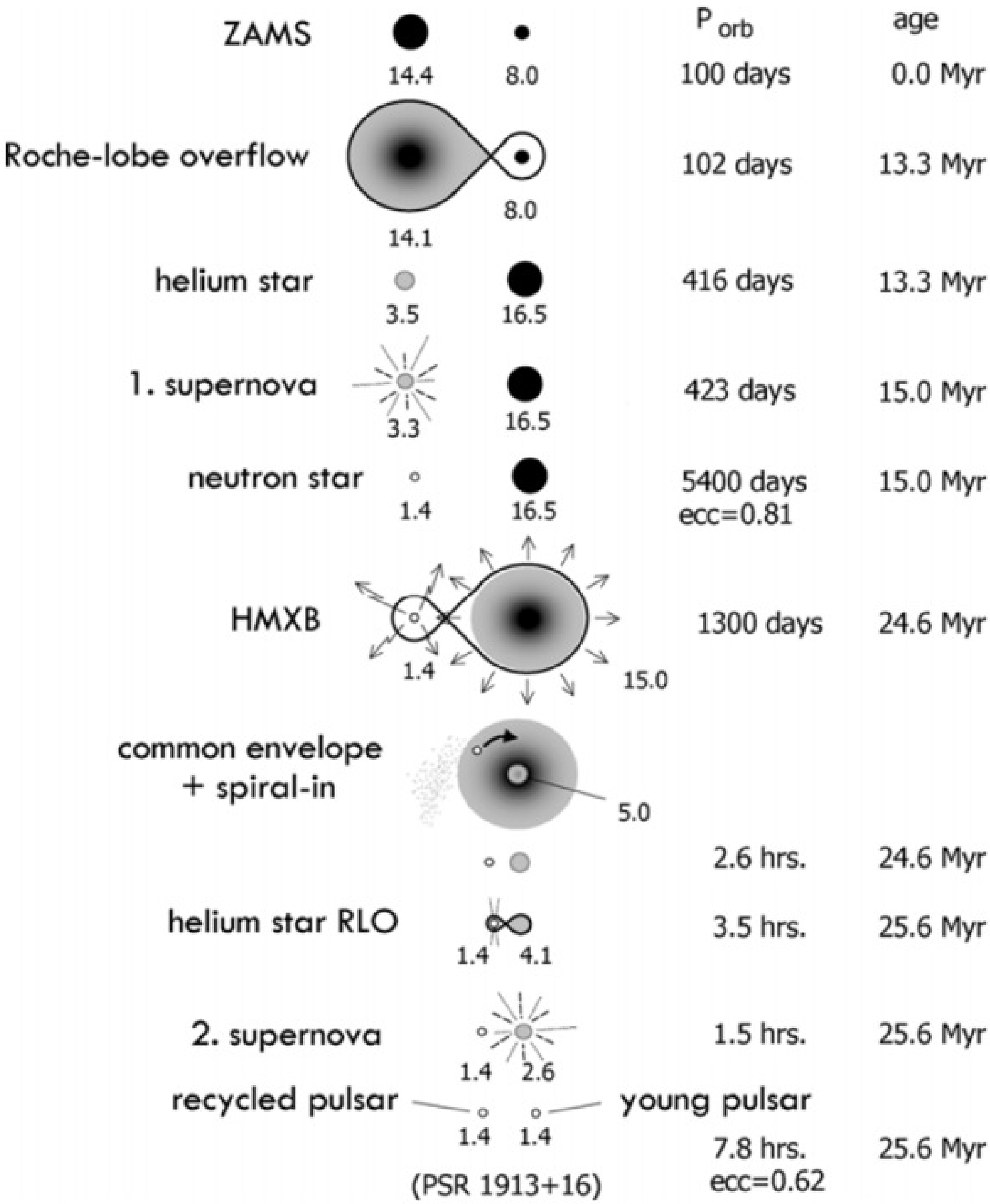

Figure 1.2: Illustration depicting the formation and evolution processes of High Mass X-ray Binaries (HMXBs). The diagram showcases the evolutionary stages of a binary system, starting from the Zero-age main sequence (ZAMS) to the formation of HMXBs, highlighting the mass transfer between the progenitor stars and the resulting transformation into compact objects. Orbital period changes throughout the evolutionary phases are also indicated (Tauris & van den Heuvel, 2006).

LMXBs are relatively old X-ray binary systems, with a characteristic age of $\geq 10^9$ years (Arnason et al., 2021). They are primarily found in regions associated with old star populations, such as the Galactic center, Galactic bulge, and Globular clusters. According to the recent catalog of LMXBs published by Arnason et al. (2021), there are 349 well-known systems. The LMXBs are further divided into two types: Z sources and atoll sources, based on their evolution in hardness-intensity diagram (HID) and color-color diagram (CCD) (Hasinger & van der Klis, 1989). In the CCD, the Z sources typically trace out a Z-shaped pattern and are thought to be accreting at around $L_X \simeq L_{\rm Edd}$ (Eddington luminosity). Conversely, the atoll sources trace a C-shaped pattern in the CCD and typically emit at one to one-tenth of $L_{\rm Edd}$.

The formation process of LMXBs is suggested in Tauris & van den Heuvel (2006). The formation process starts with stars of masses 15 and 1.6 $M_\odot$. The 15 $M_\odot$ star evolves to its giant phase and fills the Roche lobe. Once the massive star fills its Roche lobe, the mass transfer takes place from the massive star to the 1.6 $M_\odot$ star. However, this is an unstable mass transfer scenario that brings the stars close into a common envelope. Then, the entire envelope of the giant star is ejected, leaving a close binary consisting of a helium star and a normal star. At this stage, it is presumed that the 1.6 $M_\odot$ star has accreted a minimal amount of mass from the giant star. The He star then undergoes a core-collapse supernova, leaving a neutron star and the 1.6 $M_\odot$ star in a wider and eccentric orbit. After a very long time ($\sim$2.24 Gyr), the 1.6 $M_\odot$ star evolves to the giant phase and fills its Roche lobe, and then the mass transfer occurs onto the neutron star. Now, the binary system can be detected as an LMXB. Further, the Roche lobe filling star evolves into a white dwarf, and finally, the binary will consist of a neutron star and a white dwarf. Figure 1.3 illustrates the evolutionary process that leads to an LMXB system and then to a millisecond pulsar with a white dwarf companion.

The distinct properties of the secondary stars in HMXBs and LMXBs result in significant variations in the mass transfer mechanisms. These differences in the mass transfer mechanisms consequently lead to X-ray emissions with unique and distinguishable characteristics. The following subsections explore various mass transfer mechanisms and corresponding X-ray emission characteristics in the HMXBs and LMXBs. We delve into the physical processes underlying these mechanisms, examining how the nature of the secondary star influences the dynamics of mass transfer and how these processes shape the X-ray emission properties. Understanding these mechanisms is crucial for interpreting the complex behaviors of X-ray binaries and gaining insights into the evolution and life cycle of these fascinating astronomical systems.

1.3 Accretion mechanisms: insights from X-ray binaries

Accretion is the most crucial mechanism that powers the compact objects in XRBs. In simple terms, accretion is the accumulation of matter on an object due to the influence of its gravity. During the accretion process, the gravitational potential energy of the accreting matter particles is converted into radiation due to the effect of the gravitating object. The importance of accretion onto compact objects was initially widely recognized observationally

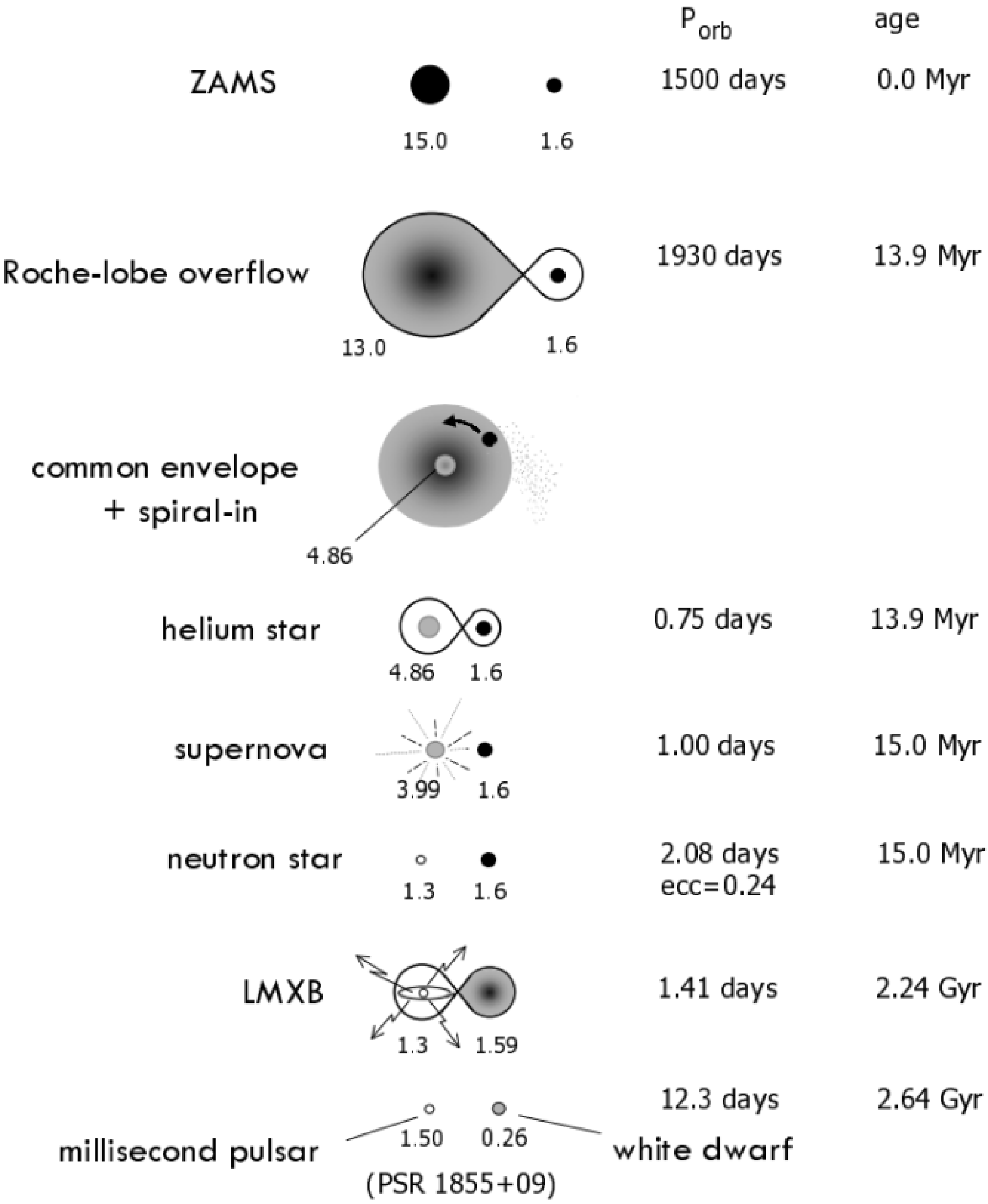

Figure 1.3: Illustration depicting the evolution of two main sequence stars in binary that leads to the formation of Low Mass X-ray Binaries (LMXBs) (Tauris & van den Heuvel, 2006)

in the case of XRBs (Zeldovich & Guseynov, 1966; Cameron & Mock, 1967). Through this mechanism, the compact objects proved their existence. However, the theoretical foundations of accretion were established as early as the 1940s by pioneers such as Bondi, Hoyle, and Lyttelton (Bondi & Hoyle, 1944). Beyond its significance in X-ray binaries, accretion is also crucial in various fields across different scales, including its vital role in the interstellar medium and Active Galactic Nuclei (AGNs). Accretion is one of the most efficient mechanisms in the universe for converting matter into energy and is more powerful than the nuclear fusion process. An order-of-magnitude estimation of the efficiency of accretion and nuclear fusion processes is provided in Frank et al. (2002). When a particle of mass m is accreted onto a compact object of mass M and radius R, the total amount of gravitational potential energy released is given by:

$$\Delta E_{acc} = \frac{GMm}{R} \tag{1.1}$$

where G is the gravitational constant and is equal to 6.6743×10^{-11} m^{3}kg^{-1}s^{-2}. If we consider the compact object to be a neutron star of mass $M \sim M_\odot$ and radius $R \sim 10$ km, then the ΔE_{acc} is coming out to be 10^{20} erg gm^{-1}. For comparison, in the case of nuclear fusion of hydrogen into helium, the most basic fusion process in astrophysics, the amount of energy released is

$$\Delta E_{nuc} = 0.007mc^2 \tag{1.2}$$

where c is the speed of light and is equal to 3×10^8 s^{-1} and using Equation 1.2, ΔE_{nuc} is coming out to be 6×10^{18} erg gm^{-1}. Hence, if we convert one gram of mass into energy, then the accretion process will yield about 20 times more energy than the nuclear fusion process.

The rate at which $\Delta E_{\rm acc}$ is released from the system is called the accretion luminosity ($L_{\rm acc}$). Suppose a compact object is accreting matter at the rate of $\dot{M}$ and accretes an amount ΔM of matter in time Δt. Using Equation 1.1, we can calculate the total amount of energy released as:

$$\Delta E_{acc} = \frac{GM\Delta M}{R} = \frac{GM\dot{M}\Delta t}{R} \tag{1.3}$$

Then the luminosity (amount of energy released per unit time) of the source, if radiated in the same rate as generated, is given by

$$L_{acc} = \frac{GM\dot{M}}{R} \tag{1.4}$$

Equation 1.4 indicates that for a given mass accretion rate, the accretion luminosity increases with the compactness (M/R) of the accreting object. This is due to the fact that, for a fixed mass M, the gravitational potential well becomes deeper as the radius R decreases.

The ratio M/R called the compactness of the accreting object, is typically denoted as $\eta_{\rm acc}$. This implies that the more compact the object, the higher the efficiency of mass-to-energy conversion. For example, for a solar mass neutron star, $\eta_{\rm acc} \sim 0.2$, while for a solar mass white dwarf, $\eta_{\rm acc} \sim 10^{-4}$.

For a particular compact object, the accretion luminosity ($L_{\rm acc}$) increases with an increase in the mass accretion rate ($\dot{M}$). However, $L_{\rm acc}$ does not continue to increase indefinitely with $\dot{M}$ due to an upper limit known as the Eddington luminosity ($L_{\rm Edd}$). $L_{\rm Edd}$ represents the maximum possible luminosity in an accreting system, where the radiation pressure from the outgoing radiation balances the gravitational pressure from the incoming matter, thereby limiting further mass accretion. To calculate this, consider spherical accretion onto a compact object with mass M and radius R, where the outgoing radiation and incoming plasma interact through Thomson scattering. Then, the Eddington luminosity is given by:

$$L_{\rm Edd} = 4\pi G M m_p c/\sigma_T \simeq 1.3 \times 10^{38} (M/M_\odot)\ erg\ s^{-1} \tag{1.5}$$

where σ_T is the Thomson scattering cross-section and m_p is the mass of the proton.The above expression suggests that if a compact object with a mass of 1 $M_\odot$ is accreting matter from its surroundings, the maximum possible luminosity is 1.3 $\times$ 10^{38} (M/$M_\odot$) erg s^{-1}. Beyond this luminosity, the radiation pressure will dominate, pushing the incoming matter outward and halting the accretion process. It is important to note that this calculation represents simplified conditions; various complexities surrounding the compact object can alter the theoretical limits. For example, the presence of a magnetic field and an accretion disc around a neutron star can modify the theoretical value of $L_{\rm Edd}$.

Up to this point, we understand that compact objects in XRBs accrete matter from their surroundings and convert the gravitational energy of the accreted matter into radiation. In XRBs, the companion or secondary star supplies the matter for accretion and acts as a fuel reservoir. The compact object captures this matter whenever it enters its gravitational sphere of influence. The region of gravitational influence around each star in XRBs differs significantly from the shape it would have if the stars were isolated. Therefore, before delving into the various modes of mass accretion, it is essential to discuss the shape of the gravitational influence region in XRBs. One effective method is to consider a test particle placed at different positions and examine the direction and magnitude of the forces acting on it. The assumption is that the test particle is affected by the gravitational forces of both binary star components but does not influence the orbits of the binary star components. This type of problem is known as the restricted three-body problem and was first recognized by the French mathematician Edouard Roche. Consider a binary system consisting of two stars with masses M_1 and M_2 orbiting around the common center of mass. Suppose the orbital period and separation of the binary are given by P and a, respectively. If the stars were isolated, they would have spherical equipotential surfaces around them. However, as they are in a binary system, the shape of their equipotential surfaces is distorted, as shown

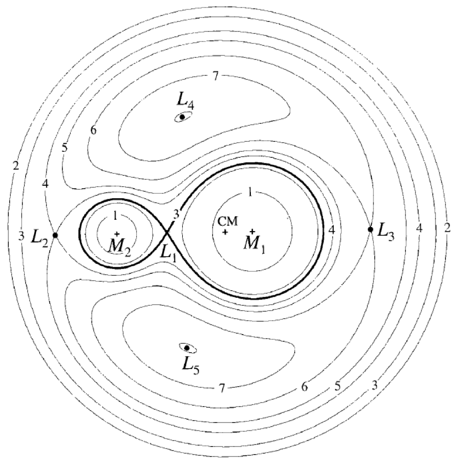

Figure 1.4: Equipotential surfaces surrounding two stars of mass M_1 and M_2 in a binary system (Frank et al., 2002). Two teardrop shape-like equipotential surfaces joined at L_1 point called Roche lobes.

in Figure 1.4.

The mathematical expression for gravitational potential due to both the stars, also called Roche potential, in a frame of reference rotating with the binary is given by:

$$\Phi_R(r) = -\frac{GM_1}{\mid r - r_1 \mid} - \frac{GM_2}{\mid r - r_2 \mid} - \frac{1}{2}(\omega \times r)^2 \tag{1.6}$$

where r is the position vector of the test particle, and ω is the angular velocity of the binary, r_1 and r_2 are the position vector of two stars. The first two terms represent potential due to individual stars. The third term is the potential that arises due to centrifugal forces as both stars rotate around the center of mass. As we can see from Figure 1.4, at a distance very close to and far from the stars, the equipotential surfaces are circular (in 2D) in shape. In between regions, the equipotential surfaces have distorted shapes that differ from those of the circular ones. In the figure, L_1, L_2, L_3, L_4, and L_5 are called the Lagrangian points, equilibrium points of the system. L_1, L_2, and L_3 are the unstable equilibrium points that lie in the binary plane. L_4 and L_5 are two stable equilibrium points that lie on the plane perpendicular to the binary plane. Among them, the most important point is the L_1 point where two equipotential surfaces (in bold Figure 1.4) are connected. These equipotential surfaces are called Roche lobes. The net force acting on any particle at L_1 point is zero. However, due to its unstable equilibrium nature, any small disturbance can push the particle (matter) to the gravitational well or Roche lobe of any of the stars. In XRBs, if, for any reason, the secondary star matter crosses the L_1 point, then the compact object will capture the matter. In XRBs, the accretion of matter onto compact objects can happen through three different processes, which depend upon the physical properties and the evolutionary stage of the companion star. These three modes of accretion are (i)- *accretion through Roche lobe Overflow (RLOF)*, (ii)- *accretion through stellar wind accretion*, and (iii)- *accretion through Be circumstellar disc*. The following subsections will discuss these three accretion modes or processes in detail.

1.3.1 Accretion through Roche lobe overflow

Roche lobe overflow (RLOF) is one of the primary modes of mass accretion in LMXBs (Savonije, 1978). As discussed above, in LMXBs, the companion star is a less massive star of mass $\leq 1\ M_{\odot}$. Hence, the secondary star possesses a feeble stellar wind. The companion star can fill its Roche lobe in two ways during evolution. *First*, at a certain stage of evolution, the companion star expands its outer envelope and fills its Roche lobe. *Second*, if the binary separation decreases because of loss of angular momentum from the system due to gravitational radiation or any other reason, then the compact object significantly distorts the outer envelope of the companion star to fill the Roche lobe. Both processes described above initiate a mass transfer from the companion star through the L_1 point. This process is called mass accretion through RLOF. If the accreted matter has sufficient angular momentum, then the matter would not directly fall onto the compact object. Instead, it gets accreted through the accretion disc (see below for a detailed discussion on the formation of the accretion disc). Figure 1.5 shows a cartoon diagram for Roche lobe overflow in a binary system.

The stream of matter accreted through the L_1 point, having certain initial angular momentum, starts rotating at a distance $\mathrm{R}_{\mathrm{cir}}$ (called circularization radius) from the center of the compact object. At $\mathrm{R}_{\mathrm{cir}}$, the angular momentum of the accreting material is equal to the Keplerian angular momentum corresponding to the compact object. Mathematically, it is given by:

$$R_{\mathrm{cir}} = \frac{J^2}{GM} \tag{1.7}$$

where J is the specific angular momentum (angular momentum per unit mass), and M is the mass of the compact object (Pringle, 1981). $\mathrm{R}_{\mathrm{cir}}$ also gives an estimate of the outer radius of the accretion disc. Hence, accretion onto the compact object occurs if the radius of the compact object (R_*) is less than the $\mathrm{R}_{\mathrm{cir}}$. In terms of orbital period (P_{hr}) of the binary, $\mathrm{R}_{\mathrm{cir}}$ is given by:

$$R_{\mathrm{cir}} \geq 3.5 \times 10^9 P_{\mathrm{hr}}^{2/3} cm \tag{1.8}$$

Since the radius of the compact can not be more than the radius of White Dwarf ($\sim 10^9$ cm), we can infer that the accretion disc is inevitable in the case of RLOF. It is important to note that the mass accretion through the RLOF is not a continuous process. It depends upon how the size of the Roche lobe and binary separation varies with time as the mass accretion continues.

1.3.2 Accretion through the capture of stellar wind

Accretion through the capture of stellar wind is one of the important processes of mass transfer in HMXBs (Shapiro & Lightman, 1976; Kaper, 1995). The massive secondary stars in the HMXBs, O & B type stars, eject much of their mass through the stellar wind. The HMXBs in which stellar wind is the dominant mode of mass accretion form a specific subgroup called supergiant X-ray binaries (SGXBs; see Figure 1.1). The outward ejection of mass from the massive companion occurs because of strong outward radiation pressure from the core of the star. Due to this, even before the RLOF, the compact object accretes

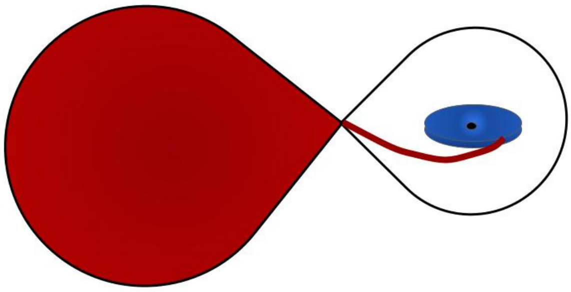

Figure 1.5: Mass transfer occurring through the Roche lobe overflow, a phenomenon where material from one star in a binary system spills over its Roche lobe due to gravitational interaction, eventually accreting onto its companion.

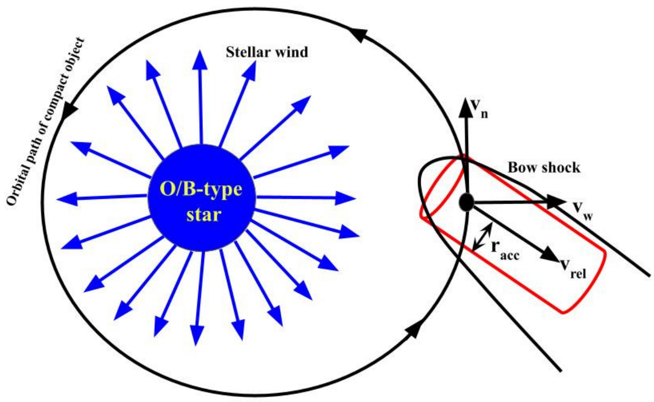

Figure 1.6: Mass accretion process facilitated through the capture of stellar wind, leading to the formation of a bow shock near the compact object as the accreting material interacts with the surrounding medium of the compact object.

matter and emits radiation. Figure 1.6 shows the schematic diagram for compact object accreting matter through stellar wind.

The secondary star emits stellar wind in all directions with a rate of 10^{-6}-10^{-5} $M_\odot$ yr^{-1}, at speed given by:

$$v_w \sim v_{\rm esc} = \left(\frac{2GM_{\rm sec}}{R_{\rm sec}}\right)^{1/2} \tag{1.9}$$

where $M_{\rm sec}$ sand $R_{\rm sec}$ are the mass and radius of the secondary star, respectively. $v_{\rm esc}$ is the escape velocity at the surface of the star, and its typical value is a few thousands of kilometers per second (1000-3000 km s^{-1}; Kudritzki & Hummer 1990), which is significantly higher than the typical sound speed of the medium 10 km s^{-1}. Hence, the stellar wind particles travel at supersonic speed, and a strong bow shock forms near the compact object. When the kinetic energy of the stellar wind becomes less than the potential energy of the wind and compact object system, the matter gets accreted by the compact object. If this distance is $\rm r_{acc}$, the mass accretion happens within a cylindrical region with axes along the relative wind velocity direction (see Figure 1.6). The accretion radius is given by:

$$r_{\mathrm{acc}} \sim \left(\frac{2GM}{v_{\mathrm{rel}}^2}\right) \tag{1.10}$$

where M is the mass of the compact object and v_{rel} is the relative velocity between the stellar wind and the compact object, which is given by:

$$v_{rel} \simeq \left(v_n^2 + v_w^2\right)^1 /2 \tag{1.11}$$

The fraction of the stellar wind accreted by the compact object can be calculated by using the mass conservation formula. For simplicity, we assume that $v_w \gg v_n$, which is a good approximation for these systems. Using the above Equations,

$$\frac{\dot{M}}{-\dot{M}_w} \simeq \frac{\pi r_{acc}^2 v_w(a)}{4\pi a^2 v_w(a)} = \frac{G^2M^2}{a^2 v_w^4(a)} \tag{1.12}$$

where a is the binary separation. Using Equation 1.9, we can write

$$\frac{\dot{M}}{-\dot{M}_w} \simeq \frac{1}{4}\left(\frac{M}{M_E}\right)^2\left(\frac{R_E}{a}\right)^2 \tag{1.13}$$

Using typical values of HMXBs, Equation 1.13 implies that the compact object only accretes 10^{-4}- 10^{-3} of the total mass loss rate of stellar wind. Hence, this process is less efficient than the RLOF. Although the mass accretion rate by the compact object is very low, the rate of stellar wind emitted by the secondary star itself is very large, so these systems could be highly luminous. The typical luminosity of these systems is given by:

$$L_{acc} \sim 10^{37}\left(\frac{\dot{M}}{-10^{-4}\dot{M}_w}\right)\left(\frac{-\dot{M}_w}{10^{-5}M_{\odot}yr^{-1}}\right) erg\ s^{-1} \tag{1.14}$$

The SGXBs are generally persistent and moderately bright with luminosity $L_X \sim 10^{37}$ erg s^{-1}. Some of the known bright stellar wind accreting systems or SGXBs are Cen X-3, SMC X-1, Vela X-1, and Cyg X-1.

1.3.3 Mass transfer through Be circumstellar disc

Some specific high-mass stars (O & B-type) exist with an equatorial circumstellar disc around them. The circumstellar disc forms because of the high rotational velocity of the stars. Be stars typically rotate at a speed of 250 km s^{-1}, which is 70-80 % of their critical or break-up velocity (Slettebak, 1982; Porter, 1996). Critical velocity is the velocity at which the centrifugal force exactly balances the gravitational force at the equator. The circumstellar disc around the Be stars is also called the decretion disc, where matter travels outward from the central star. These binary systems are called Be/X-ray binaries (BeXRB) and are the largest subclass of HMXB. In BeXRB, if the circumstellar disc is sufficiently evolved, the compact object accretes matter from the disc while passing through the periastron of the binary orbit and emits X-rays. Therefore, these systems show periodic X-ray outbursts with a periodicity equal to the orbital period of the binary. It is important to note that

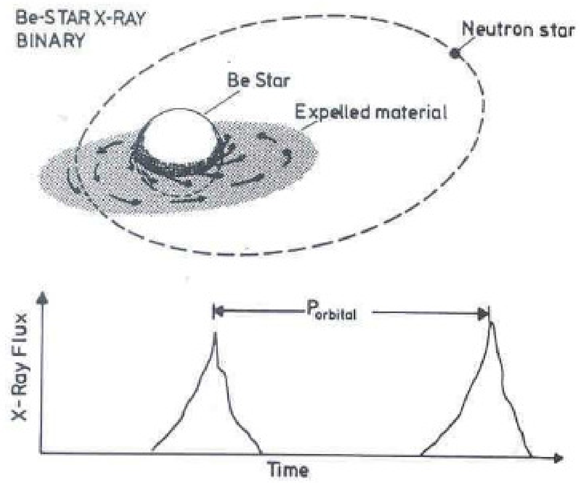

Figure 1.7: Schematic representation illustrating mass accretion onto compact objects from the circumstellar decretion disc of the companion Be star in BeXRBs (van den Heuvel, 2004).

in these systems, the inclination angle of the Be disc with respect to the orbital plane also plays a crucial role in mass accretion by the compact object from the disc. Figure 1.7 shows the schematic diagram for mass accretion onto compact objects from the Be decretion disc during the periastron passage. BeXRBs generally show two types of X-ray outbursts, such as Type I (normal) outburst and Type II (giant) outburst (Reig, 2011). The source luminosity at the peak of normal outbursts can reach up to 10^{37} erg s^{-1}. These outbursts are periodic, and the periodicity is attributed to the periastron passage of the neutron star in the binary system. These outbursts can last up to a fraction ($\sim$20%) of the orbital period of the binary. On the other hand, the giant X-ray outbursts exhibit contrasting properties. The luminosity at the peak of the giant outbursts can reach up to 10^{39} erg s^{-1}. These outbursts do not show any orbital modulation. In some cases, the outburst duration is several orbital periods (Kretschmar et al., 2012). In Sections 1.5.1, 1.5.3, and 1.5.7 optical and X-ray properties of the BeXRBs are discussed in great detail.

1.4 Neutron star X-ray binaries (NS-XRBs)

In the preceding section, we explored the diverse modes of mass transfer from the secondary star to the compact object, a process primarily dictated by the nature of the secondary star. However, the trajectory through which this matter approaches the surface of the compact object is contingent upon the nature of the compact object itself. In alignment with the focus of this thesis, we delve into the process of mass accretion onto the surface of the neutron star and the subsequent generation of X-ray emissions.

As discussed above, if the matter fell into the Roche lobe of the compact object (neutron star in our case), then it starts rotating around the compact object at R_{cir} (see Equation 1.7). The matter at R_{cir} needs to lose its angular momentum to move towards the inner region. In the absence of external force/torque, some internal torque must exist to initiate the angular momentum loss. In this case, viscosity plays an important role. The viscous torque between two thin layers of matter transfers the angular momentum between each other. Consequently, one layer of matter loses angular momentum and moves inward, whereas

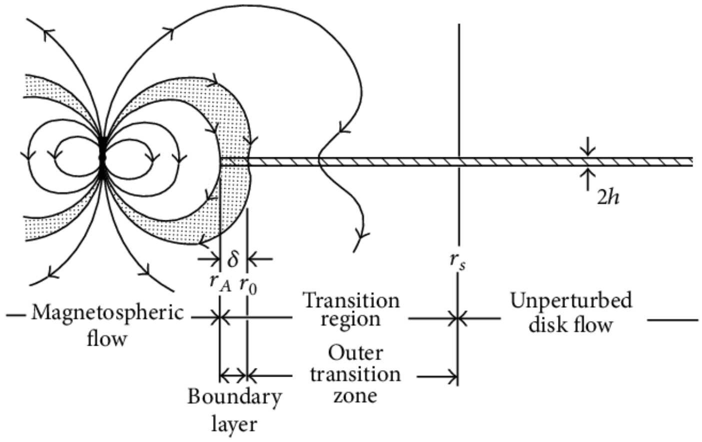

Figure 1.8: Accretion of matter onto the polar regions of the neutron star along the magnetic field lines of the neutron star (Ghosh & Lamb, 1979).

another layer gains angular momentum and moves outwards. This process continues, and matter gets accreted close to the compact object. When a sufficient amount of matter gets transferred from the secondary, angular momentum redistribution forms an accretion disc around the compact object. The frictional force between gas particles in the disc is expected to be much less than the gravitational force. Hence, the disc locally rotates with Keplerian velocity. Since matter in a Keplerian disc rotates differentially, the gas in the disc will be heated by internal friction. The temperature of the matter within the accretion disc rises in the inward direction, leading to the generation of high energy X-ray emission (Pringle & Rees, 1972; Shakura & Sunyaev, 1973). Hence, the accretion disc is a machine that harnesses gravitational potential energy and angular momentum from plasma.

The inner region of the accretion disc may or may not directly reach the surface of the neutron star due to its strong magnetic field. However, in other cases, like a black hole, matter reaches the last stable orbit, depending on the spin of the black hole and the direction of rotation of the disc. Neutron stars possess a wide range of magnetic fields between 10^8 and 10^{14} Gauss. Here, we discuss the accretion of matter onto the surface of a neutron star considering a dipolar magnetic field (White et al., 1983).

In the case of NS-XRBs, the accretion disc is truncated at a distance far away from the neutron star due to the magnetic pressure of the magnetic field of the neutron star. For a dipole geometry, the magnetic field strength of the neutron star at a distance r from the center is given as:

$$B(r) \sim \frac{\mu}{r^3} \tag{1.15}$$

where μ is the magnetic dipole moment. Using this equation, we can write the magnetospheric pressure as

$$P_{\text{mag}} \sim \frac{B^2}{8\pi} = \frac{\mu^2}{8\pi r^6} \tag{1.16}$$

Equation 1.16 shows that $P_{\text{mag}} \propto \mathrm{r}^{-6}$. This implies that as we move closer to the surface of a neutron star, the magnetic pressure increases rapidly. The incoming accreted matter also carries matter or ram pressure, which is given as $P_{\text{ram}} = \rho v^2$, where ρ and v are the density and velocity of incoming matter, respectively. v can be approximated as the free fall velocity ($v = (2\mathrm{GM/r})^{1/2}$)). ρ can be calculated using the mass conservation equation

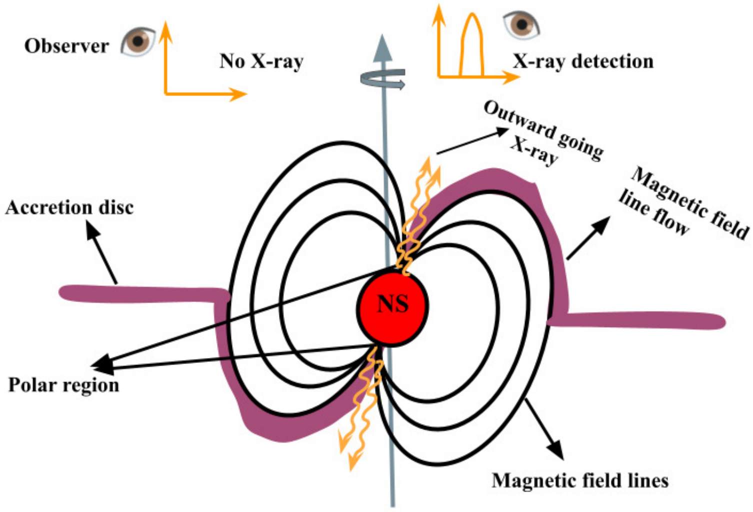

Figure 1.9: Accretion onto magnetized neutron star with magnetic and spin axes misaligned. The distant observers see pulsed emission due to the rotation of the neutron star (NS) around its spin axis.

with steady-state accretion, where the mass accretion rate can be expressed as $\dot{m}= 4\pi\rho$v r^2. Using value of v and ρ, $P_{\rm ram}$ finally can be written as

$$P_{\rm ram} = \left(\frac{\dot{m}}{4\pi r^2}\right)\sqrt{\frac{2GM}{r}} \tag{1.17}$$

The incoming matter pushes the magnetic field lines inward until the magnetic pressure dominates. At a certain distance from the compact object, $P_{\rm ram}$ and $P_{\rm mag}$ balance each other. This radius is called the Alfven radius or magnetospheric radius of the neutron star. Equalizing Equations 1.16 and 1.17, expression for the Alfven radius ($r_{\rm A}$) can be expressed as

$$r_{\rm A} = 5.1 \times 10^8 \dot{m}^{-2/7} M^{-1/7} \mu^{4/7} \quad cm \tag{1.18}$$

This equation can be rewritten in terms of luminosity using Equation 1.4 as

$$r_{\rm A} = 2.9 \times 10^8 M^{1/7} R_6^{-2/7} \mu_{30}^{4/7} L_{37}^{-2/7} \quad cm \tag{1.19}$$

Equation 1.18 and 1.19 show the dependency of $r_{\rm A}$ on mass accretion rate or luminosity. As the luminosity increases, $r_{\rm A}$ decreases, which means the accretion disc remains closer to the neutron star in the higher luminosity phase of the system. These equations also suggest that the accretion disc is truncated at the magnetospheric radius from where the magnetic field lines dictate the path of the accreted plasma. Figure 1.8 shows the interaction of the accretion disc with the magnetic field lines of the neutron star at the magnetospheric radius $r_{\rm A}$ where the accretion disc gets truncated. At the magnetospheric radius, matter from the inner edge of the accretion disc follows the magnetic field lines and gets accreted onto the polar regions of the neutron star. When the accreted matter gets deposited on the polar region of the neutron star, the kinetic energy of the particles gets converted to X-ray radiation, which is emitted in the form of beams along the magnetic axis.

If the magnetic and spin axes of the neutron star are not co-aligned, the distant observers detect pulses of X-ray radiation from the neutron star when the radiation beam crosses the line of sight due to the rotation of the neutron star. For observers, these objects appear to emit pulses of X-ray radiation with a periodicity equal to the spin period of the neutron star. Therefore, these rotating neutron stars with misaligned magnetic and spin axes are called accretion-powered X-ray pulsars. A geometric representation of an accretion-powered X-ray pulsar is presented in Figure 1.9.

However, there are conditions at which matter from the accretion disc does not get accreted onto the neutron star. There exists another characteristic radius of the accreting pulsars, called co-rotation radius (R_{co}), at which the angular velocity of the magnetosphere is equal to the angular velocity of the neutron star. Mathematically, it can be written as:

$$r_{\rm co} = \left(\frac{2GM}{\omega^2}\right)^{1/3} \quad cm \tag{1.20}$$

As matter in the accretion disc interacts with the magnetic field of the neutron star at magnetospheric radius, the interplay between the magnetospheric radius ($r_{\rm A}$) and co-rotation radius ($r_{\rm co}$) decides the accretion of matter onto the neutron star. If $r_{\rm A} < r_{\rm co}$, the matter gets accreted onto the surface of the neutron star. If $r_{\rm A} > r_{\rm co}$, the neutron star rotates faster than the Keplerian speed of matter in the disc. This creates a centrifugal barrier for the incoming matter and ceases the accretion of matter onto the neutron star. This phase of accretion is also called *propeller regime state* (Illarionov & Sunyaev, 1975).

1.5 Be/X-ray binaries (BeXRBs)

This section discusses some of the known X-ray and optical properties of BeXRBs. The BeXRBs represent the largest population of HMXBs (Fornasini et al., 2023). These BeXRBs primarily consist of a neutron star as the compact object and a non-supergiant star as the companion star (e.g., Ziolkowski 2002; Paul & Naik 2011; Reig 2011). Till date, only one BH-BeXRB (MWC 656; Casares et al. 2014) and one probable WD-BeXRB (γ-Cas; Lopes de Oliveira et al. 2010) are known. As shown in Figure 1.7, the neutron stars in BeXRBs are powered by mass accretion from the circumstellar disc of the companion Be star.

1.5.1 Observational properties of BeXRBs in optical regime

In BeXRBs, most of the optical emissions come from the companion Be star. The companion Be stars are early-B or late-O type stars and bright in optical and infrared wavebands. The primary observational signature that exhibits the presence of a Be star in the binary is the detection of emission lines, unlike classical O/B-type stars, which show photospheric absorption lines in the infrared and optical spectra. The Be star in the XRBs commonly exhibits strong Hα emission line along with other lines such as He I and Fe II emission lines at a certain phase of its evolution (Porter & Rivinius, 2003). Since they exhibit emission lines, the letter 'e' is associated with their name, i.e., Be-type stars instead of B-type stars. Another observational signature of the Be stars is the excess infrared emission above the thermal continuum (Gehrz et al., 1974). Such distinctive characteristics are attributed to

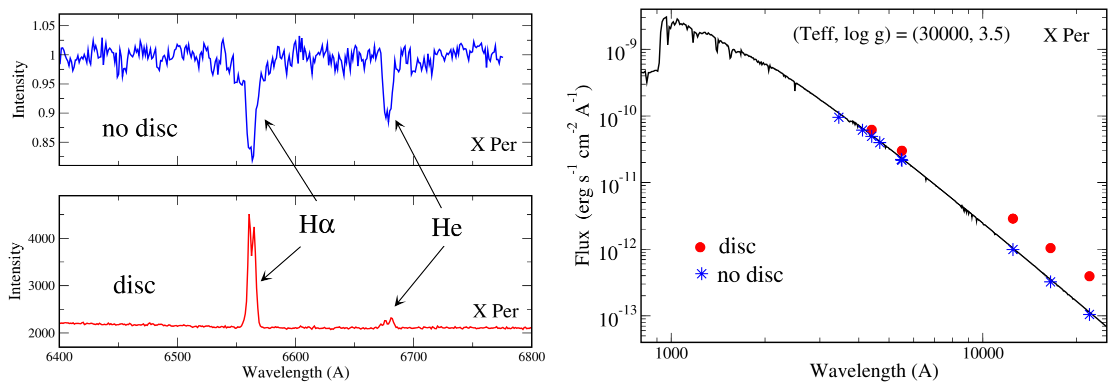

Figure 1.10: Detection of emission lines and infrared excess due to the presence of Be circumstellar disc of BeXRB X Per. The Figure is taken from Reig (2011).

the presence of an equatorial circumstellar disc around the Be star. It is important to note that the formation of the Hα emission line and infrared excess are due to the processes of absorption and subsequent emission of continuum photons of the central star. Due to this, a correlation exists between the equivalent width of the emission line and infrared excess (Coe et al., 2005). However, it is important to notice that the Hα emission line and infrared excess have a different spatial origin from the disc. Gies et al. (2007) using long-baseline interferometric observations in the K$'$ band found that infrared emission is consistently coming from the smaller region that Hα line. Furthermore, substantial evidences suggest that an increase in disc brightness is first observed in the near-infrared band and subsequently in Hα emission line, as expected from an outwardly propagating density enhancement (Clark & Steele, 2000; Grundstrom et al., 2007). In Figure 1.10, the observational signatures of the BeXRB X Persei (X Per) are shown. In the presence of a circumstellar disc, a strong Hα emission line appears in the spectrum along with the He I emission line. An excess infrared emission (red-filled circles) is also observed above the continuum emission (modeled with atmospheric Kuruzc model for T_{eff}=30000 K and log g=3.5) due to the presence of the circumstellar disc.

Then, the question may arise as to why only specific stars harbor circumstellar discs. One of the answers to this is that these stars possess very fast rotational speed (~220 km s^{-1}, Slettebak 1982). The circumstellar disc is understood to be formed due to the discharge of material from the fast-rotating Be star, which rotates close to the 70-80% of its critical velocity (Slettebak, 1982; Porter, 1996). To date, a significant number of BeXRBs (about 172) have been detected in Large Magellanic Cloud (LMC), Small Magellanic Cloud (SMC), and in Milky Way galaxy (Antoniou & Zezas, 2016; Coe & Kirk, 2015; Haberl & Sturm, 2016; Fortin et al., 2023; Liu et al., 2024). Detection of such a large number of BeXRBs holds up the idea of gaining a huge amount of rotational speed during the binary evolution (Kriz & Harmanec, 1975; Gies, 2000). According to this theory, the heavier star evolves faster in a binary with two massive stars and fills its Roche lobe. Once the Roche lobe is filled, the less massive star accretes mass from the heavier one through Roche-lobe overflow. During this process, it gains a significant amount of angular momentum. In the later phase, the donor star becomes a neutron star or any other compact object, and the mass-accreting star becomes a Be star. It is important to note that there are other mechanisms by which the Be stars gain significant rotational speed. Otherwise, isolated Be stars would not have existed (Porter & Rivinius, 2003). One such model for isolated Be stars is the efficient coupling of core and envelop which is mediated by internal magnetic fields, due to which the outer part of the star gains sufficient angular momentum (for details check Hastings et al. 2020 and references therein). Though the origin of matter ejection from the high-speed rotating photosphere is known, the exact triggering mechanism still needs to be understood clearly (see Reig 2011 for a concise overview).

The circumstellar discs are considered to be quasi-Keplerian (Hanuschik, 1996). Initially, the theory of radial outflow of matter from the Be star was proposed to explain the X-ray emission from the compact object. This theory did not explain the range of relative velocity required to explain the observed X-ray luminosities in BeXRBs (Waters et al., 1989). The radial outflow theory can not also explain the transient nature of the BeXRBs. The model of the quasi-Keplerian circumstellar disc around the Be star was verified with some observational signatures like V/R ratio (Hanuschik, 1996; Okazaki, 1997). The most promising model that explains most of the observational properties of Be stars is the viscous decretion disc model (Lee et al., 1991; Okazaki, 2001). According to this model, the angular momentum is transferred from the Be star to the inner part of the disc, increasing its angular velocity to the Keplerian value. Further, viscosity plays a vital role in transferring the angular momentum outwards, operating in a way opposite to an accretion disc. Then, the mater in the disc moves in quasi-Keplerian orbits, and the radial velocity component is highly subsonic in nature (Okazaki, 2001). The calculated outflow velocity of matter in the circumstellar disc is very subsonic at distances where the neutron star orbits in the BeXRB ($v(r) < 1$ km s^{-1}) and still subsonic for the orbital sizes of all BeXRBs for which there is an orbital solution. The viscous decretion disc model successfully accounts for most of the observational characteristics of the Be discs. Negueruela et al. (2001) applied this model to the decretion disc around the Be star in BeXRB transient 4U 0115+63 and found that the tidal interaction of neutron star truncates the circumstellar disc. This result resonated with the results of Reig et al. (1997), where they found a correlation between the orbital size of the binary and maximum Hα equivalent width. This model also explains well the X-ray outbursts in other BeXRBs like V 0332+53, 1A 0535+262, GRO J1008-57, 2S 1417-624, and EXO 2030+375 (Okazaki & Negueruela, 2001).

1.5.2 Dynamics of circumstellar disc

Here, we discuss the observational signatures of BeXRBs in optical wavebands and associated variabilities. The shape and strength of emission lines are indicators of the physical properties of the circumstellar disc around the Be star. The dynamic behavior of the disc can be understood by looking at changes in the properties of emission lines over time in the optical/infrared spectra of BeXRBs. Of all the emission lines, Hα is the most robust emission line found in the optical spectra of BeXRBs. Hence, a long-term study of the Hα line is usually carried out to understand the properties of the Be circumstellar disc. One of the long-term variations seen in the Be stars is the change in state from Be to B-type. This generally occurs in time scales of several years to tens of years, the time scale of formation and dissipation of disc (Reig et al., 2001). During the presence of the disc, the Hα line appears in

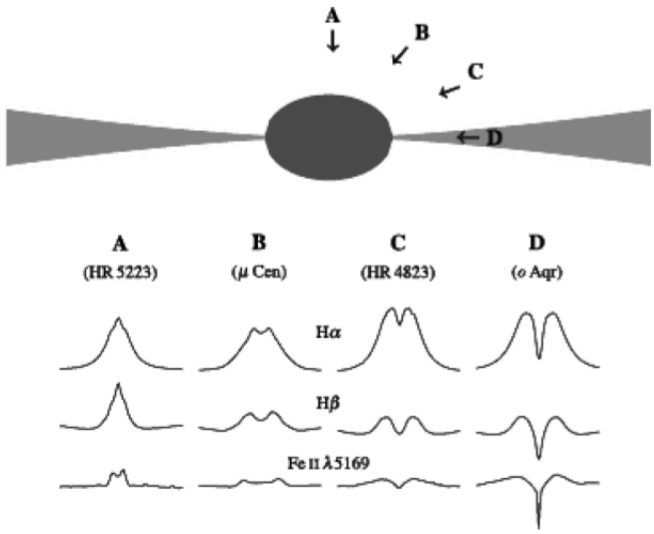

Figure 1.11: Different shape of emission lines due to the distinct viewing angle of the observer (Rivinius et al., 2013).

emission form, while in the absence of the disc, the Hα line is seen in absorption. The shapes of the emission line profiles are found to be different, depending on the viewing angle of the observer(see Figure 1.11) and the circumstellar disc. Hα emission lines can be morphologically divided into two classes: *first,* symmetric (single-peaked and double-peaked), and shell profiles and *second*, asymmetric profiles, showing variability on time scales of months to years. These line profiles are not specific to different types of stars. Instead, a single Be star can show different emission line profiles (Reig 2011 and references therein). These changes are usually slow (of the order of years to decades in isolated Be stars and months to years in BeXRB). Symmetric profiles are believed to be generated in quasi-Keplerian discs, while asymmetric profiles are associated with distorted density distributions (Hanuschik et al., 1995; Hummel & Hanuschik, 1997).

Most sources exhibit asymmetric Hα line profiles. The parameter V/R (pronounced as V by R ratio) quantifies the asymmetry in line profiles. The V/R is defined as the ratio of the blue-shifted peak intensity to the red-shifted peak intensity above the continuum spectrum. Sometimes, it is also represented as a $\log(V/R)$. A positive value of $\log(V/R)$ signifies a blue-dominated profile, whereas a negative value represents a red-dominated profile. Variability in the V/R ratio can be attributed to a non-axisymmetric equatorial disc featuring a single-arm density perturbation that propagates through it (Papaloizou et al., 1992; Okazaki, 1997). When the denser portion of the disc is either in front of or behind the star, we expect symmetric double-peak profiles. Conversely, asymmetric profiles arise when the high-density perturbation is located on either side of the disc. Specifically, if the denser part aligns with the side of the disc where rotational motion moves away from the observer, we observe heightened red emission (V $<$ R). Conversely, when the denser portion moves toward the observer, we anticipate blue-dominated profiles (V $>$ R)(Telting et al., 1994). For systems with high inclinations, distinguishing between the two symmetric scenarios is more feasible. This is because the central dip between the symmetric peaks becomes more pronounced, potentially extending beyond the continuum, forming what is known as a shell profile when

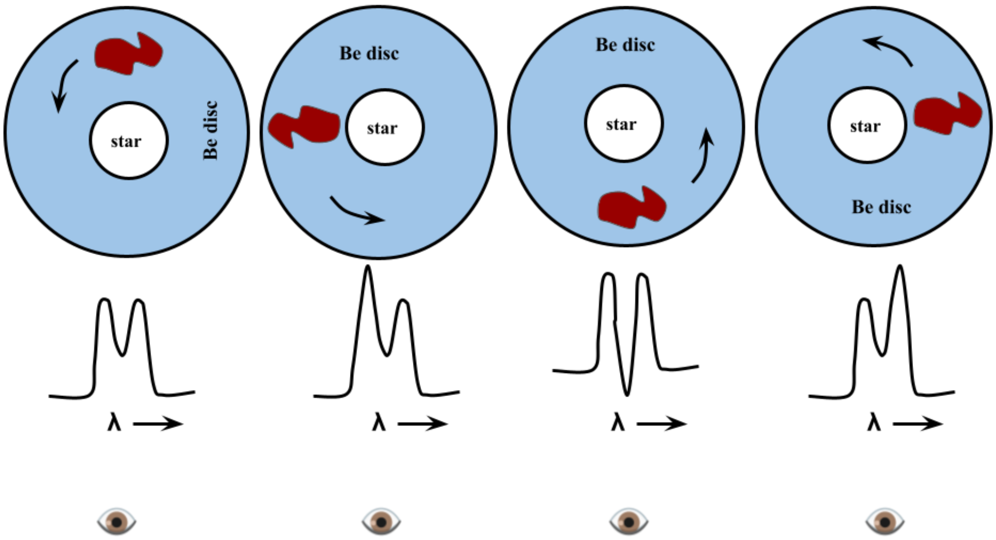

Figure 1.12: Change in shape of the emission line depending upon relative position between perturbed region and observer.

the perturbation lies between the observer and the star. This is believed to be a perspective effect, where the line of sight toward the star intercepts the equatorial disc, causing self-absorption (Rivinius et al., 2006). Figure 1.12 shows the schematic diagram for the change in the shape of the emission line due to the relative position of the perturbed region of the disc with respect to the observer.

Figure 1.13 and 1.14 exhibit long-term variation of Hα line in BeXRB Swift J0243.6+6124 and IGR J06074+2205, respectively. A significant variation in the shape of the line profile can be seen. Along with the shape, the strength of various emission lines also changes over a long period. The strength of the emission line is generally characterized by equivalent width (EW), which is mathematically expressed as :

$$EW = \sum \left(1 - \frac{F(\lambda)}{F_c(\lambda)}\right) \delta\lambda \quad \text{Å} \tag{1.21}$$

where F(λ) represents the total flux, including contributions from the emission line and the continuum of the source spectrum at wavelength λ, and F$_c$(λ) represents only the underlying continuum flux at wavelength λ. Hence, for emission lines, the value of the EW is negative, and for absorption lines, it is positive. The variation in the EW depends on the amount of the line emitting particle in the circumstellar disc. If the central star continuously provides matter to the circumstellar disc, then the density and size of the disc increase with time, which increases the EW of the emission lines. In BeXRBs, the effect of the interaction of the circumstellar disc and the neutron star is also very important for the strength of the emission lines. This part will be discussed in later sections.

Figure 1.15 shows the long-term variation of different parameters of Hα line like EW, V/R, and ΔV (peak velocity separation between blue and red-shifted peaks) for BeXRBs IGR J06074+2205 and Swift J0243.6+6124. In this section, we discussed some of the important optical properties of the BeXRBs, and next, we will discuss the X-ray properties of

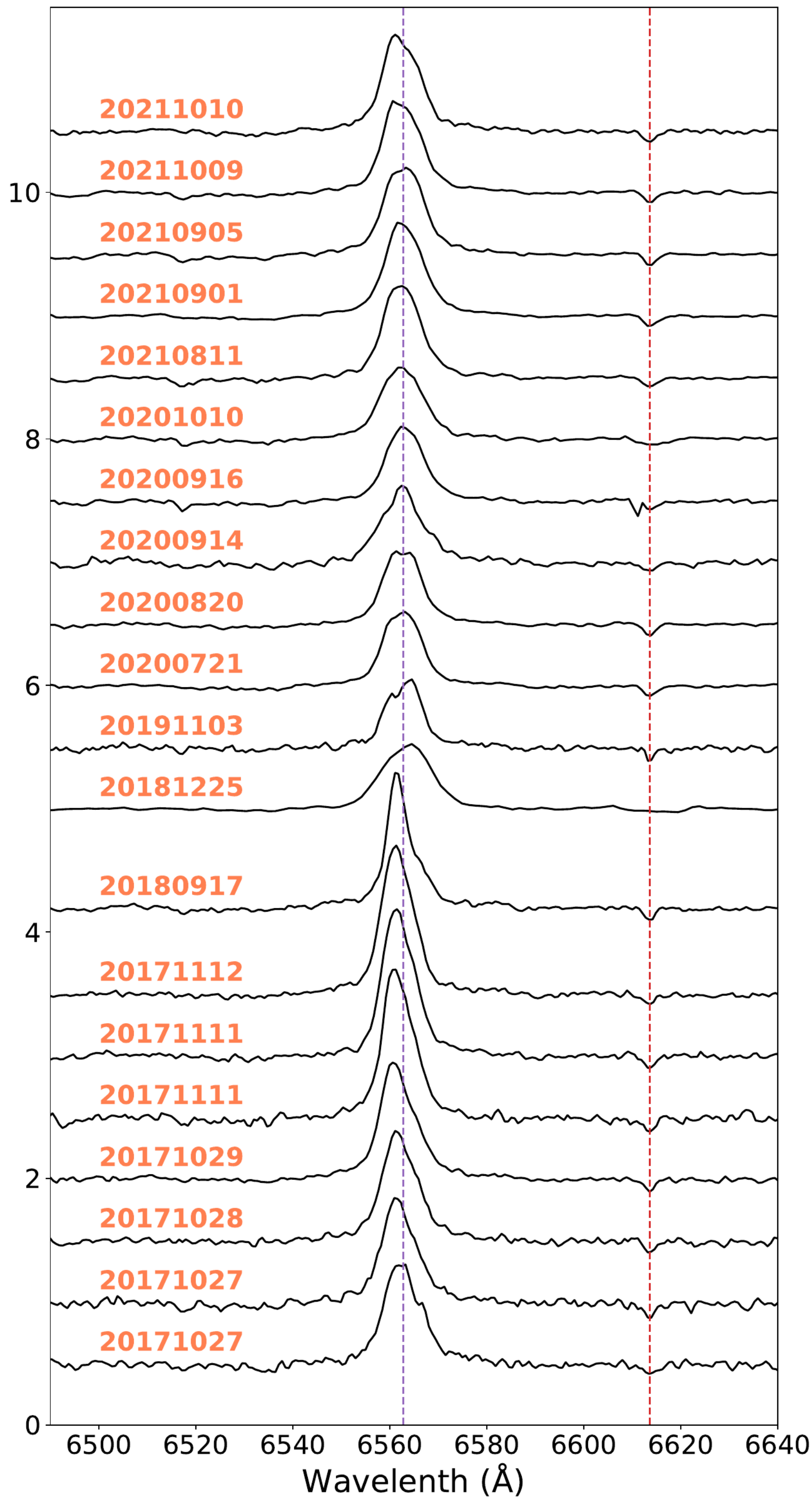

Figure 1.13: Variation in shape of Hα emission line of BeXRB Swift J0243.6+6124 between 2017 and 2022 (Liu et al., 2022).

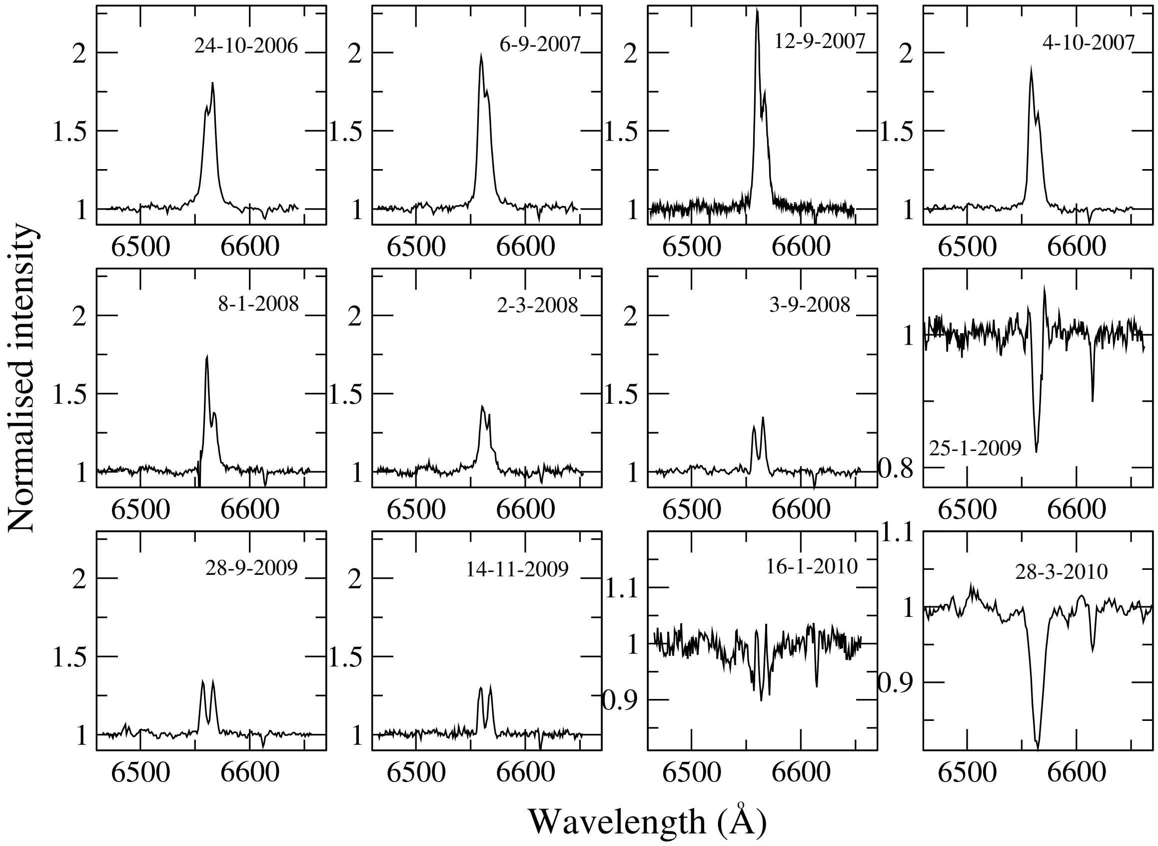

Figure 1.14: Variation in shape of Hα emission line of BeXRB IGR J06074+2205 between 2006 and 2010 (Reig et al., 2010).

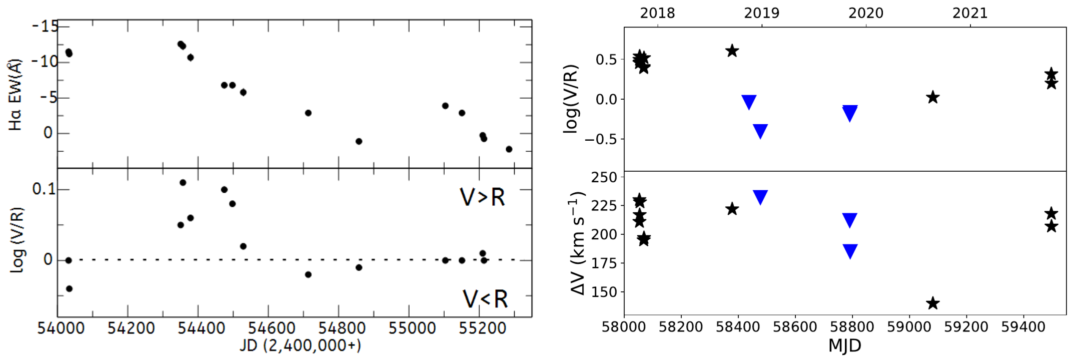

Figure 1.15: Left panel: Variation of Hα line EW and V/R of IGR J06074+2205 between 2006 and 2010 (Reig et al., 2010). Right panel: Variation of V/R and Δ V of Hα emission line of BeXRB Swift J0243.6+6124 between 2017 and 2022 (Liu et al., 2022).

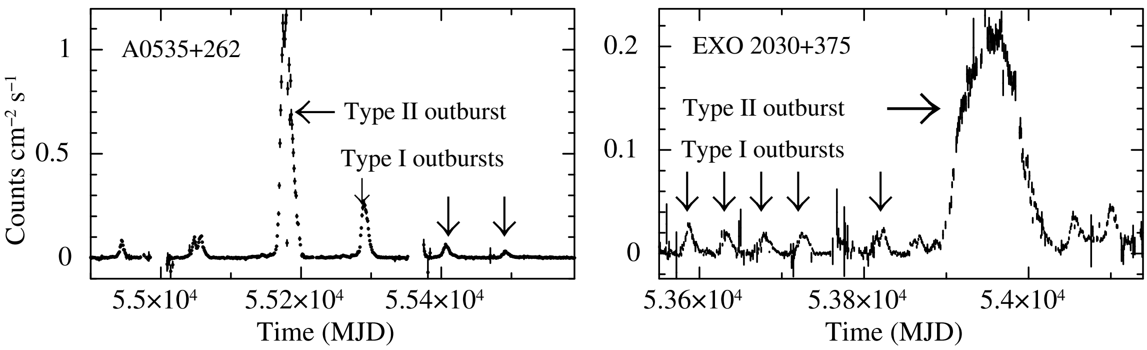

Figure 1.16: Long-term Swift/BAT (15-50 keV) light curves of A0535+262 and EXO 2030+375 displaying Type I and Type II X-ray outbursts (Paul & Naik, 2011).

the BeXRBs.

1.5.3 Observational properties of BeXRBs in X-ray regime

In XRBs, the compact object emits X-rays, whereas the companion star emits in optical/infrared bands. As discussed in Section 1.4, the neutron star in an NS-XRB accretes matter from the companion star. The accreted matter gets channelized through the magnetic field lines onto the polar regions of the neutron star. In the polar region, the kinetic energy of the accreted particles is converted to X-ray radiation. In the case of BeXRBs, the orbits are wide and eccentric (e $\geq$ 0.3) with an orbital period of $\geq$10 days. Because of higher eccentricity, the neutron star interacts with the equatorial circumstellar disc of the Be star for a short duration at the periastron of the orbit. During this interaction, mass transfer from the Be star disc to the compact object leads to a transient X-ray outburst (a rise in X-ray intensity) at the periastron passage. Hence, most of the BeXRBs are transient. However, all BeXRBs are not transient (Reig & Roche, 1999). The BeXRBs show two types of X-ray outbursts during the active phase: normal (Type I) and giant (Type II) X-ray outbursts.

The Type I X-ray outbursts are periodic or quasi-periodic events that occur close to the periastron passage of the neutron star. These short-lived outbursts last for a small fraction of the orbital period ($\sim$20%). During these outbursts, the peak X-ray luminosity of the neutron star increases by up to two orders of magnitude above the quiescent phase, reaching up to $L_X \sim 10^{37}$ erg s^{-1}. The Type II X-ray outbursts, however, are irregular and rare without any preferred orbital modulation and last for several orbital periods. At the peak of these outbursts, the luminosity of the neutron star increases by more than two orders of magnitude compared to the quiescent state. Most of the time, the peak X-ray luminosity becomes $L_X \geq 10^{37}$ erg s^{-1} and crosses the Eddington luminosity ($L_{Edd} \sim 10^{38}$ erg s^{-1}) (Stella et al., 1986; Negueruela, 1998). Figure 1.16 shows Type I and Type II X-ray outbursts in BeXRBs A0535+262 and EXO 2030+375. The periodic and less intense outbursts are Type I X-ray outbursts, whereas the brightest X-ray outbursts are Type II outbursts.

It has been observed that during X-ray outbursts, the neutron stars in BeXRBs display significant variabilities in their timing and spectral properties. Specifically, during the Type II X-ray outbursts, the accreting pulsars undergo various transitions (Paul & Naik,

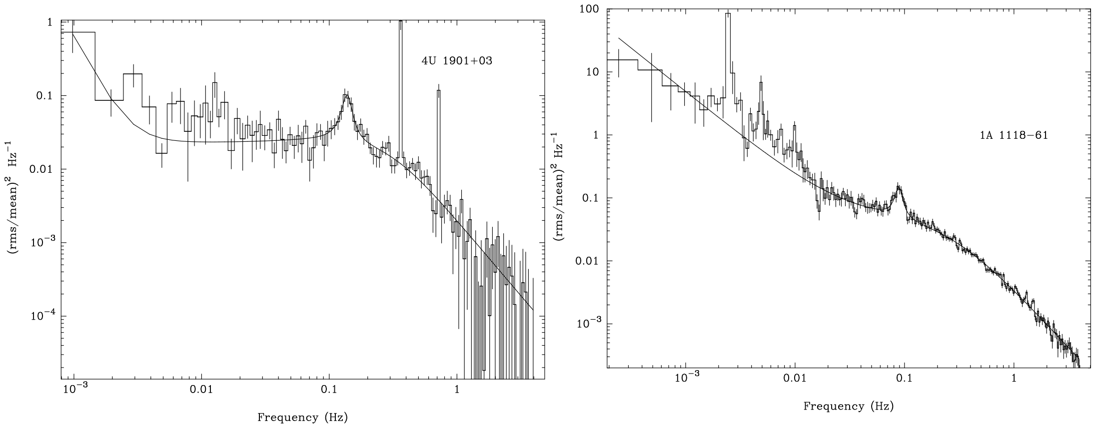

Figure 1.17: The PDS of two HMXBs 4U 1901+03 and 1A 1118-61. The sharp peaks correspond to periodic variability in X-ray light curve due rotation of the neutron star and its harmonics. The broad peaks correspond to the quasi-periodic variability present in the light curve (Paul & Naik, 2011).

2011; Reig, 2011). The BeXRB pulsars show various temporal changes in their physical properties, which are quantified with the following quantities: spin/pulsation period (periodic variability), quasi-periodic oscillation (QPO; quasi-periodic variability), and variation in the shape of the pulse profiles with energy and luminosity.

1.5.4 Periodic and quasi-periodic variabilities

The periodic variabilities are associated with the rotation of a neutron star about its spin axis. The spin period is the time the neutron star takes for a complete rotation. The standard technique for estimating the spin period is the power density spectra (PDS) analysis. In PDS analysis, the power corresponds to each time scale variabilities, measured through the Fourier analysis of the X-ray light curves. Multiple sharp and narrow peaks are observed in the PDS at frequencies corresponding to the coherent pulsations due to the neutron star rotation and its harmonics. Broad peaks are sometimes observed alongside the sharp peaks due to the quasi-periodic variability signatures of the accreting pulsars.

Figure 1.17 shows the detection of pulsation in the PDS of two HMXBs 4U 1901+03 and 1A 1118-61. Accreting BeXRB pulsars possess a wide range of spin periods from a few seconds to 1000 seconds. One of the fastest and slowest known accreting BeXRB pulsars are A0538-66 (Skinner et al., 1982) and 4U 2206+54 (Reig et al., 2009), respectively. However, the spin period of pulsars in BeXRBs does not remain constant. These pulsars undergo spin-up and spin-down phases. During major X-ray outbursts, a significant change in the spin period of the neutron star occurs. During major X-ray outbursts, an accretion disc forms around the neutron star, and the material in the disc with an angular frequency greater than the angular frequency of the neutron star transfers angular momentum to the neutron star (Ghosh & Lamb, 1979). Hence, significant spin period/frequency changes are observed in many accreting pulsars during giant X-ray outbursts. Figure 1.18 shows the long-term spin frequency (upper panel) and pulsed flux (lower panel) evolution of BeXRB pulsar A0535+262 and EXO 2030+375. It can be seen that during a significant change in X-ray intensity (giant X-ray outburst phase), the spin frequency of the source changes

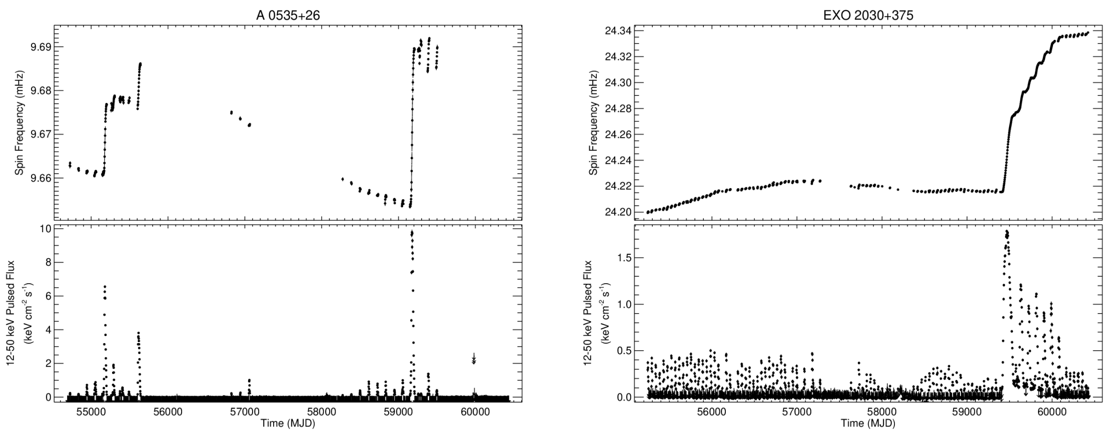

Figure 1.18: Long-term spin frequency and pulsed flux evolution of famous BeXRB pulsars A0553+262 and EXO 2030+375 measured with Fermi/GBM in 12-50 keV range (Malacaria et al., 2020).

significantly. During the normal X-ray outbursts, the spin frequency change is insignificant. One interesting observational signature is the negative change in the spin frequency during the quiescent phase. During this phase, the neutron star loses angular momentum because of the coupling between the magnetic field and material in the outer envelope. The outer envelope materials have minimal angular momentum, so they extract angular momentum from the neutron star.

Apart from the periodic variabilities, the BeXRBs also exhibit quasi-periodic variabilities. Since these are quasi-periodic variabilities, they appear as broad features in the *PDS*. Figure 1.17 shows broad features in the PDS of two HMXBs 4U 1901+03 and 1A 118-61. These broad features are usually modeled with *Lorentzians* and arise because of the presence of quasi-periodic oscillations (QPO) in the source (Belloni et al., 2002). The QPO features are usually observed in the 1 mHz – 40 Hz frequency range in HMXB accreting pulsars (Paul & Naik, 2011). The HMXBs exhibit QPOs, whose physical origins are explained through two models: the Keplerian Frequency Model (KFM; van der Klis et al. 1987) and the Magnetospheric Beat Frequency Model (MBFM; Alpar & Shaham 1985). These QPOs arise from the interaction between the co-rotating magnetosphere and irregularities in the inner accretion disc during the accretion process, leading to fluctuations in the mass accretion rate. According to KFM, these fluctuations occur at the Keplerian frequency. At the same time, MBFM suggests the QPOs occur at a beat frequency between the pulsar spin frequency and the rotational frequency of matter in the inner accretion disc. Hence, the KFM is applicable when the QPO frequency exceeds the neutron star spin frequency; otherwise, when the spin frequency of the pulsar exceeds the Keplerian frequency at the inner edge of the accretion disc, the co-rotating magnetosphere throws away the accreted matter outwards, which is also called centrifugal inhibition of accretion (Lamb et al., 1973). The KFM explained the QPOs in many transient BeXRB pulsars like EXO 2030+375 (Angelini et al., 1989) and 1A 0535+262 (Finger et al., 1996). Whereas in some other sources like 4U 0115+634 (Dugair et al., 2013), KS 1947+300 (James et al., 2010) and Swift J0243.6+6124 (Chhotaray et al., 2024), the origin of QPOs is explained with MBFM.

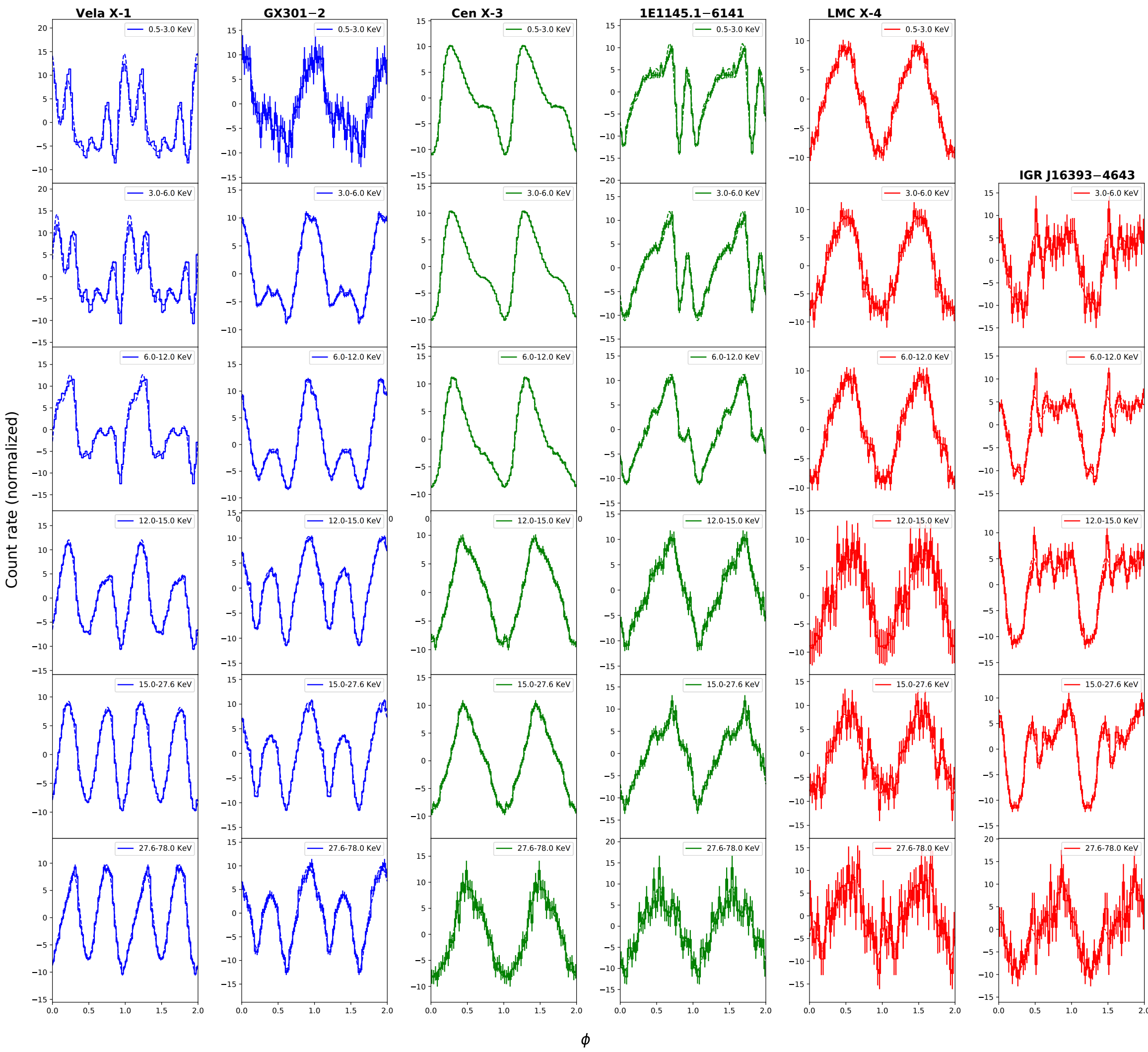

Figure 1.19: Pulse profile and its energy dependence for different accreting pulsars (Alonso-Hernández et al., 2022). Two phases are shown for clarity.

1.5.5 Pulse profiles of accreting X-ray pulsars

The pulse profile of a pulsar represents the intensity distribution over its spin phases. Pulse profiles give crucial information about the emission geometry and beam pattern of radiation in accretion-powered X-ray pulsars (Bildsten et al., 1997). Pulse profiles also carry information on the region surrounding the neutron star. Pulse profiles are generated by folding the X-ray light curve at the pulsation period of the pulsar. Accreting pulsars exhibit various shapes of pulse profiles that vary with luminosity and also from source to source (White et al., 1983; Bildsten et al., 1997). The pulse profiles are single-peaked, double-peaked, or even contain multiple peaks. The shape of the pulse profile depends upon various factors such as the angle between the magnetic axis and rotation axis with respect to the line-of-sight of the observer, mass accretion rate, region of X-ray emission, light bending effect, the geometry of magnetic field, etc. (Nagase, 1989). Accreting pulsars show single-peaked pulse profiles due to the dominant contribution to the observed flux from one of the poles of the neutron stars. Other pulsars that show double-peaked pulse profiles are also present due to contributions from both magnetic poles.

In a basic scenario featuring a dipolar magnetic field and an emission pattern symmetric around the axis, one would anticipate pulse profiles that are nearly sinusoidal in shape. Such profiles are evident in accreting millisecond pulsars, which typically have weaker magnetic fields (Poutanen et al., 2009). However, the pulse profiles of most accreting X-ray pulsars are unique and more intricate (Kanno, 1980; Alonso-Hernández et al., 2022). Figure 1.19 shows pulse profiles of different accreting pulsars. It can be seen that some pulsars like Vela X-1 and GX 301-2 have double-peaked pulse profiles. However, pulsars like Cen X-3, 1E 1145.1-6141, LMC X-4, and IGR J16393-4643 have single-peaked structure. The pulse profiles seem to be highly dependent on energy. The pulse profiles have multiple peak-like structures in the lower energy < 12 keV. These signatures are common in accreting pulsars and are attributed to the absorption of soft X-rays by material in the magnetosphere, which are distributed asymmetrically with pulse phases. Specifically these signatures are observed in various other BeXRB pulsars such as V0332+53, 1A 0535+262, EXO 2030+375, GX 304-1, and RX J0209.6-7427 (Tsygankov et al., 2006; Naik et al., 2008, 2013; Naik & Jaisawal, 2015; Epili et al., 2017a; Jaisawal et al., 2016; Vasilopoulos et al., 2020; Chhotaray et al., 2024).

Another important property of pulse profiles is their luminosity dependency. Till now, we have understood that with an increase in mass accretion rate, the luminosity of the source increases. It is important to note that the dynamics of photon matter interaction near the polar region change with increased luminosity. At a certain luminosity, called critical luminosity ($L_{\rm crit}$), a complete transition in the properties of the pulsar can be seen observationally. Pulse profile analysis is one of the important indicators of transition in properties of the pulsar at critical luminosity. At low luminosities, most of the photons are primarily generated from the thermal mound formed at the polar regions of the neutron star in the parallel direction to the magnetic field axis. Conversely, at higher luminosities, a radiation-dominated shock develops in the accretion column due to the generation of a high number of photons. This, combined with the accretion mound, influences the whole dynamics of photon generation, such as direction and energy distribution. To distinguish between these scenarios, Basko & Sunyaev (1976) introduced the concept of critical luminosity. Critical luminosity represents the threshold at which the radiation emitted from the surface of the neutron star becomes sufficiently intense to halt the accretion material above the magnetic poles, forming a radiation-dominated shock.

$$L_{\rm crit} = 2.72 \times 10^{37} \left(\frac{\sigma_T}{\sqrt{\sigma_{\parallel}\sigma_{\perp}}}\right) \left(\frac{r_o}{R}\right) \left(\frac{M}{M_{\odot}}\right) \quad erg\ s^{-1} \tag{1.22}$$

where r_o is the radius of the polar cap, σ_T is the Thomson scattering cross section, $\sigma_{\parallel}$ and $\sigma_{\perp}$ are the angle averaged cross sections for the scattering of X-ray photons propagating parallel and perpendicular to the magnetic field, respectively. Becker et al. (2012) calculated the scattering cross sections by considering the Comptonization processes (discussed below) and expressed the critical luminosity in terms of the magnetic field of the pulsar as:

$$L_{crit} = 1.49 \times 10^{37} w^{-28/15} \left(\frac{\Lambda}{0.1}\right)^{-7/5} \left(\frac{M}{1.4M_{\odot}}\right)^{29/30} \left(\frac{R}{10km}\right)^{1/10} \left(\frac{B}{10^{12}G}\right)^{16/15} \quad erg\ s^{-1} \tag{1.23}$$

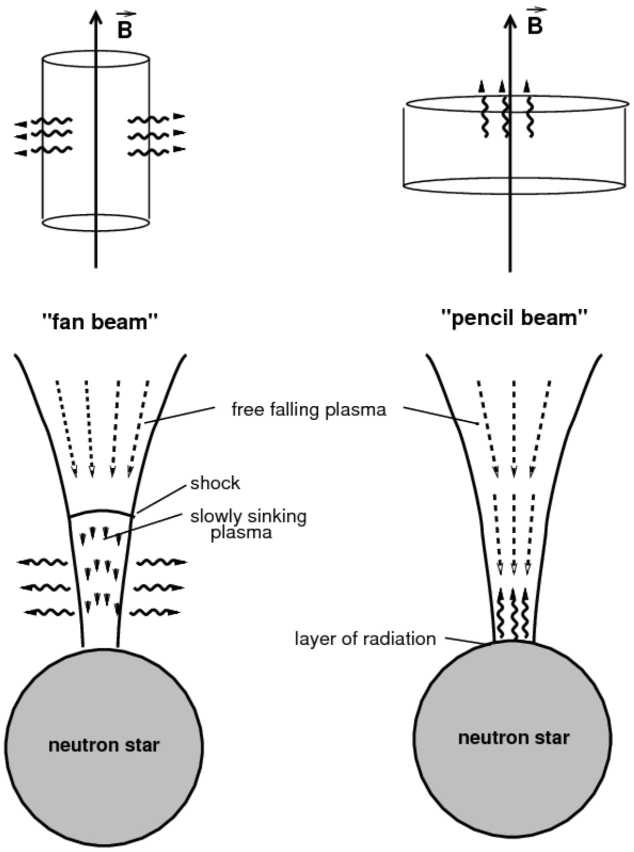

Figure 1.20: Emission of photons during the low and high luminosity phases showing the signatures of pencil and Fan beam patterns.

Here, w is a parameter that describes the shape of the continuum spectrum, and Λ characterizes the mode of accretion. Other parameters, i.e., M, R, and B, are typical mass, radius, and magnetic field strength of the neutron star, respectively. Therefore for standard neutron star parameters, the above equation simplifies to:

$$L_{\rm crit} = 1.49 \times 10^{37} \, (B_{12})^{16/15} \quad erg \; s^{-1} \tag{1.24}$$

The luminosity of the pulsar below and above this critical luminosity could thus be termed as sub-critical and super-critical luminosity, respectively. For the sources in the sub-critical luminosity regimes ($L << L_{\rm crit}$), the accreting matter is brought to rest at the surface of the neutron star via Coulomb interactions (Langer & Rappaport, 1982) near the pole. In this situation, the radiation is emitted from the accretion mound formed at the base of the accretion column, such that most of the photons are emitted parallel to the direction of the magnetic field in the form of a 'pencil beam' (see the right panel of Figure 1.20). However, in super-critical luminosity regimes ($L \geq L_{\rm crit}$), the accretion column becomes optically thick due to the development of radiation-dominated shock above the surface of the neutron star. Due to this, the parallel component of the Thomson scattering cross section is drastically reduced compared to the perpendicular one (i.e., $\sigma_{\parallel} << \sigma_{\perp}$). As a result, most of the X-ray photons escape the accretion column through the side walls in the form of a 'fan-beam' emission pattern (see the left side of Figure 1.20).

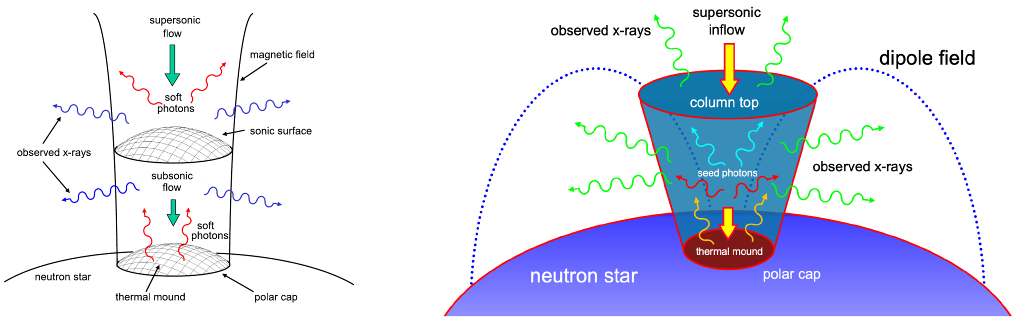

Figure 1.21: Schematic diagram of gas accreting onto magnetic poles of a neutron star. The left panel shows the accretion process in a cylindrical column, and the right panel shows the accretion process in a conical column. The seed photons due to blackbody emission, cyclotron emission, and bremsstrahlung emission are reprocessed via electron scattering and emitted through the wall of the accretion column and top of the accretion column (Becker & Wolff, 2007, 2022).

1.5.6 Spectral properties of accretion-powered pulsars

Accreting pulsars emit X-rays in a broad energy range starting from about 0.1 keV to a few hundred keV. This wide range of X-ray emission is attributed to various radiative processes in the accretion column, like blackbody emission, cyclotron emission, bremsstrahlung emission, Compton scattering, and inverse Compton scattering (Becker & Wolff, 2007, 2022). Figure 1.21 shows different regions from which seed photons are originated. The blackbody photons are created from the optically thick thermal mound, formed just above the magnetic pole due to the accumulation of accreting plasma from the companion star. The cyclotron photons are created by deexcitation of electrons from Landau level n=1 to n=0. The electrons are excited by colliding with protons. Hence, this process acts as a cooling mechanism of plasma in the accretion column. Unlike blackbody photons, created only from thermal mounds at the bottom of the accretion column, cyclotron photons can be created throughout the column. The acceleration or deceleration of a charged particle near another charged particle creates bremsstrahlung photons. Again, bremsstrahlung photons can be created in the accretion column. The low-energy seed photons are up-scattered in the accretion column by undergoing inverse comptonization with highly energetic plasma and converted hard X-rays. The inverse Compton scattering happens in the accretion column in two ways: (I) Bulk comptonization and (II) Thermal comptonization. Bulk comptonization is the process in which the hard X-ray photons are generated when the seed photons undergo inverse comptonization and gain energy from the bulk motion of the plasma onto the surface of the neutron star. The photons gain energy through first-order Fermi mechanism (Laurent & Titarchuk, 1999; Turolla et al., 2002). Thermal comptonization is the process in which photons gain energy due to stochastic or random motion of motion electrons via second-order Fermi mechanism (Sunyaev & Titarchuk, 1980; Becker, 2003).

For accretion-powered X-ray pulsars, the empirical modeling of broadband spectra is well established. The spectra are usually modeled with an absorbed power law with a cutoff in the high energy regime, a blackbody component, a Gaussian emission line, and a Gaussian absorption line. The power law component contains information about the spectral energy

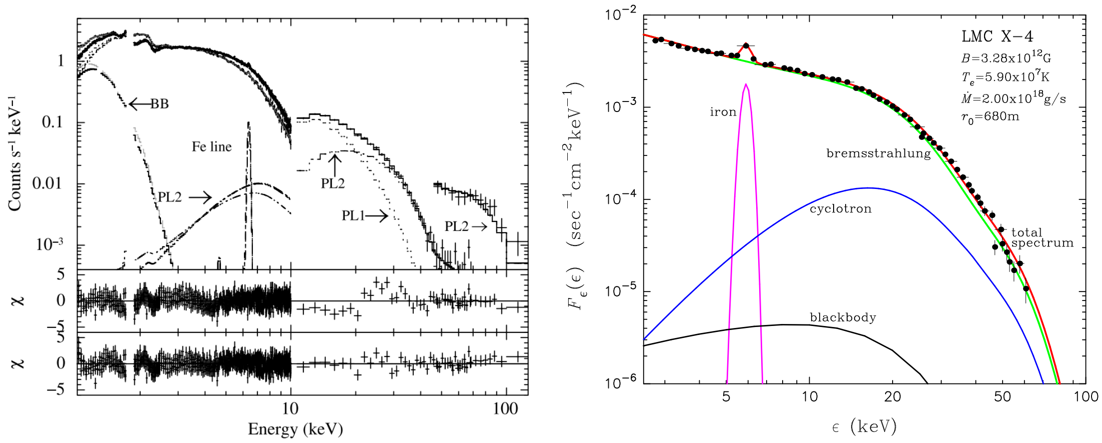

Figure 1.22: Left side: Broadband spectral fitting of A0535+262 spectrum obtained with Suzaku, along with the best-fit model comprising a blackbody component (BB), an NPEX (negative and positive power laws are marked by PL1 and PL2), a narrow iron emission line (Fe line), and cyclotron resonance scattering feature. The middle and bottom panels show the residuals after fitting with the cutoff power law continuum model and the NPEX continuum model, respectively (Naik et al., 2008). Right side: Theoretical spectral modeling of LMC X-4 with various emission components as described in Becker & Wolff (2007).

distribution of seed photons and bulk Comptonized photons. The absorption component of the continuum model quantifies the line-of-sight absorption of soft X-rays. The cutoff energy provides information about the thermal Comptonization related to the incoming plasma temperature in the accretion column. The Gaussian emission line is used to model the iron emission line from the source, and sometimes, multiple Gaussian emission lines are used to model the multiple iron line components. The Gaussian absorption component is usually used to model the cyclotron resonance scattering feature (CRSF) in the pulsar spectra. Various X-ray emission components are described below.

Blackbody component: Thermal emission (soft X-ray excess) from an accretion-powered X-ray pulsar is usually modeled with a blackbody component with peak temperature in 0.1-3 keV energy range (White et al., 1983; Coburn et al., 2002). In accretion-powered X-ray pulsars during the low luminosity phase, the region from where the thermal emission originates is considered to be the thermal mound, which is also called hot spot (Basko & Sunyaev, 1976; White et al., 1983). With increased mass accretion rate or luminosity, another region can provide optically thick emission. At higher luminosity, the top of the accretion column and the optically thick outflow from the source can emit soft-X-ray emission that can be modeled with blackbody component (e.g., Swift J0243.6+6124 Tao et al. 2019; Beri et al. 2021). In most of the cases, the blackbody emission from accretion powered X-ray pulsars is modeled with "*bbodyrad*" model, which is expressed as :

$$A(E) = \frac{K \times 1.0344 \times 10^{-3} E^2 dE}{exp(E/kT) - 1} \tag{1.25}$$

where, kT is the temperature in keV and K is the normalization constant. The normalization constant K is an important parameter, which is used to calculate the size of the blackbody emitting region if the distance to the source is known, and mathematically, it is given by K $= R_{km}^2 / \ D_{10}^2$. R_{km} is the source radius in km, and D_{10} is the distance to the source in units of 10 kpc.

Power law with high energy cutoff: The broadband continuum emission from accreting X-ray pulsars can be described using a power law with a high energy cutoff model. This model gives two critical parameters such as power law photon index (Γ) and cutoff energy (E_{cut}). Typical values of Γ and E_{cut} for accreting X-ray pulsars are between 0.5–1.5 and 10–30 keV, respectively (White et al., 1983). A higher value of Γ signifies that the source emits more soft X-ray photons. Similarly, a higher value of E_{cut} means the temperature of the incoming plasma in the accretion column is very high. Various empirical models are used to describe the spectral properties of the accretion-powered pulsars. A brief description of these models is given below.

1. The cutoff power law: This model consists of a power law modified with cutoff energy and mathematically expressed as,

$$Cutoffpl(E) = NE^{-\Gamma} e^{-E/E_{cut}} \tag{1.26}$$

   Here, N is the normalization constant that represents the flux in the unit of photons s^{-1} cm^{-2} keV^{-1}.

2. High energy cutoff model (HighECut): This model has been effective in replicating the spectra of most accretion-powered X-ray pulsars and is extensively utilized among various empirical models (White et al., 1983). However, as evident from the analytical expression, the functional form lacks continuous differentiability at the roll-over energy ($E_{\rm cut}$). Consequently, it occasionally generates spurious absorption-like features around $E_{\rm cut}$. Mathematically, this model is expressed as,

$$HighECut(E) = NE^{-\Gamma} \times \begin{cases} 1 & (E \leq E_{cut}), \\ e^{-(E-E_{cut})/E_{fold}} & (E > E_{cut}) \end{cases} \tag{1.27}$$

3. The NPEX model: The NPEX model combines two power-law components with the same cutoff energy, reflecting the physical processes in the accretion column of X-ray pulsars. Soft X-ray photons, emitted from the hot spot at the magnetic poles of the neutron star, follow a blackbody spectrum. The hard X-ray photons result from the inverse Compton scattering of these soft photons, forming a power-law distribution. The NPEX model includes a positive power-law, usually fixed at a photon index of 2 (Mihara, 1995) to represent Wien's peak, and a negative power-law with a variable photon index. Mathematically, it is expressed as,

$$NPEX(E) = (A_1 E^{-\alpha} + A_2 E^{+\beta}) e^{-E/E_{\rm cut}} \tag{1.28}$$

   where A_1 and A_2 are the normalization constants, α and β are power-law indices, and $E_{\rm cut}$ is the cutoff energy. The normalization constants A_1 and A_2 represent the flux in the unit of photons/s/cm^2/keV.

Gaussian component: The Gaussian component is usually used to model the iron emission lines in the 6-7 keV energy. The 6.4 keV Fe K_α line is the most common feature in the spectra of accretion-powered X-ray pulsars, though it is occasionally absent at low luminosity phases. The strength and shape of the Fe K_α line varies with luminosity. In the spectra of some accreting pulsars at high luminosity phase, multiple Gaussian components are required to model the 6.4 keV, 6.67 keV, and 6.98 keV iron lines (Jaisawal et al., 2019). These lines are modeled with a Gaussian function (`gauss`), expressed as :

$$gauss(E) = \frac{A}{\sigma\sqrt{2\pi}} \exp\left(\frac{-(E-E_0)^2}{2\sigma^2}\right) \tag{1.29}$$

where A is the normalization of the Gaussian component in units of photons cm^{-2} s^{-1} and E_0 and σ are line energy (Gaussian centroid) and line width in keV, respectively.

Cyclotron resonant scattering feature (CRSF): Apart from the broadband continuum and emission lines, broad absorption lines are usually seen in the spectra of accretion-powered X-ray pulsars in 10-100 keV range (Staubert et al., 2019). Detection of such absorption features in the X-ray spectrum of accreting pulsars with strong magnetic field ($\sim 10^{12}$ G) is attributed to the CRSFs. According to classical electrodynamics, an electron moving in the presence of magnetic field follows a helical trajectory with the gyration radius (Larmour radius) expressed as:

$$r_L = \frac{m_e v_\perp}{Be} \tag{1.30}$$

With increasing magnetic field strength, this radius decreases. Once this radius r_L approaches the de-Broglie wavelength (λ=h/m_e v), the quantum mechanical effects start to dominate. Consequently, the electron momentum ($p_\perp$) (and hence energy) perpendicular to the direction of the magnetic field becomes quantized. Hence, the electrons can only be present in specific energy levels. These energy levels are called Landau levels. While interacting with the relativistic plasma in the accretion column, the X-ray photons undergo scattering processes with these electrons. The corresponding scattering cross section is resonantly increased at the energies corresponding to the separation between these Landau levels. For accreting pulsars, these discrete energy levels seemed to be equispaced with the energy difference of

$$E_{CRSF} = 11.57 \times B_{12}(1+z)^{-1} \tag{1.31}$$

Where, B_{12} is the magnetic field in units of 10^{12} G, and z is the gravitational red-shift (z $\simeq$ 0.3 for typical neutron star). The X-ray photons with energies n E_{cycl} could thus get absorbed and, therefore, are missing from the line of sight of the observer. Consequently, the lack of these photons manifests as absorption features in the observed spectrum of the pulsar. Figure 1.23 exhibit detection of multiple CRSFs in the broadband spectra of 4U 0115+63. From Equation 1.31, it is clear that the cyclotron line energy is directly proportional to the magnetic field strength of the pulsar. Therefore, detecting CRSF in the pulsar spectrum is a direct method to estimate and probe the high magnetic field of the pulsars. The CRSF is

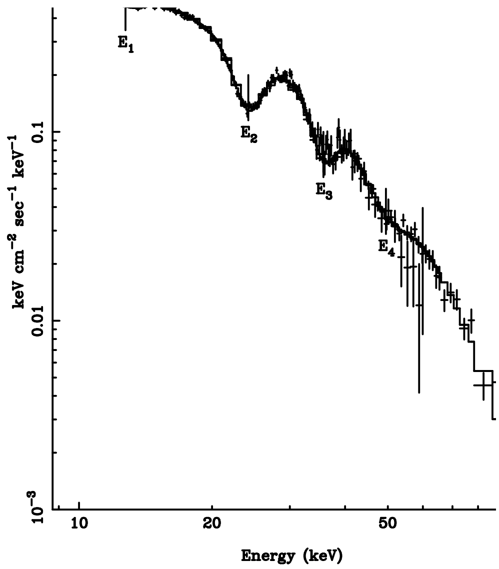

Figure 1.23: Detection of multiple CRSF in the broadband spectra of 4U 0115+63 (Santangeo et al., 1999)

usually modeled with the GABS model, and mathematically, it is expressed as,

$$GABS(E) = \exp\left(-\frac{\tau}{\sqrt{2\pi}\sigma}\exp\left(-\frac{(E - E_{\rm line})^2}{2\sigma^2}\right)\right) \tag{1.32}$$

where E is the photon energy, τ is the optical depth of the line, line $E_{\rm line}$ is the centroid energy of the absorption feature, and σ is the width (standard deviation) of the Gaussian.

1.5.7 Interaction between neutron star and the circumstellar disc of the Be star

For several years, it has been suggested that the circumstellar (decretion) discs around the isolated Be stars and Be stars in binaries have similar physical origins. The viscous decretion disc model can explain the observational properties of both isolated and binary Be stars. However, the density and size of the disc of the Be star in BeXRBs are very different from the isolated Be star because of the interaction of the neutron star with the decretion disc. According to the viscous decretion disc model, the angular momentum is added to the disc through viscous torques (T$_{vis}$) and removed by the tidal torques (T$_{tid}$) exerted by the neutron star (Negueruela et al., 2001). The disc truncation occurs at a specific radius where the ratio between the angular frequency of the disc rotation and the mean angular frequency of the binary motion is a rational number. The condition for this disc truncation is defined as follows:

$$T_{vis} + T_{tid} \leq 0 \tag{1.33}$$

Hence, due to disc truncation, the circumstellar discs are denser for the Be stars in binaries than the isolated Be stars (Zamanov et al., 2001). In neutron star BeXRBs, a correlation between the maximum size of the decretion disc and the orbital period (P$_{orb}$) is observed. In the case of a smaller orbital period neutron star BeXRB, the circumstellar disc

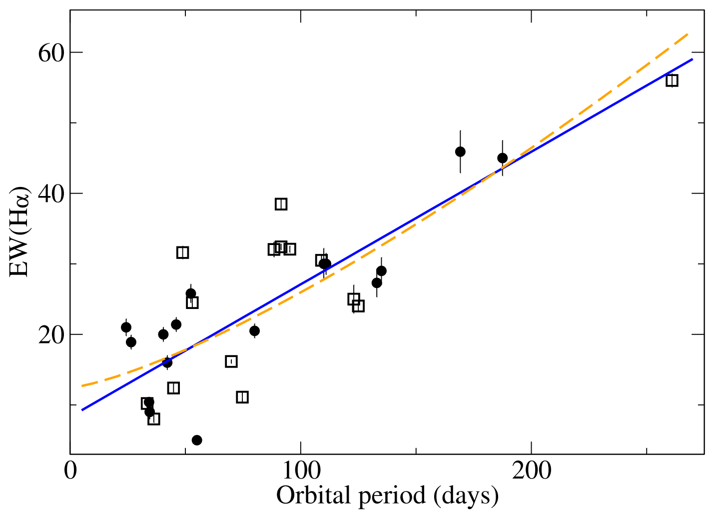

Figure 1.24: P_{orb}–EW(Hα) diagram: Milky Way objects are represented by circles, and BeXRBs in the Small Magellanic Clouds are represented by squares. The solid line shows the linear regression for the combined data sample, while the dashed line indicates a power law fit with an exponent of n=4/3 (Reig, 2011).

of the Be star gets truncated at a smaller radius (see Figure 1.24).

Additionally, in BeXRBs, it has been seen that the changes in the X-ray properties of the compact object are also reflected in the optical/infrared properties of the companion Be star. Specifically, during any giant X-ray outburst of the neutron star in the system, the Be star in the binary also shows significant changes in its optical/infrared properties. The most-studied parameters for tracking the properties of the circumstellar disc during giant X-ray outbursts are the equivalent width (EW) and optical/infrared magnitude of the system. Figure 1.25 shows variation in the X-ray and optical properties of the BeXRB Swift J0243.6+6124 over a long period of time (Liu et al., 2022). It can be seen that the X-ray intensity of the source varies significantly during the mentioned period. The critical optical parameters mimicking the disc properties, like Hα equivalent width and V-band magnitude, also considerably varied throughout the period.

In phase I, the source undergoes a giant X-ray outburst. It is expected that the neutron star must have affected the circumstellar disc around the Be star. However, this phase does not present any clear trend in the EW of the Hα line and the V-band magnitude of the Be star. In phase II, we can see that the EW of the Hα is found to be small, and the V-band magnitude also increases in this phase. These variations are expected because, during the Type II X-ray outburst, the neutron star must have captured a considerable amount of material. Lower EW of Hα line suggests a decrease in the Hα emitting particle. The V-band and infrared magnitudes signify the amount of continuum emission from the circumstellar disc. In phase II, an increase in these values means a decrease in the visible and IR flux as the density of emitting particles in the disc decreases. In phase III, an increase in the EW of Hα line and a decrease in the V-band magnitude indicates that the disc has started to grow again Haigh et al. (2004). Hence, we can say that the physical properties of the circumstellar disc change significantly during any giant X-ray outburst. This verifies the interaction of neutron stars on the circumstellar disc.

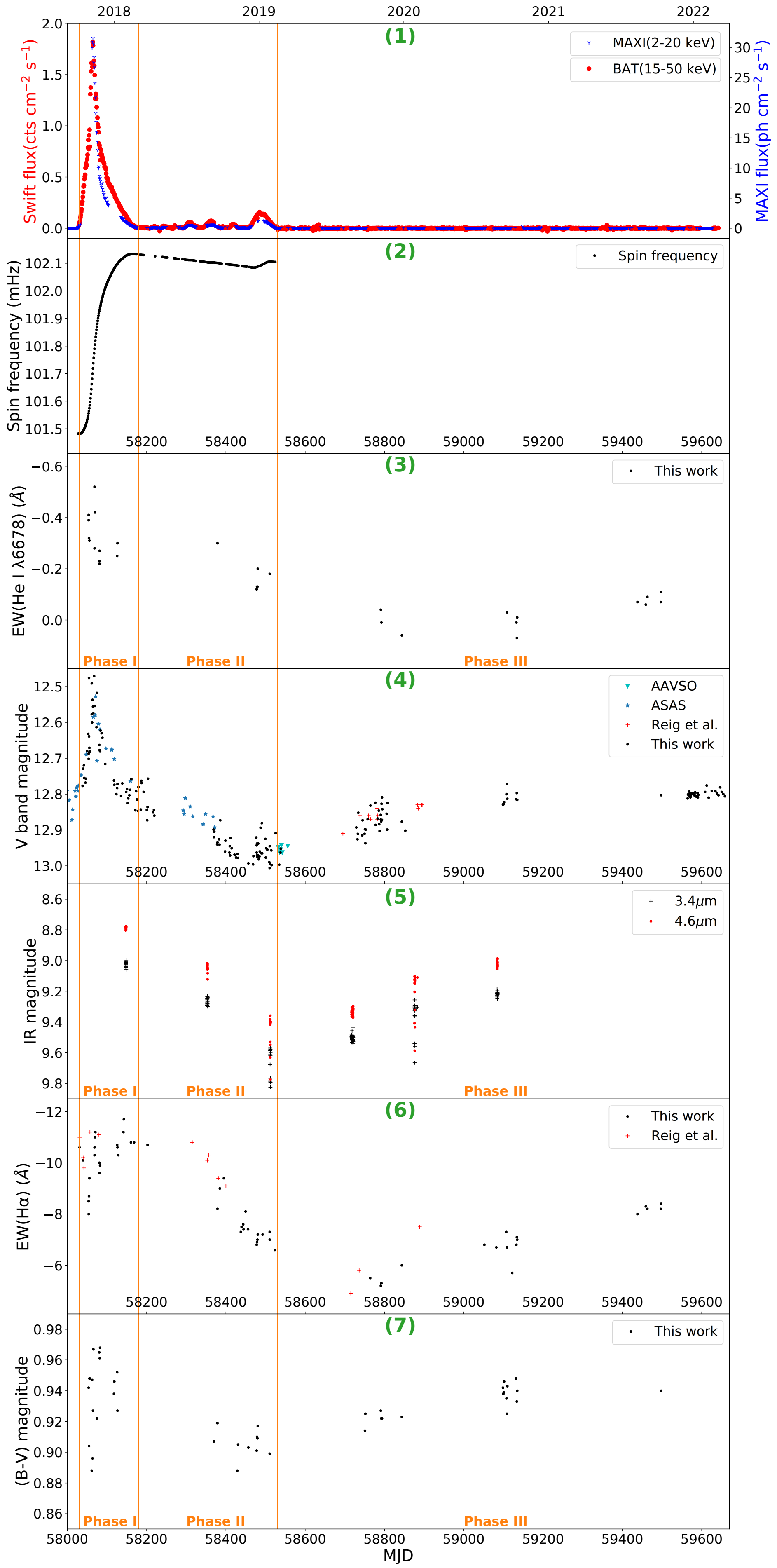

Figure 1.25: Long-term evolution of X-ray and optical properties of Swift J0243.6+6124 (Liu et al., 2022).

1.6 Motivation and objective of the thesis

X-ray binary systems (XRBs) are the brightest X-ray sources in our Galaxy. Depending on the mass of the companion, the XRBs are classified as LMXBs and HMXBs. The BeXRBs are known to be the largest subclass of HMXBs. In these systems, the compact object is usually a neutron star, which exhibits a wide range of variations in X-ray emission. These systems display two types of X-ray outbursts, Type I and Type II, fueled by the material from the companion Be star.

Type I outbursts are periodic, occurring during the periastron passage of the neutron star, and can reach luminosities up to 10^{37} erg s^{-1}. In contrast, Type II outbursts are aperiodic, irregular, and significantly more luminous, with peak luminosity reaching up to 10^{39} erg s^{-1}. These outbursts in BeXRBs are rare, occurring once or twice in a particular system in a decade. Therefore, the underlying mechanisms causing these outbursts remain poorly understood. Our motivation is to elucidate the complex interactions between the neutron star and the circumstellar disc during these giant outbursts.

In accreting pulsars, the majority of radiation originates from the accretion column. The physical processes in the accretion column, influenced by the mass accretion rate or luminosity, significantly affect the X-ray properties of the pulsar. These pulsars can occasionally reach super-Eddington luminosities, a rare phenomenon. Given the strong gravitational and magnetic fields ($\sim 10^{12}$ G) of neutron stars, our goal is to understand the dynamics of these complex processes, particularly in the extreme environments at super-Eddington phases.

The major research objectives of this study are:

- To investigate changes in the Hα line properties (an indicator of the Be circumstellar disc) before, during, and after Type II X-ray outbursts, aiming to understand the disc conditions leading to these outbursts.
- To analyze BeXRBs through simultaneous X-ray and optical observations to identify correlations between X-ray and optical emissions.
- To examine variations in the pulse period of the neutron star and pulse profile with luminosity, seeking insights into the mass accretion mechanisms and the dynamic nature of the surrounding region.
- To explore changes in the continuum emission properties of pulsars across a wide range of luminosities (up to four orders of magnitude) to better understand the complex interactions between plasma and photons near the accretion column.

1.7 Outline of the thesis

This chapter of the thesis provides information about XRBs, their classifications, and different mass accretion mechanisms in XRBs. A detailed picture of BeXRBs and their X-ray and optical emission properties, as well as a current understanding of the topic, are also presented. The rest of the thesis is organized as follows:

`Chapter-2`: This chapter provides an overview of various X-ray and optical instruments onboard respective X-ray astronomical observatories and ground-based optical observatories, respectively, from which the data have been acquired to study the BeXRBs under investigation. It also offers a detailed explanation of the data reduction procedures, software, various tools, and techniques used in the timing and spectral data analysis of BeXRBs.

`Chapter-3`: This chapter describes the results obtained from optical and X-ray observations of a Be/X-ray binary 1A 0535+262. We studied the optical properties of 1A 0535+262 covering the epochs before, during, and after the 2020 giant X-ray outburst over a time span of two years. To investigate the changes in the properties of the Be star and its circumstellar disc, we observed the source using 16 epochs of observations before, during, and after the giant X-ray outburst in the optical band using the 1.2 m telescope at Mount Abu Infrared Observatory (MIRO). Apart from the optical observations, we also carried out a pointed X-ray observation of the pulsar with AstroSat during the rising phase of the outburst to investigate its X-ray properties. From this work, we suggest that during the 2020 giant outburst, the neutron star accreted matter from a precessing, inclined warped circumstellar disc around the Be star. The neutron star was spinning at a period of $\sim$103 second, and the magnetic field of the neutron star was estimated to be 5.2 $\times$ 10^{12} G.

`Chapter-4`: In this chapter, we discussed the properties of IGR J06074+2205 using X-ray and optical observations of the binary. We used X-ray data obtained during the X-ray outbursts in October and December 2023 from NuSTAR and NICER. The optical observations were also carried out during November & December 2022, October & December 2023, and February 2024 using Mount Abu Infrared Observatory (MIRO) and Indian Astronomical Observatory (IAO) to understand the optical properties of the binary. During X-ray outbursts, the accreting pulsar exhibits a spin period of $\sim$374.6 seconds. The pulse profiles of the pulsar are highly dynamic, varying with luminosity and energy. Broadband spectral analysis using NuSTAR observations indicates the magnetic field of the neutron star as 4.4×10^{12} G. Optical studies of the binary system suggest that the circumstellar disc properties remain largely unchanged during the X-ray outbursts, although the strength of the disc is increasing, potentially leading to future outbursts.

`Chapter-5`: In this chapter, we describe the properties of the first Galactic Ultra-Luminous X-ray (ULX) pulsar Swift J0243.6+6124. The ULX Swift J0243.6+6124 showed giant and subsequent normal X-ray outbursts within MJD 58029 (3 October 2017) and MJD 58533 (19 February 2019). The source also went into an outburst phase between MJD 60097 (2 June 2023) and 60190 (3 September 2023), as shown in Figure 1. We used Neutron star Interior Composition Explorer (NICER) observations for the long-term study of Swift J0243.6+6124 in the soft X-ray band. We conducted a thorough spectral study of the source during the giant and subsequent normal X-ray outbursts, including the new outburst in 2023. Moreover, our timing analysis primarily focuses on the multiple normal outbursts, including the recent outburst in 2023, during the post-giant outburst period between MJD 58303-60190. During the 2023 outburst, the spin frequency of the pulsar increased, indicating that the neutron star was spinning up. The pulse profile of the pulsar are found to vary significantly with luminosity. Transitions in the continuum parameter evolution are observed at $L_1 \approx 7.5 \times 10^{37}$ erg s^{-1} and $L_2 \approx 2.1 \times 10^{38}$ erg s^{-1}, suggesting that the source underwent three distinct accretion modes as luminosity increased. A $\sim$ 1 keV emission line is detected during the super-Eddington state, indicating the presence of an ultra-fast outflow in this state.

`Chapter-6`: The conclusive remarks on the present work and the prospects for future studies are discussed in this chapter.

Chapter 2

X-ray and optical observatories, data reduction, and analysis

This chapter discusses various X-ray and optical observatories and corresponding instruments, data reduction, and analysis techniques relevant to this thesis. As outlined in Chapter 1, the atmosphere of Earth is opaque to X-ray radiation and allows visible light to pass through it. Consequently, the X-ray observatories are space-based, unlike ground-based optical observatories.

X-ray observations of cosmic source evolved significantly since the launch of the first X-ray mission, `Uhuru`, in 1970, with substantial improvements in effective area, resolution (spatial, temporal, and energy), sensitivity, and energy coverage of modern instruments. Even before 1970, people used to do X-ray astronomy using balloon and rocket-borne experiments that carried X-ray detectors above the atmosphere of Earth. In the early days, the detectors used were simple instruments like gas-filled proportional counters, which detected X-ray photons by photo-ionizing the filled gases. The sensitivity of these detectors depended on their size and the absorption cross-section of the filled gases. Despite their simplicity, proportional counters enabled numerous scientific discoveries in observatories such as the Rossi X-ray Timing Explorer (RXTE), European X-ray Observatory Satellite (EXOSAT), and AstroSat. However, these detectors are only effective for bright X-ray sources, while many X-ray sources in the universe are very faint. Increasing the size of detectors is an option to collect more photons. However, practical limitations exist for proportional counters. Additionally, these detectors struggle to detect weak X-ray sources amidst strong background noise, limiting their sensitivity. Therefore, designing telescopes and detectors with large collecting areas and high sensitivity is essential. This challenge was addressed by developing the concept of the X-ray focusing technique. Focusing X-ray photons onto an imaging detector increases the signal-to-noise ratio (SNR) and allows simultaneous observation of multiple X-ray sources.

Reflecting and focusing X-ray photons onto a detector poses technical challenges, as X-rays, due to their higher energy, are either absorbed by the atoms of the reflecting mirror or pass through. According to Snell's law, X-rays need to be reflected at grazing angles (θ) for a material of refractive index (n) < 1, where $\theta \propto \frac{Z^{1/2}}{E}$, with Z being the atomic number and E the energy of the radiation. Materials such as Ni, Au, Pt, and Ir are used as reflectors for telescope mirrors to reflect high-energy X-rays. H. Wolter proposed a specific telescope mirror design in 1952 to focus X-rays, using parabolic and hyperbolic mirrors in a configuration known as the Wolter configuration. The advent of focusing X-ray telescopes significantly increased the effective area and sensitivity, enabling the detection of nearly half a million X-ray sources by the last decade (Reig, 2011). In this thesis, data from several X-ray observatories have been utilized, including the Neutron Star Interior Composition Explorer (NICER; Gendreau et al. 2016), AstroSat (Singh et al., 2014), Nuclear Spectroscopic Telescope Array (NuSTAR; Harrison et al. 2013), Swift (Gehrels et al., 2004), Fermi (Malacaria et al., 2017), and MAXI (Mihara & Maxi Team, 2010). Detailed discussions on these observatories are provided below.

In contrast to X-ray radiation, the atmosphere of Earth is transparent to visible light, allowing most of the optical observatories to be ground-based. Although the atmosphere is transparent to visible light, it can alter the direction of incoming photons from a point source, causing the light to spread and affect the angular resolution of optical telescopes. Space-based optical observatories like the Hubble Space Telescope (HST) have been deployed to mitigate this atmospheric distortion. The HST has made significant discoveries, including observing distant stars and galaxies, due to its ability to operate above the distorting effects of the atmosphere. Ground-based optical observatories are also highly effective for scientific studies, primarily due to their large telescope sizes, which provide substantial light-gathering power. For the optical studies of BeXRBs in this thesis, data are collected using two ground-based optical observatories: the Mount Abu Infrared Observatory (MIRO; Shah et al. 2005) & Indian Astronomical Observatory (IAO; Cowsik et al. 2002) of India. These observatories offer excellent facilities for detailed optical observations despite being subject to atmospheric effects.

This thesis presents X-ray and optical observations of three BeXRBs: 1A 0535+262, IGR J06074+2205, and Swift J0243.6+6124. The X-ray and optical data are acquired through proposal submissions to various observatories and from publicly available archives. The data reduction and analysis are performed using publicly available software, a self-developed pipeline, and Python-based scripts, ensuring thorough and accurate scientific processing of the observational data.

2.1 X-ray & optical observatories

2.1.1 NICER: a soft X-ray observatory

We have extensively utilized the long-term timing and spectral monitoring capabilities of NICER in studying the X-ray properties of Be/X-ray binaries. NICER, a NASA telescope launched on 3 June 2017, is mounted on the International Space Station (ISS). Figure 2.1 illustrates the mounting of NICER on the ISS. NICER is dedicated to studying the extraordinary electromagnetic, gravitational, and nuclear physics environment of neutron stars through timing and spectroscopy in the soft X-ray (0.2-12 keV) band. The primary scientific instrument of NICER is the X-ray Timing Instrument (XTI; Gendreau et al. 2016), designed to operate in the 0.2-12 keV energy range. The XTI comprises 56 X-ray concentrator (XRC) mirrors (see Figure 2.2) arranged in a Wolter I configuration to focus grazing

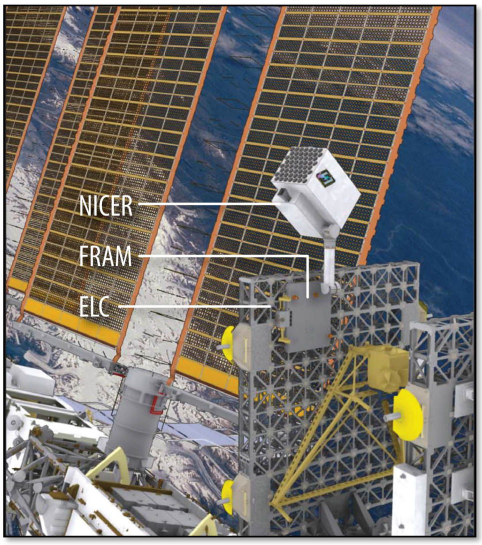

Figure 2.1: NICER experiment mounted on the International Space Station (ISS).

incidence X-ray photons onto the detectors. Since NICER is designed to observe on-axis point sources, imaging capabilities are unnecessary. The mirrors in NICER are specifically designed to provide a smaller field of view and focus light onto smaller detectors, utilizing parabolic mirrors to reduce costs and weight. Each XRC consists of 24 nested, grazing-incidence, gold-coated aluminum foil mirrors of parabolic shape. These concentrator optics are paired with silicon drift detectors, enabling non-imaging observations (Prigozhin et al., 2016). The XTI offers a high time resolution of approximately 100 ns (rms) and a spectral resolution of about 85 eV at 1 keV. Its field of view covers approximately 30 arcmin^2 in the sky. The effective area of NICER is approximately 1900 cm^2 at 1.5 keV, utilizing 52 active detectors. The XTI is divided into seven groups of eight focal plane modules (FPMs), each managed by a Measurement/Power Unit (MPU) slice, allowing for independent operation and control of the FPMs within each group.

2.1.2 AstroSat: a broadband energy facilitated observatory

AstroSat is India's first multi-wavelength astronomical satellite (Agrawal, 2006) dedicated to the observations of cosmic sources in a broad energy range from optical to X-ray bands. It was launched by the Indian Space Research Organization (ISRO) on 28 September 2015. AstroSat is equipped with five major payloads (Figure 2.3): Ultra Violet Imaging Telescope (UVIT; Tandon et al. 2017), Scanning Sky Monitor (SSM; Ramadevi et al. 2017), Soft X-ray Telescope (SXT; Singh et al. 2017), Large Area X-ray Proportional Counter (LAXPC; Yadav et al. 2016), and Cadmium Zinc Telluride Imager (CZTI; Bhalerao et al. 2017). Along with the payloads mentioned above, an auxiliary payload known as a Charged Particle Monitor (CPM) is also deployed to apprise other detectors about the presence of the South Atlantic Anomaly (SAA) region along the orbit. In the thesis, we used data from X-ray payloads such as SXT, LAXPC, and CZTI to study the X-ray properties of 1A 0535+262, as UVIT was not operational during our observation.

The SXT is an X-ray focusing imaging instrument consisting of coaxial and con-focal shells of conical mirrors arranged with Wolter I configuration. SXT has 40 complete shells

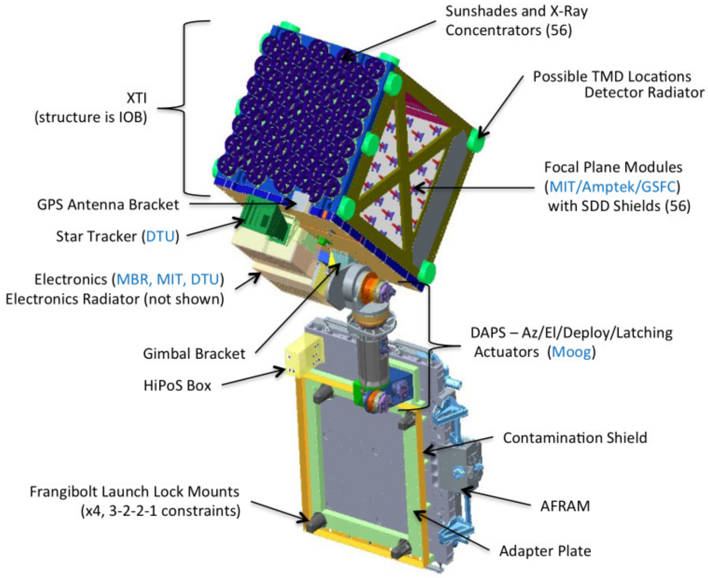

Figure 2.2: Schematic of NICER in its normal observing configuration. The X-ray Timing Instrument, featuring an array of 56 X-ray concentrator mirrors and sunshades, focuses X-ray emissions from cosmic sources onto a corresponding array of 56 Focal Plane Modules (FPMs) at the backplane of the XTI (Okajima et al., 2016).

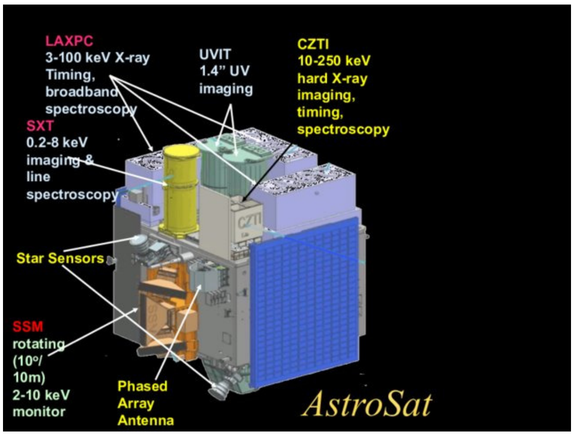

Figure 2.3: A schematic view of the AstroSat with folded solar panels showing its principal instruments (Singh, 2018).

of mirrors assembled quadrants-wise (320 mirrors) for paraboloid and hyperboloid mirrors. The focal length of the telescope is 2000 mm, constrained by the available space in the launch vehicle. Mirrors are made of aluminum and covered with gold on the reflecting sides. SXT is a soft X-ray focusing telescope sensitive to photons in the 0.3-8 keV range. Due to its focusing characteristics, it is close to 1000 times more sensitive than any other non-focusing instrument with the same photon collecting area. The on-axis effective area of SXT is 90 cm^2 at 1.5 keV with an energy resolution of 90 eV and 136 eV at 1.5 keV and 5.9 keV, respectively. The time resolution of SXT is 2.4 s in *Photon Counting (PC)* mode.

The LAXPC is a non-imaging instrument consisting of three identical, co-aligned, independently operated proportional counters to achieve a large effective area. The three LAXPC (detectors) are identified as LAXPC10, LAXPC20, and LAXPC30. The proportional counters are filled with Xenon gas at two atmospheric pressure. These detectors are sensitive to X-ray photons with energy in the range of 3-80 keV and provide a total effective area of 8000 cm^2 at 5-30 keV. The energy and time resolutions of the LAXPC units are 12% at 22 keV and 10 μs, respectively. The dead time of the detectors is 42 μs.

The CZTI is designed to perform simultaneous X-ray imaging and spectroscopic observations. CZTI operates in the hard X-ray regime, covering the energy range of 20–150 keV. Utilizing an array of Cadmium Zinc Telluride (CZT) detectors, this instrument provides high sensitivity and energy resolution, which is crucial for detecting and analyzing faint X-ray sources in hard X-rays. The CZTI features a coded aperture mask, which enables precise imaging capabilities in the specified energy band. Its primary scientific objectives include studying high-energy processes in various astrophysical sources such as pulsars, black holes, and gamma-ray bursts. Moreover, the ability of CZTI to detect polarization in hard X-ray emissions provides invaluable data for understanding the magnetic field structures and emission mechanisms of celestial sources. The CZTI has a total effective area of 2000 cm^2 for the energy range of 20-300 keV. Time tagging of an event can be estimated within 20 μs.

2.1.3 NuSTAR: a hard X-ray focusing telescope

NuSTAR, the first hard X-ray focusing observatory, was launched on 13 June 2012 as a Small Explorer satellite mission (SMEX) led by the California Institute of Technology (Caltech) and managed by the Jet Propulsion Laboratory (JPL). After being positioned in low equatorial Earth orbit (with an inclination of $\sim 6°$) at an altitude of 600 km, the NuSTAR X-ray optics and detector benches were separated using a deployable mast. Figure 2.4 shows a schematic view of the satellite before and after deployment. The X-ray optics consist of two co-aligned grazing incidence Wolter I telescopes, each with a focal length of 10.14 m. Each telescope comprises 133 mirror shells arranged in a conical approximation of the Wolter I configuration. These shells are coated with alternating layers of Pt/SiC and W/Si, enabling NuSTAR to achieve efficient reflectivity up to 78.4 keV, corresponding to the Pt K-edge. Above this energy, the mirror coating absorbs instead of reflecting the hard X-ray photons (Harrison et al., 2013).

The two telescopes focus hard X-rays onto separate focal plane modules, FPMA and FPMB (hereafter FPMs). Each module contains a 2×2 array of CdZnTe (CZT) crystal detectors with 32×32 pixels each, resulting in a field of view of approximately $\sim$12 arcmin. Each pixel has an independent discriminator, triggering the readout process upon individual X-ray interactions. Consequently, the NuSTAR observations do not suffer from pileup effects until a source flux of 10^5 count s^{-1} pixel^{-1} is reached. The energy resolution of each detector is 0.4 keV at 10 keV and 0.9 keV at 68 keV (FWHM). Each FPM is shielded with an anti-coincidence CsI scintillator. The X-ray events registered simultaneously in the CsI shield and CZT detectors are rejected as background by the onboard electronics. The high temporal resolution of 2 μs can be achieved with the NuSTAR.

2.1.4 MIRO: a 1 m class ground-based observatory

MIRO is a ground-based optical/infrared observatory located at Mount Abu, Rajasthan, India. Figure 2.5 presents a panoramic view of the observatory. The observatory is located at an altitude of 1680 m and is adjacent to Guru Shikhar, the highest peak of the Aravalli Range. MIRO is being managed by the Physical Research Laboratory (PRL), India. MIRO

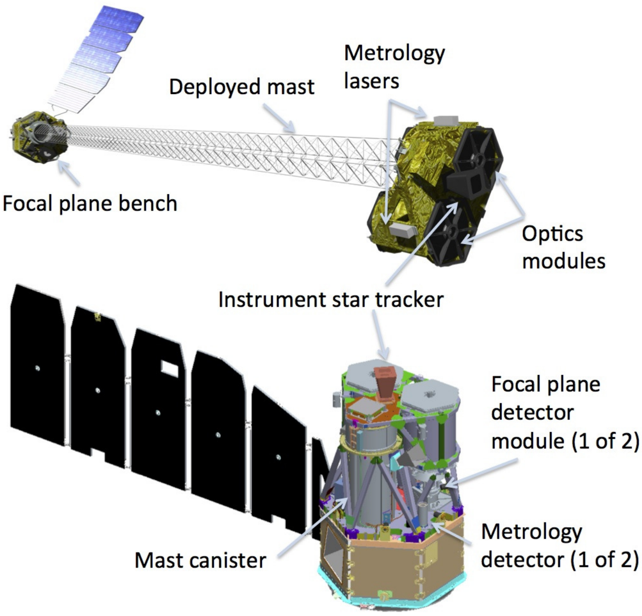

Figure 2.4: Diagram of the NuSTAR observatory in the stowed (bottom) and deployed (top) configurations.

is equipped with a 1.2 m f/13 telescope along with various back-end instruments. This work used data from Mount Abu Faint Object Spectrograph and Camera-Pathfinder (MFOSC-P) instrument (Srivastava et al., 2018; Srivastava et al., 2021). MFOSC-P has both imaging and spectroscopic capabilities. The instrument is designed to provide seeing limited imaging ($\sim 1'$ spatial resolution) with a sampling rate of 3.3 pixels per arc-second over a 5.2×5.2 arc-minute^2 field-of-view (correspond to 1K × 1K CCD). Bessel's broadband BVRI filters have been considered to cover the visible regime of 4500-8500 Å. The MFOSC-P is facilitated with three plane reflection gratings, named R2000, R1000, and R500, with 500, 300, and 150 lp/mm at wavelengths of ∼6500 Å, 5500 Å and 6000 Å, respectively. R2000, R1000, and R500 represent the spectral resolutions ($R=\frac{\lambda}{\Delta\lambda}$) of 2000, 1000, and 500, respectively. These three modes provide standard spectral coverages of ∼6000-7000 Å, ∼4700-6650 Å, and ∼4500-8500 Å, respectively. The spectroscopic observations were carried out on several nights using a 75 μm slit which is equivalent to $1''$ on the sky. The spectroscopic observations used in this thesis were carried out in R2000 mode, the highest resolution available for the MFOSC-P instrument.

2.1.5 IAO: a 2 m class ground-based observatory

IAO (Cowsik et al., 2002) is located in Hanle village near Leh in Ladakh. IAO is situated at an altitude of 4500 meters atop Mt. Saraswati in the vast Nilamkhul Plain in the Hanle Valley of Changthang. The observatory is managed by the Indian Institute of Astrophysics (IIA), India. IAO is equipped with many instruments. We carried out optical studies using the Himalayan Faint Object Spectrograph and Camera (HFOSC) mounted on the 2.01 m telescope (also known as the Himalayan Chandra Telescope). Figure 2.6 shows the

Figure 2.5: Panoramic view of the Mount Abu Infrared Observatory (MIRO), Mount Abu. Credit: Prof. Shashikiran Ganesh

Himalayan Chandra Telescope (HCT) dome located at IAO, Hanle, Ladakh, India. HFOSC is an optical imager and spectrograph developed in collaboration with the Copenhagen University Observatory. This focal reducer-type instrument allows the coverage of a larger field for any given detector and enables both low and medium-resolution grism spectroscopy. The instrument can switch between imaging and spectroscopic modes within a few minutes. The HFOSC instrument features a camera focal length of 147 mm and a collimator focal length of 252 mm. It is mounted at the Cassegrain focus of the HCT and equipped with a 2K $\times$ 4K SiTe CCD system. Each pixel corresponds to 0.3 $\times$ 0.3 arcseconds (unvignetted), providing a field of view (FOV) of 10 $\times$ 10 arcminutes. With a reduction factor of 0.58, the instrument achieves resolutions ranging from R $\sim$ 150 to R $\sim$ 4500 using a set of 11 grisms. The HFOSC instrument has a gain of 1.22 e^-/ADU and a readout noise of 4.8 e^-. In our study, the spectra are taken with Grism 8 and 167 l slit setup, which covers a wavelength range of 5500–8350 Å, providing an effective resolution of 2000 at Hα. Halogen lamp frames are taken to flat field the images.

2.2 Data reduction

In this section, we present the details of the data reduction procedures applied to X-ray and optical data obtained from observatories mentioned in the previous section.

2.2.1 NICER

The `nicerl2` pipeline, available in `HEASoft` version 6.32, is used to process the unfiltered event data of NICER. The analysis is performed in the presence of gain and calibration database files of version `xti20221001`. We selected good time intervals (GTI) using the `nimaketime` tool, applying standard filtering criteria based on various factors such as the

Figure 2.6: The 2-m class Himalayan Chandra Telescope (HCT) at the Indian Astronomical Observatory (IAO). Credit: www.iiap.res.in

South Atlantic Anomaly (SAA), an elevation angle exceeding 15° from the Earth limb, a $> 30°$ offset from the bright Earth, and a pointing offset of 0.015°, all on clean data post-`nicerl2`. Additionally, we applied a magnetic cutoff rigidity of 4 GeV/c to filter out any potential high-energy charged particle background. In this thesis, data from the NICER observations of BeXRBs IGR J06074+2205 and Swift J0243.6+6124 are used.

2.2.2 AstroSat

Data from three major payloads of AstroSat, i.e., SXT, LAXPC, and CZTI, are used in this thesis. The level2 (cleaned event data) SXT data from 17 orbits of the PC mode observation of 1A 0535+262 are downloaded from the *AstroSat Archive-ISSDC*. For further analysis, a single $eventfile$ was created by combining the event files of all orbits using the *sxteventmergertool* module. For a generation of high-level products, we selected source region. The source region is selected in such a way that there will be minimal loss of photons. We also checked for the presence of a pile-up effect. The background region for the background light curve is selected far away from the source region to avoid contamination from source photons. The effective area file is generated, and the files correspond to the spectral redistribution matrix and background provided by the instrument team. The data from LAXPC20 were collected in Event Analysis (EA) mode, then reduced and processed using the latest *LAXPCsoftware* package to generate the scientific products. For CZTI data, screening, cleaning, and high-level products are generated from level1 data using modules provided within the *CZTpipeline* task. In our work, AstroSat data of the BeXRB 1A 0535+262 are used.

2.2.3 NuSTAR

For NuSTAR, the data reduction was carried out using the HEASoft v.6.32 and the calibration files of version 20231017. We followed the standard data processing routines where

NUPIPELINE task is executed to generate calibrated and filtered event files. These event files are then further used for generating high-level scientific products. Light curves, spectra, ARF, and RMF are generated by carefully selecting the source and background region. Source and background regions were selected to ensure minimal loss of source photons and to prevent any contamination between the source and background regions. In this thesis, NuSTAR data of the BeXRB IGR J06074+2205 have been used.

2.2.4 MIRO

As mentioned in the previous section, MIRO is equipped with various back-end instruments. In this work, we used data from the MFOSC-P instrument. The raw data of the MFOSC-P observations are reduced using the in-house developed data analysis routines in Python[1] with the assistance of open-source image processing libraries (ASTROPY[2]) (also refer to Kumar et al. 2022 for the analysis method). In the beginning, the bias is subtracted, cosmic rays are removed, and sky-subtracted images are created. Using a halogen lamp, the pixel-to-pixel efficiency variation is found to be less than 1%; hence, no correction is applied. In the second step, the spectra of Neon and Xenon calibration lamps (taken after each source exposure) are used for the wavelength calibration of the data. These wavelength-calibrated data are used for further analysis. In our work, MFOSC-P data of the BeXRBs 1A 0535+262 and IGR J06074+2205 are used.

2.2.5 IAO

We have used data from the HFOSC instrument mounted on HCT at IAO. The reduction of HFOSC data is performed using self-developed data analysis routines in Python with the assistance of open-source image processing libraries (ASTROPY, etc.) and standard IRAF tasks. In the first step, bias subtraction, cosmic-ray removal (van Dokkum, 2001), and flat-fielding are done for all frames. Then, one-dimensional spectra are extracted after removing the mean sky background taken from both sides of the spectrum. In the second step, we extract wavelength-calibrated spectra using FeNe lamp spectra. In this thesis, HFOSC data of the BeXRB IGR J06074+2205 are used.

2.3 Timing and spectral analysis technique

The reduced data from the X-ray and optical observations of the BeXRBs are stored in a Flexible Image Transport System (FITS) format and ready for further scientific analysis. For analysis of X-ray data, we utilized the High Energy Astrophysics Software (HEASoft[3]) package. The HEASoft package is publicly available on NASA's High Energy Astrophysics Science Archive Research Centre (HEASARC[4]). It is a multi-mission platform and can be used to analyze data from various observatories that are publicly available on this platform. A Calibration Data Base (CALDB) is maintained on HEASARC for each mission, which regularly gets updated as per the performance of instruments and conditions in space. We

[1] https://www.python.org/
[2] https://www.astropy.org/
[3] https://heasarc.gsfc.nasa.gov/docs/software/heasoft/
[4] https://heasarc.gsfc.nasa.gov/

utilized HEASoft versions 6.27 and 6.32 and an up-to-date CALDB to derive the scientific products for each observation.

X-ray photons from astrophysical sources are stored as event lists after being detected in the X-ray detectors. The event list contains information regarding the arrival time and position of the photon on the detector plane, along with its energy. In order to study the timing properties of a given source, its light curve (i.e., the distribution of photon counts over time) could be extracted by using XRONOS[5] package. The XRONOS is a timing analysis software package available as a subpackage of FTOOLS[6]. We extensively use three timing tasks `efsearch`, `efold`, `powspec` provided by XRONOS. To obtain the periodicity in the light curve, we used `efsearch` task, which is based on χ^2-maximization technique. The `efold` task generates the pulse profile using the light curve. This task folds the light curve at a particular period and presents intensity variation between phases 0 and 1, where phase 1 corresponds to the complete rotation of the neutron star (a complete period). The `powspec` task is used to analyze the power density spectra (PDS) of the light curve. The `powspec` task displays different variability and its corresponding power present in the light curve using the Fourier Transformation (FT) technique.

The X-ray spectral analysis is conducted using the XSPEC package within the HEASoft software suite. XSPEC is an interactive spectral fitting program designed to be detector-independent, making it applicable to various spectrometers. In this thesis work, the Python interface of XSPEC is also utilized. In reality, the observed spectrum is not the actual source spectrum as it is modified by the detector response and effective area. Therefore, it is necessary to back-calculate the source spectrum, which can be achieved through modeling. XSPEC provides a robust platform for modeling observed spectra with various empirical and physical models. It is also equipped with advanced statistical techniques to determine the best-fit models and their corresponding parameters within a certain confidence range. The following paragraphs explain the spectral analysis procedure in detail.

The observed X-ray spectrum (D(I)) represents photon counts across instrument channels (I). This spectrum includes background noise (B(I)), so it does not directly describe the source properties. The true spectrum (f(E)) relates to the observed spectrum (D(I)) through the equation:

$$D(I) = \int_0^\infty R(I,E) f(E) A(E) dE + B(I) \tag{2.1}$$

Where R(I, E) is the response matrix function, indicating the probability of detecting a photon of energy (E) in the channel (I), and A(E) is the effective area of the telescope. The net source counts per channel, after subtracting the background, are (D(I) - B(I)). Given N discrete channels, the integral can be written as a summation:

$$D(I) - B(I) = C(I) = \sum_{i=1}^{N} f_i(E) R_i(I,E) \tag{2.2}$$

[5]`https://heasarc.gsfc.nasa.gov/docs/xanadu/xronos/xronos.html`
[6]`https://heasarc.gsfc.nasa.gov/docs/software/ftools/ftools_menu.html`

Since the response matrix function is non-invertible, this equation cannot be directly solved to find the actual source spectrum (f(E)). Instead, empirical or physically motivated spectral models (M(I)) are fitted to the observed spectrum (C(I)). The fit is evaluated using the chi-square statistic:

$$\chi^2 = \sum_{i=1}^{N} \frac{(C_i(I) - M_i(I))^2}{\sigma_i(I)^2} \tag{2.3}$$

where, ($\sigma_i(I) = \sqrt{C_i(I)}$) is the error in the observed counts (C(I)), assuming a Gaussian distribution. For a good fit, the reduced chi-square, (χ^2/dof), should be about one, where the number of degrees of freedom (DOF) is the difference between the number of energy channels/bins and the number of free parameters in the model. Multiple models might fit the data equally well, and the choice of the best-fit model depends on scientific judgment and parameter feasibility. The best-fit parameter values are determined within a 90% confidence interval.

Chapter 3

Optical and X-ray studies of Be/X-ray binary 1A 0535+262 during its 2020 giant outburst

This chapter investigates the optical properties of the BeXRB 1A 0535+262 before, during, and after its 2020 giant X-ray outburst. Long-term optical data from the 1.2 m Mount Abu Infrared Observatory (MIRO) are utilized for detailed analysis. Additionally, we conducted a pointed X-ray observation of the pulsar using India's first multi-wavelength space observatory, AstroSat, during the rising phase of the outburst to explore its X-ray characteristics. The chapter is organized as follows: Section 3.1 provides an introduction to 1A 0535+262. Section 3.2 gives details about optical and X-ray observations. Section 3.3 reports the results from optical observations, and Section 3.4 presents the X-ray data analysis results. Section 3.5 discusses our findings, and Section 3.6 concludes the chapter.

3.1 An introduction to 1A 0535+262

1A 0535+262 is one of the most active BeXRBs, frequently exhibiting Type I X-ray outbursts. 1A 0535+262 was discovered in 1975 by the Ariel V space telescope (Rosenberg et al., 1975). The source was undergoing a giant X-ray outburst during the time of its discovery. The binary system comprises a neutron star as a compact object rotating around its spin axis at a period of around 104 seconds (Rosenberg et al., 1975). The optical companion or the secondary star HDE 245770 was identified as a Be star of spectral type O9.7 IIIe (Giangrande et al., 1980). The BeXRB has a relatively wide and eccentric orbit. The orbital period of the binary ($P_{\rm orb}$) is approximately 110 days, and the eccentricity is around 0.47 (Finger et al., 1994). Steele et al. (1998) estimated the distance of the source as $\sim$2 kpc, based on a spectral class of B0III and a reddening E(B-V) = 0.75.

Since its discovery, 1A 0535+262 has experienced several giant X-ray outbursts (Camero-Arranz et al. 2012 and references therein). Clark et al. (1999) analyzed the variability of the source using ten years of UBV-band photometry data and found that the X-ray outbursts in 1A 0535+262 occurred during the optical fading phase of the Be star. Camero-Arranz et al. (2012) used contemporaneous X-ray and optical data spanning over thirty years and discovered an anti-correlation between the V-band magnitude and the equivalent width of the Hα line before the giant X-ray outbursts. Yan et al. (2012) interpreted this observed anti-correlation before the 2009 giant X-ray outburst in terms of mass ejection from the inner part of the circumstellar disc. Spectroscopic observations revealed significant Hα line variability in 1A 0535+262/V725Tau (Moritani et al., 2011). Prior to the giant outburst, the Hα line evolved from any shape to a single-peaked profile with increasing strength and Full Width at Zero Intensity (FWZI) (Clark et al., 1998; Coe et al., 2006; Camero-Arranz et al., 2012). This Hα line behavior is attributed to the warping of the circumstellar disc of the companion Be star before the giant outburst. Using high dispersion optical spectroscopic observations during the 2009 and 2011 giant X-ray outbursts, Moritani et al. (2013) suggested that a precessing warped Be disc triggers the giant outburst in 1A 0535+262.

The optical and infrared observations of the BeXRBs provide information on the properties of the Be star and the circumstellar disc that swirls around it, as discussed in the previous paragraph. The 104 s spin period neutron star, which exists in the binary, emits in the X-ray band. Consequently, the observations in the X-ray regime could be utilized to understand the dynamics of mass transfer from the companion Be star onto the neutron star and its ambient region. Timing analysis of the neutron star during various giant outbursts of 1A 0535+262 hinted that the pulsar spun up as its X-ray luminosity augmented (Bildsten et al., 1997; Sartore et al., 2015). The spinning up of the pulsar is seen as a result of the angular momentum transfer from the accreted mass to the neutron star, which escalates with the increase in the accumulation rate. Change in the shape of the pulse profile of the pulsar with luminosity is understood to be due to the change in the accretion environment around the neutron star with the change in luminosity (Parmar et al., 1989). During the giant outburst in 2011, this particular feature was similarly detected in 1A 0535+262 (Sartore et al., 2015). Throughout X-ray outbursts, the wide-range X-ray spectrum of 1A 0535+262 has primarily been modeled with a power-law continuum model with an exponential cutoff, together with a blackbody component of temperature in the 1-2 keV range for soft X-ray surplus and a Gaussian function at 6.4 keV for iron line emission (Caballero et al., 2013; Sartore et al., 2015). The cyclotron resonance scattering features, the tools for the direct measurement of the magnetic field of the pulsar, with fundamental and first harmonic at $\sim$ 45 keV and $\sim$ 100 keV, respectively, are also observed in the spectrum of 1A 0535+262 (Kendziorra et al., 1994; Terada et al., 2006; Sartore et al., 2015; Kong et al., 2021). Though the change in the cyclotron line energy with luminosity in 1A 0535+262 does not show a clear trend, some of the measurements support a positive correlation (Reig & Nespoli, 2013; Sartore et al., 2015).

1A 0535+262 went into a giant X-ray outburst on 29 October 2020 (MJD 59151; Mandal et al. 2020). According to Swift/BAT monitoring data, the peak intensity of the pulsar during this outburst reached approximately 11 Crab in the 15-50 keV range on MJD 59172 (19 November 2020). This peak intensity is the highest recorded among the previously observed giant X-ray outbursts of 1A 0535+262 (Camero-Arranz et al., 2012) since its discovery (Jaisawal et al., 2020b,a). To investigate changes in the properties of the Be star and its circumstellar disc, we conducted optical observations of the source before, during, and after the giant X-ray outburst using the 1.2 m telescope at MIRO. Additionally, we performed a pointed X-ray observation of the pulsar with AstroSat during the rising phase of the outburst to study its X-ray characteristics.

3.2 Optical and X-ray observations of 1A 0535+262/HD 245770

We conducted optical and X-ray observations to understand the properties of the Be companion and the neutron star in the BeXRB 1A 0535+262/HD 245770. X-ray outbursts in BeXRB systems are known to result from the abrupt accretion of a large amount of matter from the Be circumstellar disc onto the neutron star. Consequently, the X-ray properties of the neutron star during outbursts are expected to be associated with changes in the Be star properties. Therefore, studying such BeXRBs in optical/infrared and X-ray bands during X-ray outbursts is crucial. To understand the change in properties of the Be star due to X-ray outbursts, optical/infrared observations before, during, and after X-ray outbursts are crucial. The neutron star in 1A 0535+262 experienced a giant X-ray outburst in October 2020. As part of our ongoing monitoring project, we carried out optical observations of the system at several epochs before the giant X-ray outburst using the 1.2 m, f/13 telescope at the MIRO with the MFOSC-P instrument. We continued optical spectroscopic observations of 1A 0535+262 with the MFOSC-P instrument to investigate the properties of the Be star before, during, and after the giant X-ray outburst. We conducted 16 epochs of optical observations over two years, from 4 February 2020 to 14 February 2022, with exposure times ranging from 250 to 1000 seconds. We performed spectroscopic observations using a 75 μm slit in R2000 mode, the highest resolution available for the MFOSC-P instrument, which covers a wavelength range of $\sim$6000-7200 Å. The data reduction procedures followed to reduce MFOSC-P data are presented in Chapter 2. For the instrument response correction of the reduced spectra, we used the spectra of the standard star SAO 77466. SAO 77466 is observed at a similar airmass as the Be star HD 245770. At first, the response function was determined by dividing the observed continuum spectra of SAO 77466 by a blackbody curve that matches the effective temperature of the standard star. Finally, the response function was applied to the source spectra to create the science spectra. Our proposal for a 42 ks observation of 1A 0535+262 was successfully used to observe the pulsar on 11 November 2020, during the rising phase of the giant outburst using SXT, LAXPC, and CZTI. The details on the data reduction of SXT, LAXPC, and CZTI data are presented in Chapter 2. For SXT, using the *FTOOLS* task *XSELECT* and considering a circular region of size $15'$ from the center of the Point Spread Function (PSF), the science products were generated from the merged event file. In SXT PC mode, the observations of sources fainter than $\sim$200 mCrab do not get affected by photon pile-up. As the intensity of 1A 0535+262 was more than 1 Crab during our AstroSat observation, the SXT data were severely affected due to photon pile-up. The data were corrected for the piled-up effect by excluding the central circular region of four arc-min radii while extracting light curves and spectra. A corresponding effective area file (*ARF*) was also generated. The *sxt_pc_mat_g0.rmf* & *SkyBkg_comb_EL3p5_Cl_Rd16p0_v01.pha* files, provided by the SXT team, were used as spectral redistribution matrix and background spectrum, respectively. Standard procedures are followed to generate light curves, spectra, arf, and rmf files for LAXPC and CZTI data. Optical

Table 3.1: Log of optical and X-ray observations for the BeXRB 1A 0535+262/HD 245770

Date of observation	MJD	Days since outburst (29 Oct 2020)	Exposure time (s)
MIRO			
04 FEB 2020	58883	−276	1000
27 FEB 2020	58906	−253	1000
12 MAR 2020	58920	−239	1000
19 NOV 2020	59172	+13	400
20 NOV 2020	59173	+14	1000
29 NOV 2020	59182	+23	400
03 DEC 2020	59186	+27	250
24 DEC 2020	59207	+48	800
30 DEC 2020	59213	+54	500
03 JAN 2021	59217	+58	700
10 JAN 2021	59224	+65	500
29 JAN 2021	59243	+84	500
09 FEB 2021	59254	+94	1000
15 DEC 2021	59563	+404	800
23 JAN 2022	59602	+443	350
14 FEB 2022	59624	+465	600
AstroSat			
11 NOV 2020	59165	+6	94331

and X-ray observation details are provided in Table 3.1. In Figure 3.1, we marked the MIRO and AstroSat observations above the Swift/BAT daily monitoring light curve to show the X-ray intensity levels during our optical and X-ray observations.

3.3 Optical spectroscopic results of 1A 0535+262/HD 245770

In this section, we present the changes observed in the emission line parameters of 1A 0535+262 during the 2020 giant X-ray outburst, compared to those before and after the event, using our optical observations. The optical spectroscopic observations of the BeXRB were carried out in the 6000-7200 Å band using the MFOSC-P instrument in R2000 mode. Initial observations were conducted on 4 February, 27 February, and 12 March 2020, when the neutron star in the system was in a quiescent state (see Figure 3.1). These observations provide information about the Be circumstellar disc prior to the giant X-ray outburst. As the neutron star entered the giant X-ray outburst phase, we performed closely spaced optical spectro-

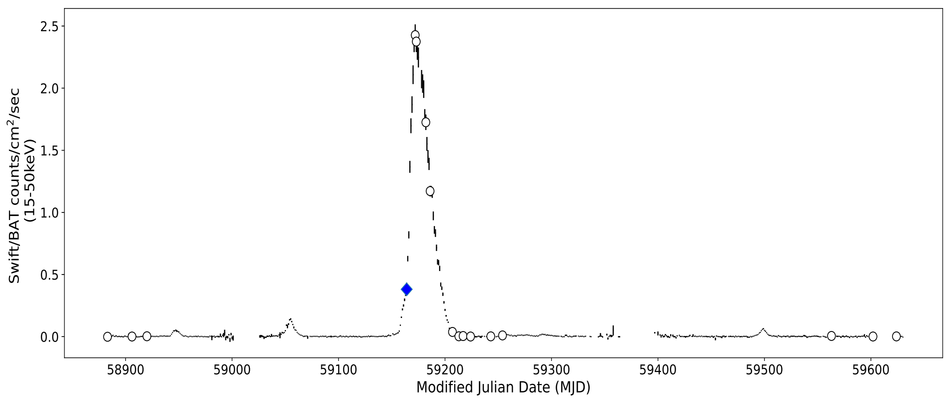

Figure 3.1: Swift/BAT monitoring light curve of 1A 0535+262 in the 15-50 keV range during the 2020 giant X-ray outburst. The black open circles mark the dates of optical observations of the binary system with the 1.2 m telescope at Mount Abu using the MFOSC-P instrument. The blue diamond indicates the date of the AstroSat observation of the pulsar. At the peak of the X-ray outburst around MJD 59172, the source reached an intensity of approximately 11 Crab; for reference, 1 Crab is equivalent to 0.220 counts cm^{-2} s^{-1} in the 15-50 keV band.

scopic observations from 19 November 2020 (close to the peak of the X-ray outburst) to 9 February 2021, when the neutron star returned to the X-ray quiescent phase. Subsequent observations were made on 15 December 2021, 23 January 2022, and 14 February 2022, when the system was again in a quiescent state.

3.3.1 Optical spectra at different phases of the outburst

The spectra in the 6000-7200 Å range obtained from the MFOSC-P observations of 1A 0535+262 in R2000 mode are presented in Figure 3.2. For clarity, the continuum-normalized intensity for each observation epoch is shown with offsets. The date of each observation and the number of days before and after the onset of the giant X-ray outburst are indicated. Spectra obtained before the giant outburst are shown in blue, those obtained during the outburst are in magenta, and those obtained after the outburst are in red. The numbers in days, marked with minus and plus signs, indicate the timing of the optical observations relative to the beginning of the outburst. The quoted orbital phases (ϕ) represent the position of the neutron star in its orbit at the time of the optical observation, estimated using the method described by Moritani et al. (2010), where $\phi = 0$ corresponds to the periastron passage of the neutron star.

Throughout our observations, various emission and absorption lines were detected. The emission lines are associated with the source, while the absorption lines originate from other sources, such as the interstellar medium (ISM) and Earth's atmosphere. Diffuse Interstellar Bands (DIBs) related to the ISM and atmospheric telluric features were present in all the epochs of our observations (Figure 3.2). The DIBs are absorption features that appear when photons pass through significant column densities in the ISM, though their specific origins are not well understood. We identified four DIBs at 6203.06 Å, 6283.86 Å, 6379.20 Å, and 6613.62 Å (Herbig, 1995). The telluric features, resulting from the absorption of photons by molecules in the atmosphere of the Earth, were also superimposed on the stellar spectra. One prominent telluric feature observed in our spectra was the O_2 B band at

$\lambda \sim 6870$ Å (Angeloni et al. 2019 & reference therein).

In the 6000-7200 Å range spectra of 1A 0535+262/HD 245770, spanned over two years of duration, three emission lines at 6562.8 Å, 6678 Å and 7065 Å are detected (Figure 3.2). The presence of emission lines in the optical spectra confirms the existence of the circumstellar disc in the BeXRB system (Coe et al., 2006). This signifies that the disc is not entirely vanished even during/after the giant X-ray outburst (see, e.g., Haigh et al. 1999 for 1A 0535+262 and Reig & Zezas 2014 for IGR J21343+4738).

3.3.2 Evolution of Hα (6562.8 Å), HeI (6678 Å), and HeI (7065 Å) emission lines

The evolution of the Hα (6562.8 Å), HeI (6678 Å), and HeI (7065 Å) emission line profiles during our optical observations are shown in Figure 3.3. The X-axis is expressed in terms of velocity rather than wavelength to visualize the emission from the approaching and receding parts of the circumstellar disc. The velocity corresponding to each wavelength is calculated using the Doppler formula as follows:

$$\text{velocity} = \left(\frac{\text{wavelength} - \lambda_i}{\lambda_i} \right) \times 3 \times 10^5 \tag{3.1}$$

where, λ_i is the central wavelength for Hα, HeI (6678 Å), and HeI (7065 Å) lines, i.e., 6562.8 Å, 6678 Å, and 7065 Å, respectively. 3×10^5 is considered as the velocity of light in km/s unit.

The negative velocities exhibit the blue-shifted part, whereas the positive velocity depicts the red-shifted component. In the Y-axis, the normalized intensities with arbitrary vertical offsets are shown. The offsets are given for clarity only. The blue, magenta, and red color profiles represent observations during the pre-outburst (quiescent), outburst, and post-outburst quiescent phases, respectively, as in Figure 3.2. The date of observation and the corresponding orbital phase of the neutron star (ϕ) are annotated in each profile. The vertical dotted line corresponds to 0 km/s velocity. The errors on the data points for He I (6678 Å) and He I (7065 Å) emission lines are larger than those for Hα line due to their low flux levels.

During the pre-outburst or quiescent phase observations, the Hα lines exhibit a single-peaked structure with moderate asymmetry and a broad red wing. Conversely, the He I (6678 Å) and He I (7065 Å) line profiles are double-peaked, showing a higher peak intensity in the blue component compared to the red component.

During the X-ray outburst, the Hα line profile changes to an asymmetrical shape with a broader blue component, opposite to what was observed in the pre-outburst phase. The He I (6678 Å) and He I (7065 Å) lines become more complex and multi-peaked during this phase.

In the post-outburst phase, from 30 December 2020 to 9 February 2021, the Hα line profile remains unchanged except for a distinct hump-like structure in the blue wing. Meanwhile, the He I (6678 Å) and He I (7065 Å) lines exhibit multiple components. In the last three observations (15 December 2021, 23 January, and 14 February 2022), the Hα, He I (6678 Å), and He I (7065 Å) lines return to a double-peaked profile with comparable

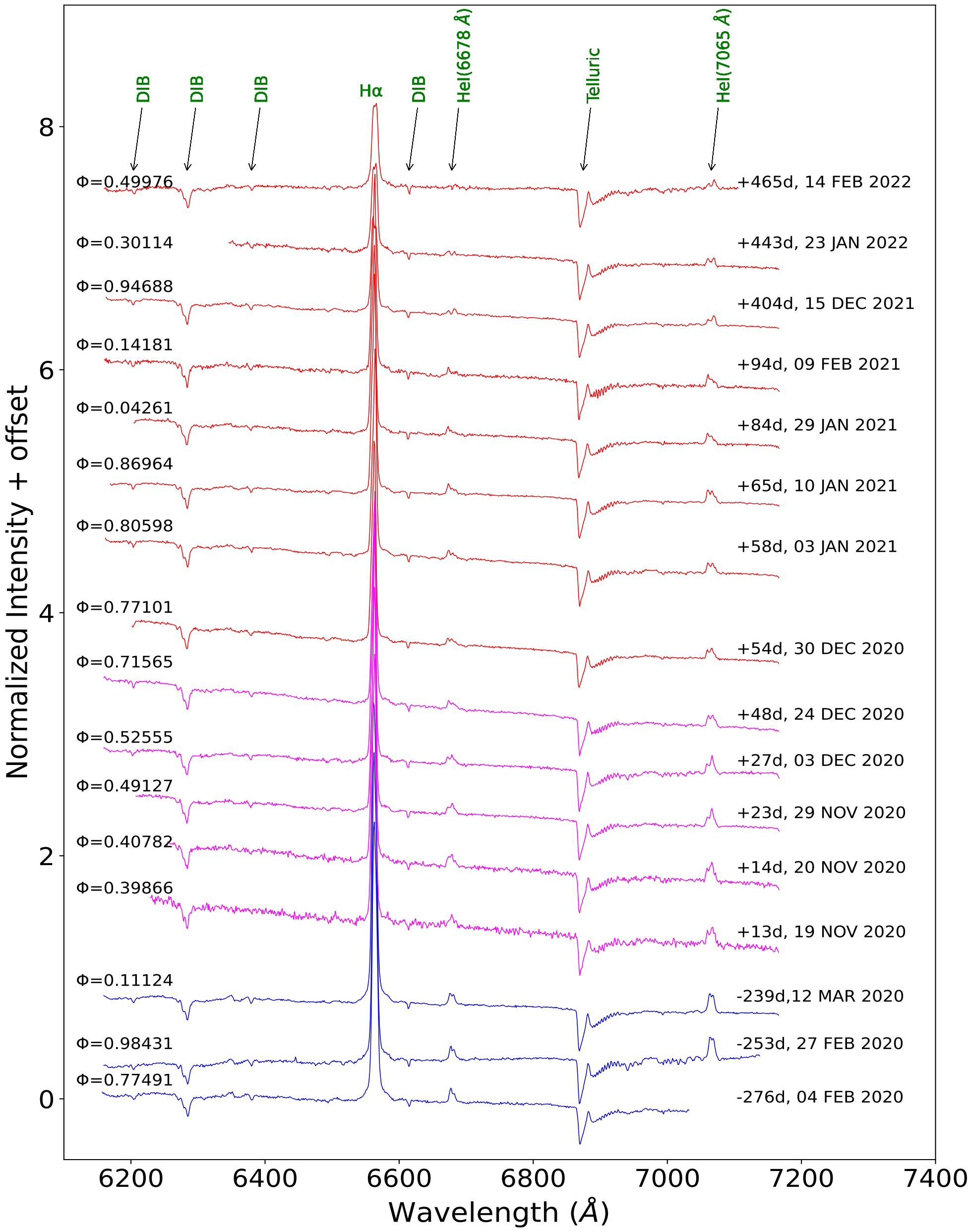

Figure 3.2: Evolution of the optical spectrum of the Be/X-ray binary 1A 0535+262 as observed with the MFOSC-P instrument. The spectra are not corrected for reddening. Each spectrum is annotated with the observation date and the orbital phase (ϕ) of the neutron star. The numbers in days, shown in minus and plus, indicate the days before and after the onset of the giant X-ray outburst on MJD 59151, respectively. The spectra obtained before, during, and after the giant outburst are represented by blue, magenta, and red colors, respectively.

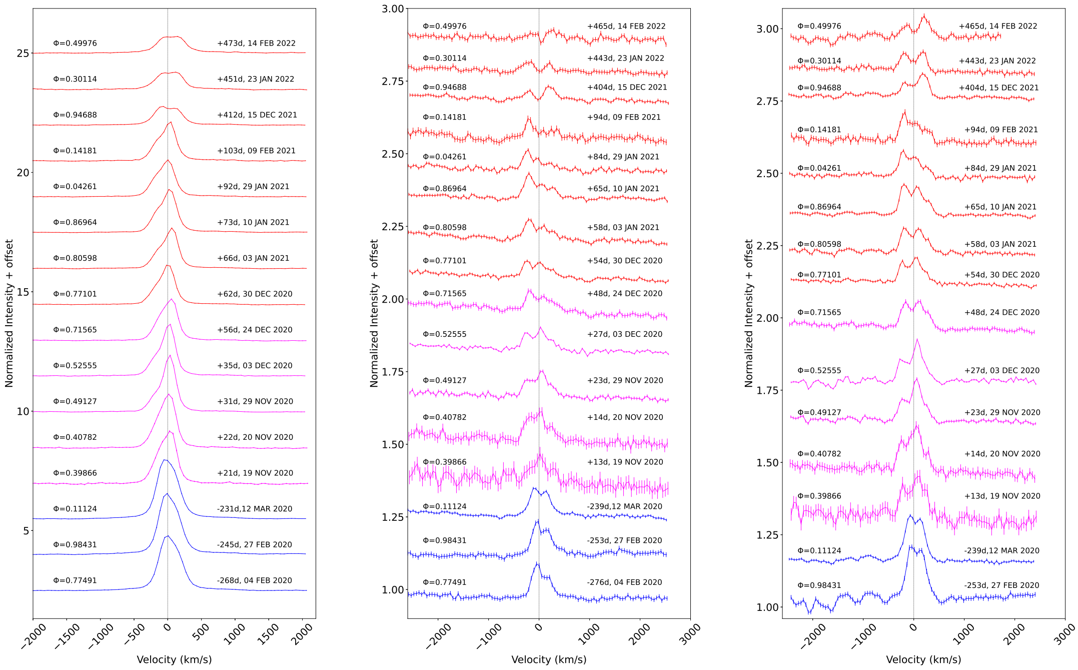

Figure 3.3: The Hα (extreme left), He I (6678 Å; middle), and He I (7065 Å; extreme right) emission lines of 1A 0535+262/HD 245770 during the pre-outburst (blue), outburst (magenta), and post-outburst (red) epochs of our observation campaign are shown. The errors on the flux values are at the 1σ level. The observation date and corresponding orbital phase (ϕ) of the neutron star are noted on each profile. The numbers, given in days with plus and minus signs, indicate the days after and before the onset of the giant X-ray outburst, respectively. The profiles are plotted with offsets for clarity.

peak intensities.

3.3.3 Variation in the properties of Hα emission line

In the previous subsection, we presented the evolution of the shape of emission lines throughout our observation period. In this subsection, we extensively study the Hα emission line parameters.

Equivalent width

We determined the equivalent width (EW) of the Hα emission lines from all our observational epochs. The EW quantifies the strength of emission or absorption lines, representing the area of the line in a wavelength vs intensity plot. This measure is dimensionless and calculated using Equation 1.21. The errors in the EWs were assessed through error propagation, accounting for continuum flux and wavelength calibration errors. For Hα lines, the chosen emission line waveband is 6550-6575 Å. The continuum flux was obtained by calculating the median flux counts in the 6517-6550 Å and 6575-6607 Å wavebands. The calculated EWs of the Hα lines, including 1σ uncertainties, are listed in Column 4 of Table 3.2. The negative sign of EW values indicates emission lines.

From Table 3.2, it is evident that the Hα line equivalent width shows an increasing trend from 4 February 2020 to 12 March 2020 (239 days before the outburst). In absolute terms,

Table 3.2: Equivalent width, disc radius, and other spectral parameters of Hα emission line and equivalent width of the HeI (7065 Å) emission line.

Date of observation	MJD (ϕ)	Days since outburst	EW(Hα) (Å)	ΔV (km/s)	$FWHM$ (km/s)	V/R	EW (HeI) (Å)	Disc Radius (R_*)
04 FEB 2020	58883 (0.78)	−276	-20.67 ± 0.27	183.8 ± 9.6	369.4 ± 5.0	1.56 ± 0.01	–	7.62 ± 0.55
27 FEB 2020	58906 (0.98)	−253	-21.03 ± 0.28	176.5 ± 11.4	353.9 ± 5.0	1.32 ± 0.01	-1.77 ± 0.21	7.71 ± 0.69
12 MAR 2020	58920 (0.11)	−239	-22.09 ± 0.17	169.7 ± 11.1	358.9 ± 4.9	0.94 ± 0.01	-1.81 ± 0.12	7.96 ± 0.70
19 NOV 2020	59172 (0.39)	+13	-17.70 ± 0.77	146.4 ± 14.1	331.5 ± 6.1	1.35 ± 0.15	-2.11 ± 0.72	6.88 ± 0.96
20 NOV 2020	59173 (0.40)	+14	-17.88 ± 0.52	147.8 ± 22.3	323.7 ± 5.7	0.92 ± 0.04	-2.00 ± 0.47	6.93 ± 1.51
29 NOV 2020	59182 (0.49)	+23	-15.97 ± 0.19	208.0 ± 7.1	294.6 ± 8.0	0.24 ± 0.01	-1.49 ± 0.15	6.43 ± 0.33
03 DEC 2020	59186 (0.52)	+27	-15.22 ± 0.11	196.6 ± 8.5	310.8 ± 8.2	0.31 ± 0.01	-1.44 ± 0.08	6.23 ± 0.41
24 DEC 2020	59207 (0.71)	+48	-13.75 ± 0.27	152.2 ± 11.0	324.9 ± 5.7	0.88 ± 0.01	-1.50 ± 0.25	5.82 ± 0.66
30 DEC 2020	59213 (0.77)	+54	-12.51 ± 0.15	182.9 ± 12.1	321.7 ± 6.7	0.36 ± 0.02	-1.13 ± 0.13	5.47 ± 0.58
03 JAN 2021	59217 (0.80)	+58	-12.60 ± 0.19	185.3 ± 8.7	330.9 ± 8.1	0.48 ± 0.01	-1.20 ± 0.16	5.50 ± 0.42
10 JAN 2021	59224 (0.86)	+65	-13.69 ± 0.16	195.3 ± 7.7	337.3 ± 6.8	0.33 ± 0.01	-1.33 ± 0.13	5.81 ± 0.36
29 JAN 2021	59243 (0.04)	+84	-12.12 ± 0.17	184.4 ± 9.6	340.4 ± 6.0	0.43 ± 0.01	-0.99 ± 0.15	5.36 ± 0.46
09 FEB 2021	59254 (0.14)	+94	-12.24 ± 0.33	185.2 ± 8.3	336.3 ± 7.5	0.38 ± 0.01	-1.12 ± 0.28	5.39 ± 0.40
15 DEC 2021	59563 (0.94)	+404	-8.37 ± 0.17	230.2 ± 5.1	435.3 ± 8.6	1.19 ± 0.02	-0.91 ± 0.15	4.19 ± 0.17
23 JAN 2022	59602 (0.30)	+443	-8.19 ± 0.25	220.3 ± 10.5	439.1 ± 8.7	1.44 ± 0.04	-0.76 ± 0.21	4.14 ± 0.37
14 FEB 2022	59624 (0.49)	+465	-7.76 ± 0.24	221.0 ± 9.1	454.3 ± 8.8	0.85 ± 0.02	-0.66 ± 0.21	3.99 ± 0.31

$R_* = 1.04 \times 10^{10}$ m

the maximum EW observed during the 2009 and 2011 X-ray outbursts was approximately 18 Å (Moritani et al., 2013), whereas we recorded an absolute value of EW about 22 Å on 12 March 2020.

Following the same methodology, we also calculated the EW for the He I (7065 Å) line. The selected emission line waveband for He I (7065 Å) is 7052-7078 Å, with continuum flux derived from the 7020-7052 Å and 7078-7110 Å wavebands. These values are presented in Column 8 of Table 3.2 with 1σ uncertainties. The EW of the He I line (6678 Å) was not calculated due to a low signal-to-noise ratio (SNR).

V/R & ΔV

Most BeXRBs, including 1A 0535+262, exhibit asymmetric Hα line profiles (Yan et al., 2012; Moritani et al., 2013). These asymmetries are typically quantified using the V/R ratio, which compares the blue-shifted line flux to the red-shifted line flux. Although the emission lines in our observations are mostly asymmetric and single-peaked, we fitted all Hα emission lines with Voigt profiles to separate the contributions of the red and blue-shifted components. Initial attempts to fit the profiles with Gaussian functions were unsuccessful, particularly in the wing regions. The original and fitted line profiles are shown in black and green in Figure 3.4, with the red and blue components highlighted in their respective colors. From these fits, we derived parameters such as the central wavelengths, standard deviations, and intensities of the blue and red components of the Hα line.

The central wavelengths of the blue and red components were calculated from the Voigt profile to fit the Hα line. The logarithm of the V/R ratio is plotted in the third panel of Figure 3.5. A negative V/R value indicates that the red component is more intense than the

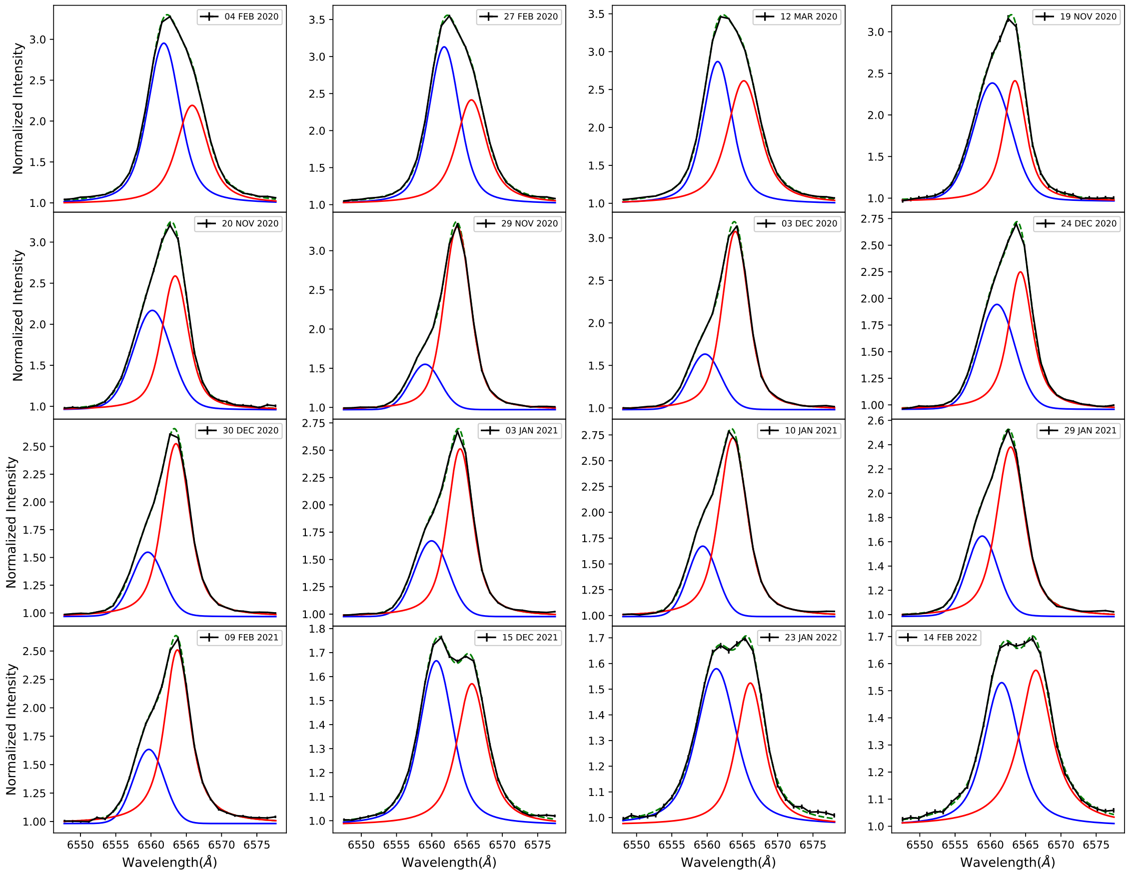

Figure 3.4: The observed Hα line profiles (solid black line) of 1A 0535+262/HD 245770 during our observations and corresponding best-fitted Voigt functions (dashed green line) are shown. The observation dates are quoted on the right of the corresponding profiles. The red and blue color profiles correspond to the red and blue shifted components of the Hα line, respectively.

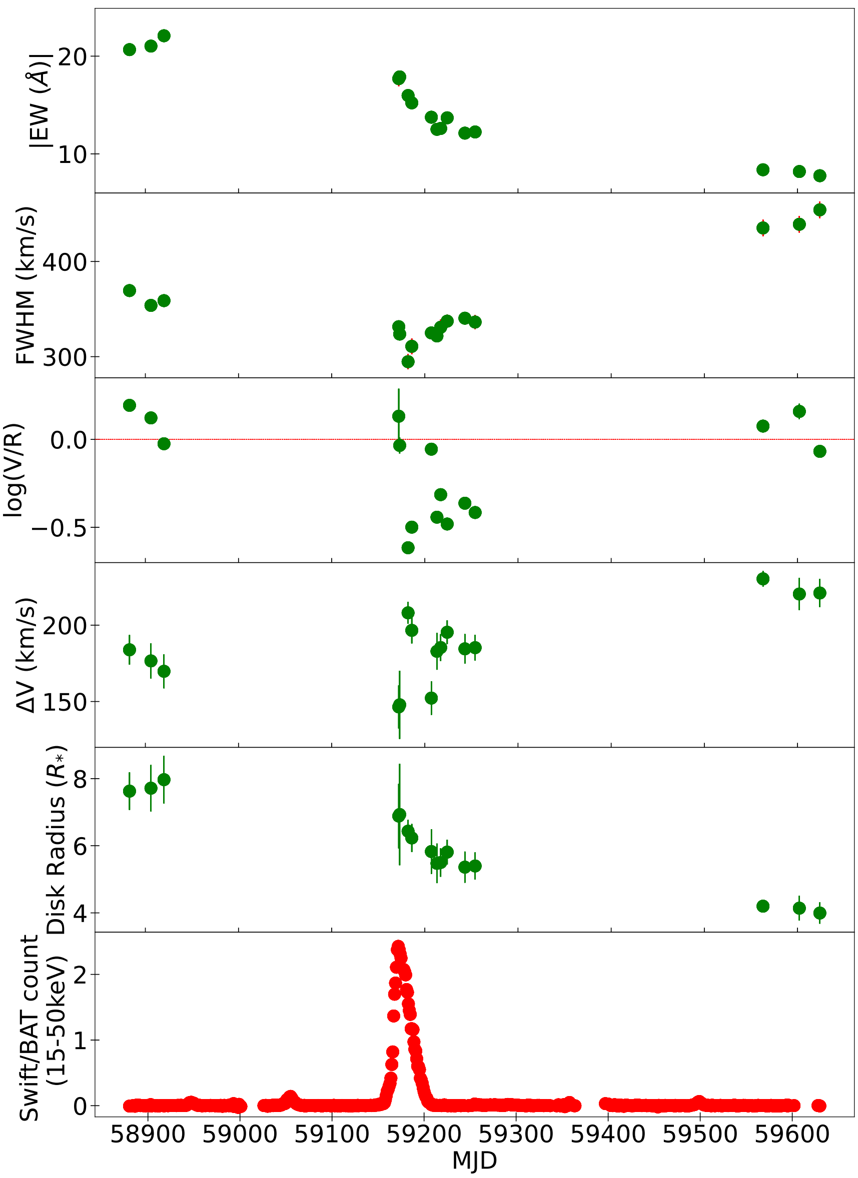

Figure 3.5: Variation of the Hα line parameters of the Be star and the X-ray count rate from the pulsar in 1A 0535+262/HD 245770 binary system during our observations are shown. The changes in line equivalent width (EW), Full Width at Half Maximum ($FWHM$), V/R ratio, peak separation of fitted components (ΔV), circumstellar disc radius, and Swift/BAT X-ray count rate are shown in panels from top to bottom, respectively. The radius of the Be star is estimated to be (R_*)= 15 $R_\odot$ (Okazaki & Negueruela, 2001).

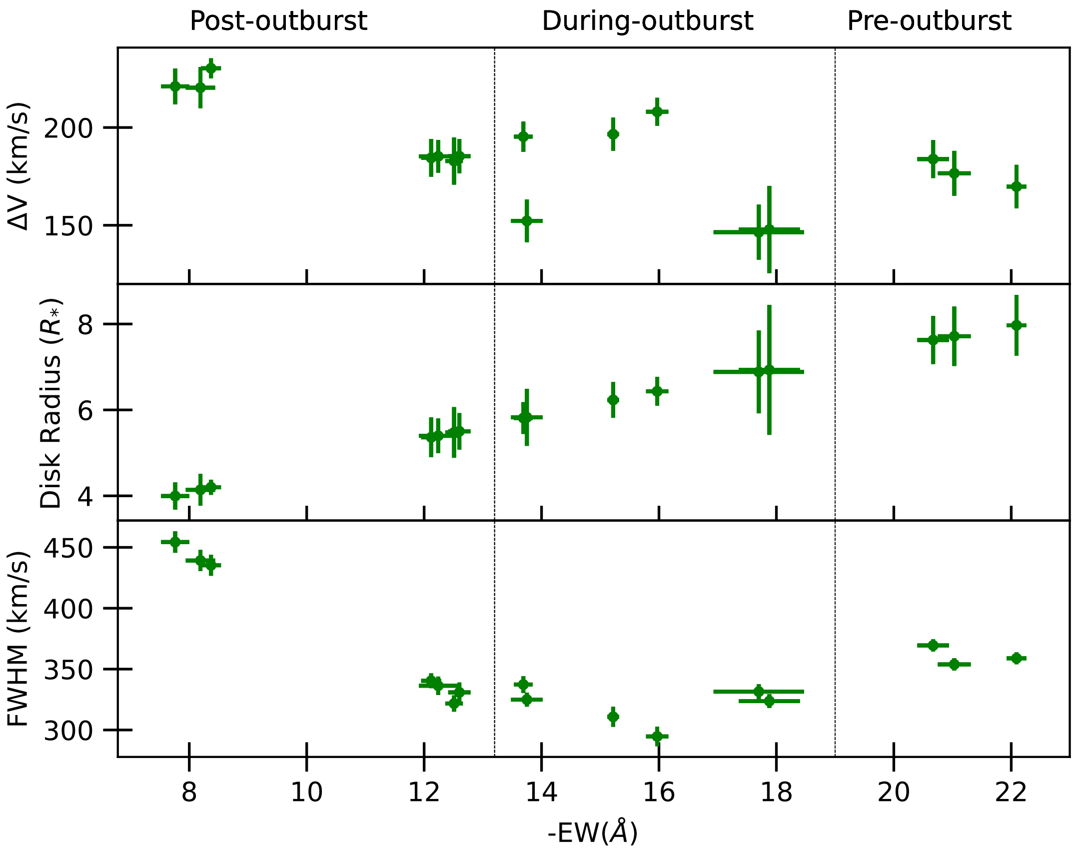

Figure 3.6: Changes in the separation between the peaks of the blue and red-shifted components of the Hα line (ΔV), circumstellar disc radius, and the $FWHM$ of the Hα line are shown in the top, middle, and bottom panels, respectively, as a function of the equivalent width. The regions separated by vertical dotted lines correspond to the observations before, during, and after the giant X-ray outburst, respectively.

blue component, while a positive V/R value indicates the opposite. Significant variability in the V/R ratio is evident. On 4 February 2020 (276 days before the X-ray outburst), the blue component was approximately 1.6 times brighter than the red component. On 29 November 2020 (23 days after the onset of the X-ray outburst), the red component was about five times brighter than the blue component. By 23 January 2022 (443 days later), the blue component had become roughly 1.4 times brighter than the red component again. This variability in V/R is crucial for tracking activity in the circumstellar disc, providing insights into its density distribution. Significant V/R variations suggest asymmetries in the density distribution in the circumstellar disc. Long-term data from 2005-2009 analyzed by Moritani et al. (2010) and Grundstrom et al. (2007) indicated a periodicity of about 500 days in V/R variability (see Figures 5 and 7 of Moritani et al. 2010), consistent with Reig et al. (2005). This periodicity was not observed during the 2009 and 2011 outbursts. Although our data sampling is insufficient to verify periodicity in V/R variability, significant variations are apparent in our measurements.

We also measured the peak separation (ΔV), which is the difference between the central wavelengths of the red and blue components of the Hα line. In velocity units, ΔV is given by $\Delta\lambda/\lambda_0 \times c$, where c is the speed of light, $\Delta\lambda$ is the wavelength separation, and λ_0 is the central wavelength of the Hα line. The errors in ΔV were calculated using error propagation. The peak separation helps estimate the radius of the Be circumstellar disc (Huang, 1972). A small peak separation may indicate a large disc and a small inclination (face-on) system, while a large peak separation suggests a small disc and a large inclination (edge-on) system (Malacaria et al., 2017). In terms of velocity, the peak separation between the fitted blue and red wings is plotted in the fourth panel of Figure 3.5.

Full width at half maximum

The Full Width at Half Maximum ($FWHM$) represents the width of the emission or absorption line at half its peak flux. When expressed in velocity units, the $FWHM$ estimates the radial velocity of the Hα emitting particles in the disc relative to the observer. In this study, the $FWHM$ was determined by fitting a single Gaussian function to the entire Hα emission line using a Python routine, which effectively captured the overall line shape. The temporal variation of the $FWHM$ is depicted in the second panel of Figure 3.5. During our observations, the $FWHM$ ranged from 6.44 to 9.93 Å (294-454 km/s).

Estimation of the size of Hα emitting region

The disc size can be estimated using the parameters of the Hα line. Huang (1972) showed that the peak separation (ΔV) of the double-peaked Hα emission line can be used to determine the size of the Hα emitting region of the circumstellar disc, assuming a Keplerian velocity distribution of the disc matter. Additionally, Hanuschik (1989) established a linear relationship for single-peaked profiles between ΔV, V$\sin i$, and EW, which is expressed as:

$$log(\frac{\Delta V}{2V \sin i}) = -a \times \log(-EW/\text{Å}) + b \tag{3.2}$$

where a and b are the slope and intercept of the plot log($\frac{\Delta\ V}{2V\ \sin i}$) vs log(-$EW$/Å), and i is the inclination angle of the disc with respect to the observer. For a sample of BeXRBs, Monageng et al. (2017) calculated the values of a and b to be 0.334 and 0.033, respectively. Using the values of $\Delta\ V$ from our Hα line profile fitting, we calculated $V \sin\ i$ by using the following equation :

$$V\ \ \sin i = \frac{\Delta V}{2 \times 10^{-0.334 \times \log(-EW/\text{Å}) + 0.033}} \tag{3.3}$$

The average value of $V \sin\ i$ is estimated to be 236.84±13.55 km s^{-1} which is in agreement with the reported value of 225 ±10 km s^{-1} (Reig 2011 & references therein). The velocity separation between the red and blue shifted components of emission lines can be used to calculate the radius of the emitting region (Huang, 1972). The relationship between the peak separation and the rotational velocity of the gas particles at the emitting region is $\Delta\ V = 2V_{rot} \sin\ i$. Then the size of H$\alpha$ emitting region can be derived by :

$$R_d = (2V \sin i/\Delta V)^j \epsilon R_* \tag{3.4}$$

where j=2 for Keplerian rotation, R_* is the Be star radius, and ϵ is a dimensionless parameter that considers several effects that would over-estimate the disc radius (ϵ=0.9±0.1 ; Zamanov et al. 2013). For 1A 0535+262, the radius of the Be companion star is 15 $R_\odot$ (Okazaki & Negueruela, 2001). We estimated the radius of the circumstellar disc during our observations and plotted this in the fifth panel of Figure 3.5. From the figure, it can be noticed that before the giant X-ray outburst, the size of the disc was increasing until the onset of the outburst and decreased continuously after the onset to a value of $4R_*$.

3.3.4 Correlations between EWs and other parameters of Hα line

Figure 3.6 illustrates the relationship between various Hα line parameters and the line equivalent width (EW). The top panel shows the peak separation, the middle panel displays the disc radius, and the bottom panel represents the $FWHM$. The vertical dashed lines divide the data points into three distinct sections: the first section corresponds to the post-outburst periods. In contrast, the middle and right sections correspond to the outburst and pre-outburst periods. An anti-correlation between the peak separation (ΔV) and the equivalent width of the Hα line is evident in the top panel during both the pre-and post-2020 giant X-ray outburst phases. However, these parameters do not follow a specific trend during the outburst. A clear correlation between the disc radius and EW is observable across all observation periods. In the post-outburst phase, an anti-correlation between the $FWHM$ and EW is noted, but no distinct relationship is found before and during the outburst.

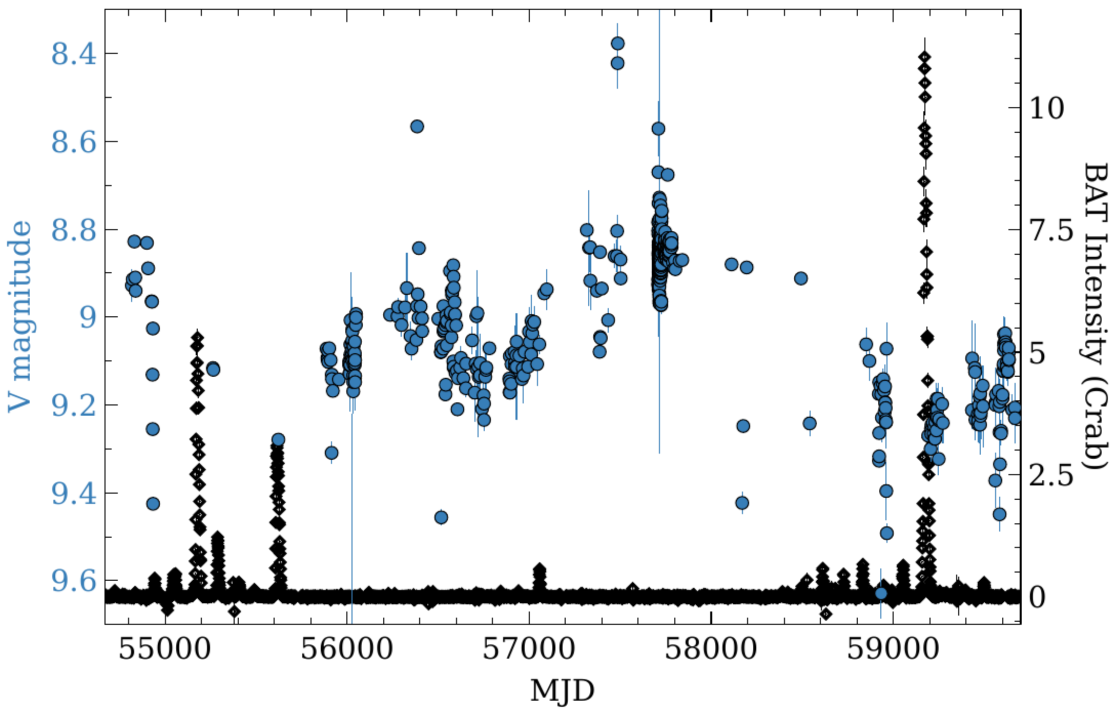

Figure 3.7: Long-term time evolution of V-band magnitude and X-ray flux of 1A 0535+262 obtained from AAVSO international database and Swift/BAT (in 15-50 keV energy range), respectively. The cyan-filled circles represent V-band magnitudes, while the open black diamonds represent BAT intensity in Crab units.

3.3.5 Long-term optical and X-ray variation of the system

We examined the long-term evolution of the Be star in the V-band using publicly available data from the American Association of Variable Star Observers (AAVSO[1]) international database. These data were combined with the X-ray monitoring light curve of the pulsar from Swift/BAT in the 15-50 keV range (Figure 3.7). This analysis aimed to understand the properties of the companion star before, during, and after the giant X-ray outbursts occurring between MJD 54670 (23 July 2008) and 59700 (1 May 2022). Figure 3.7 shows the star dimming prior to the 2020 giant outburst, with the V-magnitude peaking above 9.4 around MJD 58965. Concurrently, an increase in the equivalent width of the Hα line was observed (first three points in Figure 3.5, corresponding to the pre-outburst phase). This behavior is similar to what was observed before the 2009 giant outburst (Camero-Arranz et al., 2012; Yan et al., 2012).

3.4 X-ray properties of the source during the rising phase of the outburst

After the giant X-ray outburst began, AstroSat observed 1A 0535+262 during the rising phase on 11 November 2020 (MJD 59165), as illustrated in Figure 3.1. The pulsar was monitored for approximately 94 ks across a broad energy range using the SXT, LAXPC, and CZTI instruments onboard AstroSat. We conducted timing and spectral analysis on the data from all these detectors and presented our findings in this work.

[1]https://www.aavso.org/LCGv2/

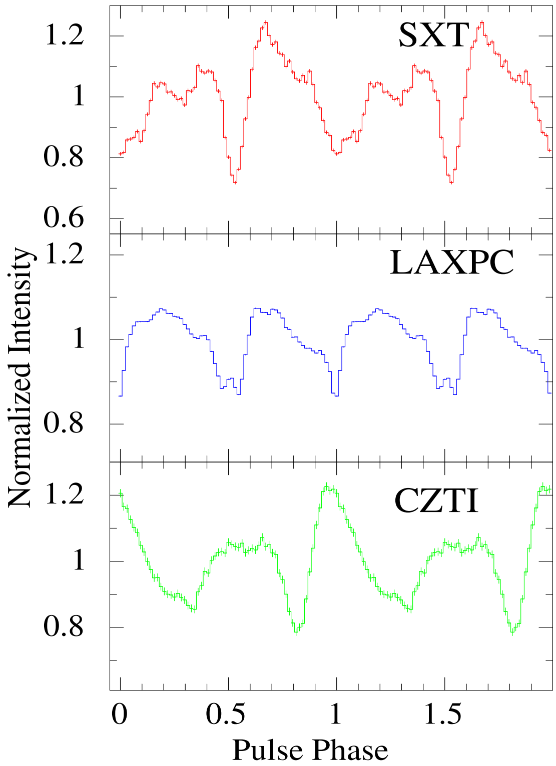

Figure 3.8: Average pulse profiles of 1A 0535+262 obtained from barycenter corrected and background subtracted light curves obtained from SXT (0.3-7 keV; Red), LAXPC (3-80 keV; Blue) and CZTI (20-110 keV; Green) from top to bottom panels, respectively. The errors on the data points are of 1σ level. Two cycles are shown for clarity.

3.4.1 Timing analysis and results

The source and background light curves for the SXT instrument in the 0.3-7 keV energy range were extracted from the reprocessed and merged SXT event file using a bin size of 2.4 seconds. The light curves were extracted for the LAXPC and CZTI instruments with a bin size of 0.1 seconds in the 3–80 keV and 20–110 keV ranges, respectively. Barycenter corrections were applied to the background-subtracted light curves using the *as1bary* tool. We then searched for pulsations in the light curves using the χ^2 maximization technique (Leahy, 1987), implemented through the *efsearch* task of the FTOOLS package. The pulse period of the pulsar was determined to be 103.548(4) seconds. Using this period, the background-subtracted and barycenter-corrected SXT, LAXPC, and CZTI light curves were folded in the 0.3-7 keV, 3-80 keV, and 20-110 keV energy ranges, respectively. While generating pulse profiles with the *efold* task of FTOOLS, we used a suitable epoch to align the profile minimum to phase zero. The resulting folded pulse profiles are displayed in the top, middle, and bottom panels of Figure 3.8. The pulse profiles exhibit a double-peaked structure across the SXT, LAXPC, and CZTI energy ranges, with a noticeable phase shift of approximately 0.1 in the CZTI (hard X-ray) profile compared to the SXT and LAXPC profiles.

To further investigate the energy dependence of the pulse profile, we extracted light curves in narrow energy bands from the SXT, LAXPC, and CZTI data. For the SXT data, light curves were extracted in the 0.3–3 keV and 3–7 keV energy bands. For the CZTI data, light curves were extracted in seven energy bands: 20–25 keV, 25-30 keV, 30-35 keV, 35-40 keV, 40-50 keV, 50-80 keV, and 80-110 keV. For the LAXPC data, light curves were extracted in nine energy bands: 3-7 keV, 7-15 keV, 15-20 keV, 20-25 keV, 25-30 keV, 30-35 keV, 35-40

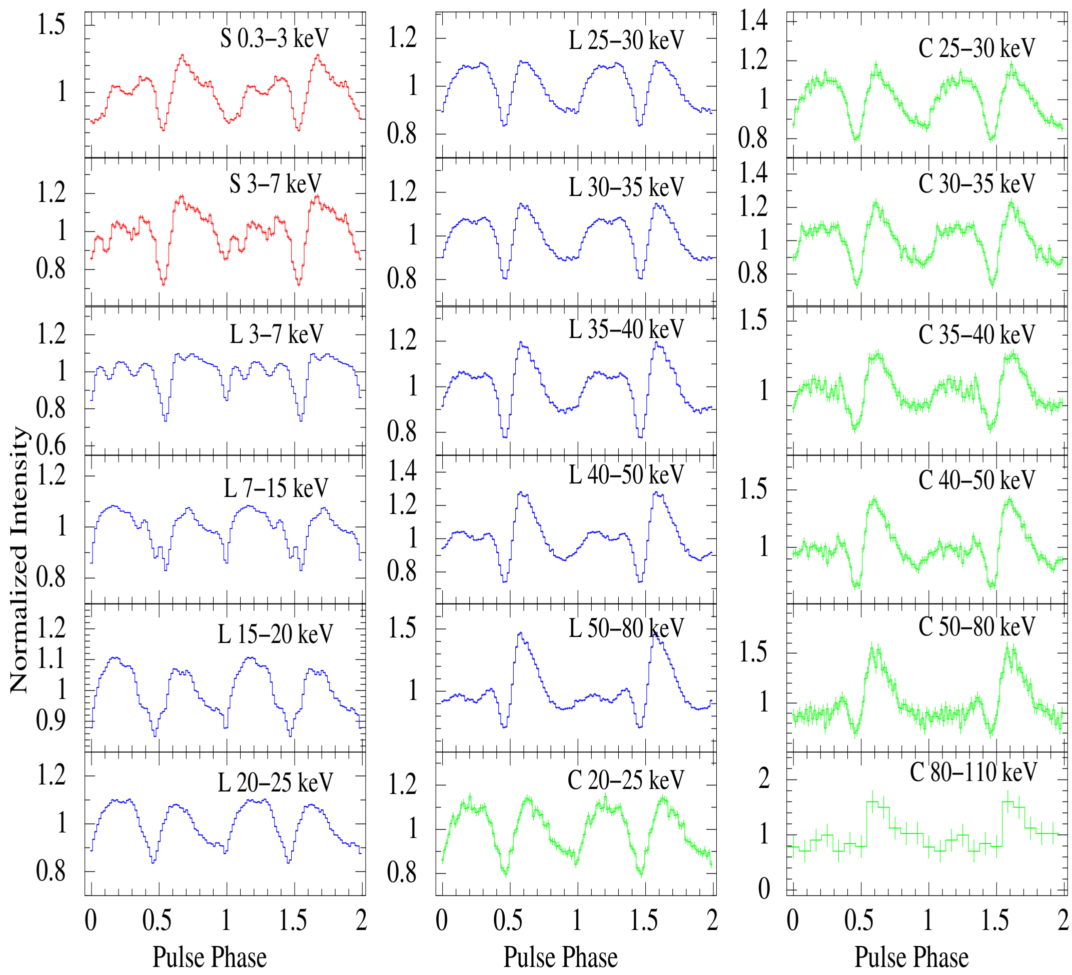

Figure 3.9: Energy-resolved pulse profiles of 1A 0535+262 obtained from barycenter corrected and background subtracted light curves of SXT (S; Red), LAXPC (L; Blue), CZTI (C; Green). The errors on the data points are of 1σ level. Two cycles are shown for clarity.

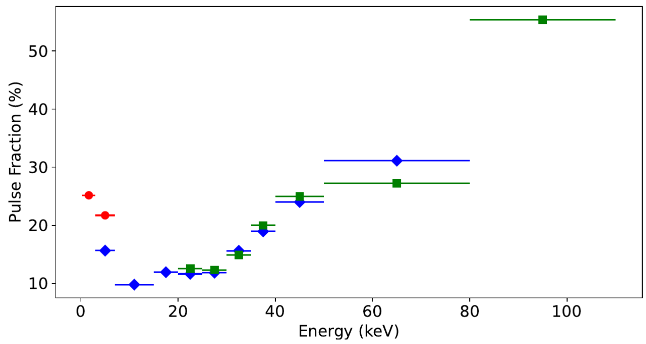

Figure 3.10: Energy-resolved pulse fraction of 1A 0535+262 for SXT (red), LAXPC (blue), and CZTI (green). Energy bin sizes are depicted by horizontal bar.

keV, 40-50 keV, and 50-80 keV. Using the estimated spin period of the neutron star, we generated pulse profiles from these energy-resolved light curves, as shown in Figure 3.9. The same epoch as used previously was applied to generate these energy-resolved profiles. The figure indicates that pulsations in the light curve are detectable up to 110 keV. Besides the primary dip in the 0.45-0.55 phase range, several small and narrow dip-like features (secondary dips) are observed in the pulse profiles of the pulsar in the 0.3-3 keV and 3-7 keV ranges (Figure 3.9). There is also a marginal phase shift in the profiles beyond 15 keV. The shape of the profile changes with increasing energy. Beyond 35 keV, one of the peaks diminishes in the profiles from the LAXPC and CZTI data, eventually becoming a single peak at higher energies. This observed change in the shape of the pulse profiles signifies its evolution with energy. Additionally, apart from the appearance and disappearance of secondary dips, indicating changes in the pulse profiles across various energy ranges, there is an indication of a minor dip in the 0.2-0.3 pulse phase range in the profiles beyond 25 keV. The appearance of this dip coincides with a reduction in the intensity of the first peak.

To further investigate the energy dependency of the pulse profiles, we calculated a quantity called the pulse fraction (PF) using minima and maxima method. The PF is defined as the ratio between the difference and the sum of maximum (I_{max}) and minimum (I_{min}) intensities in the pulse profile.

$$PF = \frac{I_{max} - I_{min}}{I_{max} + I_{min}} \tag{3.5}$$

In Figure 3.10, the variation of PF with energy is shown. We found that the PF decreases from ∼25% to 9% from 0.3 to ∼ 15 keV. Beyond ∼15 keV, the PF of the pulsar showed an increasing trend with energy. In the energy range of 15-110 keV, the PF increases from 10% to 55%.

3.4.2 Spectral analysis and results

The spectral analysis of the AstroSat observation of 1A 0535+262 was conducted using the XSPEC v-12.9.0 package (Arnaud, 1996). The SXT spectrum, obtained in the 0.7-7.0 keV energy range, was grouped to ensure a minimum of 30 counts per bin using the *grppha* task of FTOOLS. Similarly, the LAXPC spectrum was grouped with a minimum of 30 counts per bin. Since the LAXPC data were background-dominated above 60.0 keV, we restricted our analysis to the 3.0-60.0 keV range. For the CZTI instrument, data in the 30.0-90.0 keV range were also grouped to have a minimum of 30 counts per bin. We performed spectral fitting in the 0.7-90.0 keV range using simultaneous data from the SXT, LAXPC, and CZTI instruments. To account for Galactic absorption, we applied the *tbabs* model component with abundances from Wilms et al. (2000) and cross-sections from Verner et al. (1996).

A relative normalization constant was included during the simultaneous spectral fitting to address calibration differences between the three instruments. This constant was fixed to 1 for the SXT data and allowed to vary for the LAXPC and CZTI data. Initially, we used a power-law with an exponential cutoff model to fit the spectrum. The presence of positive residuals in the soft X-ray range necessitated adding a blackbody component to the continuum model. Further, the spectral fitting required an additional blackbody component to accurately model the spectrum in the soft X-ray range. Two blackbody components, one hotter (kT $>$ 1 keV) and one cooler (kT $<$ 1 keV), were added to account for the soft X-ray excess observed in the spectrum, as reported in previous studies (Jaisawal et al., 2020b; Kong et al., 2021). We applied the `gain fit` command to the SXT data for gain correction, fixing the slope at 1 to flatten residuals at 1.8 and 2.2 keV. Despite this correction, a feature at 1.8 keV was present and modeled with a Gaussian emission line, which is related to detector calibration and not intrinsic to the source. A gain correction was also applied to the LAXPC data as recommended by Antia et al. (2021).

A weak iron emission line was detected at 6.4 keV and modeled with a Gaussian function. Negative residuals in the 40.0-50.0 keV range were addressed by adding a Gaussian absorption (*GABS*) model with a central energy of $\sim$46.3 keV, significantly improving the fit. The line width was fixed at 10 keV, as per Kong et al. (2021). This absorption feature is interpreted as the cyclotron resonance scattering feature (CRSF) in the spectrum of the pulsar. The broad-band spectrum of the source and the best-fit spectral model are shown in the top panel of Figure 3.11. Residuals without and with the Gaussian absorption component at 46.3 keV are shown in the middle and bottom panels, respectively. The spectral parameters obtained from our fitting are detailed in Table 3.3.

3.5 Discussion

We conducted optical and X-ray studies of 1A 0535+262 during its 2020 giant X-ray outburst, utilizing observations from the Mount Abu Infrared Observatory and AstroSat. In BeXRB systems, neutron stars typically exhibit Type I X-ray outbursts at periastron passage. These outbursts are influenced by the evolution of the circumstellar disc of the Be star (Okazaki & Negueruela, 2001). When the circumstellar disc is sufficiently developed, the neutron star accretes matter from the disc while passing through the periastron, resulting in increased X-ray luminosity that lasts for about 20% of the binary orbital period. The mass loss from the circumstellar disc also impacts the optical and infrared emissions of the Be star. However, the X-ray luminosity increases by several orders of magnitude during giant X-ray outbursts and persists for several orbital periods, unlike the shorter Type I outbursts. It is essential to investigate the dynamics of the circumstellar disc of the Be star during both active and quiescent X-ray states. To this end, we analyzed the evolution of Hα and He emission lines in the 1A 0535+262/HD 245770 system before, during, and after

Table 3.3: Best-fit parameters obtained from spectral analysis of AstroSat observation of 1A 0535+262

Model	Parameters	Parameters Values
TBabs	$N_H(10^{22}\ cm^{-2})$	$0.64^{-0.03}_{-0.03}$
Cutoffpl	Photon Index (Γ)	$-1.08^{+0.12}_{-0.14}$
	E_{cut} (keV)	$10.02^{+0.33}_{-0.34}$
	norm (10^{-2}	$1.62^{+0.5}_{-0.4}$
Bbodyrad1	kT (keV)	$0.28^{+0.01}_{-0.01}$
	norm	5758^{+626}_{-567}
Bbodyrad2	kT (keV)	$2.25^{+0.03}_{-0.03}$
	norm	$49.67^{+2.0}_{-2.2}$
Gabs	E_{cyl} (keV)	$46.30^{+0.81}_{-0.74}$
	width σ (keV)	10.00 (fixed)
	depth τ	$7.58^{+0.76}_{-0.73}$
Gaussian	E (keV)	$6.34^{+0.03}_{-0.03}$
	width σ (keV)	$0.06^{+0.04}_{-0.03}$
	norm (10^{-2})	$0.54^{+0.1}_{-0.1}$
Unabsorbed flux	(10^{-8} erg cm^{-2} s^{-1})	7.25 ± 0.95
Fit Statistics	χ^2_{red}/d.o.f.	1.1/781

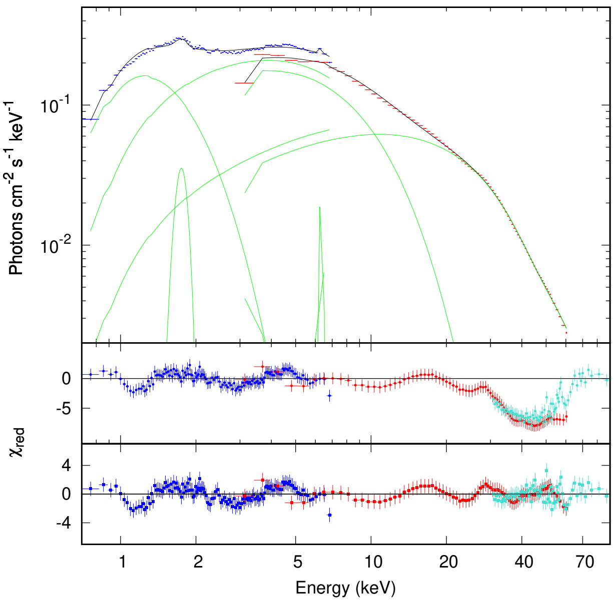

Figure 3.11: Top panel : Broadband AstroSat (SXT+LAXPC+CZTI) spectra of 1A 0535+262 are shown along with the best-fit spectral model. The red, blue, and cyan color data points correspond to the SXT, LAXPC, and CZTI instruments, respectively. The cut-off power law, two blackbody components, and Gaussian lines are shown in green colors. The best-fit spectrum in the 0.7-90.0 keV range is shown in black color. The middle and bottom panels show the residuals without and with the CRSF component in the spectral model, respectively.

the 2020 giant X-ray outburst, covering two years. This section discusses the changes in the circumstellar disc observed during this period.

3.5.1 Evolution of the circumstellar disc around Be star in 1A 0535+262

In this study, we examined the evolution of the Hα emission line profile before, during, and after the 2020 giant X-ray outburst to understand the evolution of the circumstellar disc. Figure 3.3 illustrates these changes. Before the outburst, the Hα line profile was single-peaked and moderately asymmetric, with a broad red wing. During the outburst, the profiles remained asymmetric and single-peaked but showed a broader blue wing instead of the red wing seen during pre-outburst. After the outburst, the profile maintained its shape for about a month, except for a hump-like structure in the blue wing, and then evolved into a double-peaked profile within a year.

Similar studies were conducted during the 2009 and 2011 giant X-ray outbursts of the 1A 0535+262/HD 245770 system, as reported by Camero-Arranz et al. (2012), at a spectral resolution of R$\sim$5000. The emission lines were single-peaked and marginally asymmetric before and during these outbursts. Specifically, the 2009 outburst showed a broader blue wing in the Hα line, while the 2011 outburst exhibited a broader red wing (left and right panels of Figure 4 in Camero-Arranz et al. 2012). Comparing the Hα line profile observed during and before the 2020 outburst with past observations, we find that it resembles the profile seen during the 2009 outburst. Our current observations indicate that the post-2020 outburst profiles are red-shifted with broader blue wings, whereas the pre-outburst profiles were blue-shifted with broader red wings.

High-resolution studies of the Hα emission line (R$\sim$30000-60000) around the 2009 X-ray outburst, as discussed in Moritani et al. (2013), revealed that the basic structure of the emission line (Figure 2 in Moritani et al. 2013) is consistent with our findings and those reported by Camero-Arranz et al. (2012), though some additional absorption features were noted later due to higher instrument resolution. These features suggest a complex structure of the Be circumstellar disc. Camero-Arranz et al. (2012) proposed that the warping of the Be disc could explain the observed Hα line profile structure. Long-term observations of 4U 0115+634/V635 Cas by Negueruela & Okazaki (2001) and Reig et al. (2007) indicated that a precessing warped Be disc caused the shift from a normal double-peaked to a single-peaked profile during the giant X-ray outburst. Similar behavior was noted by Moritani et al. (2011) during the 2009 giant outburst in 1A 0535+262.

In this study, we estimated the size of the Be circumstellar disc during the 2020 giant outburst using the observed Hα emission line parameters. The evolution of the disc size is shown in the fifth panel of Figure 3.5. The disc size was the largest before the 2020 giant X-ray outburst. It began to decrease at the onset of the outburst and remained small even after it. Before the giant outburst on MJD 58920 (12 March 2020), the disc radius was approximately 8.27×10^{10} m, equivalent to about 7.62 times the radius of the Be star. According to the viscous decretion model (Negueruela & Okazaki, 2001), the calculated 4:1 resonance truncation radius for 1A 0535+262 is 7.27×10^{10} m. The Roche lobe radius at periastron passage is estimated to be 7.08×10^{10} m (Okazaki & Negueruela, 2001). The viscous decretion model suggests that the truncation radius limits the Be circumstellar disc size as the viscous and tidal torques balance each other.

Okazaki & Hayasaki (2007) extended this model for highly eccentric and misaligned systems, showing that truncation is less efficient when the inclination (i) is $\geq 60°$. The estimated Be disc size in 1A 0535+262 (prior to the giant X-ray outburst) being larger than the truncation radius confirms that the Be circumstellar disc and the binary plane are highly misaligned. As suggested by Moritani et al. (2011) and Okazaki et al. (2013), such a misaligned disc could warp before the 2020 giant X-ray outburst, allowing the neutron star to capture a large amount of matter. Warping of the disc before the 2009 giant X-ray outburst in 1A 0535+262 has also been proposed (Moritani et al., 2011).

As depicted in Figure 3.5, the Hα line equivalent width (indicative of the size of the Hα emitting region) was at its maximum before the giant X-ray outburst. However, the equivalent width decreased from its pre-outburst values during and after the outburst. This decrease suggests significant matter loss from the circumstellar disc during the outburst. Observing the change in the quantified IR excess flux, Haigh et al. (2004) suggested that in the 1A 0535+262 system, the Be disc grows and decays in a quasi-cyclic period of 1500 days. Consequently, the disc size is expected to grow or remain comparable (if no mass is ejected from the Be star). However, we found that the equivalent width or disc size continued to decrease (albeit slowly) even after approximately 465 days from the onset of the outburst (our last optical observation). After the outburst, the optical brightness increased by about 0.2 mag (see Figure 3.7), indicating mass transfer from the central star to the inner disc region. The Hα line EW may have recovered after the mass ejection from the star, but it slowly decreased from MJD 59213 to 59624, with a drastic decrease from MJD 59254 to

59563, possibly due to a normal outburst around MJD 59500. No significant decrease in EW was observed for the He line, as the normal outburst may only affect the outer part of the disc.

This slow decrease in EW could be due to fewer Hα photons reaching the observer because of a change in the inclination angle between the disc and the line of sight. A similar EW decrease has been reported in the BeXRB 4U 0115+63 (Figure 6 of Negueruela et al. 2001). The same figure shows that the line profile shape also changed from single-peaked to double-peaked. This change in the viewing angle is attributed to disc precession. Therefore, the observed decrease in EW in 1A 0535+262 (after the X-ray outburst) is likely due to a change in the inclination angle of the Be disc. This is supported by the observed changes in the profiles of H and He lines (Figures 3.3 from MJD 59563 to 59624), shifting from single-peaked to double-peaked and double-peaked to shell-like profiles, respectively.

The torque exerted by the Be star is crucial in the disc warping mechanism. The positive torque from the Be star, through the expulsion of matter, tends to align the disc with the equatorial plane of the Be star. However, in a torque-free scenario, where no matter is supplied from the Be star to the disc, the disc can warp toward the orbital plane of the binary. A lack of matter supply reduces the V-band flux from the inner region of the disc. Previous reports have noted the occurrence of giant X-ray outbursts during the optical fading phase in 1A 0535+262 (Camero-Arranz et al., 2012). Yan et al. (2012) observed an anti-correlation between the V-band magnitude and the EW of the Hα line before the 2009 outburst, interpreting it as an indication of mass loss from the inner part of the Be disc.

We also analyzed the V-band magnitude variation from the AAVSO database alongside the Swift/BAT data (Figure 3.7). Consistent with the 2009 giant outburst findings (Camero-Arranz et al. 2012 and Yan et al. 2012), we observe an increase in V-magnitude before the 2020 giant outburst. The V-magnitude peaked at over 9.4 around MJD 58965, suggesting a mass ejection event from the Be star that led to a dimming of the continuum emission. A substantial amount of this ejected material likely transferred to the circumnuclear disc, causing it to grow outward. Consequently, a strong Hα line with increasing equivalent width was expected, as seen below MJD 58920 in our study (Figure 3.5). At this stage, the disc was significantly large (about $8R_*$), leading to the strong X-ray outburst observed in October 2020. Following the outburst, the neutron star truncated the circumstellar disc around the Be star, causing a rapid decrease in Hα emission. The Hα line had not returned to its pre-outburst level even after more than 400 days. In contrast, a much faster disc recovery was observed during the 2009 outburst, where the Hα EW leveled up within a year. Additionally, Haigh et al. (2004) and Yan et al. (2012) reported a strong He I(7065 Å) line during the 1994 and 2009 outbursts, indicating the inner disc remained untruncated. However, a gradual decrease in He I(7065 Å) strength in our observations suggests that the inner region of the disc was affected during the 2020 giant outburst.

To further understand the inner disc condition around the 2020 giant X-ray outburst (October - December), we calculated the Full Width at Zero Intensity (FWZI) of the Hα line. The FWZI indicates the higher velocity components corresponding to the inner part of the disc. In a torque-free scenario, where the Be star does not supply matter, the density of the inner disc decreases, reducing the high-velocity component of the Hα line (FWZI).

We calculated the FWZI of the Hα line from our pre-outburst observations, estimating an average value of approximately 1017 km/s. However, during the outburst peak, the FWZI was about 771 km/s. This suggests that the inner part of the disc was missing prior to the giant outburst, influencing the warping of the outer decretion disc and possibly causing the X-ray outburst from the neutron star.

3.5.2 Timing and spectral properties of the pulsar with AstroSat

During the AstroSat observation of 1A 0535+262 in the rising phase of its giant X-ray outburst, the luminosity of the pulsar was approximately 3.91×10^{37} erg s^{-1} ($L/L_{\rm Edd} \sim$ 0.28) within the 0.7-90.0 keV energy range. This calculation assumes the source distance as 2.13 kpc away, based on Gaia observations (Bailer-Jones et al., 2018). This indicates that the pulsar was emitting at a sub-Eddington level, below the critical threshold (Sartore et al., 2015). The spin period of the pulsar is measured at 103.548 seconds. The average pulse profiles revealed a simple double-peaked structure, showing strong energy dependence. Notably, a phase shift of approximately 0.1 beyond 25 keV suggests a slight change in the emission region. One of the peaks diminishes at higher X-ray energies, resulting in a single-peaked profile. Pulsations at 103.548 seconds were detected in energy-resolved light curves up to 110 keV, beyond which CZTI data became dominated by background. The pulse profile displayed several complex dip-like features in the soft X-ray range (up to 7 keV). These features, also noted in earlier observations of 1A 0535+262 (Naik et al., 2008; Caballero et al., 2013), as well as in SAX 2103.5+4545 (Camero Arranz et al., 2007), EXO 2030+375 (Naik et al., 2013; Naik & Jaisawal, 2015; Epili et al., 2017a), and GX 304-1 (Jaisawal et al., 2016), are interpreted as being due to photon absorption by streams of matter at certain pulse phases of the neutron star. Changes in the emission region can explain the evolution from a double-peaked to a single-peaked profile with increasing energy. The pulse fraction (PF) decreased initially to its lowest value in the 7-15 keV range before showing a steady increase. The high PF value in high-energy ranges indicates that high-energy photons contribute more to the pulsation than low-energy photons. The initial decrease in PF with energy might be attributed to diffuse X-ray emission from the hot plasma above the polar region. Additionally, the contribution of reflected photons in this energy range has been proposed, as observed in RX J0440.9+4431, which exhibits a similar trend in PF evolution with energy (Li et al., 2023).

The 0.7-90 keV range pulsar spectrum was best modeled by a cut-off power-law continuum with two blackbody components for soft excess and a cyclotron resonance scattering feature (CRSF) at approximately 46.3 keV. This CRSF observed at a luminosity of around 3.91×10^{37} erg s^{-1}, is consistent with earlier reports during the rising phase of the outburst (Tsygankov et al., 2019; Kong et al., 2021; Mandal & Pal, 2022). The magnetic field of the neutron star was estimated using the relation:

$$E_{CRSF} = 11.57 \times B_{12}(1+z)^{-1} \tag{3.6}$$

where, E_{CRSF} is the cyclotron line energy in keV, B_{12} is the magnetic field in units of 10^{12} G, and z is the gravitational red-shift (z $\simeq$ 0.3 for a typical neutron star). The calculated magnetic field of the pulsar is 5.2×10^{12} G.

3.6 Conclusions

We investigated the optical properties of the Be/X-ray binary 1A 0535+262/HD 245770, focusing on the epochs before, during, and after the 2020 giant X-ray outburst over two years. Before the outburst, the Hα emission lines exhibited an asymmetric, single-peaked profile with a broad red wing. However, the line profiles displayed the opposite pattern during the outburst, featuring a broad blue wing. Approximately 400 days after the onset of the outburst, the profile transitioned to a double peak. The equivalent width (EW) of the Hα emission line increased before the giant outburst. As inferred from the Hα EW during the pre-outburst phase, the disc size exceeded the 4:1 resonance radius of the decretion disc, indicating a highly misaligned disc. The transformation of the line profile from a single to a double peak and the highly misaligned disc suggest that the mass accretion may have originated from a warped disc, leading to the giant outburst.

We also conducted timing and spectral analyses of the pulsar using a target of opportunity (ToO) X-ray observation with AstroSat. The X-ray pulsation at 103.55 seconds was detected in the light curve of the pulsar up to 110 keV. The pulse profile evolved from a double-peaked structure in lower energy ranges to a single-peaked profile in higher energy ranges. In the 0.7-90.0 keV range, the source emitted a luminosity of 3.91×10^{37} erg s^{-1}. The cyclotron resonance scattering feature (CRSF) was detected at 46.3 keV, indicating the magnetic field strength of the neutron star is approximately 5.2×10^{12} G.

Chapter 4

X-ray and optical studies of the Be/X-ray binary IGR J06074+2205

In the previous chapter, we discussed the optical and X-ray properties of the BeXRB 1A 0535+262 around the 2020 giant X-ray outburst. As a part of our optical monitoring program of a selected list of BeXRBs, IGR J06074+2205 has been observed at several epochs to investigate changes in the circumstellar disc properties during X-ray outbursts. This approach helps us to understand the physical conditions of the Be circumstellar disc during mass accretion by the neutron star. Our optical observations of IGR J06074+2205 began on 18 November 2022, and the neutron star in the binary system recently exhibited X-ray outbursts in October and December 2023. During the October 2023 X-ray outburst, IGR J06074+2205 was observed by both NuSTAR and NICER, while the December outburst was followed only by NICER. Our optical observations covered the periods before, during, and after the X-ray outburst, as detailed in Table 4.1. In this chapter, we discuss the properties of the BeXRB IGR J06074+2205 using X-ray and optical observations. As shown in Figure 4.1, we used X-ray data obtained during the X-ray outbursts in October and December 2023. The optical observations were carried out between November 2022 and February 2024, covering both October and December 2023 X-ray outbursts using the Mount Abu Infrared Observatory (MIRO) and the Indian Astronomical Observatory (IAO). The chapter is structured as follows: Section 4.1 provides an introduction to IGR J06074+2205. Section 4.2 gives details about the X-ray and optical observations of the source. Sections 4.3 and 4.4 present the results of X-ray timing and spectral analyses, respectively. Section 4.5 presents findings from the optical analysis. Finally, Sections 4.6 and 4.7 offer the discussion and conclusions, respectively.

4.1 Introduction

IGR J06074+2205, identified as a BeXRB, was initially discovered with the JEM-X telescope onboard INTEGRAL in 2003 (Chenevez et al., 2004). The source exhibited a flux of approximately 7 mCrab in the 3-10 keV range and about 15 mCrab in the 10-20 keV energy band. Additionally, a potential association between the radio source NVSS J060718+220452 and IGR J06074+2205 was suggested by Pooley (2004). Subsequently, Halpern & Tyagi (2005) reported on the potential optical counterpart of IGR J06074+2205. Their observations suggested the optical counterpart to be a Be star, as indicated by the presence of the Hα emission line with an equivalent width of -6.6 Å. Subsequently, IGR J06074+2205 was identified as a Be/X-ray binary by confirming the association of a Be star and the X-ray source using the high spatial resolution capability of Chandra X-ray observatory (Tomsick et al., 2006). Reig et al. (2010) conducted an extensive analysis of the optical counterpart in the 4000-7000 Å range between 2006 and 2008. They suggested the optical counterpart of IGR J06074+2205 to be a B0.5Ve spectral type star with a V-band magnitude of 12.3, situated at a distance of 4.5 kpc. However, recent studies by Fortin et al. (2022) suggested the source distance to be 5.99 kpc using *Gaia*. From the analysis of the Hα line, (Reig et al., 2010) found V/R (the ratio of violet-side to red-side peak intensities above continuum in units of continuum intensity representing a measure of the asymmetry of the line) variability, indicating significant changes in the structure of the circumstellar disc on timescales of months. Additionally, a decline in the equivalent width of the Hα line over approximately 3 years was noted. Furthermore, the Hα line feature in absorption was observed in March 2010, suggesting a possible disc loss event. Following this disc loss episode, a new decretion disc (characterized by Hα emission) was detected during the observations conducted between 14 and 24 April 2012, as reported by Simon et al. (2012). Schmidtke et al. (2024) carried out photometric observations in the optical waveband from 3 December 2023 to 17 March 2024 and found no optical variability associated with the X-ray outburst on 15 March 2024. Using photometric studies, Nesci et al. (2024) suggested the precession or propagation of density wave in the circumstellar disc gives rise to optical variability at a timescale of 620 days.

Reig & Zezas (2018) for the first time detected coherent X-ray pulsations from the X-ray source using the XMM-Newton observation on 29 September 2017. The pulsation was observed at 373.2 s at a low luminosity level of $\approx 10^{34}$ erg s^{-1} for a distance of 4.5 kpc. Interestingly, Reig & Zezas (2018) detected pulsations during a disc-loss phase of the Be star. Their spectral analysis in the 0.4-12 keV range was characterized by a combination of an absorbed power law and thermal (blackbody) components, with the following optimal parameters: $N_H = (6.2 \pm 0.5) \times 10^{21}$ cm^{-2}, $kT_{bb} = 1.16 \pm 0.03$ keV, and $\Gamma = 1.5 \pm 0.1$. The absorbed X-ray luminosity was determined to be $L_X = 1.4 \times 10^{34}$ erg s^{-1}, assuming a distance of 4.5 kpc. Recently, Roy et al. (2024) reported the detection of a cyclotron absorption line at $\approx$51 keV, which corresponds to a magnetic field strength of 4×10^{12} G.

4.2 X-ray and optical observations

IGR J06074+2204 was observed with NuSTAR at two epochs on MJD 60225 (ID 90901331002) and MJD 60232 (ID 90901331004) for $\approx$ 42 ks and $\approx$ 41 ks, respectively, during the October 2023 X-ray outburst (Table 4.1). The data reduction techniques used to generate cleaned event files are presented in Chapter-2. For source and background products, the source and background regions are chosen using cleaned event files with the help of `ds9` software. The source region is centered on the source position, while the background region is chosen as far from the source position as possible. Both regions are circular in shape with radii of 180 arcsec and 90 arcsec for ID 90901331002 (ID 02 hereafter) and 90901331004 (ID 04

Table 4.1: Log of X-ray & optical observations of IGR J06074+2205. Note: The NICER exposure time corresponds to the net exposure time after applying SUNSHINE==0 filter.

Obs. ID	Date of observation	MJD	Exposure time (s)
NuSTAR			
90901331002	2023-10-08	60225	42704
90901331004	2023-10-15	60232	40676
NICER			
6204040101	2023-10-12	60229	163
6204040102	2023-10-13	60230	2406
6204040103	2023-10-14	60231	36
6204040104	2023-10-15	60232	263
6204040105	2023-10-17	60234	3497
6204040106	2023-12-28	60306	10339
6204040107	2023-12-29	60307	359
6204040108	2023-12-29	60307	207
6204040109	2024-01-01	60310	472
6204040110	2024-01-05	60314	869
6204040111	2024-01-06	60316	2532
6204040112	2024-01-08	60317	572
6204040113	2024-01-10	60319	1134
MIRO			
Epoch1	2022-11-18	59901	500
Epoch2	2022-12-13	59926	400
IAO			
Epoch3	2023-10-22	60239	500
Epoch4	2023-12-15	60293	500
Epoch5	2024-02-03	60343	500

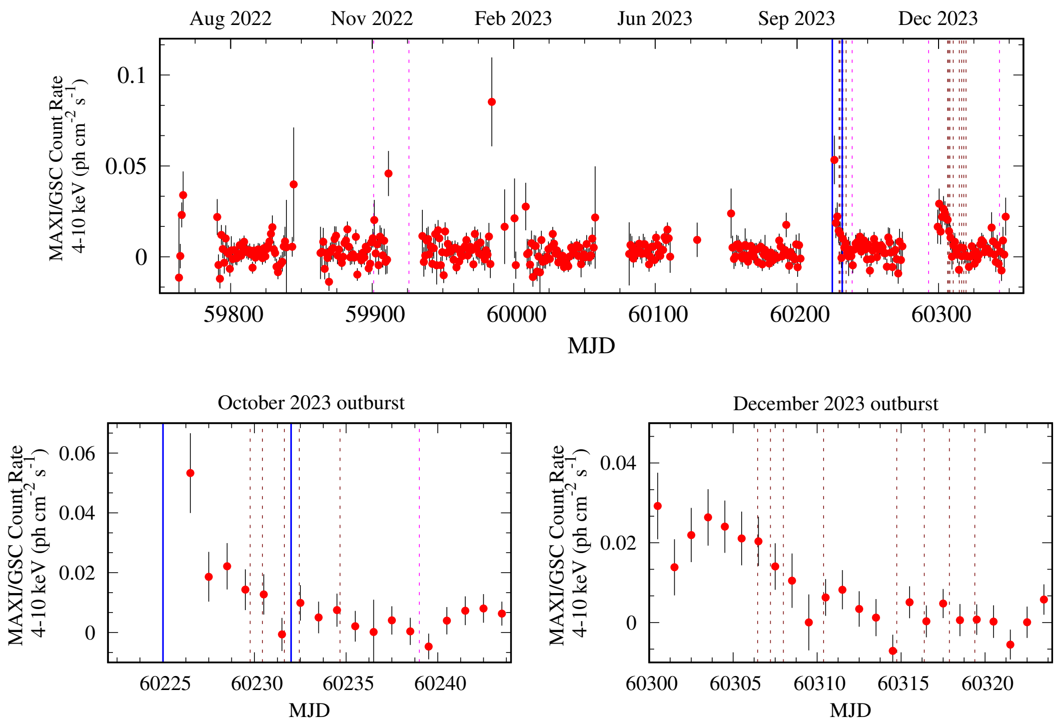

Figure 4.1: Upper panel: One-day binned MAXI/GSC light curve of IGR J06074+2205 in the 4-10 keV energy band between May 2022 and February 2024. Lower panels: MAXI/GSC count rate variations during the October and December 2023 X-ray outbursts. Vertical dashed lines indicate the epochs of NuSTAR (blue), NICER (brown), and optical (magenta) observations.

hereafter), respectively. These source and background regions are used along with cleaned event files to extract scientific products such as light curves, spectra, response matrices, and effective area files with the help of `NUPRODUCT` task. Our study also uses NICER data of IGR J06074+2205 between MJD 60229 (12 October 2023) and MJD 60319 (10 January 2024). These data are stored under observation IDs 6204040xxx with a net exposure time of ≈23 ks (see Table 4.1). The data reduction techniques followed in preparing data for scientific analysis are presented in Chapter-2. We extracted light curves and spectra from each observation using the XSELECT task. We utilized the `nibackgen3C50` (Remillard et al., 2022) tool to generate the background spectrum for each observation. Finally, we created a spectral response matrix and ancillary response files using the `nicerrmf` and `nicerarf` tasks.

We use the Mt. Abu Faint Object Spectrograph and Camera-Pathfinder (MFOSC-P) instrument (Srivastava et al., 2018; Srivastava et al., 2021) mounted on the 1.2 m, f/13 telescope of MIRO for two epochs of observations of IGR J06074+2205 as presented in Table 4.1. We carried out spectroscopic observations using a 75 μm slit in R2000 mode, the highest resolution available for the MFOSC-P instrument, which covers a wavelength range of ≈6000-7200 Å. Apart from observations with MIRO, we also use three epochs of spectroscopic observations of IGR J06074+2205 (see Table 4.1) with the Hanle Faint Object Spectrograph and Camera (HFOSC) instrument mounted on the 2.01-m Himalayan Chandra Telescope (HCT) of IAO. The spectra are taken with Grism 8 and 167 l slit setup, which covers a wavelength range of 5500–8350 Å, providing an effective resolution of 2000 at Hα.

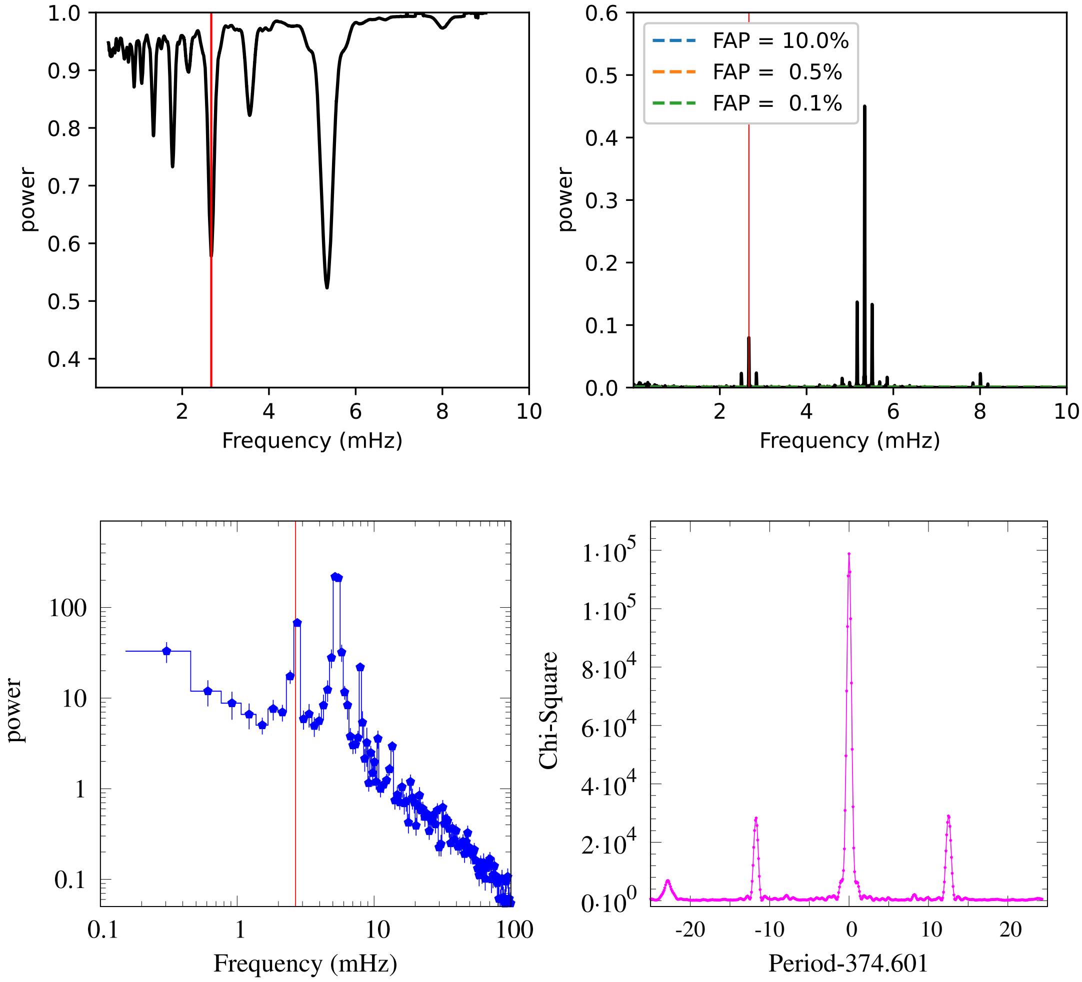

Figure 4.2: Detection of pulsation at ≈2.66 mHz (374.60 s) for observation ID 02 using various techniques such as PDM (upper left), powspec (lower left), GLS periodogram (upper right), and efsearch (lower right) are shown.

The details on the data reduction for MFOSC-P and HFOSC data are presented in Chapter-2. For the instrument response correction, a spectro-photometric standard star from the European Southern Observatory (ESO) catalogue[1], G191B2B is used. The response function is calculated by dividing the observed continuum spectra of G191B2B with a blackbody curve corresponding to the effective temperature of the standard star. The final spectra are created by applying the response function to the source spectra.

4.3 X-ray Timing Analysis & Results

X-ray timing analysis is conducted using data from the NuSTAR and NICER observations of the pulsar during its outbursts in October and December 2023 (see Table 4.1). The barycenter-corrected NuSTAR and NICER light curves are generated at a bin size of 10 ms in the energy range of 3-79 keV and 0.5-10 keV, respectively. In the beginning, we search for pulsations in the light curves at a period close to 374 s (Reig & Zezas, 2018) following the χ^2-maximization technique (Leahy, 1987) by using the `efsearch` task of `FTOOLS` package.

[1] `https://www.eso.org/sci/observing/tools/standards/spectra/okestandards_rev.html`

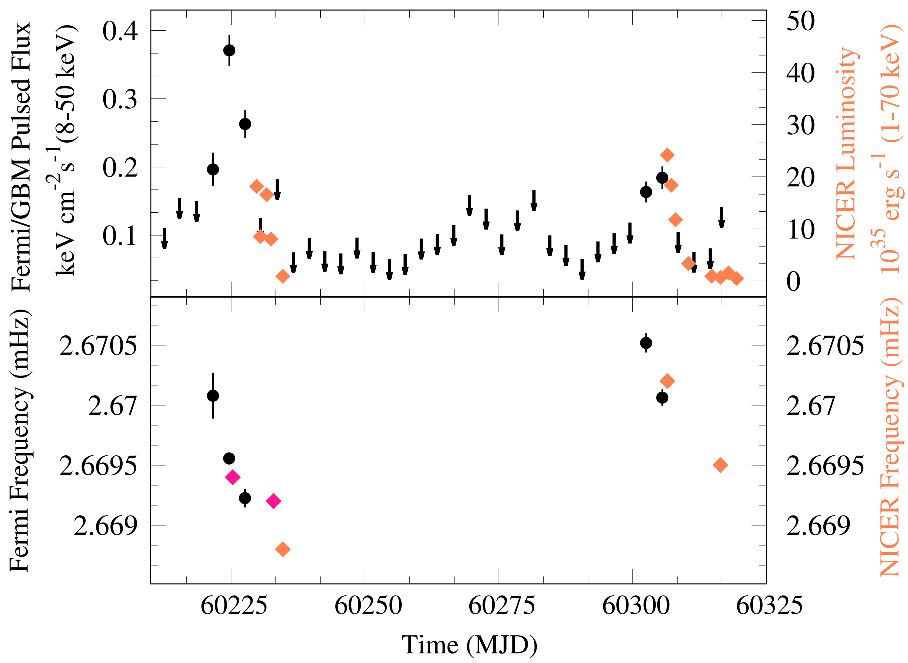

Figure 4.3: Upper panel: Evolution of Fermi/GBM flux in the 8-50 keV energy range (black) and NICER luminosity in the 1-70 keV energy range (orange) over time. Bottom panel: Time evolution of the spin frequency of IGR J06074+2205 measured using Fermi/GBM (black), NICER (orange), and NuSTAR (magenta) data.

The detection of pulsar period (period corresponding to highest χ^2) for observation ID 02 using `efsearch` task is shown in the lower right panel of Figure 4.2. Then, we search for the pulse period using the `powspec` tool of the `XRONOS` package. We employ the command `powspec norm=-2` to obtain white-noise subtracted averaged power density spectrum (PDS). In this process, the power is expressed in the units of (RMS/mean)^2/Hz. The obtained PDS is shown in the lower left panel of Figure 4.2. Then, we apply the generalized Lomb-Scargle method (GLS; Zechmeister & Kürster 2009) and Phase Dispersion Minimization (PDM; Stellingwerf 1978) method to calculate the pulsation period of the neutron star. In Figure 4.2, we show the pulse period search results for ID 02. For ID 02, the obtained pulse frequency is ≈2.66 mHz (374.60 s). The obtained pulse frequency values are found to be comparable for all the methods. The frequency corresponds to the pulsation of the neutron star or the fundamental frequency, and its corresponding power is marked as a vertical line in the figure. The other peaks/dips arise due to higher harmonics of the fundamental frequency, irregularities or gaps, and noise in the data. We observe that the power of 1st harmonic is more than the fundamental frequency, which is also the case for IGR J06074+2205 during the 2017 observation (Reig & Zezas, 2018).

The spin periods obtained using `efsearch` task are 374.60±0.30 & 374.64±0.10 s from the NuSTAR observations ID 02 & 04, respectively. From the NICER observation IDs 6204040105 (ID 105 hereafter), 6204040106 (ID 106 hereafter), and 6204040111 (ID 111 hereafter), the estimated spin periods are 374.63±0.85, 374.54±0.35, and 374.57±0.35 s, respectively. It is possible to calculate the pulse period of the pulsar only in these 3 NICER observation IDs out of 13, which may be because of a lack of sufficient exposure times and

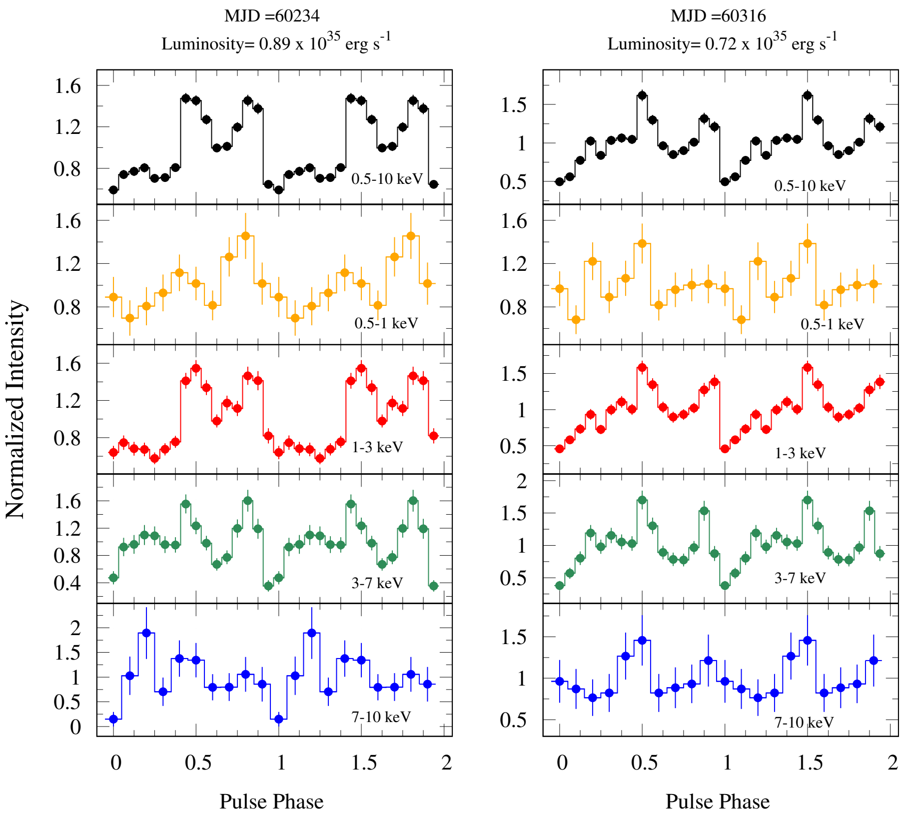

Figure 4.4: Pulse profiles of the pulsar for the NICER observation IDs 105 (left panel) & 111 (right panel), generated at energy ranges of 0.5-10 keV, 0.5-1 keV, 1-3 keV, 3-7 keV, and 7-10 keV are displayed from top to bottom, respectively. The epoch of observation (MJD) and luminosity corresponding to each observation ID are provided at the top of the figure.

low count rates. The error presented in each pulse period value is determined by fitting a Gaussian to the distribution of χ^2 values obtained from the χ^2-maximization technique and considering 1-σ standard deviation. The spin period values obtained from other methods are consistent with these measurements within the quoted uncertainties. We also use publicly available Fermi/GBM[2] spin frequency data (Malacaria et al., 2020) for IGR J06074+2205 to check the spin frequency value and it's evolution with time and luminosity. The spin frequency evolution of the source with time obtained from the NuSTAR, NICER, and Fermi/GBM observations is shown in the bottom panel of Figure 4.3. We present the evolution of 8-50 keV pulsed flux from Fermi/GBM and the source luminosity in the 1-70 keV range from the NICER observations in the top panel of Figure 4.3. The pulse frequency is found to decrease with time during the October & December X-ray outbursts.

Subsequently, we analyze the energy-averaged and energy-resolved pulse profiles of the pulsar to investigate the geometry of emission and its energy dependence. Each light curve is folded at the corresponding spin period of the pulsar utilizing the `efold` task within the `FTOOLS` package. In the beginning, we generated energy-averaged and energy-resolved pulse profiles for three NICER observation IDs to probe the emission geometry in the soft X-ray regime. The pulsar was relatively faint during IDs 105 & 111 with 1-70 keV luminosities of 8.9×10^{34} and 7.2×10^{34} erg s^{-1} (assuming a distance of 5.99 kpc), respectively. The pulse profiles of the pulsar for IDs 105 & 111 are presented in Figure 4.4. For ID 106, the pulse profiles are obtained during a relatively brighter state at a luminosity of 2.42×10^{36} erg s^{-1}

[2]`https://gammaray.nsstc.nasa.gov/gbm/science/pulsars/lightcurves/igrj06074.html`

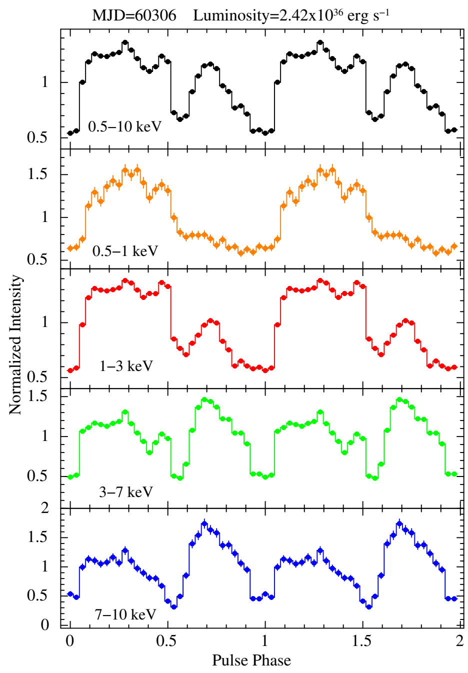

Figure 4.5: Pulse profiles are presented for NICER observation ID 106 generated at energy bands of 0.5-10 keV, 0.5-1 keV, 1-3 keV, 3-7 keV, and 7-10 keV and displayed from top to bottom, respectively. The epoch of observation (MJD) and luminosity are provided at the top of the figure.

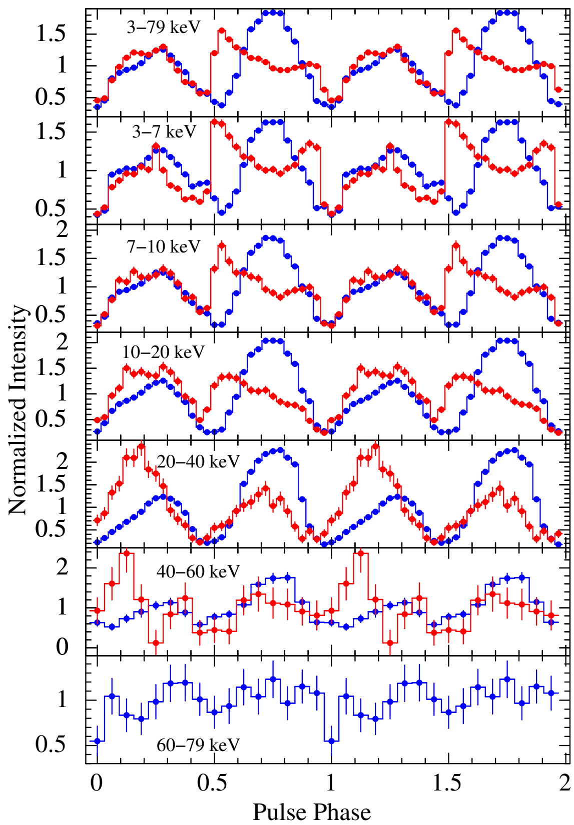

Figure 4.6: Pulse profiles for NuSTAR observation IDs 02 (blue) and 04 (red) are presented. The pulse profiles are obtained in the energy bands of 3-79 keV, 3-7 keV, 7-10 keV, 10-20 keV, 20-40 keV, 40-60 keV, and 60-79 keV displayed from top to bottom, respectively.

(see Figure 4.5).

For the fainter observations, the energy-averaged pulse profiles (top panels of Figure 4.4) are double-peaked, with the two peaks appearing at phases $\approx$0.45 and $\approx$0.85. For ID 106, the pulse profile is also double-peaked with two peaks appearing at phases $\approx$0.3 (primary peak) and $\approx$0.7 (top panel of Figure 4.5). Moreover, the primary peak also contains a minor dip at phase $\approx$0.4, unlike in the fainter observations.

The energy-resolved pulse profiles obtained in the 0.5-1, 1-3, 3-7, and 7-10 keV energy bands for NICER observations are shown in Figures 4.4 & 4.5. The pulse profiles from NICER observations IDs 105 & 111, when the source was relatively faint, do not show significant variation with energy. However, the pulse profiles at brighter state exhibit notable energy-dependent changes. Below 1 keV, the profile is single-peaked, showing only the primary peak. However, with increase in energy, a secondary peak emerges in the 0.6–1.0 phase range and eventually becomes the dominant feature in the profile as reported by Nakajima et al. (2024).

To understand the behavior of the pulse profile across a broad energy regime, we used data from both the epochs of NuSTAR observations of IGR J06074+2205 during the October 2023 outburst. For ID 02 and ID 04, the pulse profiles are generated at the luminosities of 5.56×10^{36} and 4.66×10^{35} erg s^{-1} (in 1-70 keV band), respectively. The pulse profiles obtained in the 3-79 keV energy band are double-peaked and asymmetric at lower and higher luminosity state observation (1st panel of Figure 4.6). However, the pulse profile obtained at higher luminosity is relatively smoother than that at lower luminosity, which contains dip-like features in the 0.6–0.8 phase range. Further, we generated energy-resolved pulse profiles across energy bands of 3-7, 7-10, 10-20, 20-40, 40-60, and 60-79 keV, as depicted in Figure 4.6. The basic shape of the pulse profiles at higher luminosity did not vary much with energy. However, the peak in the phase range of 0.0-0.5 becomes dimmer, and the peak between phases 0.5 and 1.0 becomes brighter as the energy increases from 3 to 40 keV. Beyond 40 keV, the pulse profiles are coarsely binned due to low SNR. We observed that the difference between the strength of both peaks in these pulse profiles decreased. For ID 04, the basic shape of the pulse profiles varied significantly with energy. The peak in the 0.5-1.0 phase range harbors a deeper absorption feature in the 3-7 keV energy band, which diminished as the energy increased and vanished beyond 20 keV. Also, as the energy increases from 3 to 60 keV, the pulse peak in the 0.0-0.5 phase range evolved from the weaker to the dominant peak in the pulse profile. Overall, the pulse profiles are asymmetric and double-peaked, with differing shapes for both IDs below $\approx$20 keV (Roy et al., 2024).

Furthermore, we derive the pulsed fraction (PF) of the pulse profiles to quantify the amount of pulsed emission from the source using the root mean square (RMS) method. The RMS method measures the deviation of the pulse from its mean value. Its strength lies in the ability to account for the complexity of even noisy pulse profiles. However, when determining the pulse fraction using the maxima-minima method (see Eq. 3.5), the result may be biased by the binning of the pulse profile. Additionally, since the computation relies on only two reference values of the pulse fraction, it does not fully capture the integral shape of the profile (Ferrigno et al., 2023). Mathematically, the PF using the rms method is given as:

$$PF = \frac{(\sum_{i=1}^{N}(r_i - \overline{r})^2/N)^{1/2}}{\overline{r}} \tag{4.1}$$

Where, r_i is the count rate in the ith phase bin of the pulse profile, $\overline{r}$ is the average count rate, and N is the total number of phase bins. The PF variation with energy for NuSTAR observation (IDs 02 and 04) and NICER observations (IDs 105, 106, 111) are shown in Figure 4.7. To calculate PF, at first, we analyze light curves generated at a narrow energy range and corresponding pulse profiles, inspired by the technique of Ferrigno et al. (2023). As the energy resolution for NuSTAR is 400 eV at 10 keV and 900 eV at 68 keV (Harrison et al., 2013), the light curves are generated with energy bin spacings of 0.4 keV below 10 keV and 1.0 keV above 10 keV. Similarly, the light curves are generated with an energy bin of 0.09 keV below 1 keV and 0.2 keV beyond 1 keV for NICER observations. Energy-resolved pulse profiles are then created with 16 phase bins per period. Finally, the pulse profiles are combined to achieve an SNR of 12 for NuSTAR and 8 for NICER data, following Ferrigno et al. (2023). The SNR is calculated using the formulas suggested by Ferrigno et al. (2023):

$$SNR = \frac{\Sigma|p_i - \bar{p}|}{\sqrt{\Sigma(\sigma_{p_i})^2}} \tag{4.2}$$

Where p$_i$, σ_{p_i} and $\bar{p}$ are the rate on the ith phase bin, uncertainty, and the average rate of the pulse profile. respectively. Then, we calculate the PF using the RMS method (Equation 4.1).

For ID 02, between 3 and 35 keV range, the PF value increases monotonically from ≈25% to ≈70%. Beyond 35 keV, it decreases sharply from ≈70% to ≈50% at 45 keV. For ID 04, the PF remains flat around 30% between 3 and 8 keV and then increases to ≈70% between 8 and 25 keV. Again, it decreases sharply from ≈70% to ≈50% between 25 and 30 keV. At higher energies, the PF is not calculated as it did not achieve the prescribed SNR.

For NICER observations, we observe a distinct PF evolution with energy. For ID 105, the PF rises from ≈20% to 40% between 0.5 and 2 keV, then decreases to ∼25% between 2 and 3 keV, and then increases again to ∼50% between 3 and 5 keV. For ID 111, the PF varied between ∼20% to 35% as energy increased from 0.5 to 5 keV. For ID 106, the PF shows a unique broad hump-like feature between 0.5 and 3 keV, varying between 20% and 40%, followed by a steady increase from ∼20% to 40% in the 3-10 keV energy band.

4.3.1 Orbital period determination of IGR J06074+2205

Though we have some information about the Be star and neutron star in the Be/X-ray binary IGR J06074+2205, the orbital parameters of the binary are yet to be determined. Mihara et al. (2023) suggested the orbital period of the binary to be 80±2 or 80/n (n=1,2,3...) by analyzing four possible X-ray outbursts in MAXI/GSC light curve. In this work, we conducted a comprehensive analysis by studying 20 possible X-ray outbursts. We started by looking at the long-term light curve of IGR J06074+2205, utilizing data from MAXI/GSC (4-10 keV range) as it provides frequent monitoring of the source compared to Fermi/GBM and Swift/BAT. Our approach is to find signatures of periodic X-ray enhancements in the X-ray light curve of IGR J06074+2205, which is assumed to occur due to mass accretion by a neutron star during its periastron passage. IGR J06074+2205 has rarely shown any

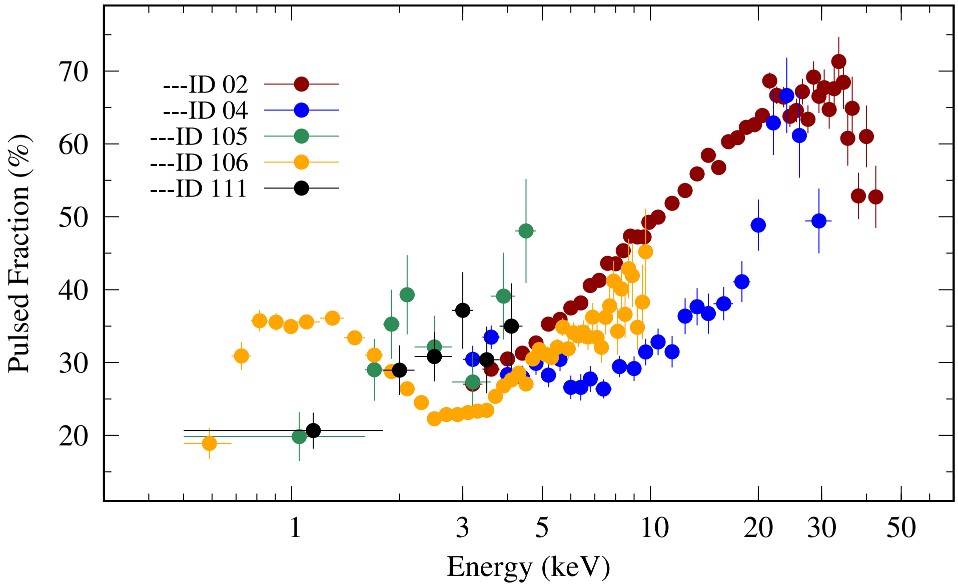

Figure 4.7: Evolution of the pulsed fraction (PF) with energy calculated at SNR of 12 and 8 for NuSTAR (ID 02 & 04) and NICER (ID 105, 106, and 111) observations, respectively.

remarkable normal or giant X-ray outbursts since its discovery in 2003. However, we attempted to find any periodic enhancement in the light curve. We initially applied two robust techniques, the GLS periodogram and the PDM method. Both techniques exhibit strong periodicity at ≈72 days using MAXI. However, this periodicity is known to arise due to the precession period of the International Space Station (Corbet et al., 2022). Then, we manually try to identify the outburst-like features in the long-term light curve. The possible 20 X-ray outbursts-like features from IGR J06074+2205 are selected using MAXI/GSC 4-10 keV band long-term light curve (see Figure 4.8). We use the 4-10 keV light curve instead of the light curve in the 2-20 keV range to avoid flare-like profiles for unexpected background increase or dip-like structure due to the shadow of solar panels, which are more prominent in 2-4 keV[3]. Then, from the sample of 20 X-ray outburst-like features, we select 12 features for further analysis. These selected outburst-like features are marked in red color in Figure 4.8. These 12 outbursts (outburst-like features) are selected considering the peak intensity as 3σ or above from the mean value and do not show sudden rise and decay of intensity. The day of occurrence (MJD) and corresponding X-ray intensities of these 12 outbursts are plotted in the bottom panel of Figure 4.9 to give a clear picture of the occurrence time of the outbursts. We find that the minimum difference between two consecutive outbursts is approximately 80 days. This result is consistent with the finding of Mihara et al. (2023).

[3]http://maxi.riken.jp/top/readme.html

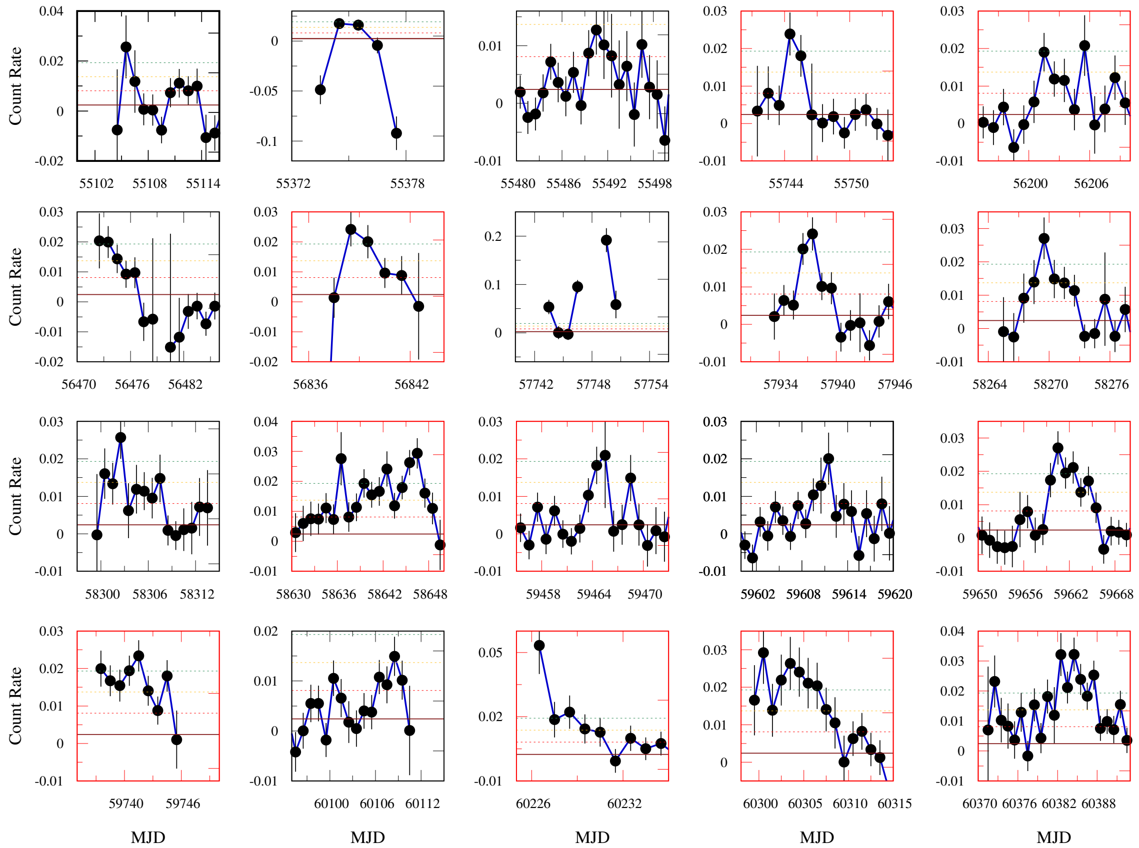

Figure 4.8: Possible Type-I X-ray outbursts observed in IGR J06074+2205 with MAXI/GSC in the 4-10 keV energy band. The brown line presents the mean count rate distribution observed in the source. The red, yellow, and green dotted lines mark the 1σ, 2σ, and 3σ count rates above the mean, respectively. The mean and standard deviations are obtained by fitting a Gaussian to the histogram plot of count distribution as shown in the top panel of Figure 4.9. Panels with a red border contain outbursts that are chosen for further analysis.

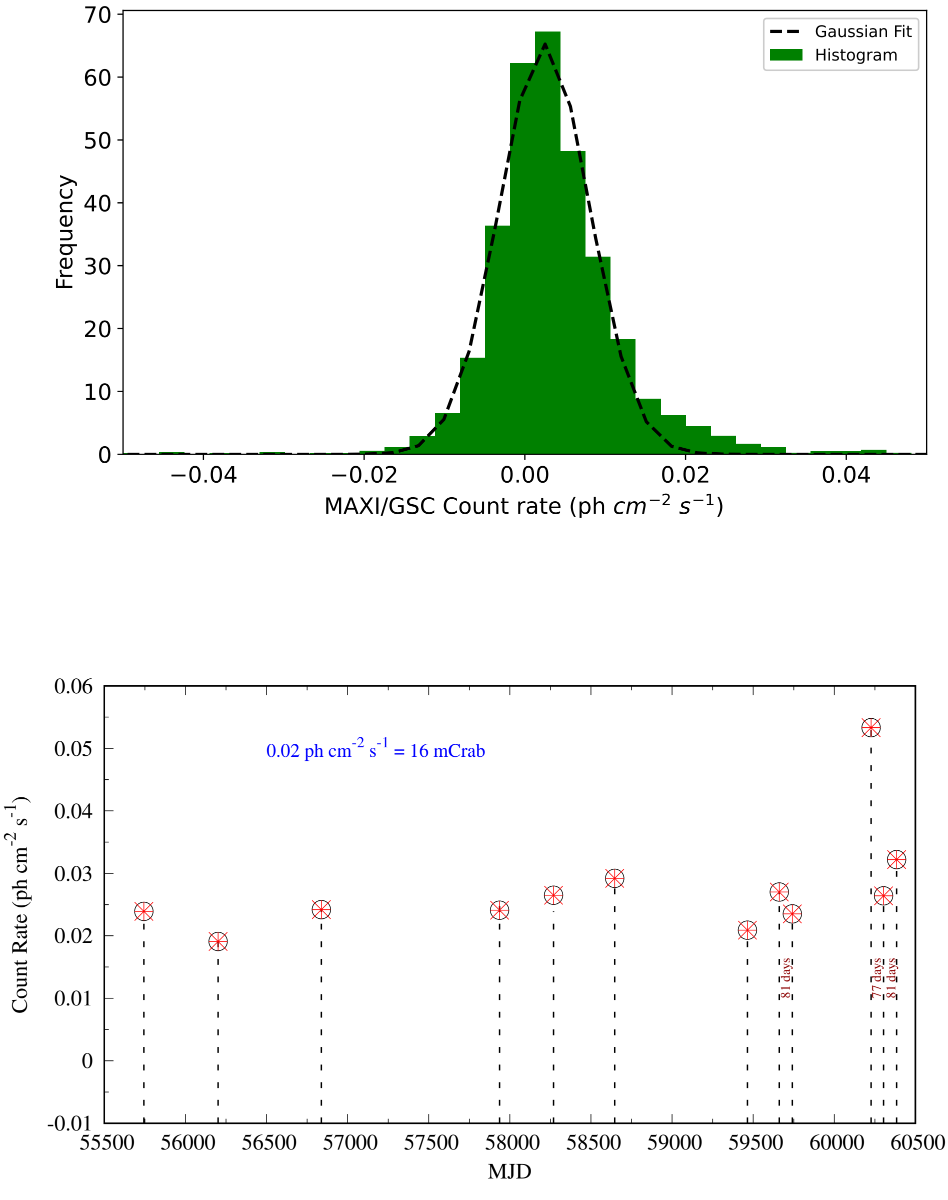

Figure 4.9: Upper Panel: Histogram distribution of MAXI/GSC count rate in 4-10 keV energy band. A Gaussian function is fitted to obtain the mean and standard deviation of the count rate distribution. Bottom panel: Occurrence times of 12 chosen X-ray outbursts and their corresponding peak intensities are shown. The time differences between closer outbursts are also annotated.

Table 4.2: Investigation of observed (source+background) and background count rates in different energy bands for ID 02 and ID 04.

Instrument	40-50 keV	50-60 keV	40-60 keV	60-70 keV	70-79 keV
ID 02					
FPMA observed (10^{-2})	4.04±0.10	2.00±0.07	6.13±0.12	1.56±0.06	1.16±0.06
FPMA bkg (10^{-2})	0.78±0.04	0.76±0.04	1.54±0.06	0.65±0.04	0.55±0.04
FPMB observed (10^{-2})	4.00±0.10	2.25±0.07	6.33±0.12	1.68±0.06	1.04±0.05
FPMB bkg (10^{-2})	0.07±0.04	0.64±0.003	1.33±0.055	0.61±0.04	0.50±0.03
ID 04					
FPMA observed (10^{-3})	2.95±0.27	1.55±0.20	5.24±0.44	1.52±0.20	0.70±0.10
FPMA bkg (10^{-3})	1.67±0.20	1.59±0.19	3.26±0.28	1.57±0.19	1.35±0.18
FPMB observed (10^{-3})	2.97±0.30	1.49±0.20	5.21±0.36	0.74±0.14	0.74±0.20
FPMB bkg (10^{-3})	1.66±0.20	1.66±0.20	3.32±0.28	1.14±0.17	1.51±0.19

4.4 X-ray spectral analysis & results

X-ray spectral analysis of thirteen NICER observations and two NuSTAR observations of IGR J06074+2205, during October and December 2023 outbursts is performed using XSPEC v-12.13.1 (Arnaud, 1996) package. We initiate spectral analysis utilizing thirteen NICER observations in the 1-7 keV energy band. The spectral analysis is restricted to the 1-7 keV energy band as in the case of some of the observations, data beyond 7 keV are background-dominated. Spectra are binned to ensure a minimum of 20 counts per energy bin, facilitating the application of `Chi-Square` statistics in our analysis. For assessing the line-of-sight X-ray absorption, we utilize the `wilm` abundance table (Wilms et al., 2000) alongside `Vern` photo-ionization cross-section. A systematic uncertainty of 1.5 percent is incorporated, as recommended by the instrument team. The spectra are effectively fitted with an absorbed power law (`TBabs*powerlaw`) model.

We observe a minimal variation in the value of equivalent hydrogen column density ($N_{\rm H}$). The variations are within the errors. Therefore, we refit the spectra using an absorbed power law model by fixing the value of $N_{\rm H}$ at 1.187$\times$ 10^{22} cm^{-2} (the average value obtained from our fitting of all the data). The temporal evolution of the best-fitted parameter values is shown in Figure 4.10. The uncertainties on the parameters are calculated within the 90% confidence range. The luminosity for both NICER and NuSTAR observations is computed within the 1-70 keV energy range to maintain coherence and enable a consistent comparison of source properties, considering the source distance of 5.99 kpc (Fortin et al., 2022). The values of the power-law photon index (PI) with and without fixed $N_{\rm H}$ exhibit similar variation. It can be noticed that the average value of PI obtained during the October outburst is relatively higher than the December outburst. The bottom panel of Figure 4.10 illustrates the luminosity variation, suggesting NICER observed the source during the declining phases of both the X-ray outbursts. Furthermore, to examine the relationship between the PI and luminosity, we plot them against each other in Figure 4.11. We observe that the PI values

Table 4.3: Broadband spectral fitting of ID 02 with different continuum models in 3-40 keV (without GABS) and 3-79 keV energy range (with GABS).

Models	Parameters	CUTOFFPL	CUTOFFPL+GABS	HIGHECUT	HIGHECUT+GABS	FDCUT	FDCUT+GABS	NPEX	NPEX+GABS
TBabs	$N_H(10^{22}\ cm^{-2})$	$0.43^{+0.04}$	0.43^{*}	$2.37^{+0.18}_{-0.18}$	$1.4^{+0.2}_{-0.2}$	$1.20^{+0.20}_{-0.20}$	$1.34^{+0.20}_{-0.20}$	$0.43^{+0.03}$	0.43^{*}
Powerlaw	Photon Index (Γ)	$0.11^{+0.05}_{-0.05}$	$0.91^{+0.07}_{-0.07}$	$1.33^{+0.01}_{-0.01}$	$1.24^{+0.02}_{-0.01}$	$1.20^{+0.05}_{-0.05}$	$1.23^{+0.01}_{-0.01}$	$0.06^{+0.04}_{-0.04}$	$0.74^{+0.03}_{-0.03}$
	E_{cut} (keV)	$10.72^{+0.30}_{-0.30}$	$38.1^{+3.6}_{-4.9}$	$18.6^{+0.3}_{-0.3}$	$35.4^{+2.5}_{-1.4}$	$29.10^{+0.50}_{-0.50}$	$71.6^{+4.9.1}_{-7.1}$	$10.3^{+0.2}_{-0.2}$	$21.2^{+0.82}_{-1.1}$
	E_{fold} (keV)	–	–	$19.7^{+0.5}_{-0.5}$	$36.3^{+6.5}_{-6.5}$	$7.90^{+0.30}_{-0.30}$	$12.8^{+6.6}_{-4.5}$	–	–
Blackbody	Temp. (keV)	$1.06^{+0.02}_{-0.02}$	$1.09^{+0.06}_{-0.05}$	–	–	–	–	$1.07^{+0.02}_{-0.02}$	$1.03^{+0.03}_{-0.03}$
	Norm	$8.31^{+0.40}_{-0.40}$	$2.11^{+0.32}_{-0.29}$	–	–	–	–	$8.5^{+0.4}_{-0.4}$	$3.9^{+0.2}_{-0.4}$
Gaussian	E (keV)	$6.31^{+0.06}_{-0.06}$	$6.29^{+0.06}_{-0.06}$	$6.28^{+0.06}_{-0.06}$	$6.28^{+0.07}_{-0.06}$	$6.28^{+0.06}_{-0.06}$	$6.28^{+0.7}_{-0.05}$	$6.29^{+0.06}_{-0.07}$	$6.29^{+0.06}_{-0.06}$
	Eqwidth (eV)	$20.2^{+5.1}_{-5.3}$	18^{+5}_{-4}	17^{+4}_{-4}	16^{+4}_{-4}	16^{+5}_{-4}	16^{+5}_{-4}	17^{+5}_{-4}	19^{+5}_{-4}
GABS	E_{CRSF} (keV)	–	$50.4^{+0.2}_{-0.4}$	–	$48.7^{+1.0}_{-1.2}$	–	$50.8^{+0.4}_{-0.4}$	–	$50.7^{+0.6}_{-0.5}$
	σ_{CRSF} (keV)	–	$13.6^{+1.3}_{-1.3}$	–	$13.9^{+0.6}_{-0.6}$	–	$14.2^{+0.4}_{-0.4}$	–	$12.6^{+0.7}_{-1.1}$
	$Strength_{CRSF}$ (keV)	–	$50.5^{+13.4}_{-7.9}$	–	$58.5^{+4.8}_{-5.2}$	–	$62.9^{+2.3}_{-1.9}$	–	$43.9.0^{+5.6}_{-6.5}$
Luminosity (1-70 keV)	(10^{36} erg s^{-1})	–	5.57	–	5.68	–	5.68	–	5.56
Fit Statistics	χ^2_{red}/d.o.f.	1.13/1652	1.04/1890	1.21/1653	1.03/1890	1.04/1653	1.04/1890	1.14/1652	1.03/1890

(*)= parameter fixed while calculating error
Note= Galactic N_H of source is $\approx 0.43\times10^{22}$ cm^{-2}

fluctuated between 1 and 2 without exhibiting any particular pattern except for data points between 1-2$\times10^{35}$ erg s^{-1}, where a sudden decrease in PI value is observed. It is challenging to draw conclusions from this due to large error bars.

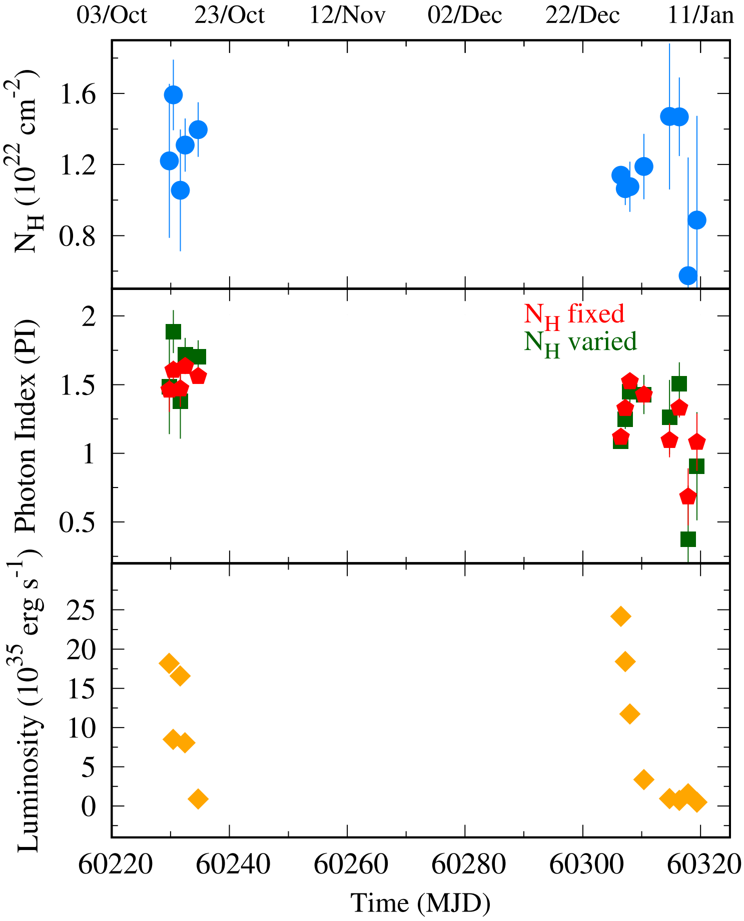

Figure 4.10: Temporal evolution of best-fitted spectral parameters N_H (top panel), photon index (middle panel), luminosity (bottom panel) obtained from the spectral fitting of the NICER observations.

Subsequently, we conducted a broadband spectral analysis of two NuSTAR observations to investigate the hard X-ray emission properties and the presence of cyclotron resonance scattering feature (CRSF) in the pulsar spectrum. In the first step, we compared the observed (source+background) and background spectra for both observations. For ID 02, It is noticed that the background and the observed spectra are comparable beyond ≈70 keV and ≈40 keV for observations ID 02 and ID 04, respectively (Figure 4.12). We confirmed this by examining the net observed (source+background) and background count rates in different energy bands (Table 4.2). For ID 02, the observed count rate remained above the 3σ background variation up to 79 keV, whereas for ID 04, this is possible below 50 keV. Therefore, spectral analysis is performed in the 3-79 keV and 3-50 keV bands for IDs 02 and 04, respectively.

Initially, fitting the 3-79 keV spectrum of ID 02 with an absorbed power-law model revealed positive residuals near 6.4 keV and negative residuals near 50 keV. Positive residuals near 6.4 keV are modeled with a Gaussian component. Then, we use the Gaussian absorption line (`GABS`) model to account for the residuals near 50 keV. The inclusion of these components fits the spectra well and improves the χ^2 value significantly. The Gaussian absorption component near 50 keV is interpreted as the CRSF, consistent with findings of Roy et al.

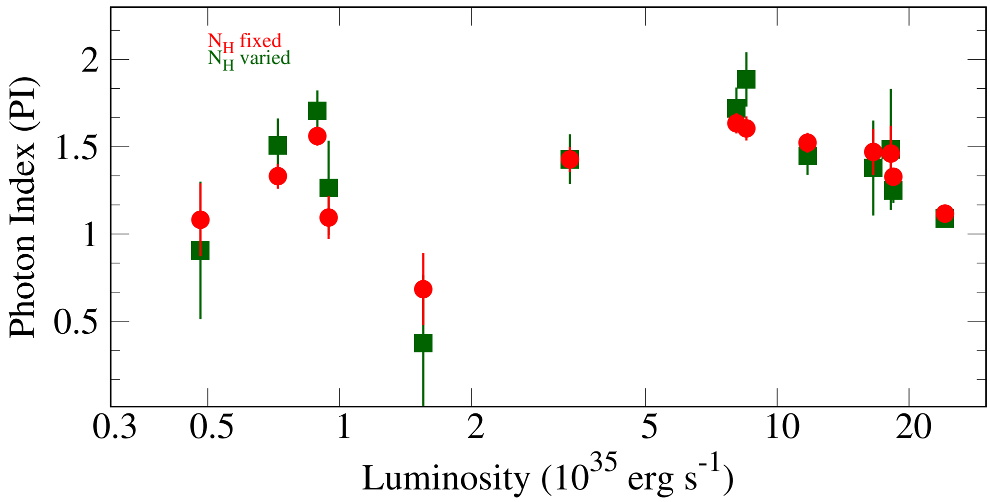

Figure 4.11: Correlation between the photon index (PI) and luminosity derived from the spectral fitting of NICER observations.

(2024) and Tobrej et al. (2024). We confirmed the presence of this absorption feature in the spectra using various continuum models, such as `CUTOFFPL`, `HIGHECUT`, `FDCUT`, and `NPEX`, all yielding comparable reduced χ^2 values. The spectral fitting results are detailed in Table 4.3. The top panel of Figure 4.13 shows the source spectra and the best-fit model consisting of the NPEX continuum model (Makishima et al., 1999), the Galactic absorption component, a blackbody, a Gaussian function for the 6.4 keV Fe emission line, and a Gaussian absorption component (GABS) for the CRSF. The middle and bottom panels of the figure show the residuals obtained after fitting the spectra with the above model without and with the GABS component. From Table 4.3, we observe that the absorption line parameters change depending on the choice of the continuum model. We also fitted the NuSTAR spectrum in 3-40 keV and 3-79 keV ranges to examine the effect of GABS on the continuum parameters (Table 4.3). We found that the cutoff energy changed significantly when the GABS component was added to the model fitted in the 3-79 keV range.

For ID 04, spectral fitting is limited to the 3-50 keV range as the data beyond 50 keV is background-dominated (Figure 4.12). The 3-50 keV range spectrum is fitted well with the `NPEX` continuum model. We also carried out simultaneous NICER and NuSTAR spectral fitting using `NPEX` model in 1-50 keV band. The best-fitted spectral parameters are presented in Table 4.4. The best-fit model and corresponding residuals are shown in Figure 4.14.

For ID 04, Roy et al. (2024) conducted spectral fitting in the 3-78 keV energy range and reported a 10 keV absorption-like feature, although they noted poor statistical significance beyond 40 keV. In contrast, Tobrej et al. (2024) focused on the 3-50 keV energy range due to background dominance beyond 50 keV and found evidence for a blackbody component with kT ≈1 keV. We also tested various empirical models, and our analysis indicates that the detection of these features is highly dependent on the chosen continuum model, with the NPEX model offering the best fit in the 1-50 keV range.

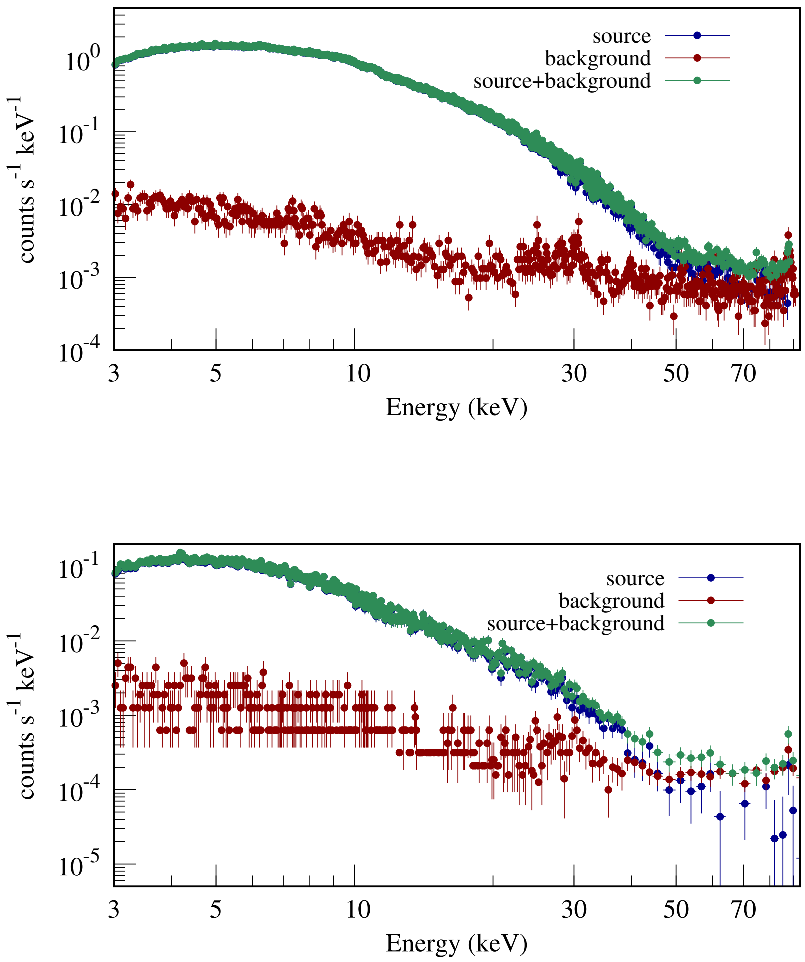

Figure 4.12: The top and bottom panels show a comparison of source (blue), background (brown), and source+background (green) count rates for NuSTAR ID 02 and ID 04, respectively.

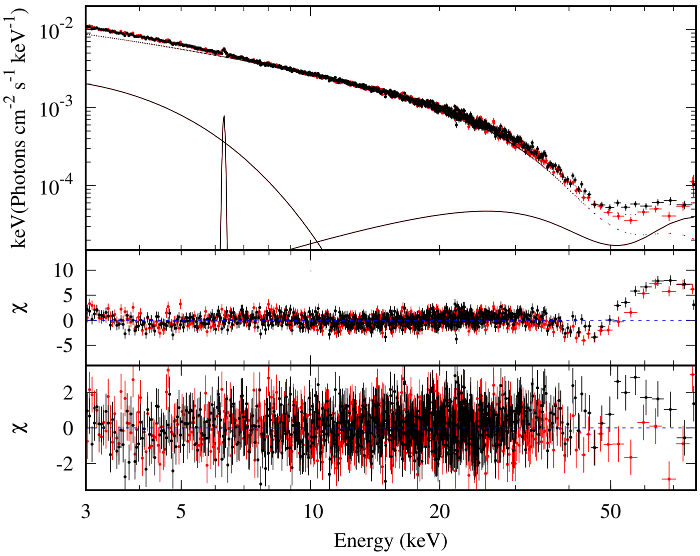

Figure 4.13: The source spectra and the best-fit model comprising an NPEX continuum model with a blackbody component, an iron emission line, and a Gaussian absorption component for CRSF are shown in the top panel. The middle and bottom panels show the residuals after applying the spectral model without and with the CRSF component, respectively.

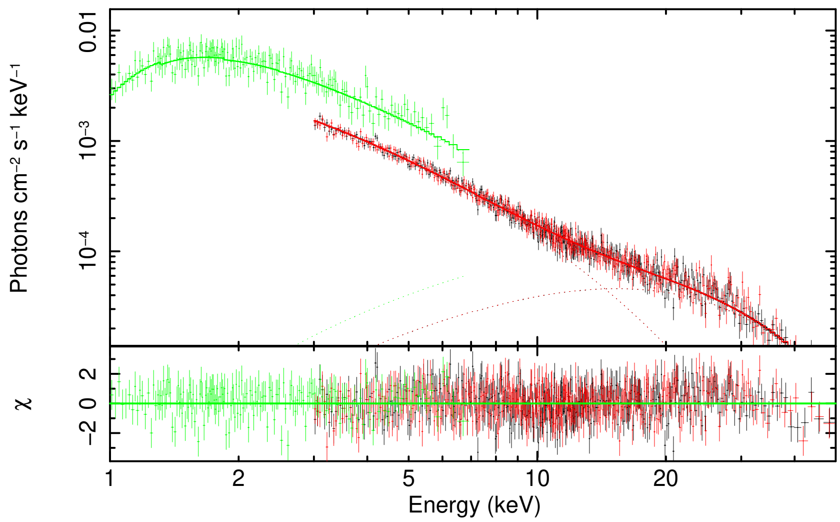

Figure 4.14: The top panel displays the spectra of IGR J06074+2205 in the 1–50 keV energy range from NuSTAR and NICER observations on MJD 60232 and NPEX continuum model spectra. The bottom panel presents the residuals after applying the best-fit model to the source spectra.

Table 4.4: Best-fit parameters obtained from the simultaneous spectral fitting of NuSTAR and NICER observations of IGR J06074+2205 on MJD 60232, using NPEX as the continuum model. A source distance of 5.99 kpc was used for luminosity calculations.

MJD		60232
Model	Parameters	NICER+NuSTAR
Energy Range		1-50 keV
TBabs	$N_H (10^{22}\ cm^{-2})$	$1.25^{+0.09}_{-0.08}$
NPEX	Photon Index (Γ)	$1.36^{+0.03}_{-0.03}$
	E_{cut} (keV)	$7.64^{+0.30}_{-0.30}$
Luminosity (1-70 keV)	$(10^{36}\ erg\ s^{-1})$	0.47
Fit Statistics	χ^2_{red}/d.o.f.	1.03/933

4.5 Optical Spectroscopy & Results

We carry out optical spectroscopic analysis using five epochs of observations taken between 2022 & 2024 with MFOSC-P/MIRO & HFOSC/IAO at wavelength ranges of 6000-7000 Å and 5500-8350 Å, respectively. The spectra from these observations are presented in Figure 4.15. The figure shows the continuum normalized spectrum for each observation epoch with certain offsets for clarity. The bottom two and top three spectra are obtained using MFOSC-P and HFOSC instruments, respectively. The date of each observation is also annotated in the figure.

In the optical spectra, we observe the presence of both emission and absorption lines. The prominent absorption lines are Diffuse Interstellar Band (DIB) and atmospheric telluric features. The DIBs are absorption features that arise when photons travel through significant column densities in the interstellar medium. We detect a DIB clearly at 6283.86 Å (Herbig, 1995). We also observe a blended interstellar sodium doublet D1 and D2 in our spectra in absorption form (KreŁowski & Schmidt, 1997). The telluric features arise because of the absorption of photons by the molecules in the Earth's atmosphere. These telluric features superimpose on the stellar spectra. Two most prominent telluric features such as O_2 B-band at $\lambda \approx 6870$ Å and O_2 A-band at $\lambda \approx 7605$ Å (Angeloni et al. 2019 & reference therein) are present in our spectra. A strong Hα (6562.8 Å) emission line is detected in the MFOSC-P and HFOSC spectra of IGR J06070+2205 (Figure 4.15). We also detect another emission line at 5577.91 Å in the HFOSC spectra due to its wider wavelength coverage towards the bluer side. In addition to that, we observe a weak signature of HeI (5875.72 Å), HeI (6678 Å), and HeI (7065 Å) emission lines in the spectra taken from HFOSC on 15 December 2023 and 03 February 2024.

To examine the structure and characteristics of the Hα line profile, we focused on plotting only the portion of the optical spectra that covers the Hα emission line region. The evolution of the Hα (6562.8 Å) emission line profile during all our optical observations is shown in the left part of Figure 4.16. We calculate the equivalent width (EW) of the Hα emission lines in the spectra from all epochs of our observations. The EW signifies the strength of the emission/absorption lines. It is a measure of the area of emission or absorption line in a wavelength vs intensity plot and is calculated by the following method:

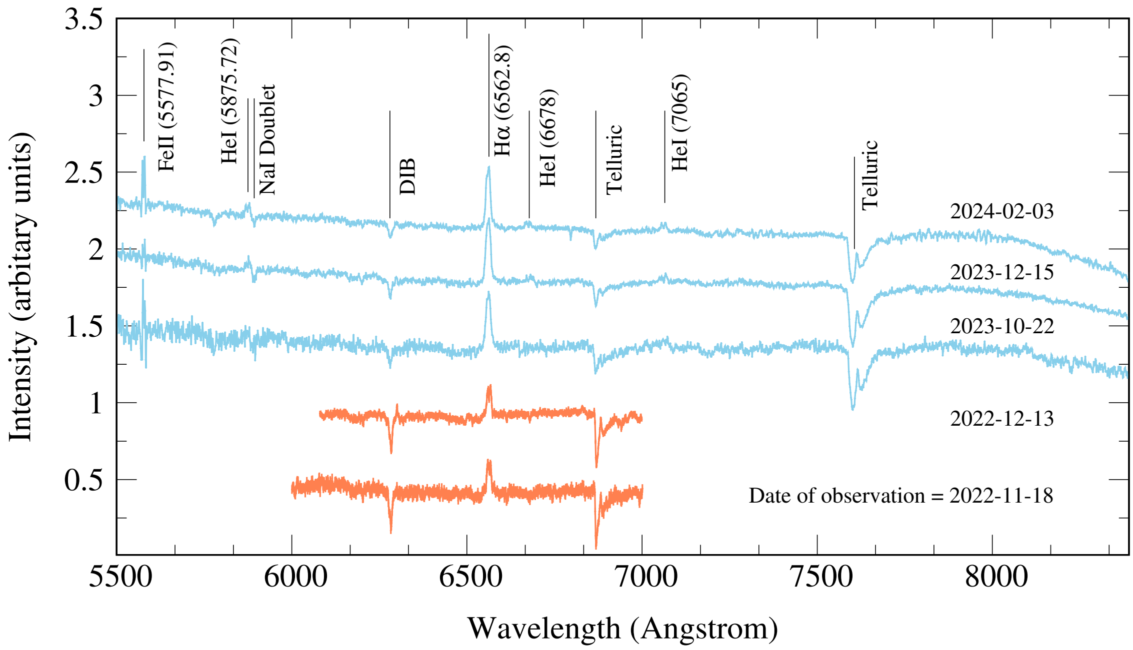

Figure 4.15: Evolution of the optical spectrum of Be/X-ray binary IGR J06074+2205 as seen with the MFOSC-P (orange) & HFOSC (blue) instruments. The observation dates are annotated on each spectrum. The spectra are plotted with certain offsets for clarity.

$$EW = \sum(1 - \frac{F(\lambda)}{F_c(\lambda)})\delta\lambda$$

where, F(λ) represents the total flux consisting of contributions from the line and the continuum of the source spectrum, and $F_c(\lambda)$ represents only the underlying continuum flux at wavelength λ. The obtained EW are presented in Table 4.5. The error in the value of EW is calculated by the propagating error in the $F_c(\lambda)$.

As shown in Figure 4.16, the Hα line evolves from a double-peaked profile, with both peaks having similar intensities to a single peak dominated shape throughout our observations. The double-peaked Hα line on 11 November 2022 has a relatively stronger blue-shifted peak than the red-shifted peak. However, the line profile on 13 December 2022 is the opposite, with a stronger red-shifted peak. After about one year, the Hα line profile is dominated by the red-shifted peak. We fit all the Hα emission lines with Voigt profiles to derive essential quantities like V/R and peak difference ($\Delta\lambda$ or ΔV) between the red and blue-shifted peaks. The V/R value gives an idea of the contribution of the blue-shifted peak with respect to the red-shifted peak and vice versa. The peak difference information helps us to calculate the Hα emitting region or the size of the circumstellar disc around the Be star. Initially, we try to fit the emission line profiles with Gaussian functions. However, the Gaussian functions do not fit well in the wing regions. The original and fitted line profiles are shown in black and green colors, respectively, in the left part of Figure 4.16. The red and blue components of the lines are shown with red and blue colors, respectively, in the figure.

Huang (1972) demonstrates that the size of the Hα line emitting region of the circumstellar disc can be estimated by using the peak separation (ΔV) of the double-peaked Hα emission line, assuming Keplerian velocity distribution of matter in the disc. The velocity

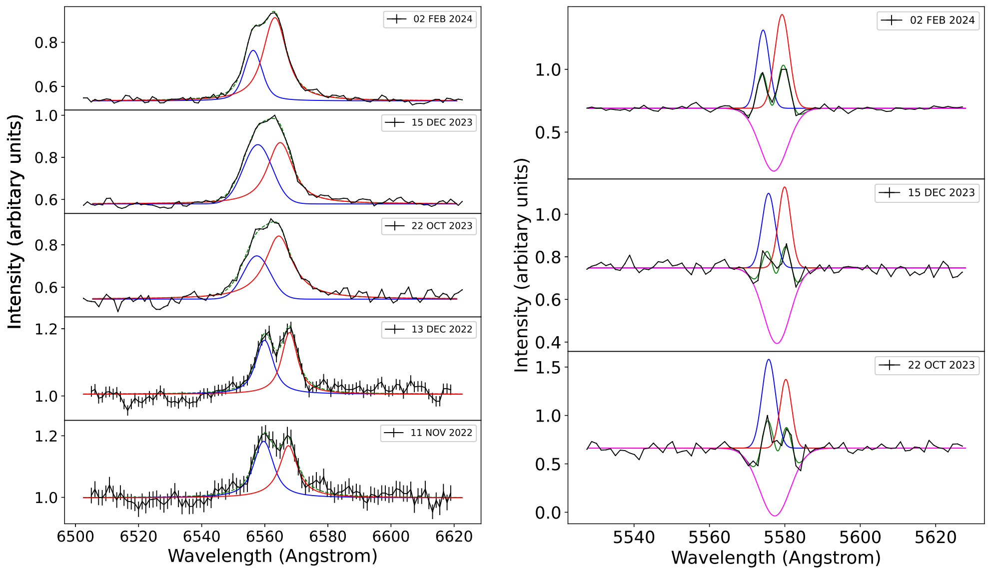

Figure 4.16: Left: The observed Hα line profiles (solid black lines) of IGR J0674+2205 during our observations and corresponding best-fitted Voigt functions (dashed green lines). Right: Observed FeII line profiles (solid black line) of IGR J0674+2205 and corresponding best-fitted Gaussian functions (dashed green line). The observation dates are quoted on the right of the corresponding profiles. The red and blue color profiles correspond to the red and blue shifted components of emission lines, respectively.

separation between the red and blue-shifted components of the emission lines can be used to calculate the radius of the emitting region (Huang, 1972). The relationship between the peak separation and the rotational velocity of the gas particles at the emitting region is given by $\Delta V = 2V_{rot}\sin i$. Following this, the size of the Hα emitting region can be derived by :

$$R_d = (2V\sin i/\Delta V)^j \epsilon R_* \tag{4.3}$$

where, j=2 for Keplerian rotation, R_* is the Be star radius, and ϵ is a dimensionless parameter that considers several effects that would over-estimate the disc radius (ϵ=0.9$\pm$0.1; Zamanov et al. 2013). The value of $V sini$ used in the calculation is 260 km s^{-1} (Reig et al., 2010). We also calculate the full width at half maximum ($FWHM$), which is the width of the line at half of the peak flux levels of the emission or absorption line. The $FWHM$ can be expressed in the velocity unit to estimate the radial velocity of the Hα emitting particles in the disc with respect to the observer. In this work, the $FWHM$ is calculated by fitting a single Gaussian function over the entire Hα emission line using a Python routine that fits the overall line shape well. The values of the calculated parameters are given in Table 4.5. The values of ΔV and FWHM are found to vary within errors between November 2022 & February 2024 and remain at around 343 km s^{-1} and 700 km s^{-1}, respectively. From Table 4.5, it can be noticed that the value of the EW increased with time from $\approx$2.5 to 11 Å. The disc radius varies within errors and remains at around 2R_*. The errors in the values of ΔV and disc radius are found to be large for observations on 22 October 2023 and 15 December 2023 because of the propagation of larger error by ΔV during the disc radius

Table 4.5: The table presents the values of parameters such as equivalent width (EW), V/R ratio, ΔV, $FWHM$, and disc radius derived from the Hα (6562.8 Å) and FeII (5577.91 Å) emission lines at various epochs.

	Hα (6562.8 Å)					FeII (5577.91 Å)				
Date of observation	EW (Å)	V/R	ΔV (km/s)	$FWHM$ (km/s)	Disc Radius (R_*)	EW (Å)	V/R	ΔV (km/s)	$FWHM$ (km/s)	Disc Radius (R_*)
2022 Nov 18	-2.51±0.20	1.08±0.33	358±24	735±40	1.89±0.25	-	-	-	-	-
2022 Dec 13	-1.56±0.18	0.92±0.27	362±19	686±44	1.85±0.20	-	-	-	-	-
2023 Oct 22	-9.83±0.87	0.47±0.27	332±96	729±23	2.22±1.29	1.03±0.98	1.53±0.48	244±21	374±138	-
2023 Dec 15	-10.33±0.38	0.81±0.21	336±50	700±13	2.15±0.63	-2.86±0.44	0.98±0.50	229±43	314±159	4.64±1.75
2024 Feb 03	-11.21±0.52	0.41±0.06	326±16	648±14	2.28±0.22	-4.42±0.40	0.71±0.23	270±39	433±58	3.33±0.95

error calculation.

We also detected another emission line at 5577.91 Å and identified the line as FeII emission line by looking at NIST Atomic Spectra Database[4]. Other atomic lines close to this wavelength are also present. However, we consider this FeII line as the FeII lines are usually observed in the spectrum of Be stars (Arias et al. 2006 & references therein). In our observations, the FeII line is detected only in the HFOSC spectra and exhibits dynamic behavior over time (Figure 4.16). The FeII line obtained on 10 October 2023 and 15 December 2023 shows a weak emission shape along with significant dips towards the wings. These profiles can be termed as emission above absorption type double-peaked profiles. The FeII emission lines are double-peaked in shape and evolve from a slightly blue-shift-dominated profile to a red-shift-dominated profile between 10 October 2023 and 15 December 2023. The FeII line observed on 3 February 2024 exhibits a red-shift-dominated shape. We calculate the V/R value and peak velocity separation (ΔV) for the FeII emission line. At first, we fit the two Gaussian models for the red- and blue-shifted peaks. However, the FeII lines observed on 10 October 2023 and 15 December 2023 are not fitted well because of the strong absorption dips close to the wings due to the photospheric absorption of the central star. Then, we add two Gaussians for the blue and red-shifted emission components above another Gaussian absorption component. The addition of the Gaussian absorption component fits the line profile reasonably well (Figure 4.16). The disc parameters derived using best-fitted spectral parameters are shown in Table 4.5. It can be seen that the EW increases from ≈1 Å to ≈4.5 Å with time, and the ΔV and FWHM, on average, remain around 250 & 380 km s^{-1}, respectively. The radius of the FeII emitting region remains at around $4R_*$.

4.6 Discussion

We carried out X-ray and optical studies of the Be/X-ray binary system IGR J06074+2205. X-ray studies are performed during the October 2023 outburst using two NuSTAR observations and thirteen NICER observations during the October and December 2023 X-ray outbursts. Optical spectroscopy was carried out using five epochs of observations from MIRO and IAO between 2022 and 2024, covering the phases of before, during, and after 2023 X-ray outbursts. These combined efforts aim to provide an understanding of the accretion emission

[4] `https://physics.nist.gov/PhysRefData/ASD/lines_form.html`

from the neutron star and the evolution of Be decretion disc in the system.

Accretion-powered X-ray pulsars possess a strong magnetic field that directs the infalling matter toward the polar regions of the neutron star. Due to the intense gravitational field near the neutron star, the accreting material gains substantial kinetic energy, which is then converted to X-rays near the magnetic poles (Basko & Sunyaev, 1976). If the rotation and magnetic axes of the neutron star are not co-aligned, we get X-ray emission when the magnetic poles cross our line of sight, giving rise to pulsation phenomena. We detected periodic signals of ≈374.6 s in NuSTAR and three NICER light curves, as detailed in Section 4.3. Additionally, we explored pulsation information from the Fermi/GBM database, the results of which are depicted in Figure 4.3. The bottom panel of Figure 4.3 shows a decreasing trend in the pulsar spin frequency during the October and December 2023 X-ray outbursts. A decrease in spin frequency or increase in spin period during X-ray outbursts is usually not observed in accretion-powered X-ray pulsars. Additionally, we calculated the rate of change of the spin period during October and December X-ray outbursts using the spin period values obtained from NuSTAR, NICER, and Fermi/GBM data. We found that the spin period is increased at the rate of 0.024 ± 0.001 and 0.02 ± 0.01 s day^{-1} during October and December 2023 X-ray outbursts, respectively. This increase in the spin period may be attributed to the binary motion of the neutron star. However, confirmation of this is hindered by insufficient detailed information regarding the orbital parameters of the binary system.

The lowest luminosity at which pulsations are detected in the light curve is estimated to be $\approx7.3\times10^{34}$ erg s^{-1} (in 1-70 keV range, assuming a distance of 5.99 kpc). This finding is close to the luminosity value of 1.8×10^{34} erg s^{-1} obtained from the spectral fitting in the 0.4-12 keV energy range for a distance of 4.5 kpc using 2017 XMM-Newton observation (Reig & Zezas, 2018). This result signifies that the source has not reached the propeller regime (Illarionov & Sunyaev, 1975) at luminosity close to $\approx7.3\times10^{34}$ erg s^{-1}. Detection of pulsation at lower luminosity could be attributed to the long spin period of the neutron star (≈374 s). Using the values of magnetic field and spin period at a lower luminosity of the pulsar as 5.69×10^{12} G and 374.57 s, the limiting luminosity for the onset of the propeller regime (Campana et al., 2002) is estimated to be 1.3×10^{33} erg s^{-1}. Previously it has been reported that sources with longer spin periods (≥100 s) exhibit pulsations at lower luminosities (10^{32-33} erg s^{-1}) because of their relatively higher co-rotation radius, although exceptions exist, such as GX 1+4 and OAO 1653-40 (White et al. 1983; Stella et al. 1986 and references therein).

Subsequently, we examined the pulse profiles of IGR J06074+2205 obtained from NICER and NuSTAR observations to assess the modulation of X-ray photons due to the rotation of the neutron star. Pulse profiles contain information on the geometry of the X-ray emitting region and its surroundings. We analyze pulse profiles at different luminosities and energy ranges. The pulse profiles are found to be strongly dependent on luminosity and energy (Figure 4.4, 4.5, & 4.6). The pulse profiles obtained at higher luminosity exhibit smoother shapes compared to those obtained at lower luminosity, which possess a complex structure in the soft X-ray regime. For a clear understanding of the above fact, we chose an energy band that is common to both NICER and NuSTAR and has sufficient SNR. The luminosity evolution of the pulse profiles obtained in the 3-7 keV energy band are shown in Figure 4.17. At lower luminosities, the pulse profiles are single-peak dominated and harbor deeper absorption features. However, as the luminosity increases, the pulse profiles evolve to a smoother double-peaked profile. We investigate the energy dependency of the pulse profiles in detail using NuSTAR data. The pulse profile from the NuSTAR observation at a luminosity of approximately 5.56×10^{36} erg s^{-1} showed an asymmetric, smooth double-peaked structure in the 3-79 keV range, with the basic shape remaining consistent across various energy bands (Figure 4.6). As the energy increased from 3 to 40 keV, the peak in the 0.0-0.5 phase dimmed, while the peak in the 0.5-1.0 phase brightened. However, beyond 40 keV, the difference in the intensity of the two peaks started diminishing. The pulse profile acquired at a luminosity of 4.66×10^{35} erg s^{-1} also exhibited a double-peaked morphology, though accompanied by a complex second peak (Figure 4.6). For the lower luminosity case (red color profiles), a broad absorption dip is found in the second peak of the pulse profile below 20 keV. The depth of the dip is more pronounced in the 3-7 keV band and decreases with an increase in energy. Dips in the pulse profiles could be due to the absorption of low energy photons by accreting material locked in the magnetosphere asymmetrically (White et al., 1983). Dips in pulse profile due to absorption of radiation from the pulsar by matter stream in a specific phase of the magnetosphere is also observed in various other Be/X-ray binary pulsars such as V0332+53, 1A 0535+262, EXO 2030+375, GX 304-1, and RX J0209.6-7427 (Tsygankov et al., 2006; Naik et al., 2008, 2013; Naik & Jaisawal, 2015; Epili et al., 2017b; Jaisawal et al., 2016; Vasilopoulos et al., 2020; Chhotaray et al., 2024).

The pulse profiles obtained from the NICER observations also exhibit distinct energy dependencies at different luminosity levels. The shape of the pulse profiles obtained at lower luminosity shows minimal variation with energy (see Figure 4.4). Conversely, at a luminosity of 2.42×10^{36} erg s^{-1}, the pulse profiles are unique and show contrasting behavior relative to the lower luminosity case. The shape of the pulse profiles appears relatively smoother compared to the previously mentioned profiles, exhibiting a double-peaked morphology (Figure 4.5). Notably, the pulse profile shows significant energy dependency. In the 0.5-1 keV band, the pulse profile consists of a single peak between 0.0-0.5 phase range (primary peak). As the energy increases, another peak arises in the 0.5-1 phase range (secondary peak). It is important to notice that the strength of the secondary peak keeps increasing with energy and eventually overtakes the primary peak at higher energy. The width of the secondary peak also keeps increasing and becomes comparable to the primary peak at higher energy. This type of energy dependency of pulse profiles is also reported by Nakajima et al. (2024). The evolution of pulse profiles in such a manner is observed in sources like GX 301-2 (Kreykenbohm et al. 2004) and Vela X-1 (Kreykenbohm et al. 2002). However, this behavior of pulse profile is in contrast to many other accreting X-ray pulsars like GRO J1008-57 (Naik et al., 2011), 4U 0115+63 (Tsygankov et al., 2007), 4U 1909+07 (Jaisawal et al., 2020c), 4U 1901+03 (Rai & Paul, 2021), 1A 0535+262 (Chhotaray et al., 2023), and 2S 1417-624 (Gupta et al., 2018), where the secondary peak intensity decreases as the energy increases. By looking at the evolution of the pulse profile with energy, it can be inferred that the soft X-ray photons dominate the primary peak, whereas the secondary peak is due to the hard X-ray photons. The double-peaked profile might not be due to fan-beam emission as the

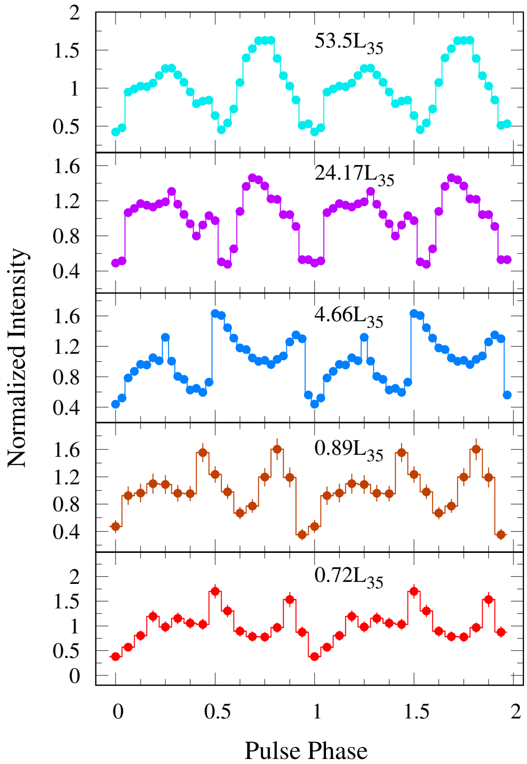

Figure 4.17: Evolution of the pulse profile of IGR J06074+2205 in the 3-7 keV energy range as a function of luminosity.

source was emitting at a luminosity one order below the critical luminosity. This could be due to the contribution from two magnetic poles where soft X-ray absorbing materials have a contrasting distribution.

We determine the possible orbital period of the source using the arguments detailed in Section 4.3.1. The minimum difference between consecutive outbursts (Figure 4.9) is nearly 80 days. We calculated the difference (in days) between all consecutive outbursts and found that the differences are close to the multiples of 80 and 80/n (n=2,3,4) days. Hence, we infer that the possible orbital period of the binary is about 80 or 80/n (n=2,3,4) days. Similar results were also reported by Mihara et al. (2023) using data from four outbursts in 4-10 keV MAXI/GSC light curve. Considering the constraint on data quality and its availability at the current stage, this is the optimum we can infer on the orbital period of the binary. To contextualize this value within the Corbet diagram, we incorporated the spin and orbital period values into the plot assembled by Cheng et al. (2014), utilizing data from Townsend et al. 2011 (see Figure 4.18).

We carried out spectral analysis during the October and December X-ray outbursts of the pulsar using NuSTAR and NICER observations. During the NICER observations, the source luminosity varied between $\approx 5\times10^{34}$-2.5×10^{36} erg s^{-1} (for a distance of 5.99 kpc), with the spectra fitting well with an absorbed power-law model in 1-7 keV energy band. The temporal variation of the spectral parameters is illustrated in Figure 4.10. The luminosity variation of the source over time indicates that NICER observed the source during the declining phases of both the outbursts. The photon index values varied between 1 and 2 without showing any particular trend.

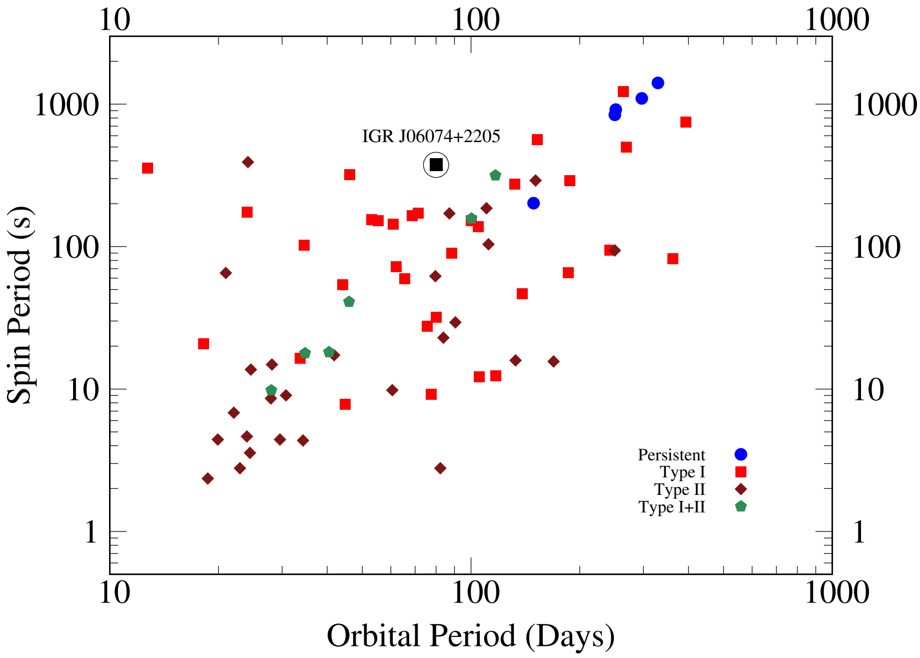

Figure 4.18: Diagram illustrating orbital and spin periods of various BeXRBs (Cheng et al. 2014 and references therein). Different colors are employed to represent the outburst behavior observed from each source. The point representing the orbital period (80 days) and spin period (374.6 s) of IGR J06074+2205 is shown in black color.

Accretion-powered X-ray pulsars possess a magnetic field of the order of 10^{12} G. Hence, the CRSFs are expected to be detected in hard X-ray (10–100 keV) ranges (Becker et al., 2012; Staubert et al., 2019). To investigate the presence of CRSF in IGR J06074+2205, we carried out broadband spectral analysis using NuSTAR observations. All the continuum models describe the broadband spectra well, and the properties of the Gaussian absorption component in the spectrum representing the CRSF depend on the chosen continuum model. We choose the NPEX model as the best-fit model because the value of photon index (PI) and cutoff energy (E_{cut}) are constrained between 0.5–1.5 keV and 10–30 keV, respectively, after adding the Gaussian absorption component, which is typical for accreting pulsars (White et al., 1983). Considering the absorption component as the CRSF, the centroid energy of CRSF is found to be ≈50.7 keV. We estimated the magnetic field of the neutron star using the relation

$$E_{CRSF} = 11.57 \times B_{12}(1+z)^{-1} \tag{4.4}$$

where, E_{CRSF} is the cyclotron line energy in keV, B_{12} is the magnetic field in units of 10^{12} G, and z is the gravitational red-shift (z ≃ 0.3 for typical neutron star). The calculated magnetic field of the pulsar is 5.69×10^{12} G. Using this magnetic field, we attempted to estimate the critical luminosity of the pulsar. According to Becker et al. (2012), the critical luminosity depends on the magnetic field, and assuming disc accretion onto a classical neutron star, the expression for the critical luminosity can be expressed as

$$L_{crit} = 1.49 \times 10^{37} (\frac{B}{10^{12} G})^{16/15} \; erg \; s^{-1} \tag{4.5}$$

Using Equation 4.5 and considering a neutron star of mass 1.4 $M_{\odot}$, radius 10 km, and magnetic field 5.69×10^{12} G, the value of L_{crit} can be estimated to be $\approx 9.52\times10^{37}$ erg s^{-1}.

This signifies that the neutron star is accreting matter in the sub-critical regime.

To probe the dynamics of the circumstellar disc around the companion Be star in the binary system, we analyzed the optical spectra of IGR J06074+2205. We observed the Hα line in emission, indicating the presence of circumstellar disc around the Be star (Coe et al., 2006; Reig et al., 2010; Chhotaray et al., 2023; Naik et al., 2024). The equivalent width (EW) of the Hα line and the disc radius are found to increase over time (Table 4.5). This signifies that a larger or denser disc is forming around the Be star with time. The Hα line evolved from a double-peaked structure to a single-peak dominated structure between 18 November 2022 and 3 February 2024 (Figure 4.16). The change in the V/R value from 1.08 to 0.41 indicates the change in the structure of the line profile from blue-peak dominated to red-peak dominated shape. The FWHM of the Hα line varies within uncertainties throughout the observation duration and remains around $\approx$700 km s^{-1}.

We also observed a FeII line in emission at a wavelength of 5577.91 Å. This is one of the rarest FeII emission lines observed at this wavelength in Be stars (Slettebak et al., 1992; Mathew & Subramaniam, 2011; Saad et al., 2006). The ionization potential of a neutral Fe atom is 7.8 eV, whereas for FeII ions, it is 16.2 eV. This indicates that FeII lines originate in regions close to the central star. Interestingly, Reig et al. (2010) observed IGR J06074+2205 between 2006 and 2010 and did not observe any signature of the FeII line. This indicates the transient nature of the FeII line. The FeII line remained double-peaked throughout our monitoring period. The FeII emission lines observed on 22 October and 15 December 2023 exhibit emission in absorption (emission lines with underlying photospheric absorption; Hou et al. 2016; Banerjee et al. 2022) type profile. After 1.5 months, it evolved to a double-peaked emission type profile (Figure 4.16). The double-peaked nature of FeII line also indicates its origin from the innermost region. The peak velocity difference between red-shifted and blue-shifted lines for FeII line varies within error bars throughout the observation duration and remains at around $\approx$380 km s^{-1}. The V/R value changes from 1.53 to 0.71, suggesting changes in the profile structure from blue peak dominated to red peak dominated shape as in the case for the Hα line. The size of the FeII emitting region is estimated to be around 4 R_*.

One interesting result we observed is the distinction in V/R variability of Hα and FeII lines. The V/R variability suggests rotation of a one-armed perturbation (a zone in the disc with higher density than the rest of the disc) in the circumstellar disc (Okazaki, 1997; Papaloizou et al., 1992). $V/R > 1$ means the perturbed region is approaching the observer, and $V/R < 1$ means the perturbed region is receding from the observer. We observed that the V/R values for Hα and FeII lines changed from greater than one to less than one on 13 December 2022 and 15 December 2023, respectively. The delay of about one year for two different emission lines indicates that the perturbed region is not symmetrically distributed in the radial direction. Different V/R variabilities for various emission lines are also observed in 1A 0535+262 (Moritani et al., 2013). The average ΔV obtained for Hα and FeII lines are $\approx$340 km s^{-1} and $\approx$250 km s^{-1}, respectively. The average FWHM obtained for Hα and FeII lines are $\approx$700 km s^{-1} and $\approx$370 km s^{-1}, respectively. These results suggest that the particles emitting Hα photons present in the higher velocity (disc region closer to central star) region (Slettebak et al., 1992) compared to the FeII line emitting particles. The appearance of other emission lines like HeI (5875.72 Å), HeI (6678 Å), and HeI (7065 Å) on the latter phases of our observation hinted towards the growing of larger or denser circumstellar disc around the Be star of the IGR J06074+2205 binary.

Nesci et al. (2024) studied the long-term variability of IGR J06074+2205 using various photometric filters covering the 4100-8100 Å range. They identified long-term optical variability with a period of approximately 620 days, which they attributed to either the precession of the circumstellar disc or the propagation of a density wave within the disc. While comparing the timelines (see Figure 1 of Nesci et al. 2024), we found that our first two optical observations were carried out during the declining phase of the V-band magnitude, while the subsequent three observations were made during the rising phase. Despite the V-band flux decreasing during the last three observations, the equivalent width (EW) of the Hα line continued to increase over time. This behavior is consistent with findings by Nesci et al. (2024), who observed that optical variability and EW variability operate on different timescales. Furthermore, Reig et al. (2010) reported that the Hα line in IGR J06074+2205 exhibited a transition from emission to absorption, and during that period, no major X-ray outbursts occurred. This phenomenon could be explained by the precession of the circumstellar disc, as suggested by Nesci et al. (2024).

Furthermore, Figure 4.15 & 4.16 exhibit dynamics of the circumstellar disc around the Be star between November 2022 and February 2024. During the later part of our observation, we get the signatures of many emission lines in the optical spectra, although most of the lines are weak. However, if we look at the evolution of two strong emission lines, Hα and FeII, we can notice that their EW increases with time. These facts highlight an essential point that the X-ray outburst that occurred during October and December 2023 (Mihara et al. 2023, Nakajima et al. 2023, also see Figure 4.1) did not have any significant effect on the line emitting region of the circumstellar disc of the Be star as the disc is continuously becoming larger or denser. This behavior of the circumstellar disc is in contrast with that during the giant or Type II X-ray outburst phase where a significant change in Hα line EW and other properties are observed after the giant X-ray outbursts (e.g., 4U 0115+63; Reig et al. 2007, 1A 0535+262; Chhotaray et al. 2023). The increase in the EW of the Hα line suggests that the Be circumstellar disc is evolving continuously, which may lead to a giant outburst in the future in IGR J06074+2205.

4.7 Conclusion

In this chapter, we carried out X-ray studies of the Be/X-ray binary IGR J06074+2205 during X-ray outbursts in October and December 2023 using NuSTAR and NICER observations of the pulsar. NuSTAR observed the source twice during the October 2023 outburst, while NICER provided coverage across various epochs during both outbursts. We observed coherent X-ray pulsations from the neutron star at ≈374.60 seconds. The pulse profiles of the pulsar exhibit a strong correlation with both luminosity and energy, revealing the intricate characteristics of the emitting region. In the low luminosity level, the pulse profiles are relatively complex compared to those at higher luminosity. The pulse profiles exhibit a dip in the soft X-ray band, which vanishes in the hard X-ray regime. Furthermore, the NuSTAR spectra unveil an iron emission line at around 6.4 keV during the brighter state, corresponding to a luminosity of approximately 5.56×10^{36} erg s^{-1}. Additionally, a cyclotron absorption line at $\approx$50.7 keV, indicative of magnetic field strength of 5.69×10^{12} G, is detected solely during this brighter observation. A simple absorbed power-law model adequately described NICER spectra within the 1-7 keV band. Expanding our analysis, we utilized the long-term MAXI/GSC light curve to estimate the potential orbital period of IGR J06074+2205, which is predicted to be approximately 80 days or 80/n days (n=2,3,4). We showed results from optical spectroscopic analysis of observations taken between 2022 and 2024 using the MIRO and IAO. We observed variable Hα and FeII emission lines, with an increase in equivalent width, indicating a dynamic circumstellar disc. Notable variations in the V/R ratio for Hα and FeII lines are also observed. The appearance of additional emission lines, such as HeI (5875.72 Å), HeI (6678 Å), and HeI (7065 Å) from the post-outbursts observation in February 2024 suggests the growth of a larger or denser circumstellar disc. This disc continues to grow without noticeable mass loss, even during the 2023 X-ray outbursts, potentially leading to a future giant X-ray outburst.

Chapter 5

Long-term study of the first Galactic ultraluminous X-ray source Swift J0243.6+6124 using NICER

Swift J0243.6+6124 went into a giant X-ray outburst, followed by several normal outbursts between MJD 58029 (3 October 2017) and MJD 58533 (19 February 2019). After five years of quiescent phase, it showed another outburst phase from MJD 60097 (2 June 2023) to MJD 60190 (3 September 2023) as shown in Figure 5.1. The Neutron star Interior Composition Explorer (NICER) has been monitoring this source since its discovery, capturing data during the giant outburst and several subsequent normal X-ray outbursts. This chapter presents timing and spectral results obtained using NICER data in the 0.5-10 keV energy band. The detailed spectral characteristics of the source in the soft X-ray band remain under investigation. Therefore, a comprehensive spectral study of the source is carried out during the giant and subsequent normal X-ray outbursts, including the new outburst in 2023. Additionally, our timing analysis primarily focuses on multiple normal outbursts, including the 2023 outburst occurring in the post-giant outburst period between MJD 58303 and 60190. As NICER has observed this source at various luminosity levels, this chapter emphasizes how the pulsar properties and surrounding environment change with luminosity. The chapter is organized as follows: Section 5.1 presents an introduction to the source. Section 5.2 gives details about X-ray observations. Section 5.3 presents the timing analysis results, and Section 5.4 discusses the spectral analysis results. Discussions and conclusions are provided in Sections 5.5 and 5.6, respectively.

5.1 Swift J0243.6+6124

Swift J0243.6+6124 was initially triggered on Swift/BAT (15-50 keV energy range) and identified as a possible candidate of gamma-ray burst (GRB) or Galactic transient (Cenko et al., 2017). Subsequent Swift observations showed that the source remains in the X-ray bright phase over six orbits, which rules out the GRB nature of the source (Kennea & Cenko, 2017). Hence, Swift J0243.6+6124 is suggested as a new Galactic X-ray transient. Kennea et al. (2017) discovered this source as an accreting pulsar using Swift/BAT data, where the neutron star rotates around its own axis at a period of 9.86 s. They localized the position of the source within the uncertainty of 1.5 arc-seconds: RA (J2000)=02h 43m 40.33s, and Dec (J2000)= +61d 26m 02.8s and also found that the position is 1.4 arc-seconds away from a B=13 mag star indicating the possible optical counterpart of Swift J0243.6+6124. Following this discovery, Stanek et al. (2017) used the ASAS-SN Sky Patrol public all-sky light curve, which contains 1000+ days of data to check the properties of the optical star. However, they did not observe any significant optical outburst or variability. The pulsation from the source is also confirmed by Jenke & Wilson-Hodge (2017). Using optical spectroscopic observation from the 1.3-m telescope of the Skinakas Observatory (Greece), Kouroubatzakis et al. (2017) found that the optical star is a Be-spectral type star, confirming Swift J0243.6+6124 as a BeXRB system. Apart from X-ray and optical observations, Swift J0243.6+6124 was also observed in the radio band using the Very Large Array (VLA). However, van den Eijnden et al. (2017) did not detect any radio emission from the source. Initially, the distance of the source was estimated to be 2.5±0.5 kpc (Bikmaev et al., 2017). Recent studies suggest that the source is at a distance of $\sim$7 kpc (Wilson-Hodge et al. 2018 and references therein). Detailed study of the source using NICER, NuSTAR, and Insight-HXMT observatories suggested that Swift J0243.6+6124 is the first Galactic ultra-luminous X-ray source (ULX) due to its intense X-ray luminosity reaching up to an order of 10^{39} erg s^{-1} (Wilson-Hodge et al., 2018; Jaisawal et al., 2019; Doroshenko et al., 2020). This BeXRB system is known to have a relatively short orbital period (P_{orb}) of around 28 days and a mildly eccentric orbit with an eccentricity (e) of approximately 0.1 (Doroshenko et al., 2018; Wilson-Hodge et al., 2018).

During the giant X-ray outburst, the pulsar exhibited a rapid spin-up rate (Doroshenko et al., 2018). Both the pulse profile and the pulsed fraction (PF) showed complex variations with luminosity, displaying significant changes around a critical luminosity of approximately 10^{38} erg s^{-1} (Wilson-Hodge et al., 2018; Tsygankov et al., 2018). A QPO-like feature at 50-70 mHz was reported in the power density spectra (PDS) within a specific luminosity range (Wilson-Hodge et al., 2018). Further analysis by Doroshenko et al. (2020) identified significant changes in the pulse profiles and power spectrum at certain luminosity levels.

The broadband continuum of the source during the outburst was effectively described by an absorbed cutoff power law model with black body components (Jaisawal et al., 2018). A two-component transition in the spectral parameters was observed during the giant outburst (Kong et al., 2020). Recent studies have made significant progress in understanding the magnetic field of the pulsar. Jaisawal et al. (2019) conducted a detailed study on the evolution of the iron line width with luminosity, suggesting that a possible disc origin would require a magnetic field in the range of 10^{11} to 10^{12} Gauss. Additionally, no cyclotron absorption line below 100 keV was detected (Jaisawal et al., 2018; Beri et al., 2021). However, Kong et al. (2022) discovered the CRSF in the 120-140 keV range using data from Insight-HXMT, estimating the magnetic field of the pulsar to be approximately 1.6×10^{13} Gauss.

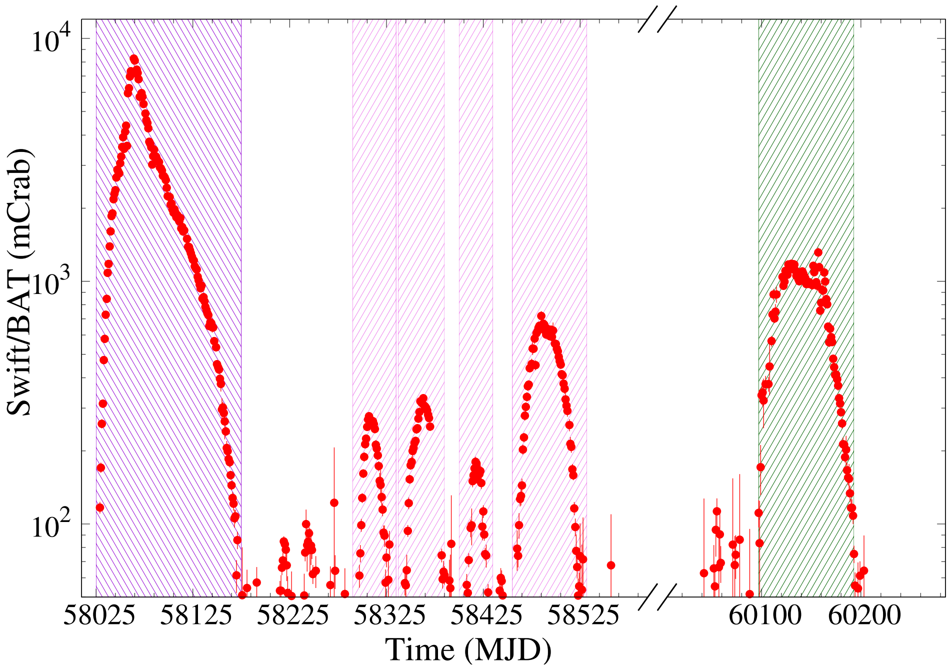

Figure 5.1: Swift/BAT monitoring light curve (red solid points) of the pulsar Swift J0243.6+6124 in 15-50 keV range, between MJD 58010 (2017-09-17) and 60220 (2023-10-03). The light curve is binned with 1 day time frame. The outbursts that are studied using NICER observations are represented with shaded regions. The dark-violet, violet, and green colors mark giant, subsequent normal outbursts, and the 2023 normal outburst phase of the source, respectively.

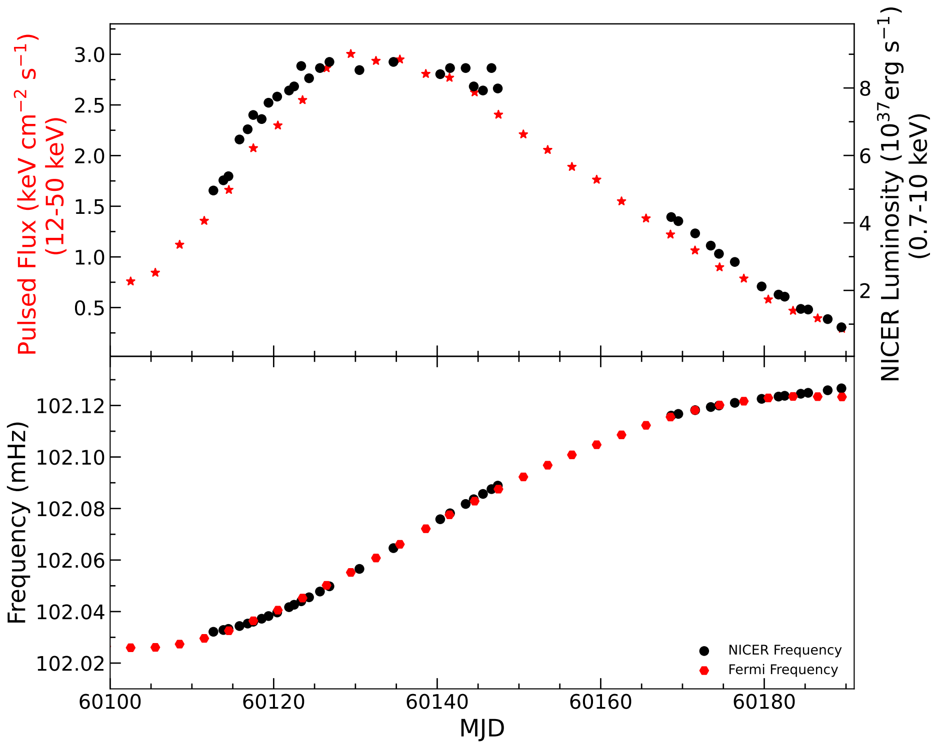

Figure 5.2: Upper panel: Fermi/GBM flux in the 12-50 keV band (red) and the source luminosity with NICER in 0.7-10 keV band (black) evolution during the 2023 outburst. Bottom panel: Spin frequency evolution of Swift J0243.6+6124 measured using Fermi/GBM (red) and NICER (black) during the 2023 outburst.

5.2 X-ray observations

NICER observed the first galactic ULX, Swift J0243.6+6124, between October 2017 and September 2023, during which the source underwent giant as well as multiple normal outbursts. We utilized publicly available NICER data of Swift J0243.6+6124 observed between MJD 58029 (3 October 2017) and 58533 (19 February 2019), stored under observation IDs 1050390xxx with a net exposure time of 408 ks. Additionally, for the recent 2023 outburst, we accumulated around 104 ks of net exposure data observed from June to September 2023 under observation IDs 6050390227 to 6050390277. Figure 5.1 displays the Swift/BAT monitoring light curve (solid red circles) in the 15-50 keV band, with shaded regions above it indicating the duration of the outburst probed using NICER data. The data reduction techniques followed in preparing data for scientific analysis are presented in Chapter-2. For the 2023 outburst data, we included the SUNSHINE==0 filtering in the GTI to extract night-side data, addressing the visible-light leak in the XTI optical bench of NICER reported on 22 May 2023. To account for the effects of the motion of the Earth and satellite during observations, we applied barycentric correction on the data using the solar system ephemeris `JPL-DE430`. Light curves and spectra were extracted from each observation using XSELECT. During the normal outbursts, the dead time correction was not applied to the light curves since the count rate was below 20000 counts s^{-1}. However, for the spectra during the 2017-18 giant outburst, we considered the effect of dead time following Wilson-Hodge et al. (2018). The corresponding spectral background for each observation was obtained using the `nibackgen3C50` tool. The response matrices and ancillary response files were created using the `nicerrmf` and `nicerarf` commands, respectively.

5.3 Timing analysis and results during post-giant outburst phase

We performed timing analysis on NICER data obtained during the post-giant outbursts and the 2023 outburst observations of Swift J0243.6+6124. The period between MJD 58303 and 60190 was selected to investigate the periodic and quasi-periodic oscillations from the neutron star. Using NICER data, the timing properties of the pulsar during the 2017-2018 giant outburst have been documented by Wilson-Hodge et al. (2018).

NICER light curves were generated with a bin size of 0.1 seconds within the 0.5-10.0 keV energy range. The timing analysis was conducted on 105 observations, each with a minimum exposure time of 1400 seconds. We searched for the pulsating signal in the light curves using the χ^2-maximization technique (Leahy, 1987) via the `efsearch` task in the `FTOOLS` package. Orbital corrections were applied to the data using the orbital parameters provided by the Fermi/GBM team[1]. These corrections were necessary to determine the intrinsic spin period of the neutron star, which is influenced by binary orbital modulation. This chapter presents the spin frequency evolution of the pulsar during the recent 2023 outburst (Figure 5.2). The spin frequency evolution during previous outbursts, including the giant and subsequent normal outbursts between MJD 58029 and 58533, has been reported by Wilson-Hodge et al.

[1] `https://gammaray.nsstc.nasa.gov/gbm/science/pulsars/lightcurves/swiftj0243.html`

Table 5.1: Observed QPO frequency, width, and its significance with luminosity. The uncertainties are presented at the 1 σ confidence level.

MJD	Luminosity 10^{37} erg s^{-1}	QPO_f (mHz)	QPO_W (mHz)	Significance
58322	0.69	40±2	7±4	3.99
58323	0.63	47±2	12.0±2	6.52
58325	0.51	34±1	9±2	8.42
58331	0.29	31±2	7.7±2	5.68
58344	0.34	30±1	8.2±2	8.58
58425	1.83	40±1.2	6.50±3	6.52
58430	0.49	38±2	19±4	10.0
58449	0.25	34±2	4±1.5	4.54
58460	0.47	32±3	9±2	4.51
58521	0.58	40±1	5±2	5.36

(2018) and Serim et al. (2023), respectively.

The bottom panel of Figure 5.2 presents the pulse frequency of the pulsar obtained from NICER and publicly available Fermi/GBM data (Malacaria et al., 2020) during the 2023 outburst. The evolution of the 12-50 keV pulsed flux from Fermi/GBM and the source luminosity in the 0.7-10 keV range observed by NICER are shown in the top panel of the figure. During the recent outburst, the spin frequency ranged from approximately 102.03 to 102.12 mHz in NICER and Fermi/GBM data.

We also generated the pulse profile of the pulsar during its normal outbursts, including the 2023 outburst, to study the geometry of the pulsed beamed emission in soft X-rays. Each light curve was folded at the corresponding spin period using the `efold` task of the `FTOOLS` package. The variation of the pulse profile with luminosity from the previous giant and subsequent normal X-ray outbursts observed between MJD 58029 and 58533 was studied by Wilson-Hodge et al. (2018), Serim et al. (2023), and Liu et al. (2023). We found no significant difference in the pulse profile evolution with luminosity during the normal outbursts between MJD 58303 and 58533 and the 2023 normal outbursts. Therefore, in Figure 5.3, we show the pulse profile evolution with luminosity during the normal outbursts between MJD 58303 and 58533 and the 2023 normal outbursts for completeness.

The pulse profiles appear complex with multiple dips/notches at certain pulse phases at luminosities below 6×10^{37} erg s^{-1}. To illustrate the detailed variation of dips/notches and profile evolution with luminosity, we presented the pulse profiles from 12 NICER observations in Figure 5.4. Below the luminosity of approximately 0.5×10^{37} erg s^{-1}, the pulse profiles are dominated by a single peak. Various dip-like structures arise in the pulse phase range of 0.5-1.0 for luminosities between approximately (0.5-2.5)$\times10^{37}$ erg s^{-1}. One of the dips becomes more profound, and the profiles evolve into a double-peaked structure at a luminosity of approximately 2.5×10^{37} erg s^{-1}. A smooth single-peaked profile is observed at luminosities beyond approximately 6×10^{37} erg s^{-1}.

Furthermore, we calculated the pulse fraction (PF) of the pulse profiles from the 2023 outburst to examine the evolution of soft X-ray emission from the pulsar. This type of analysis has yet to be conducted with NICER data, except for the 2017-2018 giant outburst. Therefore, we included the remaining post-giant outburst data in our study. The PF was

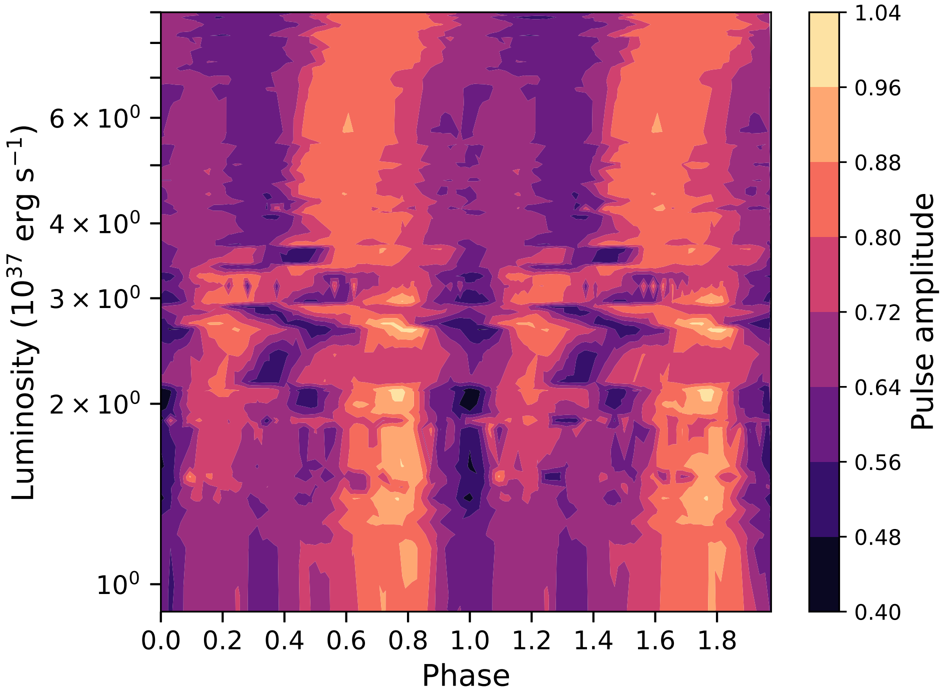

Figure 5.3: The color-coded map of the evolution of the pulse profile of the pulsar with luminosity during the normal outbursts between MJD 58303 and 60190. The pulse profiles are normalized to have values between 0 & 1. Two cycles are shown for clarity.

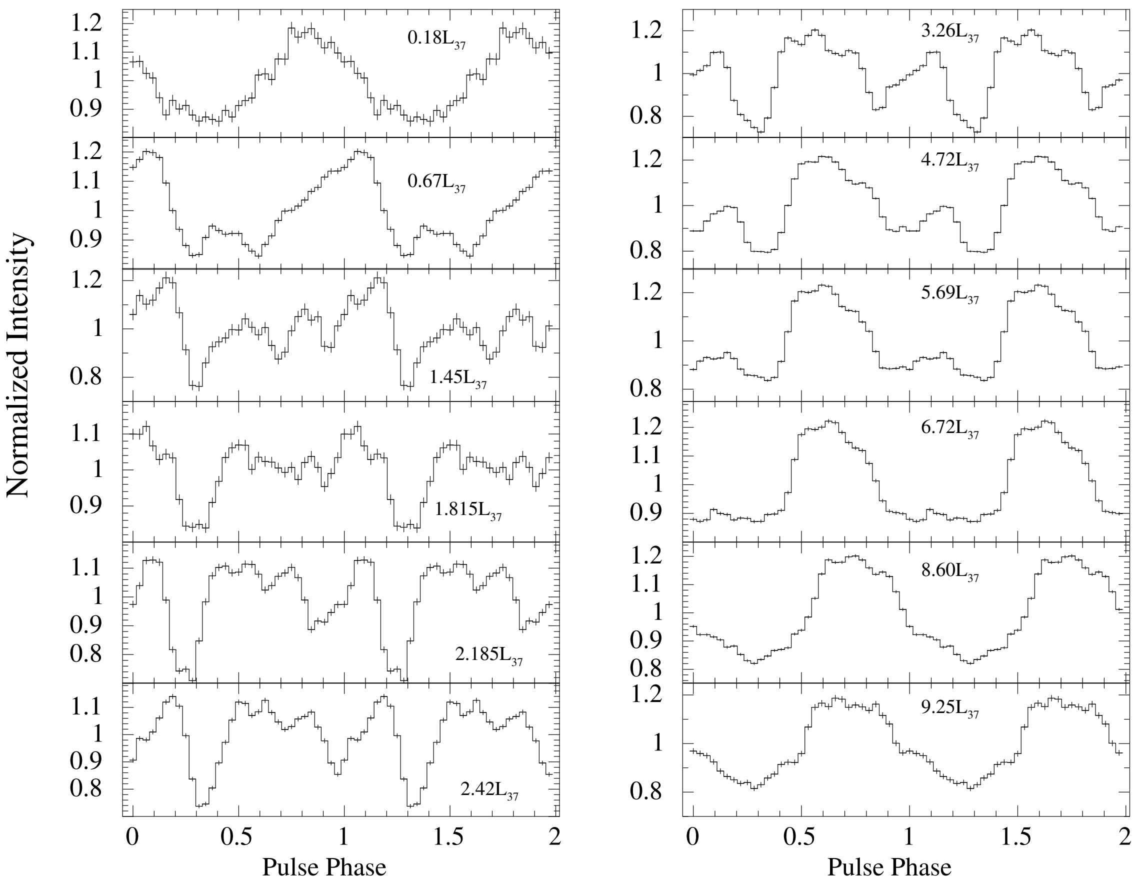

Figure 5.4: Pulse profiles of the pulsar from the NICER observations, covering a broad range of source luminosity during the normal outbursts between MJD 58303 and 60190. Two cycles are shown for clarity. Here, L_{37} stands for 10^{37} erg s^{-1}.

computed using the root mean squared method as described by Wilson-Hodge et al. (2018) (see also Ferrigno et al. 2023). It is defined as follows:

$$PF = \frac{(\sum_{i=1}^{N}(r_i - \overline{r})^2/N)^{1/2}}{\overline{r}} \tag{5.1}$$

The variation of PF with luminosity is shown in panel (a) of Figure 5.5. To understand the trend of PF evolution, we fitted a curve to the obtained PF values at different luminosities using the spline interpolation method. The red line represents the best-fit spline curve, and the shaded area indicates the moving average standard deviation of the data points. The PF varied between approximately 10% and 15% for source luminosities in the range of 2×10^{36} to 9×10^{37} erg s^{-1}. A relatively higher PF value (around 20-25%) was observed at a luminosity of approximately 2×10^{37} erg s^{-1}.

5.3.1 Power density spectrum (PDS) analysis

This study presents the first investigation of the evolution of the PDS and its features during normal X-ray outbursts, including the 2023 outburst. We conducted PDS analysis on 105 light curves within the 0.5-10 keV energy range using NICER data to track how the PDS varies with luminosity. Additionally, we looked for indications of any QPOs in the PDS to compare with those observed during the giant outburst (Wilson-Hodge et al., 2018). To generate the power density spectra, we used the `powspec` tool from the XRONOS package. The light curves were divided into intervals of approximately 400 seconds, and the PDS of each interval was generated. The final PDS was obtained by averaging the PDS from the segmented light curves, which enhances the detection probability of QPO-like features. We also applied the `powspec norm=-2` command to obtain white-noise subtracted averaged PDS, with the power expressed in units of (RMS/mean)^2/Hz. Figure 5.6 shows the resulting PDS for observation ID 1050390170 (MJD 58322).

The PDS displayed narrow peaks at multiples of the primary frequency at around 0.101 Hz, corresponding to the spin frequency of the pulsar and its harmonics, which were excluded during the PDS fitting (James et al., 2010). Initially, we attempted to fit the PDS continuum with a simple power law model (`powerlaw`) using `XSPEC`. However, this model did not adequately fit the overall PDS across a wide frequency range, approximately 0.001 Hz to 5.0 Hz. Consequently, we replaced the power law with a broken power law model (`bknpower`), which provided an acceptable chi-square (χ^2) value. We examined the evolution of the slope of the power law before the break (Γ_1), the break frequency (Br_f), and the slope of the power law after the break (Γ_2) in the PDS with respect to luminosity. This is shown in panels (d), (e), and (f) of Figure 5.5, respectively. The red line represents the best-fitted curve using the spline interpolation method to study the parameter evolution. From the figure, the break frequency Br_f varied between 50 and 80 mHz below 7.5×10^{37} erg s^{-1}. Above this luminosity, Br_f increased to 140 mHz, surpassing the pulsar frequency (101 mHz). The values of Γ_1 and Γ_2 varied between 0.5-1 and 2-3, respectively, within the

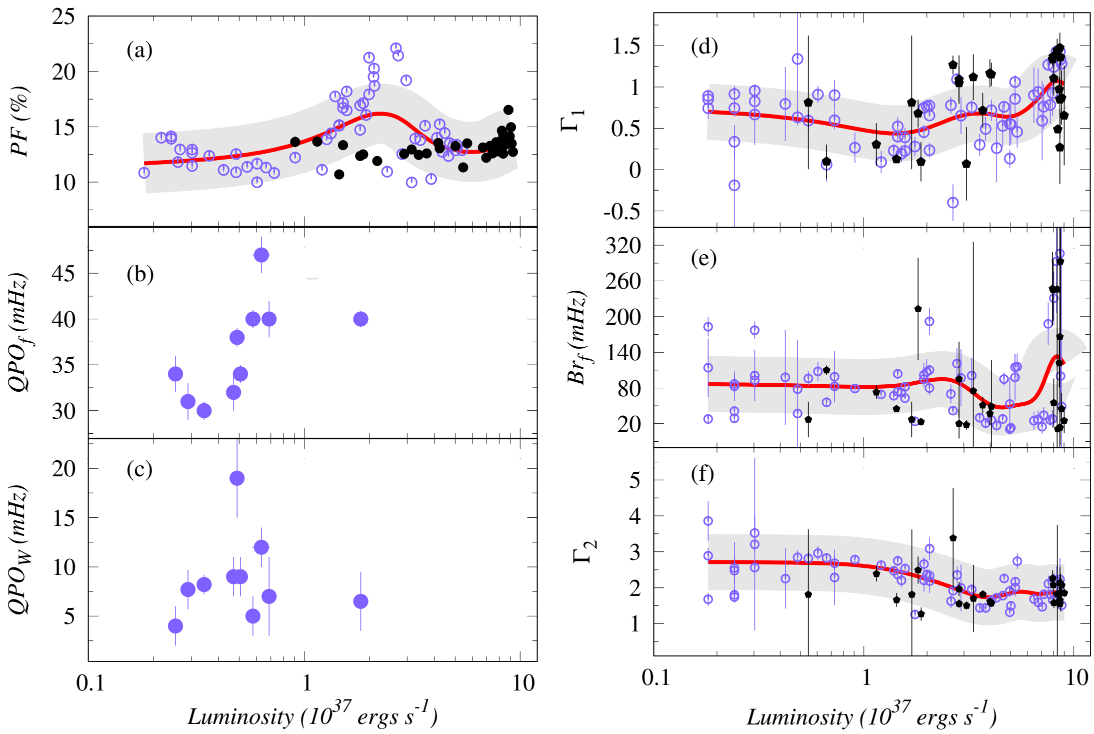

Figure 5.5: The luminosity evolution of different parameters from the PDS analysis during normal outbursts. Panels (a-f) display the values of pulsed fraction (PF), break frequency (Br_f), QPO frequency (QPO_f), QPO width (QPO_W), slope of power law before Br_f (Γ_1), and slope of power law after $Br_f(\Gamma_2)$ as functions of luminosity, respectively. The red line represents the best-fitting curve for these values using the spline interpolation method. The shaded area indicates the moving average standard deviation of data points. The purple data points represent values obtained from normal outbursts, except for the 2023 outburst that is shown in black.

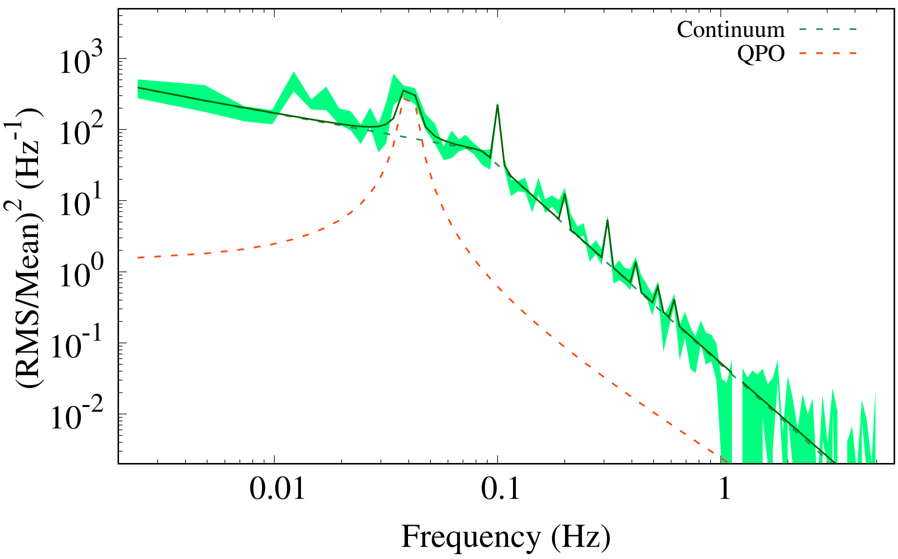

Figure 5.6: A representative power density spectrum from a NICER observation ID 1050390170 is shown. The continuum is fitted with a broken power law, and the QPO feature is described using a Lorentzian function. The observed narrow peaks correspond to the pulsar rotational frequency and its harmonics.

studied luminosity range.

After fitting the PDS continuum with a broken power law model, we examined the residuals for potential QPOs. In addition to the spin frequency of the neutron star and its harmonic components, we observed a broad hump-like residual below the pulsar spin frequency in some cases (around 16 IDs). To investigate this further, we used a Lorentzian function (`lorentz`), as the shape of this hump appeared asymmetric. The Lorentzian function has been widely used in various QPO studies (see e.g., Belloni et al. 2002). Figure 5.6 shows the best-fitted model for observation ID 1050390170 (MJD 58322) in the PDS.

Furthermore, the significance of the QPOs was determined using the method described in Boutelier et al. (2010), based on Lorentzian fitting. We found that QPOs from 10 out of 16 IDs between MJD 58322 and 58521 exhibited a significance of more than 3σ. The frequency (QPO_f) and full width at half maximum (QPO_W) of these detected QPOs and their respective significance are presented in Table 5.1. The evolution of QPO_f and QPO_W with luminosity is also shown in panels (b) and (c) of Figure 5.5, respectively. No QPO-like feature was observed during the recent 2023 outburst of Swift J0243.6+6124.

5.4 Spectral analysis and results

We conducted a spectral analysis of the pulsar using NICER data from multiple outbursts observed between 2017 and 2023, which covers giant as well as normal outbursts. A total of 150 observations were utilized, enabling us to examine changes in spectral parameters across a wide range of luminosities. The analysis was conducted in the 0.7-10.0 keV energy range using the `XSPEC` (v-12.11.0, Arnaud 1996) package. This specific energy range was chosen to avoid spectral uncertainties below 0.4 keV and above 10.0 keV and to bypass a strong

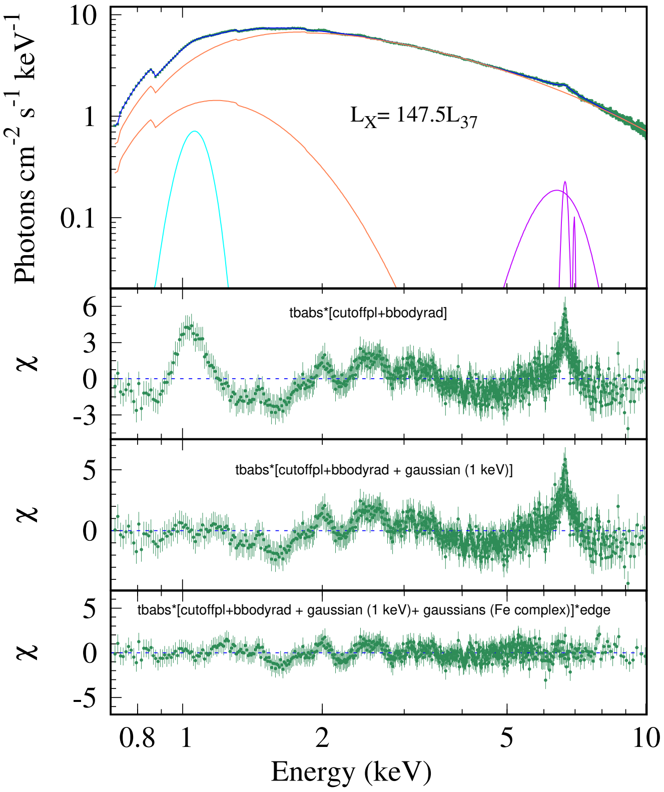

Figure 5.7: The 0.7-10 keV energy spectrum of Swift J0243.6+6124 obtained from the NICER observation on MJD 58065 (ID 1050390115) near the peak of the X-ray outburst. The second, third, and fourth panels from the top show the evolution of residual after fitting the continuum, and subsequent addition of 1 keV, 6-7 keV Fe-line complex, and edge feature, respectively.

edge-like feature near 0.5 keV that appears, especially in the brighter observations. The feature at 0.5 keV was found to be dependent on the choice of the photo-electric absorption model and assumed abundances to some extent. It may also have a calibration origin from the Oxygen edge[2]. A systematic uncertainty of 1.5% was applied, as the NICER instrument team recommended. For quantifying line-of-sight X-ray absorption, the `wilm` abundance table (Wilms et al., 2000) was used along with the `Vern`[3] photo-ionization cross-section. The spectra were binned with a minimum of 30 counts per energy bin to allow for the application of chi-square statistics in the analysis.

To understand the evolution of the pulsar emission over multiple outbursts, we employed a uniform continuum model to assess changes in parameters with varying source luminosity consistently. We used an absorbed cutoff power law model (`tbabs`×`cutoffpl`) to describe the continuum emission, following the methodology of previous studies (Jaisawal et al., 2019; Kong et al., 2020). Prominent positive residuals were detected in the energy ranges of 6-7 keV and 0.9-1.1 keV, particularly during the 2017-2018 giant outburst. Additionally, we observed a 7.1 keV iron edge feature exclusively during high luminosity phases. To address the positive residuals in the 6-7 keV range, we used one to three Gaussian components depending on the source luminosity, as recommended by Jaisawal et al. (2019). The residuals in the 0.9-1.1 keV band were modeled using a single Gaussian component. Figure 5.7 presents a representative spectral model of the pulsar emission and the spectral residuals

[2]`https://heasarc.gsfc.nasa.gov/docs/nicer/analysis_threads/arf-rmf/`
[3]`https://heasarc.gsfc.nasa.gov/xanadu/xspec/manual/node120.html`

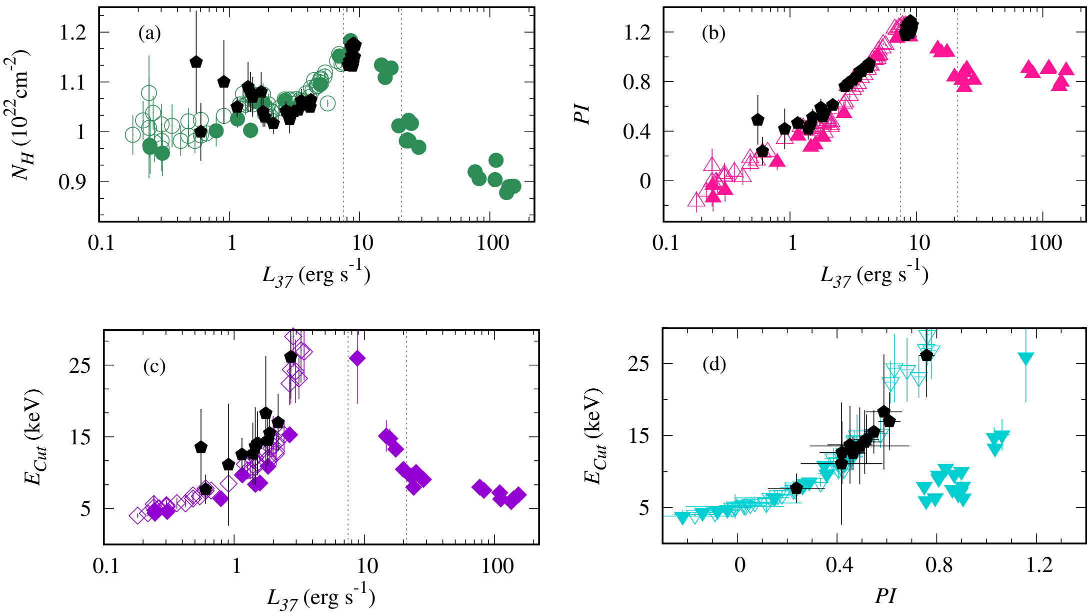

Figure 5.8: The panels (a)-(c) show the evolution of the parameters such as column density (N_H), Photon Index (PI), and Cutoff energy (E_{cut}) with luminosity obtained from multiple outbursts of Swift J0243.6+6124. Panel (d) shows the relationship between the photon Index (PI) and cutoff energy (E_{cut}). The filled and open markers represent data points obtained from the giant and subsequent normal outbursts, respectively. The black points represent the values obtained from the 2023 outburst.

after accounting for the continuum and line emission components. This data was obtained from a NICER observation near the peak of the giant X-ray outburst in 2017.

The continuum parameters obtained from the best-fit models across all NICER observations from multiple outbursts are presented in Figure 5.8. Panels (a), (b), and (c) of Figure 5.8 show the variation of spectral parameters such as hydrogen column density (N_H), photon index (PI), and cutoff energy (E_{cut}) with unabsorbed luminosity. The uncertainties in the parameter values are calculated within the 90% confidence range. The luminosity is estimated from the unabsorbed flux in the 0.7-10.0 keV energy range, assuming a distance of 7 kpc (Wilson-Hodge et al., 2018).

We observed that N_H varied narrowly between (0.9-1.2) $\times$ 10^{22} cm^{-2} across these observations. To avoid spectral degeneracies, we refitted the spectra using an absorbed cutoff power law model with a fixed average value of $N_H = 1.064 \times 10^{22}$ cm^{-2}. This approach revealed a positive residual at the lower energy side, which could be described by a soft `bbodyrad` component. The luminosity variations of the parameters obtained from this revised model are shown in Figure 5.9.

Two transition points can be identified by examining the overall behavior of these parameters in Figures 5.8 and 5.9. The photon index (PI) exhibited a two-component transition with luminosity, potentially linked to changes in the accretion mode (Figure 5.8). The first transition occurred at around a luminosity L_1 of 7.5 $\times$ 10^{37} erg s^{-1}, where PI showed an increasing trend with luminosity. A decrease in the photon index was observed up to a luminosity of 2.1 $\times$ 10^{38} erg s^{-1} (L_2), which can be identified as the second transition point. The photon index remains almost stable beyond L_2. A similar trend can also be seen in

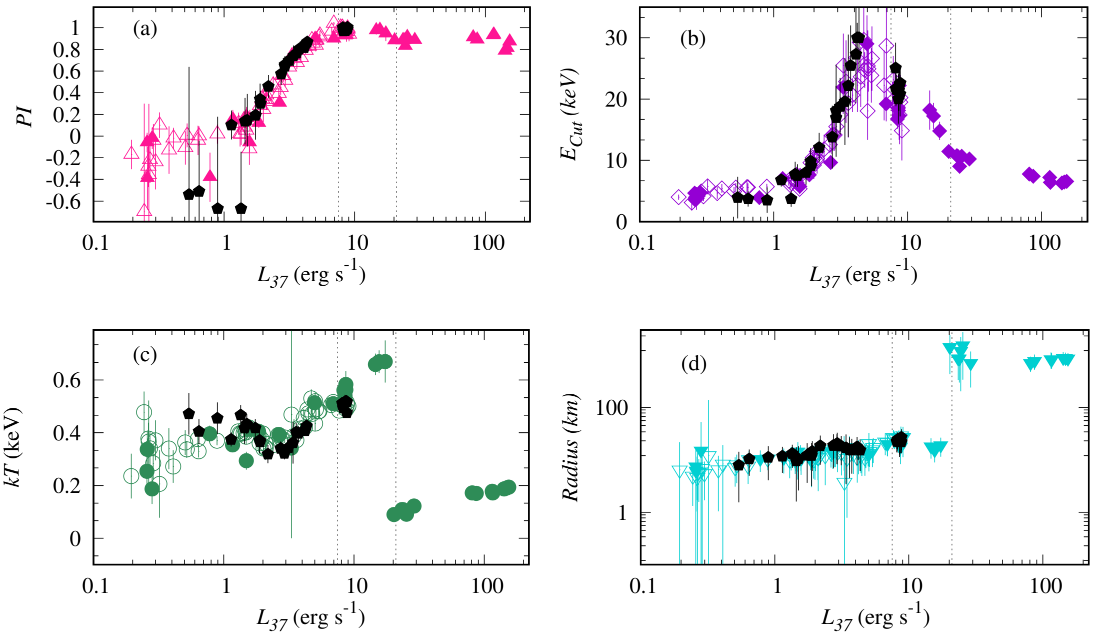

Figure 5.9: The panels (a)-(d) show the luminosity dependencies of spectral parameters such as photon index (PI), cutoff energy (E_{cut}), blackbody temperature (kT), and blackbody radius at a fixed column density over multiple outbursts of Swift J0243.6+6124. The symbols have the same meaning as Figure 5.8.

Figure 5.9. The transitional luminosities L_1 and L_2 are marked with dotted lines in these figures.

Furthermore, we observed that the cutoff energy (E_{cut}) increases with luminosity distinctly below the first transition point L_1 (Figures 5.8 and 5.9). To ensure consistency with the limited bandpass of NICER, we imposed an upper limit of 30 keV on the cutoff energy during fitting, aligning with the maximum value observed in this pulsar based on broadband spectral analysis using HXMT data (Kong et al., 2020). Between L_1 and L_2, E_{cut} steeply decreased with luminosity, whereas a gradual evolution was observed above L_2. Additionally, we noted the unique evolution of PI and E_{cut} with luminosity beyond the second transition point in our study.

Contrary to the trends reported in Figure 3 of Kong et al. (2020) in the super-Eddington regime, where a positive correlation between PI and E_{cut} and luminosity was identified, our findings indicate a constant PI and an anti-correlation trend for E_{cut} with luminosity. It is worth noting that in the super-Eddington phase, the emission from an outflow or a reflection component may alter the shape of the X-ray continuum, a factor that may not fully be captured due to the limited energy band of the NICER. Therefore, marginal variations in parameters in the super-Eddington regime can be expected.

To explore this further, we conducted spectral fitting by introducing an additional blackbody component during the super-Eddington phase, as suggested by Tao et al. (2019). The temperature of this blackbody component exhibited an evolution between approximately 1 and 3 keV, potentially stemming from the contributions of the hotspot and top of the accre-

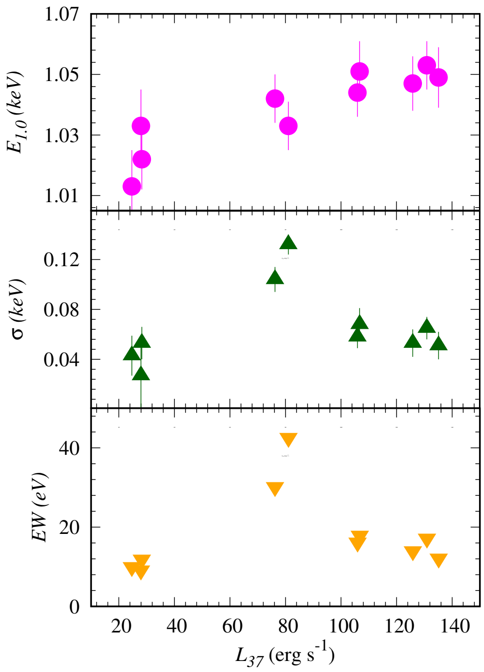

Figure 5.10: The figure illustrates the evolution of Gaussian model parameters of 1.0 keV emission line. The parameters include the central line energy ($E_{1.0}$), width (σ), and equivalent width (EW), presented from top to bottom, respectively.

tion column, with a radius between 10 and 40 km. In the presence of the second blackbody component, the photon index and cutoff energy showed a positive pattern after the second transition point, similar to Kong et al. (2020). However, caution is warranted in interpreting these findings due to the constraints imposed by the limited energy band of NICER.

In panels (c) and (d) of Figure 5.9, we present the evolution of blackbody temperature and corresponding emission radii. Below L_2, the blackbody temperature (kT) gradually varied in the 0.1-0.7 keV range. The size of the emission site also changed between 10 to 30 km, given the source distance of 7 kpc, below L_2. A sudden change in these parameters was observed around L_2.

In addition to evolving iron emission lines in the 6-7 keV band (Jaisawal et al., 2019), we detected an emission line at around 1 keV in the spectra. This feature was mainly observed during the giant outburst at luminosities above 2×10^{38} erg s^{-1}, i.e., the second transition point. The parameters obtained from the emission line analysis are presented in Figure 5.10. From this figure, it can be observed that the central energy variation with luminosity falls within the error bars. However, the line width (σ) and equivalent width (EW) of the 1 keV line showed an increase as the luminosity increased up to approximately 8×10^{38} erg s^{-1}, and beyond that, they decreased with luminosity, indicating a strong luminosity dependency of the 1 keV emission line.

5.5 Discussion

We investigated the behavior of the first Galactic ultra-luminous X-ray pulsar, Swift J0243.6 +6124, utilizing NICER observations spanning over the giant and multiple normal X-ray outbursts occurring between 2017 and 2023. This comprehensive coverage enabled us to explore the distinctive timing and spectral characteristics of the pulsar across varying mass accretion rates. Our analysis across these outbursts revealed a wide range of luminosity variation, spanning from (0.1 to 153)$\times 10^{37}$ erg s^{-1} in 0.7-10 keV energy range, with a distance assumed to be 7 kpc. We begin this section with a discussion of the timing results obtained from the analysis of data during normal outbursts. Subsequently, we delve into the implications of the observed two spectral transitions exhibited by the source.

5.5.1 Temporal characteristics of Swift J0243.6+6124 during post-giant outburst phases

We examined the spin frequency evolution of the pulsar during its recent 2023 outburst (Figure 5.2). Previous studies on the spin frequency evolution during past outbursts have been reported by Wilson-Hodge et al. (2018) and Serim et al. (2023). Before the 2023 outburst, the pulsar was in a quiescent state between MJD 58535 and 60097, during which the spin frequency decreased from 102.10 to 102.03 mHz, according to Fermi/GBM data. However, following the 2023 outburst, the spin frequency of the pulsar increased gradually to 102.12 mHz (Figure 5.2). This frequency is consistent with the spin frequency observed after the giant and subsequent normal outbursts between 2017 and 2019 (Wilson-Hodge et al., 2018; Liu et al., 2023; Serim et al., 2023). The observed increase in spin frequency is expected as due to the significant transfer of angular momentum to the neutron star due to mass accretion.

We also investigated the pulse profile of the pulsar from post-giant outbursts, including the recent 2023 outburst (Figures 5.3). Pulse profiles provide insights into the geometry of the emission region. Accretion-powered pulsars typically exhibit simpler and smoother pulse profiles in hard X-rays. In contrast, in soft X-rays, the profiles appear more complex due to the effects of circumstellar scattering and absorption (White et al., 1983). Our analysis revealed complex pulse profiles in the 0.5-10 keV energy band, characterized by various dips or notches at different pulse phases (see Figure 5.4). Similar features have been observed in the pulse profiles of other Be/X-ray binary pulsars, such as V0332+53, 1A 0535+262, EXO 2030+375, GX 304-1, and RX J0209.6-7427 (Tsygankov et al., 2006; Naik et al., 2008, 2013; Naik & Jaisawal, 2015; Epili et al., 2017a; Jaisawal et al., 2016; Vasilopoulos et al., 2020). These features are generally attributed to the absorption of photons by streams of matter locked at specific pulse phases of the neutron star, illustrating the dynamics of matter distribution within the magnetosphere.

The critical luminosity for Swift J0243.6+6124 is estimated to be $\approx 10^{38}$ erg s^{-1} based on the behavior of source during its giant outburst (Wilson-Hodge et al., 2018). Given this threshold, the pulsar was accreting in a sub-critical or near-critical luminosity regime during the normal outbursts between MJD 58303 and 58533 and the recent 2023 outburst, where the observed luminosity ranged between 0.2-9.0 $\times 10^{37}$ erg s^{-1}. We illustrated the evolution of the pulse profile with luminosity during these normal outbursts in Figure 5.3. Initially, the pulse profiles are single peak dominated when the luminosity was below $\sim 0.5 \times 10^{37}$ erg s^{-1}. Between $\sim 0.5 - 6 \times 10^{37}$ erg s^{-1}, various dips/notches appear, and the profile evolves to a double-peaked structure. A distinct double-peaked profile is observed below the first transition point L_1. Additionally, the pulse profile transitioned from a double-peaked to a smooth single-peaked structure at luminosities above $\sim 6 \times 10^{37}$ erg s^{-1}, similar to the pulse profile shapes reported by (Wilson-Hodge et al., 2018) at around this luminosity. The observed pulse profile evolution, even below the critical regime, indicates a change in the emission geometry or beam pattern depending on the mass accretion rate.

Besides the pulse profile, the pulsed fraction (PF) provides valuable insights into the pulsating emissions from a source. We observed a variation in the PF corresponding to changes in luminosity (Figure 5.5). The pulsed fraction (PF) shows a moderate variation from $\sim$ 10% to 15% within the luminosity range of $\sim 2 \times 10^{36}$ to $\sim 9 \times 10^{37}$ erg s^{-1}. Notably, during the giant outburst, Wilson-Hodge et al. (2018) found that the pulsed fraction increased with rising luminosity above the critical luminosity of 10^{38} erg s^{-1} from 20% to 55%. Below the critical luminosity, the PF varied between 15-30% during the giant outburst. This is consistent with our current findings during the post-giant outbursts. Based on the examination of PF and observed outburst luminosities, the source was accreting below or close to the critical regime at the peak of these multiple normal outbursts.

5.5.2 Detection of QPO and break feature in the PDS

We observed low-frequency QPOs from Swift J0243.6+6124 at specific epochs within a particular luminosity range during the normal outbursts following the giant outburst. The QPO frequencies detected ranged from 30 to 47 mHz within the luminosity range of (0.2-2.0) $\times 10^{37}$ erg s^{-1} (see Table 5.1). Panels (b) and (c) of Figure 5.5 display the evolution of QPO frequency and width with luminosity, respectively. The QPO frequency shows a positive correlation with luminosity, while the width remains relatively constant. No QPO-like signatures were detected in the 2023 X-ray outburst with NICER. Additionally, no QPO was found in the NuSTAR observation during the 2023 outburst (Pradhan et al., 2023). During the 2017-2018 giant outburst of Swift J0243.6+6124, QPOs with frequencies between 50-70 mHz within a luminosity range of 0.28-2.05$\times 10^{37}$ erg s^{-1} in 0.2-12 keV were observed with NICER by Wilson-Hodge et al. (2018). Furthermore, the power spectra obtained from the Insight-HXMT observation in the 20-40 keV range revealed weak QPOs with luminosity-dependent frequencies ranging from $\approx$ 50 to 200 mHz during the giant X-ray outburst (Doroshenko et al., 2020). This indicates the transient nature and energy dependency of the low-frequency QPOs. The QPO frequencies detected in our study are consistent with previous QPO studies in other HMXB accreting pulsars (Paul & Naik, 2011). Additionally, the phenomenon of QPO detection, primarily in the low luminosity phase, has been observed in other cases, such as KS 1947+300 (James et al., 2010).

In HMXBs, the physical origin of these QPOs is commonly explained by two models: the Keplerian Frequency Model (KFM; van der Klis et al. 1987) and the Magnetospheric Beat Frequency Model (MBFM; Alpar & Shaham 1985). The QPO feature arises when the accretion process is influenced by the interaction between the co-rotating magnetosphere and the inhomogeneities in the inner accretion disc, which creates variabilities in the mass accretion rate. The KFM states that this variable mass accretion rate occurs at the Keplerian frequency. For MBFM, this happens at a beat frequency between the spin frequency of the pulsar and the rotational frequency of matter at the inner disc. In the case of

Swift J0243.6+6124, the spin frequency of the pulsar is approximately 102.1 mHz, while the detected QPO frequency ranges from 30 to 47 mHz, nearly one-third of the pulsar frequency. When the spin frequency of the pulsar exceeds the Keplerian frequency at the inner edge of the accretion disc, the co-rotating magnetosphere expels the accreted matter outward, a phenomenon known as centrifugal inhibition of accretion (Lamb et al., 1973). The KFM is, therefore, applicable only when the QPO frequency is higher than the spin frequency of the neutron star, as observed in the transient Be/X-ray binary pulsars like EXO 2030+375 (Angelini et al., 1989) and 1A 0535+262 (Finger et al., 1996). Consequently, the MBFM could potentially explain the origin of the quasi-periodic variabilities in Swift J0243.6+6124, as applied in previous studies of sources like 4U 0115+634 (Dugair et al., 2013) and KS 1947+300 (James et al., 2010).

Based on the detected QPO frequency, we can also calculate the magnetic field of the neutron star using the MBFM. The magnetic field of the neutron star for a dipolar structure is given by

$$B = 4 \times 10^{11} M_{1.4}^{-5/6} R_6^{-3} \dot{M}_{-8}^{1/2} (\frac{\Omega_K}{mHz})^{-7/6} \text{ G} \tag{5.2}$$

Where, $M_{1.4}$=1.4$M_\odot$ (mass of the neutron star), $\dot{M}_{-8}$=10$^{-8}M_\odot$ yr^{-1} (mass accretion rate), and R_6=10^6 cm (radius of neutron star).

According to MBFM, $\Omega_K = \Omega_{QPO} + \Omega_s$, where Ω_K, Ω_{QPO}, and Ω_s represent the Keplerian frequency, QPO frequency, and pulsar spin frequency, respectively. For the luminosity range of 0.2-2.0 $\times$ 10^{37} erg s^{-1} (assuming a distance of 7 kpc), the mass accretion rate ($\dot{M}$) is estimated to be between 0.02-0.13 $\times$ 10^{-8} M$_\odot$ yr^{-1}. Applying these values in the relevant equation and considering the detected QPO and pulsar frequencies, the magnetic field (B) of the neutron star is estimated to be $\sim$2.5 $\times$ 10^{12} G. This magnetic field value aligns well with measurements from previous studies using indirect methods (Tsygankov et al., 2018; Doroshenko et al., 2020; Bykov et al., 2022). For instance, Tsygankov et al. (2018) found that the non-detection of the propeller effect constrained the upper limit of the magnetic field to 6 $\times$ 10^{12} G. Additionally, Doroshenko et al. (2020) analyzed various features such as the propeller effect and state transitions to estimate the magnetic field range to be $\sim$ (3-9)$\times$ 10^{12} G, with the lower limit being more probable.

Our estimated magnetic field also aligns with findings by Jaisawal et al. (2019), who suggested a lower magnetospheric radius and a relatively low magnetic field ranging from 10^{11} to 10^{12} G based on significant iron line broadening at higher luminosities. Bykov et al. (2022) calculated magnetic field of the pulsar by using the reflection model `relxilllp` during the super-Eddington phase of the source, and found that at the peak of the outburst, the inner accretion radius was approximately 2-3 $\times$ 10^7 cm, corresponding to a magnetic field of 3 $\times$ 10^{12} G. However, some other studies have suggested that the magnetic field of the pulsar might be an order of magnitude higher than our estimate. For example, Kong et al. (2022) detected a cyclotron resonance scattering feature (CRSF) in the 120-146 keV range through phase-resolved spectroscopy during the bright phase of the outburst. The calculated magnetic field from this observation is approximately 1.6 $\times$ 10^{13} G, which is the strongest magnetic field detected for a neutron star in binaries. This high magnetic field component is thought to represent the quadrupole component of the magnetic field.

A distinct break is evident in the power density spectra, as depicted in Figure 5.6. The variation of the obtained break frequency (Br_f) with luminosity is illustrated in panel (e) of Figure 5.5. Below a luminosity of $\sim$7.5$\times$10^{37} erg s^{-1}, the Br_f remains stable at $\sim$80 mHz. However, beyond this threshold, the break frequency increases to 140 mHz, surpassing the pulsar spin frequency (101 mHz). A similar evolution pattern was observed by Doroshenko et al. (2020) (Figure 6) in the 20-40 keV Insight-HXMT light curve. Notably, the first spectral transition was also noted at around 7.5$\times$10^{37} erg s^{-1}, although their connection remains unclear.

Furthermore, the slopes of the power laws below and above the break frequency exhibit variations in luminosity, ranging between 0.5-1 and 2-3, respectively. These slopes, denoted as Γ_1 and Γ_2 in the PDS, are attributed to variabilities in the accretion disc and magnetosphere of the neutron star, respectively (Hoshino & Takeshima, 1993; Revnivtsev et al., 2009). This suggests a transition of matter flow from the accretion disc to the magnetosphere. The higher values of Γ_2 compared to Γ_1 indicate a suppression of variabilities within the magnetosphere (Revnivtsev et al., 2009). Moreover, the observed break frequency, nearly 1.4 times the spin frequency, suggests that the variability timescale relative to the break frequency is not directly associated with the expected Keplerian timescale at the inner edge of the disc (Revnivtsev et al., 2009). This inference holds particularly true at low luminosity levels, where the spin period is anticipated to be around the same duration.

5.5.3 Spectral characteristics of Swift J0243.6+6124

To comprehensively understand the X-ray emission mechanisms in Swift J0243.6+6124 and complement our timing investigations, we conducted spectral analysis utilizing high-cadence NICER data. Our study spanned a broad time frame from 2017 to 2023, encompassing the giant outburst, multiple subsequent normal outbursts, and the recent 2023 X-ray outburst. Through spectral analysis, we determined that the highest luminosity of the source in the 0.7–10 keV range reached 1.53$\times$10^{39} erg s^{-1}. This finding indicates that throughout the observation period, the source surpassed the Eddington luminosity limit ($L_{Edd} = 1.25\times10^{38}$ erg s^{-1} for a typical 1.4M$_\odot$ neutron star), the theoretical maximum luminosity for a spherically symmetric emitting source. However, our observations of luminosity beyond the Eddington limit are influenced by certain assumptions in its calculation; firstly, assuming spherical accretion, and secondly, considering interactions between incoming matter and outgoing photons through Thomson scattering. However, in the case of highly magnetized neutron stars, the interaction cross-section can be significantly lower than the Thomson scattering cross-section, allowing radiation to escape in a direction perpendicular to the mass accretion direction. In aggregate, this phenomenon can elevate the luminosity of the pulsar beyond the Eddington limit (Basko & Sunyaev, 1976).

Our spectral analysis unveiled two distinct transitional luminosities, labeled as L_1 and L_2, approximately $\approx$7.5 $\times$ 10^{37} and $\approx$2.1$\times$10^{38} erg s^{-1} in 0.7-10.0 keV energy range, respectively, for a distance of 7 kpc. These transitions manifest in continuum parameters such as the photon index and cutoff energy, as depicted in Figures 5.8 & 5.9. Insight-HXMT observed similar transitions at $\sim$1.5 $\times$10^{38} erg s^{-1} and 4.4 $\times$10^{38} erg s^{-1} in 2-250 keV band at a distance of 6.8 kpc (Kong et al., 2020). These two transitions in spectral parameter evolution represent novel findings for Swift J0243.6+6124. Such behavior has potentially not been observed previously in any other accretion-powered pulsars. In a study by Reig & Nespoli (2013), spectral analysis of nine Be/X-ray binary pulsars indicated the presence of two branches, suggesting a single-luminosity transition. However, the photon index of these sources evolved differently compared to Swift J0243.6+6124, i.e., the photon index decreased with increasing luminosity up to the first transition point (Figure 6 of Reig & Nespoli 2013) except for Swift J1626.6-5156, where it remained constant. This discrepancy underscores the distinct X-ray emission mechanisms in Swift J0243.6+6124 compared to other accretion-powered pulsars. While Reig & Nespoli (2013) identified only a single transition point in the evolution of spectral parameters with luminosity, indicating the presence of two accretion modes on either side of the transition point or critical luminosity, our study of Swift J0243.6+6124 revealed two transition points. This suggests the presence of three distinct accretion modes, implying a more intricate behavior in this source.

In accretion-powered X-ray pulsars, the relationship between the photon index and luminosity evolves depending on the accretion regimes, where the primary source of X-ray emission is the accretion column. Typically, these pulsars exhibit a negative correlation between the photon index and luminosity below a single transition point or critical luminosity. Conversely, a positive correlation is anticipated between these parameters in the super-critical luminosity domain. In the sub-critical luminosity regime, the shock region within the column is positioned much closer to the neutron star surface (Becker et al., 2012). The shock region ascends as the mass accretion rate rises, resulting in a taller column in the super-critical luminosity domain. In this scenario, photons may not acquire sufficient energy through bulk Comptonization to generate high-energy photons, resulting in a softer spectrum as luminosity increases. Conversely, in the sub-critical regime (below the transition point), the size of the interaction region diminishes with increasing luminosity. This leads to a rise in optical depth, thereby stiffening the spectrum. However, in the case of Swift J0243.6+6124, a notable observation was made: there exists a positive correlation between the photon index and X-ray luminosity up to a transition point of approximately 7.5×10^{37} erg s^{-1} (first transition zone). Beyond this threshold, the correlation becomes negative up to a certain limit (2.1×10^{38} erg s^{-1}; second transition zone), and subsequently, no correlation was observed beyond a luminosity of 2.1×10^{38} erg s^{-1}.

First accretion mode ($L_X \leq L_1$): Below the luminosity threshold of $\sim7.5\times10^{37}$ erg s^{-1}, we observe a positive correlation between the photon index and luminosity within the first transition zone. This positive correlation signifies that the lower-energy X-ray photons contribute more to the continuum than bulk Comptonized photons in the accretion column. A softer spectrum suggests the possibility of blackbody emission from the source. In this accretion mode, we observe a rise in the soft blackbody emission with a temperature (kT) ranging from approximately 0.1 to 0.7 keV, emanating from a region with a radius (*Radius*) of approximately 10 to 30 km. The temperature and size of this emitting region suggest a combination of photons originating from both the surface of the neutron star and the hot spot region (Zhao et al., 2019; Elshamouty et al., 2016). This soft photon emitting region, characterized by temperatures between 0.3 and 0.4 keV and sizes ranging from 25 to 38 km, was also identified by Beri et al. 2021 using AstroSat during similar luminosity ranges. Previous studies have also indicated the presence of single or multiple blackbody components representing soft X-ray emissions from the column and/or optically thick outflow in the spectrum of Swift J0243.6+6124 (Jaisawal et al., 2018; Kong et al., 2020; Tao et al., 2019). These thermal regions may contribute to the softer spectrum observed in this accretion mode. As the X-ray luminosity increases, the gas shock region (photon emitting region) is expected to ascend within the polar region. This leads to an increase in the plasma temperature in the shocked region, resulting in a rise in shock height with the mass accretion rate. Consequently, the optical depth decreases, leading to less efficient cooling of the accreting plasma. This increase in plasma temperature in the accretion column explains the observed correlation between the photon index (PI) and cutoff energy (E_{cut}) within the first transition zone.

Second accretion mode ($L_1 \leq L_X \leq L_2$): In this regime, the photon index and the cutoff energy exhibit correlated behavior, but both parameters show an anti-correlation with the luminosity. This indicates the presence of a different emission mechanism compared to the previous accretion mode. Within the specified luminosity range, the properties of the accretion column exhibit distinct characteristics, as also observed in the timing analysis (Kong et al., 2020). This behavior aligns with observations in the sub-critical regime of several sources such as 4U 0115+63, 1A 0535+262, 1A 1118-612, GRO J1008-57, EXO 2030+375, 2S 1417-624, and SMC X-2 (Reig & Nespoli, 2013; Epili et al., 2017a; Jaisawal et al., 2021; Gupta et al., 2018; Jaisawal et al., 2023). In this luminosity range, it is expected that a radiation shock is present in the accretion column, although its strength is insufficient to bring the matter to a complete rest at the stellar surface (Basko & Sunyaev, 1976; Becker et al., 2012). Instead, the plasma velocity reduces significantly due to Coulomb interactions near the base of the accretion column (Burnard et al., 1991; Nelson et al., 1993). Consequently, the height of the emitting region decreases with increasing luminosity following the relation of $\mathrm{h}_e \propto L_X^{-5/7}$ (Becker et al., 2012). The reduction in the size of the sinking region, or the Comptonization region, leads to an increase in optical depth, producing harder photons and thus a lower photon index (Becker et al., 2012). Additionally, the cutoff energy decreases as the cooling mechanism through Comptonization dominates over the heating mechanism in this luminosity range, given the increased density resulting from the decreasing height of the emission region.

Third accretion mode ($L_X \geq L_2$): Within this luminosity range, the source enters a super-critical state, where we observed that the photon index (PI) remains nearly constant with luminosity while the E_{cut} value decreases. This state is marked by the prevalence of radiation pressure, dictating the flow dynamics of plasma, ultimately leading to plasma settling on the stellar surface (Davidson, 1973; Basko & Sunyaev, 1976). The height of the emission region in this scenario increases with luminosity, following the relation $\mathrm{h}_e \propto L_X$ (Becker et al., 2012). Here, the effective velocity of incoming electrons decreases due to the balance between advection (inwards) and diffusion (outwards) of photons (Becker et al., 2012). With the reduced effective electron velocity, the photons do not acquire enough energy through bulk Comptonization, resulting in spectral softening. Additionally, we detected a blackbody emission with a temperature of approximately 0.1 keV and a size of around 200 km. These characteristics of the blackbody emission suggest the presence of optically thick outflow during the super-Eddington phase, as proposed by Tao et al. (2019) and Beri et al. (2021).

In our spectral examination spanning from 0.7 to 10 keV, along with the evolving iron emission lines as previously noted (e.g., Jaisawal et al. 2019), we detected emission lines at around 1 keV (see Figure 5.7). These lines exhibited noticeable intensity during the super-Eddington phase. The likelihood of these lines originating from instrumental artifacts is low, as indicated by the instrument team[4]. The ∼1 keV line has also been observed in various sources with NICER, including Serpens X-1 (Ludlam et al., 2018), IGR J17062-6143 (Bult et al., 2021), and NGC 300 X-1 (Ng et al., 2022). These emission lines displayed a distinct single-peak shape, which prompted us to model them using a Gaussian function. The changes in the key parameters associated with these lines are depicted in Figure 5.10. Several other studies have also reported the presence of this line in ULX pulsars (Kobayashi et al. 2023 and references therein). These line features could originate from a combination of Fe-L emissions (Gu et al., 2019). The evolution of the 1 keV line parameters with luminosity is illustrated in Figure 5.10. The central line energy variation with luminosity remained within the error bars. However, σ and EW initially increased with luminosity up to the first transitional luminosity L_1 ($\sim 7.5\times10^{37}$ erg s^{-1}), and then decreased beyond that with luminosity. The line width reached up to 0.1 keV, implying that the velocity of the line-emitting material could be around 10% of the light speed based on Doppler broadening. This suggests that the lines might have originated from the accretion disc or an ultra-fast outflow proposed during the super-Eddington phase of the pulsar (van den Eijnden et al., 2019; Jaisawal et al., 2019).

5.6 Conclusion

In conclusion, our analysis of the ultra-luminous X-ray source Swift J0243.6+6124 using NICER data has provided significant insights into its behavior across varying luminosity phases. We observed a luminosity-dependent break in the power density spectra, suggesting alterations in the accretion dynamics, and identified quasi-periodic oscillations within a specific luminosity range. Throughout the 2023 outburst, the neutron star exhibited a spin-up state alongside variations in its pulse profile. Spectral examination unveiled two luminosity-dependent transitions occurring at $L_1 \approx 7.5\times10^{37}$ erg s^{-1} and $L_2 \approx 2.1 \times 10^{38}$ erg s^{-1} in continuum parameters, highlighting the presence of three distinct accretion modes during the giant outburst. We also detected a soft blackbody component ($kT \sim$ 0.08-0.7 keV), which underwent a discontinuous transition as the source transitioned from a sub-Eddington to a super-Eddington state. Notably, emission lines around 1 keV were observed during the super-Eddington state, indicative of X-ray reflection from the accretion disc or outflow material.

[4]https://heasarc.gsfc.nasa.gov/docs/nicer/analysis_threads/arf-rmf/

Chapter 6

Summary and Future Work

This thesis presents our studies on X-ray and optical emission mechanisms in Be/X-ray binaries using X-ray and optical observations of three binary systems with various observatories. The BeXRBs, the largest group within high mass X-ray binaries (HMXBs), typically consist of a neutron star and a massive non-supergiant Be star. The neutron stars in these systems derive their energy by accreting mass from the circumstellar disc of the Be stars, predominantly emitting in the X-ray regime. The companion Be stars are bright in optical and infrared wavebands. They commonly show HI, HeI, and FeII emission lines at specific phases of their lifetime. Such distinctive characteristics are attributed to an equatorial circumstellar disc around the Be star. The BeXRBs show two types of X-ray activities: normal (Type I) and giant (Type II) X-ray outbursts. The peak luminosity of a normal outburst can reach up to 10^{37} erg s^{-1} and are periodic. The periodic nature is attributed to mass accretion by the neutron star during the periastron passage of BeXRB. On the other hand, the giant outbursts are very bright compared to the normal outbursts. The peak luminosity during the giant outbursts can increase to $\sim 10^{37}$ erg s^{-1}. The giant outbursts are rare and occur once or twice in a decade. The cause of the giant outbursts in these systems, the interaction of the neutron star and Be circumstellar disc, and the change in the X-ray emission properties of the neutron star during these outbursts need to be understood clearly. In this thesis, we attempted to address these topics using X-ray and optical observations of a few BeXRBs during X-ray outbursts and quiescent phases.

During the giant X-ray outburst, the luminosity of pulsars changes from 3 to 4 orders of magnitude, and they can also achieve the super-Eddington state, which is very rare in accreting pulsars. The X-ray emission properties change significantly due to the large variation in luminosity. That motivates us to understand the dynamics of complex physical processes in the accretion column with mass accretion rate or luminosity, especially at the super-Eddington phase, which is rarely achieved by any accreting pulsars. To achieve our objectives, we used data from X-ray and optical observatories. This approach is crucial as pulsars emit in X-rays, while their Be companions emit in optical wavelengths.

Three BeXRBs, 1A 0535+262, IGR J06074+2205, and Swift J0243.6+6124, are studied to achieve our objective in this thesis. These sources are chosen as they provide the best scenario that aligns with our objective. We have carried out optical spectroscopic analysis using data from MIRO and IAO. We studied the evolution of the Hα line, the best tracer of the circumstellar disc around Be stars. The change in properties of the Hα line is investigated before, during, and after the outburst to check the effect of the X-ray outburst on the circumstellar disc. Using X-ray data from NICER, AstroSat, and NuSTAR, we performed timing and spectral analysis to understand the properties of the pulsar. Timing and spectroscopic analysis are carried out at various X-ray luminosities to investigate the change in emission properties of the pulsar with mass accretion rate. The results obtained from these studies are presented in previous chapters. In this chapter, a summary and future scopes are described.

6.1 Summary

In Chapter-3, we present optical spectroscopic results of the BeXRB 1A 0535+262, covering epochs before, during, and after the 2020 giant X-ray outburst. Various DIBs and telluric features are detected in the spectra alongside features like Hα, He I (6678 Å), and He I (7065 Å), which are specific to the Be star. These three line features are found to be in emission form throughout our observation, confirming the absence of the disc-loss phase. The Hα line is a good indicator of the physical condition of the circumstellar disc and also has good SNR for a detailed study. The He I line shapes vary throughout our observation. However, during our observations, the SNR of this line is very poor for a detailed study. The Hα line is found to be strongly variable as the outburst progresses. Before the outburst, the Hα emission line was asymmetric and single-peaked with a broad red wing. However, during the outburst, the shape of the line exhibited a broad blue wing. After $\sim$400 days from the onset of the outburst, the profile evolved to a double peaked profile. For a detailed quantification of the variation in shape, the Hα lines are modeled with the Voigt function. Two Voigt functions are used to model the red-shifted and blue-shifted components. By fitting the Voigt function, we calculate two important parameters: V/R (the ratio of blue-shifted to red-shifted flux) and ΔV (peak velocity difference between the blue-shifted and red-shifted components). We also calculate the equivalent width (EW) and $FWHM$ of Hα lines. The value of ΔV is used to calculate the radius of the Be disc. The size of the disc radius varies significantly during our observation period. Before the giant outburst, the size of the Be disc increased and then decreased significantly as the outburst progressed. Prior to the giant outburst, the size of the disc radius is found to be larger than the truncating radius, suggesting a highly misaligned Be disc. From the change in shape and strength of the Be disc, we suggest that during the 2020 giant outburst, the highly misaligned disc warped and precessing, and the neutron star captured a huge amount of matter from the warped disc. We also study the properties of the pulsar during the rising phase of the outburst using AstroSat pointed observation. The X-ray pulsation at 103.55 s is detected in the light curves up to 110 keV. The energy-resolved pulse profiles are generated using SXT, LAXPC, and CZTI data to study the change in its properties in a broad energy range. The pulse profile evolved from a double-peaked shape in low energy ranges to a single-peaked shape at hard X-ray ranges. Pulse profiles obtained in the lower energy ranges exhibit various absorption dips, whereas in higher energy ranges, pulse profiles are smoother. The multiple absorption dips are present because of the inhomogeneous distribution of soft X-ray absorbing material in the ambient region of the neutron star. The broadband spectroscopy is also carried out in the 0.7-90.0 keV range, and the source luminosity is estimated to be 3.91 $\times$ 10^{37} erg s^{-1}. The CRSF is detected at 46.3 keV, suggesting the magnetic field of the pulsar to be 5.2×10^{12} G.

Chapter-4 discusses the X-ray and optical studies of BeXRB IGR J06074+2205. We started our monitoring observations of IGR J06074+2205 in the optical band in November 2022. The source then underwent two X-ray outbursts in October and December 2023. IGR J06074+2205 was observed during both the X-ray outbursts with NICER, whereas NuSTAR observed the source only during the October outburst. We also carried out optical observations close to the outbursts, and the observation continued after that. X-ray timing and spectral analysis of NICER and NuSTAR observations are carried out. We detect coherent X-ray pulsations from the neutron star at $\sim$374.60 seconds. Using this period, the pulse profiles are generated at different luminosity levels in the 0.5-10 keV energy band using NICER data. The pulse profiles at lower luminosity are found to be complex in shape, whereas at higher luminosity, the pulse profiles exhibit smoother shape. Then, to investigate the energy variation of the pulse profiles, we generated pulse profiles at different energy bands. Interestingly, the shape of pulse profiles did not vary much with energy in lower luminosity levels. However, it varied significantly at the higher luminosity phase. In the 0.5-1 keV band, the pulse profile is smooth and single-peaked. With increase in energy, a second peak arises in the 0.5-1 phase range. The second peak eventually becomes dominant at higher energies. Furthermore, the NuSTAR data are used to generate pulse profiles to understand the properties of the pulse profile in the hard X-ray energy range. NuSTAR observed the source at two different luminosity levels. Energy-resolved pulse profiles are generated in narrow energy ranges. The shape of the pulse profiles in low energy ($<$ 20 keV) is significantly different for two NuSTAR observations. At the low luminosity phase only, an absorption dip is present in the 0.5-1 phase range, which is more prominent at lower energy. Hence, the pulse profiles showed a strong correlation with both luminosity and energy, highlighting the complex characteristics of the emitting region. The spectral analysis is carried out using 13 NICER observations in the 1-7 keV energy band. A simple absorbed power-law model described the NICER spectra within the 1-7 keV band. The line of sight absorption and the photon index did not vary much, highlighting the fact that there was no change in the emission properties of the source in the observed luminosity range. The luminosity evolution of the source during the two outbursts suggests that NICER observed the source during the declining phases. To understand the properties of the source in the hard X-ray regime, we carried out the spectral analysis using NuSTAR data. The NuSTAR spectra reveal an iron emission line at around 6.3 keV during the brighter phase, corresponding to a luminosity of $\sim5.56\times10^{36}$ erg s^{-1}. A cyclotron absorption line at approximately 50.7 keV, indicating a magnetic field strength of 5.69×10^{12} G, is detected only during this brighter observation. The orbital parameters of the source are not known yet. Using the long-term MAXI/GSC light curve, we estimated the potential orbital period of IGR J06074+2205 to be approximately 80 days or 80/n days (n=2,3,4). Further, we presented results from optical spectroscopic analysis of observations taken between 2022 and 2024 with MIRO and IAO, using MFOSC-P and HFOSC instruments, respectively. A prominent Hα line is observed throughout our observation. The prominent Fe II (5577.91 Å) line is only observed in recent observations due to the large wavelength coverage of HFOSC. These observations show variability in the Hα and FeII emission lines, with an increase in equivalent width. The Hα and Fe II lines are fitted with the Voigt function. Using the best-fitted parameters, the size of the line-emitting regions is calculated. We find that the size of both line-emitting regions is increasing with time. This suggests that the circumstellar disc around the Be star is growing larger and becoming denser. In our latest observation, we also observe weak signatures of He I (7065 Å), He I (6678 Å), and He I (5875.72 Å) lines, which support the presence of a stronger disc. The Hα line is found to evolve from double-peaked to single-peaked. However, the Fe II line remains double-peaked. This suggests the different orientation angle of Hα and Fe II line emitting region with respect to the observer. We also noted a distinct variation in the V/R value for Hα and Fe II, indicating a non-uniform distribution of a one-armed perturbation in the radial direction. Optical studies suggest that disc properties did not change much during the X-ray outbursts in October and November 2023, unlike during the giant outburst observed in 1A 0535+262. The strength of the disc is also increasing, which can lead to another outburst in the future.

Chapter-5 presents the long-term Study of the first Galactic ULX Swift J0243.6+6124 using NICER. Swift J0243.6+6124 was discovered during the 2017/18 giant outburst. After the giant outburst, the pulsar also showed multiple normal outbursts, including the recent one in 2023. Using the long-term monitoring capabilities of NICER, Swift J0243.6+6124 was observed during the giant and subsequent normal outbursts. We carried out a comprehensive analysis of the X-ray timing and spectral properties of the X-ray pulsar Swift J0243.6+6124 during its giant and normal outbursts between 2017 and 2023. The timing analysis is carried out on the data during the normal outbursts. During the 2023 outburst, the neutron star exhibited a spin-up state, and the pulse profile varied significantly with luminosity between 1.8×10^{36} and 9.3×10^{37} erg s^{-1}. At a lower luminosity state, the pulse profiles exhibit complex structure. With increasing luminosity, the profile becomes smoother. The pulse profile variation with luminosity suggests a change in the behavior of the ambient region with luminosity. We also observed a luminosity-dependent break in power density spectra, indicating changes in accretion dynamics close to the magnetospheric radius. Interestingly, the quasi-periodic oscillations are observed only within a specific luminosity range. Then, we carried out spectral, which includes giant as well as normal outbursts. To understand the evolution of the pulsar emission over multiple outbursts, we considered a uniform continuum model to assess the changes in model parameters with the source luminosity. Spectral analysis revealed two luminosity-dependent transitions at approximately $L_1 \approx 7.5\times10^{37}$ erg s^{-1} and $L_2 \approx 2.1 \times 10^{38}$ erg s^{-1} in continuum parameters, highlighting three distinct accretion modes during the giant outburst. In the first accretion mode, a positive correlation between the photon index (PI) & cutoff energy (E$_{cut}$) was observed, and both are correlated to luminosity. In the second accretion mode, both the PI & E$_{cut}$ exhibited a correlated behavior with each other, but both parameters showed an anti-correlation with the luminosity.

In the third accretion mode, the source is in a supercritical state, and we found that the PI remains almost constant with luminosity while the E_{cut} value decreases. These findings suggest the change in complex dynamics of physical processes near neutron stars as the source evolves from the sub-Eddington to the super-Eddington phase. We detected a soft blackbody component ($kT \sim 0.08$-0.7 keV), which underwent a discontinuous transition as the source evolved from a sub-Eddington to a super-Eddington state. We also observed an emission line around 1 keV during the super-Eddington state. The line width reaches up to 0.1 keV, suggesting the velocity of the line-emitting material is around 10% of the speed of light. Hence, ultra-fast moving material is the probable origin of the 1 keV line. The detection of ~1 keV line signifies that during the super-Eddington phase, a strong optically thin ultra-fast outflow is present in the system.

The focus of my thesis is on Be/X-ray binary systems (BeXRBs) to examine the mechanisms of giant X-ray outbursts and corresponding X-ray and optical emissions from the binary companions. The BeXRBs exhibit two types of outbursts: Type I (normal) and Type II (giant). While the basic mechanisms of Type I outbursts are well understood, the causes of giant outbursts still need to be better understood. Giant outbursts are rare, with some sources never exhibiting this kind outburst. To address this gap, I conducted a long-term optical study of a particular BeXRB source, finding that during a giant X-ray outburst, mass accretion takes place by the neutron star from a warped circumstellar disc of the companion Be star. This suggests that the accretion of mass from a warped disc could be a key mechanism behind the giant X-ray outbursts. Additionally, my research delves into the physical processes within the accretion column that influence X-ray emissions from pulsars. These processes vary significantly with the mass accretion rate or luminosity, especially when pulsars exceed the Eddington limit, a rare phenomenon. By studying a specific source, I found that the source underwent three distinct accretion modes as it evolved from sub-Eddington to super-Eddington states. This indicates that the complex physical processes in the accretion column change drastically with varying luminosity states. My contributions to the community include providing insights into the mechanisms behind the giant outbursts in BeXRBs and advancing the understanding of the dynamics of physical processes in the accretion column during different luminosity phases.

6.2 Future prospects

Building on the findings of this thesis, several directions for future research emerge that can further advance our understanding of BeXRBs. In the future, I will focus on more detailed statistical aspects of various X-ray and optical phenomena observed in BeXRBs.

Firstly, while this study has suggested that the giant X-ray outbursts in BeXRBs may be driven by the accretion of mass from a warped circumstellar disc, further investigations are needed to confirm this mechanism across different sources. Future research plan involves long-term multi-wavelength observational campaigns to track the disc dynamics and mass transfer processes in a broader sample of BeXRBs. High-resolution spectroscopy and advanced modeling techniques could provide deeper insights into the conditions that lead to the formation of warped discs and their role in triggering giant outbursts. We have been monitoring and will continue our monitoring program of six BeXRBs in the optical waveband. This will help us understand the long-term optical properties of BeXRBs and the different conditions of the disc at which X-ray outbursts occur. During our project on IGR J06074+2205, we came to know about two of its peculiar properties such as (i) the detection of pulsation when the Hα line was in absorption, and (ii) the transition of Hα line from emission to absorption without observation of any significant X-ray outburst. Future multi-wavelength simultaneous observations will help us in understanding these aspects. We also have proposed optical observation of two BeXRBs 1A 0535+262 and LS V 44+77 at higher wavelength resolution (R$\sim$30000) from the Hanle echelle spectrograph (HESP) mounted on the Himalayan Chandra Telescope (HCT) at IAO. The HESP data will help us understand the complex structure of line emission profiles that arise due to the effect of the warped discs.

Quasi-periodic oscillation (QPO) features are observed in Swift J0243.6+6124 and exhibited exciting properties. The QPOs are detected only within a specific luminosity range. Hence, studying QPOs in detail will provide us knowledge on the complex interaction between the inner accretion disc and the magnetic field of the neutron star. The energy-resolved pulse profile of IGR J06074+2205 obtained using NICER data exhibited unique properties that, at lower energy, the pulse profile is single-peaked. However, with increase in energy, another peak is found to emerge in the pulse profile. The evolution of pulse profiles in such a manner is also observed in sources like GX 301-2 and Vela X-1. However, this behavior of the pulse profile is in contrast with many other accreting X-ray pulsars like GRO J1008-57, 4U 0115+63, 4U 1909+07, 1A 0535+262, and 2S 1417-624, where secondary peak intensity decreases as the energy increases. Hence, a detailed study of this feature is required to provide a clear picture. In future, I will look into this feature in more detail at different luminosity and energy ranges.

Additionally, the study of the physical processes in the accretion column, especially during the super-Eddington phase, remains an area for exploration. My future work will focus on conducting detailed physical modeling of the accretion column dynamics under varying mass accretion rates. The physical models will be applied to broadband spectra using data from X-ray observatories like NuSTAR and AstroSat.

Bibliography

Agrawal, P. 2006, A broad spectral band Indian Astronomy satellite 'Astrosat', Advances in Space Research, 38, 2989

Alonso-Hernández, J., Fürst, F., Kretschmar, P., Caballero, I., & Joyce, A. M. 2022, Common patterns in pulse profiles of high-mass X-ray binaries, A&A, 662, A62

Alpar, M. A. & Shaham, J. 1985, Is GX5 - 1 a millisecond pulsar?, Nature, 316, 239

Angelini, L., Stella, L., & Parmar, A. N. 1989, The Discovery of 0.2 HZ Quasi-periodic Oscillations in the X-Ray Flux of the Transient 42 Second Pulsar EXO 2030+374, ApJ, 346, 906

Angeloni, R., Gonçalves, D. R., Akras, S., et al. 2019, RAMSES II: RAMan Search for Extragalactic Symbiotic Stars Project Concept, Commissioning, and Early Results from the Science Verification Phase, AJ, 157, 156

Antia, H. M., Agrawal, P. C., Dedhia, D., et al. 2021, Large Area X-ray Proportional Counter (LAXPC) in orbit performance: Calibration, background, analysis software, Journal of Astrophysics and Astronomy, 42, 32

Antoniou, V. & Zezas, A. 2016, Star formation history and X-ray binary populations: the case of the Large Magellanic Cloud, MNRAS, 459, 528

Arias, M. L., Zorec, J., Cidale, L., et al. 2006, Fe II emission lines in Be stars. I. Empirical diagnostic of physical conditions in the circumstellar discs, A&A, 460, 821

Arnason, R. M., Papei, H., Barmby, P., Bahramian, A., & Gorski, M. D. 2021, Distances to Galactic X-ray binaries with Gaia DR2, MNRAS, 502, 5455

Arnaud, K. A. 1996, in Astronomical Society of the Pacific Conference Series, Vol. 101, Astronomical Data Analysis Software and Systems V, ed. G. H. Jacoby & J. Barnes, 17

Bailer-Jones, C. A. L., Rybizki, J., Fouesneau, M., Mantelet, G., & Andrae, R. 2018, Estimating Distance from Parallaxes. IV. Distances to 1.33 Billion Stars in Gaia Data Release 2, AJ, 156, 58

Banerjee, G., Mathew, B., Paul, K. T., et al. 2022, Study of transient nature of classical Be stars using multi-epoch optical spectroscopy, Journal of Astrophysics and Astronomy, 43, 102

Basko, M. M. & Sunyaev, R. A. 1976, The limiting luminosity of accreting neutron stars with magnetic fields., MNRAS, 175, 395

Becker, P. A. 2003, Exact solution for the Green's function describing time-dependent thermal Comptonization, MNRAS, 343, 215

Becker, P. A., Klochkov, D., Schönherr, G., et al. 2012, Spectral formation in accreting X-ray pulsars: bimodal variation of the cyclotron energy with luminosity, A&A, 544, A123

Becker, P. A. & Wolff, M. T. 2007, Thermal and Bulk Comptonization in Accretion-powered X-Ray Pulsars, ApJ, 654, 435

Becker, P. A. & Wolff, M. T. 2022, A Generalized Analytical Model For Thermal And Bulk Comptonization In Accretion-Powered X-Ray Pulsars, arXiv e-prints, arXiv:2211.13894

Belloni, T., Psaltis, D., & van der Klis, M. 2002, A Unified Description of the Timing Features of Accreting X-Ray Binaries, ApJ, 572, 392

Beri, A., Naik, S., Singh, K. P., et al. 2021, AstroSat observations of the first Galactic ULX pulsar Swift J0243.6+6124, MNRAS, 500, 565

Bhalerao, V., Bhattacharya, D., Vibhute, A., et al. 2017, The cadmium zinc telluride imager on AstroSat, Journal of Astrophysics and Astronomy, 38, 1

Bikmaev, I., Shimansky, V., Irtuganov, E., et al. 2017, Determination of the distance to SWIFT J0243.6+6124, The Astronomer's Telegram, 10968, 1

Bildsten, L., Chakrabarty, D., Chiu, J., et al. 1997, Observations of Accreting Pulsars, ApJS, 113, 367

Bondi, H. & Hoyle, F. 1944, On the mechanism of accretion by stars, MNRAS, 104, 273

Boutelier, M., Barret, D., Lin, Y., & Török, G. 2010, On the distribution of frequency ratios of kHz quasi-periodic oscillations, MNRAS, 401, 1290

Bult, P., Strohmayer, T. E., Malacaria, C., Ng, M., & Wadiasingh, Z. 2021, Long-term Coherent Timing of the Accreting Millisecond Pulsar IGR J17062-6143, ApJ, 912, 120

Burnard, D. J., Arons, J., & Klein, R. I. 1991, Accretion Powered Pulsars: Continuum Spectra and Light Curves of Settling Accretion Mounds, ApJ, 367, 575

Bykov, S. D., Gilfanov, M. R., Tsygankov, S. S., & Filippova, E. V. 2022, ULX pulsar Swift J0243.6+6124 observations with NuSTAR: dominance of reflected emission in the super-Eddington state, MNRAS, 516, 1601

Caballero, I., Pottschmidt, K., Marcu, D. M., et al. 2013, A Double-peaked Outburst of A 0535+26 Observed with INTEGRAL, RXTE, and Suzaku, ApJ, 764, L23

Camero-Arranz, A., Finger, M. H., Wilson-Hodge, C. A., et al. 2012, X-Ray and Optical Observations of A 0535+26, ApJ, 754, 20

Camero Arranz, A., Wilson, C. A., Finger, M. H., & Reglero, V. 2007, Long-term pulse profile study of the Be/X-ray pulsar SAX J2103.5+4545, A&A, 473, 551

Cameron, A. G. W. & Mock, M. 1967, Stellar Accretion and X-ray Emission, Nature, 215, 464

Campana, S., Stella, L., Israel, G. L., et al. 2002, The Quiescent X-Ray Emission of Three Transient X-Ray Pulsars, ApJ, 580, 389

Casares, J., Negueruela, I., Ribó, M., et al. 2014, A Be-type star with a black-hole companion, Nature, 505, 378

Cenko, S. B., Barthelmy, S. D., D'Avanzo, P., et al. 2017, GRB 171003A: Swift detection of a burst or a Galactic Transient., GRB Coordinates Network, 21960, 1

Chenevez, J., Budtz-Jorgensen, C., Lund, N., et al. 2004, IGR J06074+2205 a new X-ray source discovered by INTEGRAL, The Astronomer's Telegram, 223, 1

Cheng, Z. Q., Shao, Y., & Li, X. D. 2014, On the Spin Period Distribution in Be/X-Ray Binaries, ApJ, 786, 128

Chhotaray, B., Jaisawal, G. K., Kumari, N., et al. 2023, Optical and X-ray studies of Be/X-ray binary 1A 0535+262 during its 2020 giant outburst, MNRAS, 518, 5089

Chhotaray, B., Jaisawal, G. K., Nandi, P., et al. 2024, Long-term Study of the First Galactic Ultraluminous X-Ray Source Swift J0243.6+6124 Using NICER, ApJ, 963, 132

Clark, J. S., Lyuty, V. M., Zaitseva, G. V., et al. 1999, Long-term variability of the Be/X-ray binary A0535+26 - III. Photometry, MNRAS, 302, 167

Clark, J. S. & Steele, I. A. 2000, A representative sample of Be stars. II. K band spectroscopy, A&AS, 141, 65

Clark, J. S., Tarasov, A. E., Steele, I. A., et al. 1998, Long-term variability of the Be/X-ray binary A0535+26 - I. Optical and UV spectroscopy, MNRAS, 294, 165

Coburn, W., Heindl, W. A., Rothschild, R. E., et al. 2002, Magnetic Fields of Accreting X-Ray Pulsars with the Rossi X-Ray Timing Explorer, ApJ, 580, 394

Coe, M. J., Edge, W. R. T., Galache, J. L., & McBride, V. A. 2005, Optical properties of Small Magellanic Cloud X-ray binaries, MNRAS, 356, 502

Coe, M. J. & Kirk, J. 2015, Catalogue of Be/X-ray binary systems in the Small Magellanic Cloud: X-ray, optical and IR properties, MNRAS, 452, 969

Coe, M. J., Reig, P., McBride, V. A., Galache, J. L., & Fabregat, J. 2006, A 0535+26: back in business, MNRAS, 368, 447

Corbet, R. H. D., Coley, J. B., Gendreau, K. C., et al. 2022, Support for a 244 day Period in XTE J1829-098 from Swift BAT, MAXI and RXTE PCA Observations, The Astronomer's Telegram, 15614, 1

Cowsik, R., Srinivasan, R., & Prabhu, T. 2002, in Astronomical Society of the Pacific Conference Series, Vol. 266, Astronomical Site Evaluation in the Visible and Radio Range, ed. J. Vernin, Z. Benkhaldoun, & C. Muñoz-Tuñón, 424

Davidson, K. 1973, Accretion at a Magnetic Pole of a Neutron Star, Nature Physical Science, 246, 1

Doroshenko, V., Tsygankov, S., & Santangelo, A. 2018, Orbit and intrinsic spin-up of the newly discovered transient X-ray pulsar Swift J0243.6+6124, A&A, 613, A19

Doroshenko, V., Zhang, S. N., Santangelo, A., et al. 2020, Hot disc of the Swift J0243.6+6124 revealed by Insight-HXMT, MNRAS, 491, 1857

Dugair, M. R., Jaisawal, G. K., Naik, S., & Jaaffrey, S. N. A. 2013, Detection of a variable QPO at ∼41 mHz in the Be/X-ray transient pulsar 4U 0115+634, MNRAS, 434, 2458

Elshamouty, K. G., Heinke, C. O., Morsink, S. M., Bogdanov, S., & Stevens, A. L. 2016, THE IMPACT OF SURFACE TEMPERATURE INHOMOGENEITIES ON QUIESCENT NEUTRON STAR RADIUS MEASUREMENTS, The Astrophysical Journal, 826, 162

Epili, P., Naik, S., Jaisawal, G. K., & Gupta, S. 2017a, Decade long RXTE monitoring observations of Be/X-ray binary pulsar EXO 2030+375, MNRAS, 472, 3455

Epili, P., Naik, S., Jaisawal, G. K., & Gupta, S. 2017b, Decade long RXTE monitoring observations of Be/X-ray binary pulsar EXO 2030+375, MNRAS, 472, 3455

Ferrigno, C., D'Aì, A., & Ambrosi, E. 2023, Energy-resolved pulse profiles of accreting pulsars: Diagnostic tools for spectral features, A&A, 677, A103

Finger, M. H., Cominsky, L. R., Wilson, R. B., Harmon, B. A., & Fishman, G. J. 1994, in American Institute of Physics Conference Series, Vol. 308, The Evolution of X-ray Binariese, ed. S. Holt & C. S. Day (AIP), 459

Finger, M. H., Wilson, R. B., & Harmon, B. A. 1996, Quasi-periodic Oscillations during a Giant Outburst of A0535+262, ApJ, 459, 288

Forman, W., Jones, C., Cominsky, L., et al. 1978, The fourth Uhuru catalog of X-ray sources., ApJS, 38, 357

Fornasini, F. M., Antoniou, V., & Dubus, G. 2023, High-mass X-ray Binaries, arXiv e-prints, arXiv:2308.02645

Fortin, F., García, F., & Chaty, S. 2022, Finding the birthplace of HMXBs in the Galaxy using Gaia EDR3: Kinematical age determination through orbit integration, A&A, 665, A69

Fortin, F., García, F., Simaz Bunzel, A., & Chaty, S. 2023, A catalogue of high-mass X-ray binaries in the Galaxy: from the INTEGRAL to the Gaia era, A&A, 671, A149

Frank, J., King, A., & Raine, D. J. 2002, Accretion Power in Astrophysics: Third Edition

Gehrels, N., Chincarini, G., Giommi, P., et al. 2004, The Swift Gamma-Ray Burst Mission, ApJ, 611, 1005

Gehrz, R. D., Hackwell, J. A., & Jones, T. W. 1974, Infrared observations of Be stars from 2.3 to 19.5 microns., ApJ, 191, 675

Gendreau, K. C., Arzoumanian, Z., Adkins, P. W., et al. 2016, in Society of Photo-Optical Instrumentation Engineers (SPIE) Conference Series, Vol. 9905, Space Telescopes and Instrumentation 2016: Ultraviolet to Gamma Ray, ed. J.-W. A. den Herder, T. Takahashi, & M. Bautz, 99051H

Ghosh, P. & Lamb, F. K. 1979, Accretion by rotating magnetic neutron stars. III. Accretion torques and period changes in pulsating X-ray sources., ApJ, 234, 296

Giacconi, R., Gursky, H., Paolini, F. R., & Rossi, B. B. 1962, Evidence for x Rays From Sources Outside the Solar System, Phys. Rev. Lett., 9, 439

Giangrande, A., Giovannelli, F., Bartolini, C., Guarnieri, A., & Piccioni, A. 1980, Optical spectra of HDE 245770 = A 0535+26., A&AS, 40, 289

Gies, D. R. 2000, in Astronomical Society of the Pacific Conference Series, Vol. 214, IAU Colloq. 175: The Be Phenomenon in Early-Type Stars, ed. M. A. Smith, H. F. Henrichs, & J. Fabregat, 668

Gies, D. R., Bagnuolo, W. G., J., Baines, E. K., et al. 2007, CHARA Array K'-Band Measurements of the Angular Dimensions of Be Star Disks, ApJ, 654, 527

Grundstrom, E. D., Boyajian, T. S., Finch, C., et al. 2007, Joint Hα and X-Ray Observations of Massive X-Ray Binaries. III. The Be X-Ray Binaries HDE 245770 = A0535+26 and X Persei, ApJ, 660, 1398

Gu, L., Raassen, A. J. J., Mao, J., et al. 2019, X-ray spectra of the Fe-L complex, A&A, 627, A51

Gupta, S., Naik, S., Jaisawal, G. K., & Epili, P. R. 2018, Spectral and timing studies of 2S 1417-624 during a giant outburst, MNRAS, 479, 5612

Gursky, H., Giacconi, R., Gorenstein, P., et al. 1966, A Measurement of the Angular Size of the X-Ray Source SCO X-1, ApJ, 144, 1249

Haberl, F. & Sturm, R. 2016, High-mass X-ray binaries in the Small Magellanic Cloud, A&A, 586, A81

Haigh, N. J., Coe, M. J., & Fabregat, J. 2004, Cyclical behaviour and disc truncation in the Be/X-ray binary A0535+26, MNRAS, 350, 1457

Haigh, N. J., Coe, M. J., Steele, I. A., & Fabregat, J. 1999, Disc loss and renewal in A0535+26, MNRAS, 310, L21

Halpern, J. P. & Tyagi, S. 2005, Be Star Counterpart of X-ray Transient IGR J06074+2205, The Astronomer's Telegram, 682, 1

Hanuschik, R. W. 1989, Stellar V/sin/i and Optical Emission Linewidths in Be-Stars, Ap&SS, 161, 61

Hanuschik, R. W. 1996, On the structure of Be star disks., A&A, 308, 170

Hanuschik, R. W., Hummel, W., Dietle, O., & Sutorius, E. 1995, V/R variability and global oscillations in Be star disks., A&A, 300, 163

Harrison, F. A., Craig, W. W., Christensen, F. E., et al. 2013, The Nuclear Spectroscopic Telescope Array (NuSTAR) High-energy X-Ray Mission, ApJ, 770, 103

Hasinger, G. & van der Klis, M. 1989, Two patterns of correlated X-ray timing and spectral behaviour in low-mass X-ray binaries., A&A, 225, 79

Hastings, B., Wang, C., & Langer, N. 2020, The single star path to Be stars, A&A, 633, A165

Herbig, G. H. 1995, The Diffuse Interstellar Bands, ARA&A, 33, 19

Hoshino, M. & Takeshima, T. 1993, A Turbulent Model of Time Variability in X-Ray Binary Pulsars, ApJ, 411, L79

Hou, W., Luo, A. L., Hu, J.-Y., et al. 2016, A catalog of early-type emission-line stars and Hα line profiles from LAMOST DR2, Research in Astronomy and Astrophysics, 16, 138

Huang, S.-S. 1972, Profiles of Emission Lines in be Stars, ApJ, 171, 549

Hummel, W. & Hanuschik, R. W. 1997, Line formation in Be star envelopes. II. Disk oscillations., A&A, 320, 852

Illarionov, A. F. & Sunyaev, R. A. 1975, Why the Number of Galactic X-ray Stars Is so Small?, A&A, 39, 185

Jaisawal, G. K., Coley, J. B., Wilms, J., et al. 2020a, Super-critical accretion onto the Be/X-ray binary pulsar 1A 0535+262 during its 2020 giant X-ray outburst, The Astronomer's Telegram, 14227, 1

Jaisawal, G. K., Naik, S., & Chenevez, J. 2018, Understanding the spectral and timing behaviour of a newly discovered transient X-ray pulsar Swift J0243.6+6124, MNRAS, 474, 4432

Jaisawal, G. K., Naik, S., & Epili, P. 2016, Suzaku view of the Be/X-ray binary pulsar GX 304-1 during Type I X-ray outbursts, MNRAS, 457, 2749

Jaisawal, G. K., Naik, S., Gendreau, K. C., et al. 2020b, NICER and NuSTAR observations of the Be/X-ray binary pulsar 1A 0535+262 during the 2020 November giant outburst, The Astronomer's Telegram, 14179, 1

Jaisawal, G. K., Naik, S., Gupta, S., et al. 2021, Detection of X-ray pulsations at the lowest observed luminosity of Be/X-ray binary pulsar EXO 2030+375 with AstroSat, Journal of Astrophysics and Astronomy, 42, 33

Jaisawal, G. K., Naik, S., Ho, W. C. G., et al. 2020c, Revisiting the spectral and timing properties of 4U 1909+07 with NuSTAR and Astrosat, MNRAS, 498, 4830

Jaisawal, G. K., Vasilopoulos, G., Naik, S., et al. 2023, On the cyclotron absorption line and evidence of the spectral transition in SMC X-2 during 2022 giant outburst, MNRAS, 521, 3951

Jaisawal, G. K., Wilson-Hodge, C. A., Fabian, A. C., et al. 2019, An Evolving Broad Iron Line from the First Galactic Ultraluminous X-Ray Pulsar Swift J0243.6+6124, ApJ, 885, 18

James, M., Paul, B., Devasia, J., & Indulekha, K. 2010, Discovery of a 0.02 Hz QPO feature in the transient X-ray pulsar KS 1947+300, MNRAS, 407, 285

Jenke, P. & Wilson-Hodge, C. A. 2017, Fermi GBM detects pulsations from Swift J0243.6+6124, The Astronomer's Telegram, 10812, 1

Kanno, S. 1980, Frequency dependence of pulse profiles of accreting X-ray pulsars., PASJ, 32, 105

Kaper, L. 1995, in Wolf-Rayet Stars: Binaries; Colliding Winds; Evolution, ed. K. A. van der Hucht & P. M. Williams, Vol. 163, 271

Kendziorra, E., Kretschmar, P., Pan, H. C., et al. 1994, Evidence for cyclotron line features in high energy spectra of A 0535+26 during the March/April 1989 outburst., A&A, 291, L31

Kennea, J. A. & Cenko, S. B. 2017, Swift Trigger 775946 is a Galactic transient, not GRB 171003., GRB Coordinates Network, 21963, 1

Kennea, J. A., Lien, A. Y., Krimm, H. A., Cenko, S. B., & Siegel, M. H. 2017, Swift J0243.6+6124: Swift discovery of an accreting NS transient, The Astronomer's Telegram, 10809, 1

Kobayashi, S. B., Noda, H., Enoto, T., et al. 2023, Decomposing the Spectrum of Ultraluminous X-Ray Pulsar NGC 300 ULX-1, ApJ, 955, 124

Kong, L. D., Zhang, S., Chen, Y. P., et al. 2020, Two Complete Spectral Transitions of Swift J0243.6+6124 Observed by Insight-HXMT, ApJ, 902, 18

Kong, L. D., Zhang, S., Ji, L., et al. 2021, Luminosity Dependence of the Cyclotron Line Energy in 1A 0535+262 Observed by Insight-HXMT during the 2020 Giant Outburst, ApJ, 917, L38

Kong, L.-D., Zhang, S., Zhang, S.-N., et al. 2022, Insight-HXMT Discovery of the Highest-energy CRSF from the First Galactic Ultraluminous X-Ray Pulsar Swift J0243.6+6124, ApJ, 933, L3

Kouroubatzakis, K., Reig, P., Andrews, J., &), A. Z. 2017, The optical counterpart to the new accreting pulsar Swift J0243.6+6124 is a Be star, The Astronomer's Telegram, 10822, 1

KreŁowski, J. & Schmidt, M. 1997, Intrinsic Profiles of Strong Diffuse Interstellar Bands, ApJ, 477, 209

Kretschmar, P., Nespoli, E., Reig, P., & Anders, F. 2012, in Proceedings of "An INTEGRAL view of the high-energy sky (the first 10 years)" - 9th INTEGRAL Workshop and celebration of the 10th anniversary of the launch (INTEGRAL 2012). 15-19 October 2012. Bibliotheque Nationale de France, 16

Kreykenbohm, I., Coburn, W., Wilms, J., et al. 2002, Confirmation of two cyclotron lines in Vela X-1, A&A, 395, 129

Kreykenbohm, I., Wilms, J., Coburn, W., et al. 2004, The variable cyclotron line in GX 301-2, A&A, 427, 975

Kriz, S. & Harmanec, P. 1975, A Hypothesis of the Binary Origin of Be Stars, Bulletin of the Astronomical Institutes of Czechoslovakia, 26, 65

Kudritzki, R. P. & Hummer, D. G. 1990, Quantitative spectroscopy of hot stars., ARA&A, 28, 303

Kumar, V., Srivastava, M. K., Banerjee, D. P. K., et al. 2022, Optical and near-infrared spectroscopy of Nova V2891 Cygni: evidence for shock-induced dust formation, MNRAS, 510, 4265

Lamb, F. K., Pethick, C. J., & Pines, D. 1973, A Model for Compact X-Ray Sources: Accretion by Rotating Magnetic Stars, ApJ, 184, 271

Langer, S. H. & Rappaport, S. 1982, Low-luminosity accretion onto magnetized neutron stars, ApJ, 257, 733

Laurent, P. & Titarchuk, L. 1999, The Converging Inflow Spectrum Is an Intrinsic Signature for a Black Hole: Monte Carlo Simulations of Comptonization on Free-falling Electrons, ApJ, 511, 289

Leahy, D. A. 1987, Searches for pulsed emission - Improved determination of period and amplitude from epoch folding for sinusoidal signals, A&A, 180, 275

Lee, U., Osaki, Y., & Saio, H. 1991, Viscous excretion discs around Be stars, MNRAS, 250, 432

Lewin, W. H. G., van Paradijs, J., & van den Heuvel, E. P. J. 1997, X-ray Binaries

Li, P. P., Tao, L., Tuo, Y. L., et al. 2023, Timing properties of the X-ray accreting pulsar RX J0440.9+4431 studied with Insight-HXMT and NICER, MNRAS, 526, 3637

Liu, B., Sartorio, N. S., Izzard, R. G., & Fialkov, A. 2024, Population synthesis of Be X-ray binaries: metallicity dependence of total X-ray outputs, MNRAS, 527, 5023

Liu, J., Ji, L., & Ge, M. 2023, The Spin-down Accretion Regime of Galactic Ultraluminous X-Ray Pulsar Swift J0243.6+6124, ApJ, 950, 42

Liu, W., Yan, J., Reig, P., et al. 2022, Multiwavelength observations of Swift J0243.6+6124 from 2017 to 2022, A&A, 666, A110

Lopes de Oliveira, R., Smith, M. A., & Motch, C. 2010, γ Cassiopeiae: an X-ray Be star with personality, A&A, 512, A22

Ludlam, R. M., Miller, J. M., Arzoumanian, Z., et al. 2018, Detection of Reflection Features in the Neutron Star Low-mass X-Ray Binary Serpens X-1 with NICER, ApJ, 858, L5

Makishima, K., Mihara, T., Nagase, F., & Tanaka, Y. 1999, Cyclotron Resonance Effects in Two Binary X-Ray Pulsars and the Evolution of Neutron Star Magnetic Fields, ApJ, 525, 978

Malacaria, C., Jenke, P., Roberts, O. J., et al. 2020, The Ups and Downs of Accreting X-Ray Pulsars: Decade-long Observations with the Fermi Gamma-Ray Burst Monitor, ApJ, 896, 90

Malacaria, C., Kollatschny, W., Whelan, E., et al. 2017, Optical spectroscopy of the Be/X-ray binary V850 Centauri/GX 304-1 during faint X-ray periodical activity, A&A, 603, A24

Mandal, M. & Pal, S. 2022, Study of timing and spectral properties of the X-ray pulsar 1A 0535+262 during the giant outburst in 2020 November-December, MNRAS, 511, 1121

Mandal, M., Pal, S., Hazra, M., et al. 2020, Swift/BAT detection of flaring activity from X-ray binary pulsar A 0535+262, The Astronomer's Telegram, 14157, 1

Mathew, B. & Subramaniam, A. 2011, Optical spectroscopy of Classical Be stars in open clusters, Bulletin of the Astronomical Society of India, 39, 517

Mihara, T. 1995, PhD thesis, -

Mihara, T. & Maxi Team. 2010, in The First Year of MAXI: Monitoring Variable X-ray Sources, 57

Mihara, T., Nakajima, M., Negoro, H., et al. 2023, MAXI/GSC observations of weak X-ray outbursts from the Be/X-ray binary pulsar IGR J06074+2205 and the possible binary orbital period, The Astronomer's Telegram, 16351, 1

Monageng, I. M., McBride, V. A., Coe, M. J., Steele, I. A., & Reig, P. 2017, On the relationship between circumstellar disc size and X-ray outbursts in Be/X-ray binaries, MNRAS, 464, 572

Moritani, Y., Nogami, D., Okazaki, A. T., et al. 2011, Drastic Spectroscopic Variability of the Be/X-Ray Binary Ariel 0535+262/V725 Tau during and after the 2009 Giant Outburst, PASJ, 63, 25

Moritani, Y., Nogami, D., Okazaki, A. T., et al. 2010, High-dispersion spectroscopic monitoring of the Be/X-ray binary A0535+26/V725 Tau - I. The long-term profile variability, MNRAS, 405, 467

Moritani, Y., Nogami, D., Okazaki, A. T., et al. 2013, Precessing Warped Be Disk Triggering the Giant Outbursts in 2009 and 2011 in A0535+262/V725Tau, PASJ, 65, 83

Nagase, F. 1989, Accretion-powered X-ray pulsars., PASJ, 41, 1

Naik, S., Chhotaray, B., & Kumari, N. 2024, Optical Spectroscopy of 1A 0535+262 Before, During, and After the 2020 Giant X-ray Outburst, Bulletin de la Societe Royale des Sciences de Liege, 93, 657

Naik, S., Dotani, T., Terada, Y., et al. 2008, Broadband X-Ray Spectroscopy of A0535+262 with Suzaku, ApJ, 672, 516

Naik, S. & Jaisawal, G. K. 2015, Suzaku observation of Be/X-ray binary pulsar EXO 2030+375, Research in Astronomy and Astrophysics, 15, 537

Naik, S., Maitra, C., Jaisawal, G. K., & Paul, B. 2013, Timing and Spectral Properties of Be/X-Ray Pulsar EXO 2030+375 during a Type I Outburst, ApJ, 764, 158

Naik, S., Paul, B., Kachhara, C., & Vadawale, S. V. 2011, Suzaku observation of the transient X-ray pulsar GRO J1008-57, MNRAS, 413, 241

Nakajima, M., Mihara, T., Negoro, H., et al. 2023, MAXI/GSC observation of the X-ray outburst from IGR J06074+2205, The Astronomer's Telegram, 16394, 1

Nakajima, M., Negoro, H., Mihara, T., et al. 2024, NICER follow-up of the Be/X-ray binary pulsar IGR J06074+2205 in outburst, The Astronomer's Telegram, 16401, 1

Negueruela, I. 1998, On the nature of Be/X-ray binaries, A&A, 338, 505

Negueruela, I. & Okazaki, A. T. 2001, The Be/X-ray transient 4U 0115+63/V635 Cassiopeiae. I. A consistent model, A&A, 369, 108

Negueruela, I., Okazaki, A. T., Fabregat, J., et al. 2001, The Be/X-ray transient 4U 0115+63/V635 Cassiopeiae. II. Outburst mechanisms, A&A, 369, 117

Nelson, R. W., Salpeter, E. E., & Wasserman, I. 1993, Nonthermal Cyclotron Emission from Low-Luminosity Accretion onto Magnetic Neutron Stars, ApJ, 418, 874

Nesci, R., Fiocchi, M., & Vagnozzi, A. 2024, Long term optical variability of two HMXB, Open European Journal on Variable Stars, 249, 1

Ng, M., Remillard, R. A., Steiner, J. F., Chakrabarty, D., & Pasham, D. R. 2022, Spectral Evolution of Ultraluminous X-Ray Pulsar NGC 300 ULX-1, ApJ, 940, 138

Okajima, T., Soong, Y., Balsamo, E. R., et al. 2016, in Society of Photo-Optical Instrumentation Engineers (SPIE) Conference Series, Vol. 9905, Space Telescopes and Instrumentation 2016: Ultraviolet to Gamma Ray, ed. J.-W. A. den Herder, T. Takahashi, & M. Bautz, 99054X

Okazaki, A. T. 1997, On the confinement of one-armed oscillations in discs of Be stars., A&A, 318, 548

Okazaki, A. T. 2001, Viscous Transonic Decretion in Disks of Be Stars, PASJ, 53, 119

Okazaki, A. T. & Hayasaki, K. 2007, in Astronomical Society of the Pacific Conference Series, Vol. 361, Active OB-Stars: Laboratories for Stellare and Circumstellar Physics, ed. A. T. Okazaki, S. P. Owocki, & S. Stefl, 395

Okazaki, A. T., Hayasaki, K., & Moritani, Y. 2013, Origin of Two Types of X-Ray Outbursts in Be/X-Ray Binaries. I. Accretion Scenarios, PASJ, 65, 41

Okazaki, A. T. & Negueruela, I. 2001, A natural explanation for periodic X-ray outbursts in Be/X-ray binaries, A&A, 377, 161

Papaloizou, J. C., Savonije, G. J., & Henrichs, H. F. 1992, On the long-term periodicities in Be stars., A&A, 265, L45

Parmar, A. N., White, N. E., & Stella, L. 1989, The Transient 42 Second X-Ray Pulsar EXO 2030+375. II. The Luminosity Dependence of the Pulse Profile, ApJ, 338, 373

Paul, B. & Naik, S. 2011, Transient High Mass X-ray Binaries, Bulletin of the Astronomical Society of India, 39, 429

Pfahl, E., Rappaport, S., & Podsiadlowski, P. 2003, The Galactic Population of Low- and Intermediate-Mass X-Ray Binaries, ApJ, 597, 1036

Pooley, G. 2004, IGR J06074+2205 - possible association with radio source, The Astronomer's Telegram, 226, 1

Porter, J. M. 1996, On the rotational velocities of Be and Be-shell stars, MNRAS, 280, L31

Porter, J. M. & Rivinius, T. 2003, Classical Be Stars, PASP, 115, 1153

Poutanen, J., Ibragimov, A., & Annala, M. 2009, On the Nature of Pulse Profile Variations and Timing Noise in Accreting Millisecond Pulsars, ApJ, 706, L129

Pradhan, P., Pike, S., Coley, J. B., et al. 2023, NuSTAR looks at Swift J0243.6+6124 during the rise of the 2023 outburst, The Astronomer's Telegram, 16139, 1

Prigozhin, G., Gendreau, K., Doty, J. P., et al. 2016, in Society of Photo-Optical Instrumentation Engineers (SPIE) Conference Series, Vol. 9905, Space Telescopes and Instrumentation 2016: Ultraviolet to Gamma Ray, ed. J.-W. A. den Herder, T. Takahashi, & M. Bautz, 99051I

Pringle, J. E. 1981, Accretion discs in astrophysics, ARA&A, 19, 137

Pringle, J. E. & Rees, M. J. 1972, Accretion Disc Models for Compact X-Ray Sources, A&A, 21, 1

Rai, B. & Paul, B. C. 2021, Timing and spectral properties of the Be/X-ray pulsar 4U 1901+03 during its 2019 outburst, Ap&SS, 366, 84

Ramadevi, M., Ravishankar, B., Sitaramamurthy, N., et al. 2017, Early in-orbit performance of Scanning Sky Monitor onboard AstroSat, Journal of Astrophysics and Astronomy, 38, 1

Reig, P. 2011, Be/X-ray binaries, Ap&SS, 332, 1

Reig, P., Fabregat, J., & Coe, M. J. 1997, A new correlation for Be/X-ray binaries: the orbital period-Hα equivalent width diagram., A&A, 322, 193

Reig, P., Larionov, V., Negueruela, I., Arkharov, A. A., & Kudryavtseva, N. A. 2007, The Be/X-ray transient 4U 0115+63/V635 Cassiopeiae. III. Quasi-cyclic variability, A&A, 462, 1081

Reig, P., Negueruela, I., Buckley, D. A. H., et al. 2001, The Be/X-ray binary LS 992/RX J0812.4-3114: Physical parameters and long-term variability, A&A, 367, 266

Reig, P., Negueruela, I., Fabregat, J., Chato, R., & Coe, M. J. 2005, Long-term optical/IR variability of the Be/X-ray binary ¡ASTROBJ¿LS V +44 17¡/ASTROBJ¿/¡ASTROBJ¿RX J0440.9+4431¡/ASTROBJ¿, A&A, 440, 1079

Reig, P. & Nespoli, E. 2013, Patterns of variability in Be/X-ray pulsars during giant outbursts, A&A, 551, A1

Reig, P. & Roche, P. 1999, Discovery of two new persistent Be/X-ray pulsar systems, MNRAS, 306, 100

Reig, P., Torrejón, J. M., Negueruela, I., et al. 2009, Discovery of slow X-ray pulsations in the high-mass X-ray binary 4U 2206+54, A&A, 494, 1073

Reig, P. & Zezas, A. 2014, Disc-loss episode in the Be shell optical counterpart to the high-mass X-ray binary IGR J21343+4738, A&A, 561, A137

Reig, P. & Zezas, A. 2018, Discovery of X-ray pulsations in the Be/X-ray binary IGR J06074+2205, A&A, 613, A52

Reig, P., Zezas, A., & Gkouvelis, L. 2010, The optical counterpart to IGR J06074+2205: a Be/X-ray binary showing disc loss and V/R variability, A&A, 522, A107

Remillard, R. A., Loewenstein, M., Steiner, J. F., et al. 2022, An Empirical Background Model for the NICER X-Ray Timing Instrument, AJ, 163, 130

Revnivtsev, M., Churazov, E., Postnov, K., & Tsygankov, S. 2009, Quenching of the strong aperiodic accretion disk variability at the magnetospheric boundary, A&A, 507, 1211

Rivinius, T., Carciofi, A. C., & Martayan, C. 2013, Classical Be stars. Rapidly rotating B stars with viscous Keplerian decretion disks, A&A Rev., 21, 69

Rivinius, T., Štefl, S., & Baade, D. 2006, Bright Be-shell stars, A&A, 459, 137

Rosenberg, F. D., Eyles, C. J., Skinner, G. K., & Willmore, A. P. 1975, Observations of a transient X-ray source with a period of 104 S, Nature, 256, 628

Roy, K., Sharma, R., Manikantan, H., & Paul, B. 2024, Detection of a cyclotron line in the Be X-ray pulsar IGR J06074+2205, arXiv e-prints, arXiv:2402.17382

Saad, S. M., Kubát, J., Korčáková, D., et al. 2006, Observations of Hα, iron, and oxygen lines in B, Be, and shell stars, A&A, 450, 427

Santangeo, A., Segreto, A., Giarrusso, S., et al. 1999, A BeppoSAX study of the pulsating transient X0115+63: the first X-ray spectrum with four cyclotron harmonic features, arXiv e-prints, astro

Sartore, N., Jourdain, E., & Roques, J. P. 2015, The INTEGRAL/SPI view of A0535+26 during the Giant Outburst of 2011 February, ApJ, 806, 193

Savonije, G. J. 1978, Roche-lobe overflow in X-ray binaries., A&A, 62, 317

Schmidtke, P. C., Hunter, T. B., & Cowley, A. P. 2024, V-Band Photometry of IGR J06074+2205, The Astronomer's Telegram, 16560, 1

Schreier, E., Levinson, R., Gursky, H., et al. 1972, Evidence for the Binary Nature of Centaurus X-3 from UHURU X-Ray Observations., ApJ, 172, L79

Serim, M. M., Dönmez, Ç. K., Serim, D., et al. 2023, Timing analysis of Swift J0243.6+6124 with NICER and Fermi/GBM during the decay phase of the 2017-2018 outburst, MNRAS, 522, 6115

Shah, R. R., Jog, N. S., Subhedar, D. V., et al. 2005, The telescope control system at Mt. Abu infrared observatory., Bulletin of the Astronomical Society of India, 33, 237

Shakura, N. I. & Sunyaev, R. A. 1973, Black holes in binary systems. Observational appearance., A&A, 24, 337

Shapiro, S. L. & Lightman, A. P. 1976, Black holes in X-ray binaries: marginal existence and rotation reversals of accretion disks., ApJ, 204, 555

Simon, A., Bondar, A. V., & Metlova, N. V. 2012, A New Decretion Disk Around IGR J06074+2205, The Astronomer's Telegram, 4172, 1

Singh, K. P. 2018, The Impact of the Indian X-ray satellite, AstroSat, on Accretion Processes in Cosmic Sources, PoS, APCS2016, 007

Singh, K. P., Stewart, G. C., Westergaard, N. J., et al. 2017, Soft X-ray Focusing Telescope Aboard AstroSat: Design, Characteristics and Performance, Journal of Astrophysics and Astronomy, 38, 29

Singh, K. P., Tandon, S. N., Agrawal, P. C., et al. 2014, in Society of Photo-Optical Instrumentation Engineers (SPIE) Conference Series, Vol. 9144, Space Telescopes and Instrumentation 2014: Ultraviolet to Gamma Ray, ed. T. Takahashi, J.-W. A. den Herder, & M. Bautz, 91441S

Skinner, G. K., Bedford, D. K., Elsner, R. F., et al. 1982, Discovery of 69 ms periodic X-ray pulsations in A0538 - 66, Nature, 297, 568

Slettebak, A. 1982, Spectral types and rotational velocities of the brighter Be stars and A-F type shell stars., ApJS, 50, 55

Slettebak, A., Collins, George W., I., & Truax, R. 1992, Physical Properties of Be Star Envelopes from Balmer and Fe II Emission Lines, ApJS, 81, 335

Srivastava, M. K., Jangra, M., Dixit, V., et al. 2018, in Society of Photo-Optical Instrumentation Engineers (SPIE) Conference Series, Vol. 10702, Ground-based and Airborne Instrumentation for Astronomy VII, ed. C. J. Evans, L. Simard, & H. Takami, 107024I

Srivastava, M. K., Kumar, V., Dixit, V., et al. 2021, Design and development of Mt. Abu faint object spectrograph and camera–Pathfinder (MFOSC-P) for PRL 1.2 m Mt. Abu Telescope, Experimental Astronomy, 51, 345

Stanek, K. Z., Kochanek, C. S., Thompson, T. A., et al. 2017, ASAS-SN Optical Light Curve of Swift J0243.6+6124 Shows Long Term Variability, The Astronomer's Telegram, 10811, 1

Staubert, R., Trümper, J., Kendziorra, E., et al. 2019, Cyclotron lines in highly magnetized neutron stars, A&A, 622, A61

Steele, I., Negueruela, I., Coe, M., & Roche, P. 1998, The distances to the X-ray binaries LSI+ 61° 303 and A0535+ 262, Monthly Notices of the Royal Astronomical Society, 297, L5

Stella, L., White, N. E., & Rosner, R. 1986, Intermittent Stellar Wind Acceleration and the Long-Term Activity of Population I Binary Systems Containing an X-Ray Pulsar, ApJ, 308, 669

Stellingwerf, R. F. 1978, Period determination using phase dispersion minimization., ApJ, 224, 953

Sunyaev, R. A. & Titarchuk, L. G. 1980, Comptonization of X-Rays in Plasma Clouds - Typical Radiation Spectra, A&A, 86, 121

Tandon, S., Ghosh, S., Hutchings, J., Stalin, C., & Subramaniam, A. 2017, Ultraviolet Imaging Telescope on AstroSat

Tao, L., Feng, H., Zhang, S., et al. 2019, Super-Eddington Accretion onto the Galactic Ultraluminous X-Ray Pulsar Swift J0243.6+6124, ApJ, 873, 19

Tauris, T. M. & van den Heuvel, E. P. J. 2006, in Compact stellar X-ray sources, Vol. 39, 623–665

Telting, J. H., Heemskerk, M. H. M., Henrichs, H. F., & Savonije, G. J. 1994, Observational evidence for a prograde one-armed density structure in the equatorial disc of a Be star, A&A, 288, 558

Terada, Y., Mihara, T., Nakajima, M., et al. 2006, Cyclotron Resonance Energies at a Low X-Ray Luminosity: A0535+262 Observed with Suzaku, ApJ, 648, L139

Tobrej, M., Rai, B., Ghising, M., & Paul, B. C. 2024, NuSTAR detection of a broad absorption line in IGR J06074+2205, Journal of High Energy Astrophysics, 42, 129

Tomsick, J. A., Chaty, S., Rodriguez, J., Walter, R., & Kaaret, P. 2006, IGR J06074+2205 is a Be X-ray Binary, The Astronomer's Telegram, 959, 1

Townsend, L. J., Coe, M. J., Corbet, R. H. D., & Hill, A. B. 2011, On the orbital parameters of Be/X-ray binaries in the Small Magellanic Cloud, MNRAS, 416, 1556

Tsygankov, S. S., Doroshenko, V., Mushtukov, A. A., Lutovinov, A. A., & Poutanen, J. 2018, On the magnetic field of the first Galactic ultraluminous X-ray pulsar Swift J0243.6+6124, MNRAS, 479, L134

Tsygankov, S. S., Doroshenko, V., Mushtukov, A. A., et al. 2019, Cyclotron emission, absorption, and the two faces of X-ray pulsar A 0535+262, MNRAS, 487, L30

Tsygankov, S. S., Lutovinov, A. A., Churazov, E. M., & Sunyaev, R. A. 2006, V0332+53 in the outburst of 2004-2005: luminosity dependence of the cyclotron line and pulse profile, MNRAS, 371, 19

Tsygankov, S. S., Lutovinov, A. A., Churazov, E. M., & Sunyaev, R. A. 2007, 4U 0115+63 from RXTE and INTEGRAL data: Pulse profile and cyclotron line energy, Astronomy Letters, 33, 368

Turolla, R., Zane, S., & Titarchuk, L. 2002, Power-Law Tails from Dynamical Comptonization in Converging Flows, ApJ, 576, 349

van den Eijnden, J., Degenaar, N., Russell, T., et al. 2017, Radio non-detection of the new accreting neutron star transient and X-ray pulsar Swift J0243.6+6124, The Astronomer's Telegram, 10886, 1

van den Eijnden, J., Degenaar, N., Schulz, N. S., et al. 2019, Chandra reveals a possible ultrafast outflow in the super-Eddington Be/X-ray binary Swift J0243.6+6124, MNRAS, 487, 4355

van den Heuvel, E. P. J. 2004, in ESA Special Publication, Vol. 552, 5th INTEGRAL Workshop on the INTEGRAL Universe, ed. V. Schoenfelder, G. Lichti, & C. Winkler, 185

van der Klis, M., Stella, L., White, N., Jansen, F., & Parmar, A. N. 1987, Intensity and Source State Dependence of the Quasi-periodic Oscillations in Scorpius X-1, ApJ, 316, 411

van Dokkum, P. G. 2001, Cosmic-Ray Rejection by Laplacian Edge Detection, PASP, 113, 1420

Vasilopoulos, G., Ray, P. S., Gendreau, K. C., et al. 2020, The 2019 super-Eddington outburst of RX J0209.6-7427: detection of pulsations and constraints on the magnetic field strength, MNRAS, 494, 5350

Verner, D. A., Ferland, G. J., Korista, K. T., & Yakovlev, D. G. 1996, Atomic Data for Astrophysics. II. New Analytic FITS for Photoionization Cross Sections of Atoms and Ions, ApJ, 465, 487

Waters, L. B. F. M., de Martino, D., Habets, G. M. H. J., & Taylor, A. R. 1989, X-ray light curves of Be/X-ray binaries., A&A, 223, 207

White, N. E., Swank, J. H., & Holt, S. S. 1983, Accretion powered X-ray pulsars., ApJ, 270, 711

Wilms, J., Allen, A., & McCray, R. 2000, On the Absorption of X-Rays in the Interstellar Medium, ApJ, 542, 914

Wilson-Hodge, C. A., Malacaria, C., Jenke, P. A., et al. 2018, NICER and Fermi GBM Observations of the First Galactic Ultraluminous X-Ray Pulsar Swift J0243.6+6124, ApJ, 863, 9

Yadav, J., Agrawal, P., Antia, H., et al. 2016, in Space Telescopes and Instrumentation 2016: Ultraviolet to Gamma Ray, Vol. 9905, SPIE, 374–388

Yan, J., Li, H., & Liu, Q. 2012, Discrete Mass Ejections from the Be/X-Ray Binary A0535+26/HD 245770, ApJ, 744, 37

Zamanov, R., Stoyanov, K., Martí, J., et al. 2013, Hα observations of the γ-ray-emitting Be/X-ray binary LSI+61°303: orbital modulation, disk truncation, and long-term variability, A&A, 559, A87

Zamanov, R. K., Reig, P., Martí, J., et al. 2001, Comparison of the Hα circumstellar disks in Be/X-ray binaries and Be stars, A&A, 367, 884

Zechmeister, M. & Kürster, M. 2009, The generalised Lomb-Scargle periodogram. A new formalism for the floating-mean and Keplerian periodograms, A&A, 496, 577

Zeldovich, Y. B. & Guseynov, O. H. 1966, Collapsed Stars in Binaries, ApJ, 144, 840

Zhao, Y., Heinke, C. O., Tsygankov, S. S., et al. 2019, Soft excess in the quiescent Be/X-ray pulsar RX J0812.4-3114, MNRAS, 488, 4427

Ziolkowski, J. 2002, Be/X-ray binaries., Mem. Soc. Astron. Italiana, 73, 1038